

Robustness and spectroscopy of the toric code in a magnetic field

Dissertation
zur Erlangung des Grades eines Doktors der Naturwissenschaften
der Fakultät Physik der Technischen Universität Dortmund

Thèse de doctorat
pour obtenir le grade de Docteur
de l'Université Pierre & Marie Curie

Michael Kamfor

Date of defense: 16.04.2013
Members of thesis committee: Dr. Kai P. SCHMIDT (thesis advisor)
Dr. Julien VIDAL (thesis advisor)
Prof. Philippe LECHEMINANT (referee)
Prof. Roderich MOESSNER (referee)
Prof. Götz S. UHRIG (referee)
Dr. Benoît DOUÇOT (examiner)
Dr. Carsten RAAS Examineur (examiner)
Prof. Bernhard SPAAN Examineur (examiner)

Abstract

We study the robustness of topologically ordered phases under perturbation by considering the specific examples of the toric code and Kitaev's honeycomb models. More precisely, by means of high-order series expansions (pCUT) combined with a variational method (iPEPS) we analyze transitions between the topological and polarized phases of the toric code in a uniform magnetic field. We first describe the phase diagram of the perturbed toric code, and develop a quasi-particle picture of its elementary anyonic excitations. The effective model of interacting quasi-particles we derive allows us to analyze spectral properties of the low-energy physics of the perturbed toric code and unveil the presence of bound states. In a second step, we compute dynamical correlation functions (spectral densities) that are relevant for potential scattering experiments. Finally, we draw a connection between Kitaev's honeycomb model in a vortex superlattice and graphene in a strongly-modulated magnetic field, and present analytical results on metal-insulator transitions in these systems.

Wir untersuchen die Stabilität topologisch geordneter Phasen unter Einfluss von Störungen, anhand zweier Gittermodelle: dem Toric Code und dem Wabengittermodell von Kitaev. Mittels Hochordnungsreihenentwicklungen (pCUT), kombiniert mit einer variationellen Methode (iPEPS), werden Phasenübergänge zwischen der topologisch geordneten und der polarisierten Phase des Toric Code in einem homogenen Magnetfeld analysiert und das Phasendiagramm bestimmt. Weiterhin finden wir eine Quasiteilchenbeschreibung der elementaren anyonischen Anregungen für den gestörten Toric Code. Das somit formulierte effektive Modell wechselwirkender Quasiteilchen ermöglicht eine Analyse des Niederenergiespektrums des Toric Code, wo gebundene Zustände eine entscheidende Rolle spielen. Zusätzlich berechnen wir die für potentielle Experimente relevanten dynamischen Korrelationsfunktionen (spektrale Dichten). Die Beziehung zwischen Kitaevs Wabengittermodell unter Einfluss eines Vortexübergitters und Graphen in einem stark modulierten magnetischen Feld wird beleuchtet und der damit zusammenhängende Metall-Isolator-Übergang in diesen Modellen erklärt.

Nous étudions la robustesse des phases topologiques en présence d'une perturbation en considérant les cas spécifiques du code torique et du modèle de Kitaev sur réseau hexagonal. Plus précisément, en utilisant une combinaison de méthodes variationnelle (iPEPS) et perturbative (pCUT), nous analysons les transitions entre la phase topologique et la phase polarisée du code torique dans un champ magnétique uniforme. Nous décrivons tout d'abord le diagramme de phase à température nulle et développons une image des excitations élémentaires en termes de quasi-particules. Le modèle effectif que nous dérivons permet d'analyser les propriétés spectrales de basses énergies et de mettre en évidence l'existence d'états liés d'anyons. Dans un second temps, nous calculons les fonctions de corrélations dynamiques (densités spectrales), pertinentes pour de potentielles expériences de diffusion. Enfin, nous établissons un lien entre le modèle de Kitaev sur réseau hexagonal en présence d'une super-réseau de vortex et le graphène sous champ magnétique fortement inhomogène et présentons des résultats analytiques concernant la transition métal-isolant dans ces systèmes.

Contents

1	Introduction	1
1.1	Topological order	2
1.2	Exotic particles and their applications	3
1.3	Modeling of topological order	5
1.4	Goals of the thesis	7
2	Perturbative continuous unitary transformations	11
2.1	Notation	11
2.2	Continuous unitary transformations	12
2.3	Perturbative solution of the flow equations	14
2.4	Continuous unitary transformation of operators	18
3	Linked-cluster expansions	21
3.1	Introduction and overview	21
3.2	Linked-cluster theorem	22
3.3	Series expansions on finite graphs	24
4	The toric code	29
4.1	Model and ground-state properties	29
4.2	Properties of elementary excitations	34
4.3	Toric code in a magnetic field: limiting cases	38
5	pCUT method for the toric code in a field	47
5.1	Applying pCUT to a topological phase	47
5.1.1	First steps: effective operators, finite clusters	47
5.1.2	General procedure	51
5.1.3	Multi-particle subspace I: translational invariance	57
5.1.4	Multi-particle subspace II: non-locality	63
5.2	Applying pCUT to the high-field phase	66
5.3	Numerical tools	70
5.3.1	Computer program	70
5.3.2	Extrapolation methods	72
5.3.3	iPEPS	76
6	Phase diagram of the toric code in a uniform magnetic field	79
6.1	Preliminaries	79
6.1.1	Series expansion results	80
6.1.2	Combining pCUT and iPEPS	82

6.1.3	Critical exponents	83
6.2	Low-field limit: Ising line	84
6.3	Low-field limit: parallel fields	88
6.4	Low-field limit: arbitrary fields	95
6.5	High-field limit	107
6.6	Chapter summary	110
7	Bound states and spectral properties of the perturbed toric code	113
7.1	Spectrum of the two-quasi-particle subspace	113
7.1.1	First steps	114
7.1.2	Bound states in \mathcal{H}^b	117
7.1.3	Bound states in \mathcal{H}^f	121
7.2	Density of states	125
7.2.1	Subspace \mathcal{H}^b	125
7.2.2	Subspace \mathcal{H}^f	128
7.3	Spectral densities	130
7.3.1	Preliminaries	130
7.3.2	Examples and checks	135
7.3.3	Results	139
7.4	Chapter summary	145
8	Kitaev's honeycomb model	147
8.1	Definitions and basic properties	148
8.2	Mapping to fermions	151
8.3	Fate of Dirac points in a vortex superlattice	154
8.4	Chapter summary	164
9	Summary and Discussion	167
A	Effective operators	171
A.1	Toric code in the low-field limit	171
A.2	Toric code in the high-field limit	172
B	Series results	177
B.1	Hopping amplitudes of a dressed charge	177
B.2	Two-particle hopping amplitudes	179
B.3	High-field series expansions	185
B.4	Spectral densities coefficients	187
C	Spectral densities	189
	Bibliography	195
	Declaration of Authorship	208
	Acknowledgements	209

Introduction

The deep relationship between phase transitions and symmetry breaking is one of the most far-reaching concepts in theoretical physics. The observation that different phases of matter have different symmetries and that a transition from one phase to another must be accompanied by symmetry breaking has been merged into a phenomenological theory by L. Landau in the late 1930's. For almost half a century, Landau's symmetry breaking theory has been successfully applied to describe phase transitions in all known materials. However, in the 1980's, its limits have been revealed by experimental evidence of emergent phenomena in a two-dimensional electron gas where, in the presence of a magnetic field, the so-called fractional quantum Hall states form various phases *not* distinguishable by symmetry. This discovery has opened up a new playground for theorists since it demanded a new classification scheme for states of matter. X. G. Wen suggested to categorize these novel phases as a class of so-called topological orders, described by topological field theory. This has led to an exciting development of a new branch of condensed matter physics during the last two decades. Topological order has been found numerically in various models, particularly in frustrated spin models for quantum magnetism. Furthermore, the robustness of topological states with respect to local perturbations has drawn attention in the field of quantum computation where the spectacular concept of a 'topological' quantum computer, protected from decoherence, has been developed. The practical aspect of topological order has been put forward even stronger by A. Kitaev who, in a series of groundbreaking works, introduced two exactly solvable lattice models (the toric code, and the eponymous honeycomb model). These models are particularly well suited to probe topological order, in analogy to the Ising model which, in statistical physics, serves as a kind of prototype to demonstrate phenomena in 'conventionally' ordered systems.

In this introductory chapter, we will discuss the basic concepts mentioned above in more detail and motivate the main goals of this thesis.

1.1 Topological order

The power of Landau's symmetry breaking theory [1–3] is the generality of the concept which is used to understand phase transitions independently of the underlying microscopic model. In this context, phase transitions can be described by using a local order parameter \mathcal{O} . When the system is tuned through a phase transition, \mathcal{O} goes from a finite value in the ordered phase to zero in the disordered phase, thus defining a transition point between the two phases. The phase transition from the disordered phase into the ordered phase involves the loss of a symmetry, commonly referred to as 'spontaneous symmetry breaking'. A representative example of this mechanism is the heating of a ferromagnet. Here, the magnetization serves as a classical order parameter. While the magnetization has a finite value in the magnetic (ordered) phase, it vanishes when the temperature of the material is tuned beyond the Curie value. Then, the system is in a non-magnetic (disordered) phase. In a similar fashion, one is able to understand phase transitions for zero as well as finite temperatures in metals, superconductors, superfluids and many other materials.

So what is topological order? And why is it so interesting? By definition, Landau's theory is local so that it might be challenging to describe, for example, a phase transition between two highly entangled quantum ground states. Such an exotic transition is not merely hypothetical, in fact, the area of research concerned with topologically-ordered matter has been initiated by actual experiments. In 1989, Wen [4, 5] introduced the term 'topological order' to emphasize the non-local character of the so-called chiral-spin states [6], proposed to describe the ground state in high-temperature superconductors. The degeneracy of chiral spin states depends on the global shape of the system. Already in 1988, Laughlin [7] pointed out a connection between the mechanism behind high-temperature superconductivity in $\text{La}_{2-x}\text{Ba}_x\text{CuO}_4$ and the fractional quantum Hall (FQH) effect¹, discovered by Tsui et al. [8, 9] in 1982.

According to Wen, a formal description of topologically-ordered quantum states is provided by topological field theory [10, 11]. However, we prefer to use a slightly more intuitive definition of topological order suggested by Nussinov and Ortiz [12, 13]. Consider a gapped quantum system at zero temperature with a set of N_g orthonormal ground states labeled by $\{|g_\alpha\rangle\}$, with $\alpha \in \{1, \dots, N_g\}$. In addition, we introduce the operator

¹We remark that while the relevance of topological order for high-temperature superconductivity is under debate, it is essential for the FQH effect.

$V = \sum_i v_i$, with *quasi-local* operators v_i . This means that V is generally a superposition of operators, each one acting in a finite area (the size of this area should not scale with system size). A system is topologically ordered if, for any V satisfying the above criteria, the following equation holds

$$\langle g_\alpha | V | g_\beta \rangle = \nu \delta_{\alpha\beta} + c_{\alpha\beta}, \quad (1.1)$$

where ν is a constant and $c_{\alpha\beta}$ is either zero or it vanishes in the thermodynamic limit. Thus, a finite-order perturbation theory does not couple any of the ground states. This is a formal way to say that a topologically-ordered state is stable against local perturbations. This robustness is a characteristic feature of all topological orders. It is also present in the generalization of the above definition to finite temperatures in Ref. [13]. The most striking implication of this property is that one cannot distinguish topologically-ordered states by *local* measurements. Since there is no local order parameter, Landau's symmetry breaking theory does not apply. So, how can we characterize topological order? Topologically-ordered states can be labeled by using *global* operators (often referred to as topological invariants). Therefore, boundary conditions are crucial in the sense that the ground-state degeneracy depends on the topology, and properties of edge excitations become important attributes. Oshikawa et al. [14] have shown that there is a fundamental connection between topological order and the fractionalization of quantum numbers. More precisely, elementary excitations of a topologically-ordered system can be Abelian or non-Abelian anyons, discussed in the next section.

1.2 Exotic particles and their applications

One of the fascinating properties of topologically-ordered systems is the emergence of anyons as elementary excitations. Anyons are often called exotic particles because they obey neither the Fermi-Dirac statistics nor the Bose-Einstein statistics. Let us shortly recall that all elementary particles (leptons, quarks, gluons, ...) are known to fall into either of the two categories: fermions or bosons. When two identical particles at positions \mathbf{r}_1 and \mathbf{r}_2 are interchanged, the probability distribution of the global wave function $\Psi(\mathbf{r}_1, \mathbf{r}_2)$ must stay the same

$$|\Psi(\mathbf{r}_1, \mathbf{r}_2)|^2 = |\Psi(\mathbf{r}_2, \mathbf{r}_1)|^2. \quad (1.2)$$

Thus, the exchange of positions yields a global phase:

$$\Psi(\mathbf{r}_1, \mathbf{r}_2) = e^{i\theta} \Psi(\mathbf{r}_2, \mathbf{r}_1). \quad (1.3)$$

Interchanging the particles one more time brings the system into its original state so that the global phase becomes $+1$. This yields the two possible solutions: $\theta = 0$ and $\theta = \pi$. In the first case, Ψ is fully symmetric and, due to the spin-statistics theorem, the particles are identified with bosons. In the second case, Ψ is fully antisymmetric so that the corresponding particles must be fermions. Leinaas and Myrheim [15] pointed out the weakness of the notation in (1.2) which does not take into account the space geometry so that the operation 'interchange' is actually not well-defined. Indeed, the above argumentation holds only in a space with three or more dimensions where all paths leading a particle to its initial position can be continuously contracted and are thus topologically equivalent. In two dimensions this is not the case. Figure 1.1 illustrates

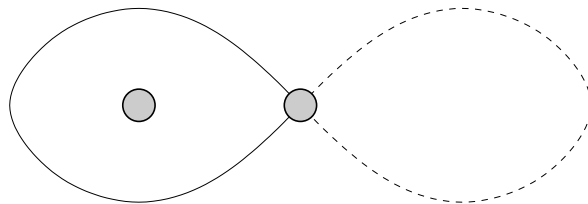


FIGURE 1.1: A pair of identical particles in two spatial dimensions. The solid and the dashed lines, represent two topologically distinct paths of a particle.

that moving one particle around the other yields a non-contractible 'knot' (also called 'braid'), in contrast to a trivial path where the particle encircles the vacuum. Using similar arguments, Leinaas and Myrheim [15] have shown that equation (1.3) admits further solutions in two dimensions, in the sense that θ may actually be *any* rational number. This defines a new type of particles, dubbed 'anyons' by Wilczek [16]. The statistics of anyons is referred to as 'fractional' because it interpolates between the one of bosons and fermions ("any-on").

Initially, anyons have drawn a purely academic interest. Although charge-flux composites show anyonic behavior [16], due to the Aharonov-Bohm effect [17], Wilczek remarked that "practical applications of these phenomena seem remote" [16]. However, it turns out that anyons not only do exist in nature, but they also play a key role in the physics of topologically-ordered systems. Most prominently, the elementary excitations of the FQH liquids are strong candidates for anyonic quasi-particles. In their famous FQH experiment, Tsui, Störmer, and Gossard [8] confined electrons to two dimensions, on the interface between two semiconductors. At almost zero temperature and in the presence of a strong magnetic field, the electrons form a correlated quantum liquid. For specific values of the magnetic field, where the filling of the lowest Landau level is $\nu = n/m$ with integer n and m , one finds gapped excitations. The corresponding ground states are, for odd m , excellently described by the Laughlin wave function [9]. Using the Laughlin

ground state, Arovas et al. [18] have shown that, for $m > 1$, the elementary excitations behave as anyons. The precise correspondence between experiment and theory (the comprehension of the FQH effect has been acknowledged by a Nobel prize in 1998) is a convincing evidence of the existence of anyons. However, a direct measurement of the braiding phase remains challenging and is an active research area [19–21].

So far, our discussion focused on the so-called Abelian anyons, where the term 'Abelian' refers to the fact that all braiding operations (moving one particle around the other) commute. The concept of anyons can be generalized to the non-Abelian case, with non-commuting braiding operations. This property enlarges the Hilbert space of anyons. This means that the $[U(1)]$ one-dimensional phase, associated with braiding of Abelian anyons, has to be replaced by a higher-dimensional operator. For more details on the physics of non-Abelian anyons we refer the reader to the review [22]. Non-Abelian anyonic states have been suggested as possible ground states in the 'even-denominator' phases of the FQH effect [23, 24], and recent experimental data seem to confirm this proposal [25–27].

Kitaev has realized that braiding properties of anyons can be used to encode information [28]. Even more fascinating, one can perform logical operations by manipulating non-Abelian anyons [28]. Thus, the idea of a topological quantum computer has been born. A topological quantum computer has the fantastic feature of being robust against decoherence, a long-standing obstacle on the way to realize a practical computer with quantum logic. This can be roughly explained by regarding a loop of one particle around another. Local perturbations caused by decoherence may distort the shape of the loop. However, the information stored in the braiding phase is saved as long as these distortions are small compared to the distances of the particles.

1.3 Modeling of topological order

Topological phases are expected to appear in systems with strongly-correlated quantum ground states. Thus it is common to work at zero temperature or, at least, in the regime where quantum fluctuations dominate over thermal fluctuations. In addition to continuous theories describing, e.g., FQH physics, topological order is also found in certain lattice models of quantum magnets. One of the earliest models featuring a fractionalization of quantum numbers has been proposed by Anderson in 1973 [29]. The so-called resonating valence bond theory describes a frustrated Heisenberg magnet by considering spin-1/2 degrees of freedom on typically triangular, kagome, or pyrochlore lattices [29–32]. The ground state is formed by a superposition of disordered singlets (a quantum spin liquid), and is usually gapped in the short range regime of the model where singlets

are formed by neighboring spins. Signatures of topological order are globally conserved parity operators (their eigenvalues cannot be changed by a local rearrangement of singlet dimers), the number of which depends on the boundary conditions. Possible elementary excitations are charge-free spin-1/2 quasi-particles (spinons) while, intuitively, one would expect (triplet) excitations with an integer spin. Pairing of spinons has been proposed to be a possible explanation of high-temperature superconductivity in cuprates [33]. While this proposal is under debate [7], the concept of quantum spin liquids has received much attention in recent years [32] because topologically-ordered ground states of various models (including the toric code) are indeed quantum spin liquids [34–36].

A particularly simple model with a topologically-ordered ground state has been proposed and solved exactly by Kitaev in his seminal paper [28]. Kitaev named the model ‘toric code’ since it has non-trivial properties on the torus and has been developed in the context of stabilizer codes [37, 38], used for topological quantum computation. It describes spins-1/2 on *bonds* of a square lattice (the toric code is closely related to Wen’s plaquette model [39] in which spins reside on vertices of the square lattice). The Hamiltonian contains solely four-body interactions between spin quadruples neighboring a vertex or sharing a plaquette of the lattice. It has become one of the standard examples of topologically-ordered systems. As will be discussed in more detail in Section 4 of this manuscript, the toric code allows to clearly demonstrate several important principles of topological order. The ground state is a \mathbb{Z}_2 quantum spin liquid protected by a gap and has a degeneracy which depends on the topology. Elementary excitations have braiding properties of Abelian anyons so that they can be used to construct a robust quantum memory [40]. The \mathbb{Z}_2 toric code can be generalized to \mathbb{Z}_N [41, 42] or to so-called string-net models on trivalent graphs [35]. While, from a technical point of view, the \mathbb{Z}_2 -toric code is a rather simple model, its particular interaction patterns are difficult to realize in an experiment. Commonly discussed experimental setups involve polar molecules [43] or Rydberg atoms [44] in optical lattices, Josephson-junction arrays [45, 46], trapped ions [47, 48] or polarized photons [49].

One of the biggest experimental obstacles in realizing the toric code in an experiment are its particular four-body interactions. This problem is less pronounced in the so-called Kitaev model on the honeycomb lattice [36] which is based on *two*-body interactions and also features a topologically-ordered ground state. We will introduce the honeycomb model in detail in Chapter 8. Here, we simply wish to point out that, in a certain limit, this model is intimately connected with (however not equivalent to) the toric code². The honeycomb model hosts gapped fermions and Abelian anyons as elementary

²In fact, the effective low-energy theory of the honeycomb model in the limit of weakly-coupled dimers is the toric code with additional effective interactions. These appear at higher orders in perturbation theory [50].

excitations. An additional feature, when comparing to the toric code, is a gapless region in the parameter space. Time-reversal symmetry breaking operators, e.g., a magnetic field, or three-spin interactions, may open a gap that gives rise to non-Abelian elementary excitations. The rich structure of the phase diagram as well as the appearance of non-Abelian anyons are particularly interesting because the honeycomb model is, by construction, easier to realize in an experiment than, e.g., the toric code. There are concrete proposals to build this model using polar molecules in optical lattices [51, 52], Josephson-junction arrays [45, 46] and quantum circuits [53]. Additionally, there is legitimate hope to discover Kitaev's honeycomb model in solid-state systems. For instance, strong spin-orbit coupling in iridates may lead to the kind of anisotropic interactions which are essential to realize this model [54, 55].

In the models discussed above, the robustness of the ground state with respect to local perturbations arises from conservation of topological invariants. In contrast, the so-called symmetry protected topological states are, as their name already suggests, robust with respect to local perturbations which conserve their symmetry. The concept of symmetry protected topological states has drawn much attention recently in the context of topological insulators [56–58]. These are band insulators with metallic edge states, protected against Anderson localization. There are several types of topological insulators. However, all of them feature gapless edge excitations with fractionalized quantum numbers (see the review in Ref. [59]). Well-controlled experiments on topological insulators give hope for a realization of a topological quantum computer [60, 61]. Remarkably, topological insulators also exist in three dimensions [62, 63] where edge excitations are proposed to be non-Abelian surface states.

1.4 Goals of the thesis

There are two important motivations to study topologically-ordered systems. On the one hand it is interesting to learn more about exotic states of matter, on the other hand there are exciting applications in the field of quantum computation. A major question in this area of research concerns the robustness of a topological phase. We have already claimed that topological phases are stable under local perturbations. A rigorous proof for small perturbations can be found in Ref. [64]. However, it should be clear that a very strong disturbance will eventually destroy a topological phase. To give a simple example, a magnetic field which is much stronger than the interactions stabilizing the toric code will polarize the system and thus lead to a conventional phase with a unique ground state and magnon excitations.

The main goal of this thesis is to study the breakdown of topologically-ordered phases. More specifically, we will investigate phase transitions between the topologically-ordered and the polarized phases of the toric code in a uniform magnetic field. Note that, at zero temperature, a magnetic field is one of the simplest perturbations in a spin system. So far, the toric code in a magnetic field has been analyzed with Monte Carlo simulations [65–67] and series expansions [68, 69]. However, these studies concentrated on specific directions of the field, referred to as 'parallel' and 'transverse'. It has been demonstrated that the low-energy physics is completely different in both cases. Generally, a magnetic field excites particles of two different types, referred to as 'charges' and 'fluxes'. As will be shown explicitly in Chapter 4, particles with different flavors behave as Abelian anyons while among themselves they are bosons. A parallel magnetic field generates quantum fluctuations consisting of pairs of dispersive charges or fluxes. The condensation of either kind of elementary excitations leads to a continuous (second-order) phase transition in the universality class of the 3d transverse-field Ising model. Except in a symmetric point, where fluxes and charges condense simultaneously. Here, a different universality class is found [68]. When the toric code is perturbed by a transverse magnetic field, charges and fluxes are always excited simultaneously. They form bound states which are either non-dispersive, or dispersive in only one spatial dimension. In deep contrast to the parallel-field case one finds that the phase transition is discontinuous (first-order). In this manuscript, we go beyond these limiting cases, treated by previous studies, and consider a general field direction in order to determine the full phase diagram of the toric code and study the interplay of the described physical properties. For which parameters of the magnetic field is the phase transition of first or second order? What is the fate of bound states when a parallel field is added to the transverse field? Does the system stay in the universality class of the 3d transverse-field Ising model when a transverse field is included? These are typical questions we shall address in this thesis.

Interestingly, the robustness of a topological phase with respect to thermal fluctuations has been the topic of several recent papers. General studies of the stability with respect to temperature [70–72] indicate that topological order in the toric code might break down at finite temperatures. The robustness of the quantum memory property of the toric code with respect to noise and disorder has been discussed in Refs. [73, 74]. It has been found that, due to localization effects, the memory is stable under certain noise thresholds.

Let us shortly discuss some methodological aspects of this study. From a technical point of view, the difficulty to investigate phase transitions in topologically-ordered matter stems from the fact that there is no local order parameter. Often, the sign problem prevents an efficient use of quantum Monte Carlo. One can use a variational ansatz to

simulate ground states of strongly-correlated quantum systems with tensor networks [75–77]. Especially the so-called projected entangled-pair state (PEPS) seems to be well suited to the problem at hand since, as has been shown in Ref. [78], it represents the *exact* ground state of the unperturbed toric code. However, it should be stressed that often the necessary computational effort to simulate states with pronounced *long-range* entanglement exceeds the available resources. In Refs. [50, 68, 69, 79–81] it has been successfully demonstrated that the breakdown of topological order can be studied by means of high-order perturbative expansions. The advantage of this approach is that it does not suffer from the sign problem, neither is it generally sensitive to the amount of entanglement in the system. Consequently, we shall use perturbative continuous unitary transformations [82, 83] (pCUT) in order to perform perturbation theory for the toric code in the limit of small magnetic fields. Besides being a powerful tool to perform perturbation theory, the pCUT approach provides a systematic way to obtain a quasi-particle picture of the model which leads to an intuitive and clear illustration of the essential physics governing the low-energy regime of a topological phase. Note that it is a nontrivial task to develop a quasi-particle picture for the elementary (anyonic) excitations of the toric code because of their non-local properties. However, the description of the low-energy subspace via quasi-particles is utterly important since their condensation defines a critical point. Furthermore, we shall use the effective model of quasi-particles to study interactions between anyons which, depending on the field direction, may lead to bound states. Moreover, we are interested in observables that can be ingeniously computed with the pCUT technique. We shall also compute dynamical equal-time correlation functions (spectral densities) relevant for scattering experiments, and discuss their behavior as a function of the direction of the magnetic field.

We begin our study with a short introduction to the pCUT method in Chapter 2 and continue by discussing formal properties of series expansions on graphs in Chapter 3. In Chapter 4, we discuss the unperturbed toric code and the exact construction of its ground state as well as elementary excitations. The exact solvability is lost when a magnetic field is included. However, we show that, in certain limiting cases, exact mappings onto known models exist. In Chapter 5, we develop a concrete scheme which allows one to apply pCUT on finite-size graphs to the toric code in a field. We provide a detailed guidance on how to perform this task in the low-field as well as high-field limits of the model. Being a technical chapter, the Chapter 5 also includes a short discussion on our computer program as well as methods used to extrapolate the series expansions. We compute the series expansion of the ground-state energy and the single-anyon dispersion for the toric code and present the results in Chapter 6. We use the limiting cases where exact mappings and numerical studies exist to check our method and estimate its accuracy. In order to study phase transitions of first *and* second order, we introduce a new approach

based on a combination of a variational method (iPEPS) with pCUT. In Chapter 7, the two-particle subspace inside the topological phase is considered. Here, we analyze the spectral properties by means of exact diagonalization of the effective model. We discuss the main features of the spectrum consisting of a two-particle continuum and bound states that appear to depend on the field direction and strength. We are interested in the general properties of these bound states. Additionally it would be interesting to find out whether they can even drive phase transitions in the perturbed toric code. Finally, our study of the toric code in a field is completed by the computation of the density of states as well as spectral densities. With these results, we gain an insight to interesting features one might observe in potential scattering experiments. In Chapter 8, we discuss Kitaev's honeycomb model which seems closer to an experimental realization. We propose a generalization of this model to an infinite set of exactly solvable models. Furthermore, we show that the spectrum of certain subspaces of the honeycomb model (non-trivial vortex configurations) is equivalent to the one of graphene in a strongly-modulated magnetic field. We discuss how the commensurability of the superlattice triggers the gap opening. Our most important results are summarized and discussed in Chapter 9 where we also give perspectives for further studies on this topic.

Perturbative continuous unitary transformations

Most of the results in this work are based on series expansions obtained with perturbative continuous unitary transformations (pCUT). With pCUT, a Hamiltonian can be transformed into an optimal basis, in which the low-energy physics of a many-body system can be described by quasi-particles. This quasi-particle picture is very useful for an intuitive understanding of the low-energy physics. For specific Hamiltonians where the CUT can be performed in a perturbative fashion one profits from the fact that, in the optimal basis, the perturbative expansion can be pushed to rather high orders. If one is interested in the non-perturbative regime of a model, a *high*-order expansion is inevitable in order to obtain quantitative results with significant precision. The main goal of this chapter is to introduce the basic ideas behind this method in a short but consistent way. For a detailed introduction to the pCUT technique we refer to original works by Wegner [82], Głazek and Wilson [84], Stein [85], and Uhrig, Knetter, and Schmidt [83, 86, 87].

2.1 Notation

For discussions involving quasi-particles we will first specify a useful notation. Let us, consider a particle-counting operator Q with an eigenbasis $\{|n\rangle\}$, where $n \in \mathbb{N}$, and $|n\rangle$ represents an n -particle state:

$$Q|n\rangle = n|n\rangle. \tag{2.1}$$

Naturally, we will need a particle creation (or annihilation) operator $T_m = T_{-m}^\dagger$ (with $m \in \mathbb{Z}$) which changes the number of particles in a state by m :

$$T_m |n\rangle = \begin{cases} |n+m\rangle, & \text{for } m+n \geq 0, \\ 0, & \text{for } m+n < 0. \end{cases} \quad (2.2)$$

From the above definitions it follows the important relation

$$[Q, T_m] = mT_m, \quad (2.3)$$

which can be easily checked by letting the operators act in the eigenbasis of Q . As shall become clear in the next section, we will benefit from a compact notion of sequences of T_m operators, where it is useful to denote a k -tuple of indices $m_i \in \mathbb{Z}$ as follows

$$\mathbf{m} = (m_1, m_2, m_3, \dots, m_k), \quad (2.4)$$

$$|\mathbf{m}| = k, \quad (2.5)$$

$$M(\mathbf{m}) = \sum_{i=1}^k m_i. \quad (2.6)$$

A k -fold product of creation or annihilation operators will thus be denoted as:

$$T(\mathbf{m}) = T_{m_1} T_{m_2} T_{m_3} \dots T_{m_k}. \quad (2.7)$$

For later purposes, we generalize Eq. (2.3) to:

$$[Q, T(\mathbf{m})] = \sum_{i=1}^k m_i T(\mathbf{m}) = M(\mathbf{m}) T(\mathbf{m}). \quad (2.8)$$

2.2 Continuous unitary transformations

As it is well known, most many-body problems in physics cannot be solved directly by diagonalization. In an attempt to 'almost diagonalize' a Hamiltonian, Wegner [82] introduced the concept of a continuous unitary transformation (CUT) and successfully applied it to the one-dimensional n -orbital model in the thermodynamic limit. In a parallel work, Głazek and Wilson [84] suggested an akin approach, motivated by an optimization of perturbation theory in high-energy physics.

As will be explained in more detail below, one aims to find a transformation which decouples certain subspaces of the Hilbert space, in order to be able to study them separately. Thus, the problem would be greatly simplified, while the unitarity of the

transformation ensures that the spectrum does not change. Formally, the transformation rotates the initial Hamiltonian H into a block-diagonal shape.

Generally, a continuous unitary transformation can be represented by an infinite sequence of discrete unitary transformations. However, it is more convenient to parametrize the transformation by a running parameter l , defined implicitly by

$$H(l = 0) = H, \quad (2.9)$$

$$H(l > 0) = U(l)H(0)U^\dagger(l), \quad (2.10)$$

where H is the initial Hamiltonian, and $U(l)$ an arbitrary unitary transformation. The dependence of H on the parameter l can now be formulated in terms of flow equations

$$\frac{d}{dl}H(l) = \left[\frac{d}{dl}U(l) \right] H(0)U^\dagger(l) + U(l)H(0) \left[\frac{d}{dl}U^\dagger(l) \right], \quad (2.11)$$

$$= \left[\frac{d}{dl}U(l) \right] U^\dagger(l)H(l) + H(l)U(l) \left[\frac{d}{dl}U^\dagger(l) \right], \quad (2.12)$$

$$= [\eta(l), H(l)], \quad (2.13)$$

$$\eta(l) = \left[\frac{d}{dl}U(l) \right] U^\dagger(l) = -U(l) \left[\frac{d}{dl}U^\dagger(l) \right], \quad (2.14)$$

where in the second line, the identity $U^\dagger(l)U(l) = \mathbf{1}$ has been used. The CUT can thus be performed by choosing a function $\eta(l)$ (usually referred to as the 'generator') which, due to (2.12), must be antihermitian. The choice of the generator can be problem-dependent. Nevertheless, generally, one is interested to make off-diagonal matrix elements vanish in the limit $l \rightarrow \infty$. Our special interest is to derive an effective Hamiltonian

$$H_{\text{eff}} = \lim_{l \rightarrow \infty} H(l), \quad (2.15)$$

which conserves the number of quasi-particles. To say this differently, we want to decouple Hilbert spaces with different numbers of quasi-particles. Requiring quasi-particle conservation leads to the condition

$$[Q, H_{\text{eff}}] = 0. \quad (2.16)$$

With (2.13), a possible choice for the generator is

$$\eta(l) = [Q, H(l)]. \quad (2.17)$$

As long as the right-hand side of (2.17) is non-zero, $H(l)$ is subject to a finite flow, governed by (2.13). If it does turn zero, the flow stops and $H(l)$ is converged into its $l \rightarrow \infty$ limit. This generator has been designed by Mielke [88] and generalized by Knetter

and Uhrig [83]. Furthermore, it has the property to preserve a possible block diagonality of the initial Hamiltonian. The modified generator can be best defined through its matrix elements:

$$\eta_{ij}(l) = \text{sgn}(q_{i,i} - q_{j,j}) h_{ij}(l) = \begin{cases} h_{ij}(l), & \text{for } q_{i,i} > q_{j,j} \\ -h_{ij}(l), & \text{for } q_{i,i} < q_{j,j} \\ 0, & \text{for } q_{i,i} = q_{j,j} \end{cases}, \quad (2.18)$$

where $\eta_{ij}(l)$ and $h_{ij}(l)$ are the respective matrix elements of $\eta(l)$, and $H(l)$ in the eigenbasis of Q , and $q_{i,i}$ is the number of quasi-particles in the state $|i\rangle$.

Finally, CUT can be applied to a Hamiltonian by discretizing (2.13) and thus generating a set of coupled differential equations which can be successively solved under certain (problem-dependent) approximations [82, 89–92]. Often, these approximations are based on various truncation schemes which close the flow equations thus keeping the number of differential equations finite. In the next chapter, we will follow an alternative route by solving the flow equations perturbatively.

2.3 Perturbative solution of the flow equations

Generally, a perturbatively treatable problem can be represented by

$$H = H_0 + \lambda V, \quad (2.19)$$

where the exact solution of H_0 is known, and V is a perturbation, kept small by λ . There are two different strategies to obtain a perturbative solution of the flow equations (2.13). One approach is to apply a series ansatz in order to directly solve the flow equations by a numerical algorithm, e.g., Runge-Kutta methods [93]. However, for specific Hamiltonians, it is possible to solve (2.13) in an analytical way. We will explain this second approach (referred to as pCUT) in more detail since it is well suited for an application to the toric code. The constraints which must be introduced in order to use this technique are listed in the following.

- (i) **The spectrum of the unperturbed Hamiltonian H_0 is discrete and bounded from below.**

In other words, H_0 can be represented by a finite or a semi-infinite matrix. For later purposes, we label the discrete energy levels by ϵ_i (with $i \in \mathbb{N}$) and define elementary excitation energies $\Delta\epsilon_i = \epsilon_i - \epsilon_0$.

- (ii) **There must be a $\Delta\epsilon$, such that any elementary excitation can be written as**

$$\Delta\epsilon_i = n_i\Delta\epsilon, \quad (2.20)$$

with $n_i \in \mathbb{N}$. Note that the most simple realization of this condition is an equidistant spectrum. It is natural to set $\Delta\epsilon = 1$ so that the energy cost of an elementary excitation corresponds to the number of particles. Within this description, H_0 turns out to be exactly the particle-counting operator Q , defined in (2.1).

- (iii) **There exists a number $N \in \mathbb{N}$ such that the perturbation V can be written as:**

$$V = \sum_{m=-N}^{m=+N} T_m, \quad (2.21)$$

where the operator T_m changes the number of particles in the system by m [as defined in (2.2)].

Surely, the above conditions restrain the applicability of pCUT; still there exists a notable amount of models suitable for this method, e.g., in the area of low-dimensional quantum magnets including frustration, spin ladders, supersolids, nuclear physics, as well as stabilizer codes and cluster Hamiltonians including topologically-ordered spin models [42, 50, 68, 69, 80, 81, 87, 94–99], to name just a few.

In the following, we will follow the route of Stein, Knetter, and Uhrig [83, 85], and reduce the flow equation problem to coupled differential equations for which a recursive solution is presented. The commutator structure of the flow equations leads to the following general ansatz for the flow-dependent part of the Hamiltonian, namely $V(l)$:

$$V(l) = \sum_{k=1}^{\infty} \lambda^{k-1} \sum_{|\mathbf{m}|=k} F(l; \mathbf{m}) T(\mathbf{m}). \quad (2.22)$$

The second sum runs over all permutations of k -tuples of $m_i \leq N$ with $N \in \mathbb{N}$. The unknown functions $F(l; \mathbf{m})$ are determined below. See also Section (2.1) for notations. In order to directly use the definition of the quasi-particle-conserving generator (2.18), we consider the matrix elements of our Hamiltonian in the eigenbasis of its unperturbed part Q

$$\langle n_i | H(l) | n_j \rangle = \langle n_i | Q + \lambda V(l) | n_j \rangle = q_{i,j} + \lambda v_{i,j}, \quad (2.23)$$

$$\langle n_i | T(\mathbf{m}) | n_j \rangle = t_{i,j}(\mathbf{m}). \quad (2.24)$$

Note that there is no l -dependence in Q since it already is diagonal. The generator can now be expressed in terms of T operators:

$$\langle n_i | \eta(l) | n_j \rangle = \eta_{i,j}(l) \quad (2.25)$$

$$= \text{sgn}(q_{i,i} - q_{j,j}) (q_{i,j} + \lambda v_{i,j}(l)) \quad (2.26)$$

$$= \text{sgn}(q_{i,i} - q_{j,j}) \lambda v_{i,j}(l) \quad (2.27)$$

$$= \sum_{k=1}^{\infty} \lambda^k \sum_{|\mathbf{m}|=k} F(l; \mathbf{m}) \text{sgn}(q_{i,i} - q_{j,j}) t_{i,j}(\mathbf{m}), \quad (2.28)$$

where we used the diagonality of Q in the second line. Using (2.8), one can perform a crucial simplification, by eliminating the unperturbed part of the Hamiltonian from the generator:

$$M(\mathbf{m})T(\mathbf{m}) = [Q, T(\mathbf{m})], \quad (2.29)$$

$$M(\mathbf{m})t_{i,j}(\mathbf{m}) = [Q, T(\mathbf{m})]_{i,j} \quad (2.30)$$

$$= (q_{i,i} - q_{j,j}) t_{i,j}(\mathbf{m}), \quad (2.31)$$

$$\text{sgn}[M(\mathbf{m})] t_{i,j}(\mathbf{m}) = \text{sgn}(q_{i,i} - q_{j,j}) t_{i,j}(\mathbf{m}). \quad (2.32)$$

The equation (2.32) inserted into (2.28), yields the following operator identity:

$$\eta(l) = \sum_{k=1}^{\infty} \lambda^k \sum_{|\mathbf{m}|=k} F(l; \mathbf{m}) \text{sgn}[M(\mathbf{m})] T(\mathbf{m}). \quad (2.33)$$

Inserting $\eta(l)$, as well as the ansatz for $V(l)$, into the flow equation (2.13) yields (note that $\frac{d}{dl}Q = 0$):

$$\frac{d}{dl}H(l) = \lambda \frac{d}{dl}V(l), \quad (2.34)$$

$$= \lambda [\eta(l), V(l)] - [Q, \eta(l)], \quad (2.35)$$

$$= \lambda [\eta(l), V(l)] - \sum_{k=1}^{\infty} \lambda^k \sum_{|\mathbf{m}|=k} F(l; \mathbf{m}) \text{sgn}[M(\mathbf{m})] \underbrace{[Q, T(\mathbf{m})]}_{M(\mathbf{m})T(\mathbf{m})}. \quad (2.36)$$

Now, we insert the ansatz (2.22) for $V(l)$, and collect powers of λ on the right-hand side of (2.34)

$$\begin{aligned} \sum_{k=1}^{\infty} \lambda^k \sum_{|\mathbf{m}|=k} \frac{d}{dl} F(l; \mathbf{m}) T(\mathbf{m}) &= \sum_{\substack{k_1, k_2 \\ |\mathbf{m}_1|=k_1 \\ |\mathbf{m}_2|=k_2}} \lambda^{k_1+k_2} F(l; \mathbf{m}_1) F(l; \mathbf{m}_2) \text{sgn}[M(\mathbf{m}_1)] [T(\mathbf{m}_1), T(\mathbf{m}_2)] \\ &\quad - \sum_{\substack{k \\ |\mathbf{m}|=k}} \lambda^k F(l; \mathbf{m}) |M(\mathbf{m})| T(\mathbf{m}). \end{aligned} \quad (2.37)$$

The functions $F(l; \mathbf{m})$ are thus determined through coupled differential equations, found by comparing coefficients in (2.36) and (2.37):

$$\begin{aligned} \frac{d}{dl} F(l; \mathbf{m}) = & - |M(\mathbf{m})| F(l; \mathbf{m}) \\ & + \sum_{\substack{\{\mathbf{m}_1, \mathbf{m}_2\} = \mathbf{m} \\ |\mathbf{m}| \geq 2}} \{ \text{sgn}[M(\mathbf{m}_1)] - \text{sgn}[M(\mathbf{m}_2)] \} F(l; \mathbf{m}_1) F(l; \mathbf{m}_2). \end{aligned} \quad (2.38)$$

In the second term of the right-hand side the sum runs through all possible partitions $\{\mathbf{m}_1, \mathbf{m}_2\} = \mathbf{m}$, which for the general case $|\mathbf{m}| = k$ are defined as follows:

\mathbf{m}_1	\mathbf{m}_2	
(m_1)	(m_2, \dots, m_k)	
(m_1, m_2)	(m_3, \dots, m_k)	
\vdots	\vdots	
(m_1, \dots, m_{k-1})	(m_k)	.

(2.39)

An elegant way to get rid of the linear term in (2.38) is to introduce

$$F(l; \mathbf{m}) = e^{-|M(\mathbf{m})|l} f(l; \mathbf{m}). \quad (2.40)$$

Finally we obtain

$$\begin{aligned} \frac{d}{dl} f(l; \mathbf{m}) = & \sum_{\substack{\{\mathbf{m}_1, \mathbf{m}_2\} = \mathbf{m} \\ |\mathbf{m}| \geq 2}} e^{(|M(\mathbf{m})| - |M(\mathbf{m}_1)| - |M(\mathbf{m}_2)|)l} \\ & \times \{ \text{sgn}[M(\mathbf{m}_1)] - \text{sgn}[M(\mathbf{m}_2)] \} f(l; \mathbf{m}_1) f(l; \mathbf{m}_2). \end{aligned} \quad (2.41)$$

The recursive nature of (2.41) allows us to compute the $f(l; \mathbf{m})$, with $|\mathbf{m}| = k$, given that all $f(l; \mathbf{m})$, with $|\mathbf{m}| < k$, are known. Initial conditions can be derived from $V(0)$ in (2.21):

$$F(0; \mathbf{m}) = \begin{cases} 1, & \text{for } |\mathbf{m}| = 1 \text{ and } m \in \{0, \pm 1, \pm 2, \dots, \pm N\} \\ 0, & \text{else} \end{cases}. \quad (2.42)$$

Since we are interested in the limit $l \rightarrow \infty$, it is convenient to define coefficients $C(\mathbf{m})$:

$$C(\mathbf{m}) = \lim_{l \rightarrow \infty} F(l; \mathbf{m}). \quad (2.43)$$

After successively computing the functions $F(l; \mathbf{m})$, the quasi-particle-conserving, effective Hamiltonian is known exactly order by order. It has the general structure:

$$\lim_{l \rightarrow \infty} H(l) = H_{\text{eff}} = Q + \sum_{k=1}^{\infty} \lambda^k \sum_{\substack{\mathbf{m}=k \\ M(\mathbf{m})=0}} C(\mathbf{m})T(\mathbf{m}). \quad (2.44)$$

Note that all terms with $M(\mathbf{m}) \neq 0$ disappear in the limit $l \rightarrow \infty$, due to the exponential function in (2.40) so that H_{eff} indeed does not change the number of quasi-particles in the system. Thus, our initial goal of decoupling subspaces with different numbers of quasi-particles is achieved, and the effective Hamiltonian in fact gains a block-diagonal structure. We would like to emphasize that the coefficients $C(\mathbf{m})$ are problem independent, in the sense that they can be used for *any* Hamiltonian meeting the constraints listed in Section (2.3). They have been computed once and for all up to high orders. This is in contrast to the alternative approach by Krull et al. [93] where the restrictions from Section (2.3) are not necessary while H_{eff} has to be numerically recomputed for every new problem.

2.4 Continuous unitary transformation of operators

In addition to the transformation of the Hamiltonian H , one would like to be able to apply *the same* transformation to any operator acting in the Hilbert space of H . This is crucial since observables, in particular correlation functions, can be much easier accessed experimentally than the characteristic energies of the spectrum. Moreover, correlation functions can provide useful insights into the spectral properties of a model, as will be discussed in detail in Chapter 7.

An operator \mathcal{O} can be transformed in *exactly* the same way as the Hamiltonian if its flow is governed by the same generator. In the following, we will use the same strategy as in Section (2.2) and (2.3), by first introducing a running parameter l so that the transformation can be defined by

$$\frac{d}{dl} \mathcal{O}(l) = [\eta(l), \mathcal{O}(l)]. \quad (2.45)$$

We concentrate on a special case, assuming that H fulfills the conditions necessary for pCUT since then it is possible to write \mathcal{O} as a sum over quasi-particle creation and annihilation operators T_m . Then, the initial conditions for the above equation can be

written as $\mathcal{O}(l=0) = \sum_m T_m$. One uses a similar ansatz as in (2.22) of the form

$$\mathcal{O}(l) = \sum_{k=0}^{\infty} \lambda^k \sum_{i=1}^{k+1} \sum_{|\mathbf{m}|=k} G(l; \mathbf{m}; i) \mathcal{O}(\mathbf{m}; i), \quad (2.46)$$

where $G(l; \mathbf{m}; i)$ are numerically valued functions and $\mathcal{O}(\mathbf{m}; i)$ are defined (given $|\mathbf{m}| = k$) through

$$\mathcal{O}(\mathbf{m}; i = 1) = \mathcal{O} T_{m_1} \dots T_{m_k}, \quad (2.47)$$

$$\mathcal{O}(\mathbf{m}; i > 1) = T_{m_1} \dots T_{m_{i-1}} \mathcal{O} T_{m_i} \dots T_{m_k}. \quad (2.48)$$

One now can proceed systematically by inserting the ansatz (2.46) and the generator (2.33) into the flow equation and successively finding solutions for $G(l; \mathbf{m}; i)$ order by order. The details of this calculation can be found in literature [86, 100, 101]. Finally, in the $l \rightarrow \infty$ limit, the effective operator acquires the general shape

$$\mathcal{O}_{\text{eff}} = \sum_{k=0}^{\infty} \lambda^k \sum_{i=1}^{k+1} \sum_{|\mathbf{m}|=k} \tilde{C}(\mathbf{m}; i) \mathcal{O}(\mathbf{m}; i), \quad (2.49)$$

where $\tilde{C}(\mathbf{m}; i)$ are rational numbers. We would like to point out the generality of (2.49). Since the only condition demanded for \mathcal{O} was that it is an operator acting in the Hilbert space of H , it is possible to use the computed coefficients $\tilde{C}(\mathbf{m}; i)$ for a wide range of problems. Unlike H_{eff} , the operator \mathcal{O}_{eff} is generally *not* quasi-particle conserving. For this reason, it will turn out to be quite useful to split up the effective operator according to the quasi-particle subspaces it connects:

$$\mathcal{O}_{\text{eff}} = \sum_{d'=-\infty}^{\infty} \sum_{d=0}^{\infty} \mathcal{O}^{d',d}, \quad (2.50)$$

where $\mathcal{O}^{d',d}$ acts on a state with at least d quasi-particles in such a way that the resulting state contains precisely $d + d'$ quasi-particles (under condition that $d' > -d$, otherwise the result is zero). Throughout this work, we will be interested exclusively in zero-temperature physics, which corresponds to setting $d = 0$. Particularly relevant for local measurements (e.g., neutron scattering) are observables acting locally at site \mathbf{r} (contrary to H_{eff} which acts on every site). An effective $T = 0$ local observable can thus be written as

$$\mathcal{O}_{\text{eff}}(\mathbf{r}) = \sum_{d'=0}^{\infty} \mathcal{O}^{d',0}(\mathbf{r}). \quad (2.51)$$

Linked-cluster expansions

One of the strengths of the pCUT method presented in the previous chapter is that it allows to consider a problem directly in the thermodynamic limit, as long as elementary excitations are local¹ in real space. The physical argument for this is the fact that the effective particle-conserving Hamiltonian (2.44) is as a sum over local terms. Therefore, the dressed quasi-particles it represents must also be local (a formal proof of this statement will be given in Section 3.2). This leads to the important conclusion that effective Hamiltonians constructed with pCUT are suitable for a treatment with finite-cluster methods [86, 87, 102].

The aim of this chapter is to give a short introduction to the so-called linked-cluster expansions, allowing to perform efficient calculations on finite graphs, and to present general recipes on how series expansions can be generated for local effective Hamiltonians.

3.1 Introduction and overview

Finite-cluster calculations can be performed for local Hamiltonians [see (3.9)] with a variety of methods, e.g., exact diagonalization, Monte Carlo, or renormalization group. In order to avoid finite-size scaling one can first perform a graph expansion and then treat the systems on local graphs, e.g., with exact diagonalizations (an optimization to the low-energy part of the spectrum is known as the contractor renormalization approach [103]), CUT (this approach is known as gCUT [104]), or series expansion methods. Series expansions in general have the advantage that one is able to directly compute them in the thermodynamic limit. In addition, the pCUT approach yields *analytic* series, unlike

¹To be precise, *local* means that there is no dependence on the system size.

the numerical techniques mentioned above. Furthermore, one benefits from the fact that the computations are split in two separated tasks: perturbation theory is performed on clusters which previously have been identified by an independent algorithm. This feature makes it possible to optimize each part of the job independently. Also the self-consistent nature of the computation (namely the cluster subtraction, see Section 3.3) can be used for internal checks. To be more specific, an error in an expansion on a certain graph or even missing graphs would inevitably lead to discrepancies in the resulting series, destroying symmetries of certain terms, for example. Series expansions are especially powerful, if the so-called 'linked-cluster theorem' can be applied, then the number of finite clusters to consider is substantially reduced.

In the following sections, we will give more details on some of the concepts mentioned above, in particular on the ones relevant for our applications. A general review about the topic of series expansions on finite graphs can, for example, be found in Refs. [105–107].

3.2 Linked-cluster theorem

An essential premise for our method to work, is the linked-cluster theorem which is actually not a theorem in a strictly mathematical sense but rather a universal concept often used in perturbation theory (most prominently in the formalism of Feynman diagrams [108]). The main statement is that in a diagrammatic expansion it is sufficient to consider only connected (linked) diagrams, and to eliminate the disconnected ones, which greatly simplifies the calculation. However, we must emphasize that while, for example, Feynman diagrams correspond to some physical processes, the term 'cluster' (or equivalently 'graph') in this manuscript will always refer to a set of lattice sites and bonds which provide coordinates for the degrees of freedom of a model.

There exists plenty of literature on the topic of linked-cluster expansions, therefore we would like to redirect the interested reader to a brief selection of references [106, 107, 109–111] and focus on how the linked-cluster approach naturally emerges from pCUT. The ideas presented in the following can also be found in Ref. [102].

The effective Hamiltonian (2.44) can alternatively be represented by an infinite sum of nested commutators² of T_m , weighted by numerical coefficients. Generally, terms of order r are $(r-1)$ -fold nested commutators. This is a direct consequence from the perturbative treatment of the flow equations, as will be shown below. Next, let us take into account the structure of operators T_m . These are generally defined as sums of

²To be precise concerning our definition of nesting, a commutator without nesting, e.g., $[a, b]$ is indexed by a nesting number 0, terms like $[a, [b, c]]$ or $[[a, b], c]$ have a nesting number 1 and so on.

locally acting operators $\mathcal{T}_{m,\nu_1\dots\nu_n}$, where $\nu_1\dots\nu_n$ is a local (usually neighboring) set of sites:

$$T_m = \sum_{\langle\nu_1\dots\nu_n\rangle} \mathcal{T}_{m,\nu_1\dots\nu_n}. \quad (3.1)$$

Before proving the statements about the nested commutators, we can already anticipate the main result by pointing out that the commutator structure, combined with local properties of T_m operators, guarantees that only spatially connected processes contribute to H_{eff} since any pair of $\mathcal{T}_{m,\nu_1\dots\nu_n}$ commutes, when they do not share a common lattice site. Thus, the fulfillment of the linked-cluster theorem appears to be an intrinsic property of our method.

Let us once again consider the equations (2.22), (2.33) and (2.34):

$$\begin{aligned} V(l) &= \sum_{k=1}^{\infty} \lambda^{k-1} \sum_{|\mathbf{m}|=k} F(l; \mathbf{m}) T(\mathbf{m}), \\ \eta(l) &= \sum_{k=1}^{\infty} \lambda^k \sum_{|\mathbf{m}|=k} F(l; \mathbf{m}) \text{sgn}(M(\mathbf{m})) T(\mathbf{m}), \\ \frac{d}{dl} H(l) &= \lambda \frac{d}{dl} V(l) = \lambda [\eta(l), V(l)] - [Q, \eta(l)]. \end{aligned}$$

We shorten the notation by including the l -dependence into the T_m operators and expanding them in λ

$$T_m(l) \equiv \sum_{k=1}^{\infty} T_m^{(k)}(l), \quad (3.2)$$

$$T_m^{(k)}(l) \equiv \lambda^k F^{(k)}(l; m) T_m \equiv \lambda^k F(l; \mathbf{m}) T(\mathbf{m}), \quad \text{with } m = M(\mathbf{m}). \quad (3.3)$$

With this, the perturbation and the generator can be written as

$$V(l) = \lambda^{-1} \sum_m T_m(l), \quad (3.4)$$

$$\eta(l) = \sum_m \text{sgn}(m) T_m(l). \quad (3.5)$$

Now, the flow equation of the effective Hamiltonian can be split into a set of coupled flow equations for the $T_m(l)$.

$$\frac{d}{dl} \sum_m T_m(l) = \sum_{n,n'} [\text{sgn}(n) T_n(l), T_{n'}(l)] - \sum_m [Q, \text{sgn}(m) T_m(l)] \quad (3.6)$$

$$= \sum_{n,n'} [\text{sgn}(n) T_n(l), T_{n'}(l)] - \sum_m |m| T_m(l), \quad (3.7)$$

where we again have used (2.8). Expanding in λ , leads to

$$\frac{d}{dl} T_m^{(k)}(l) = \sum_{\substack{n, n' \\ n+n'=m}} \sum_{q=1}^{k-1} [\text{sgn}(n) T_n^{(k-q)}(l), T_{n'}^{(q)}(l)] - |m| T_m^{(k)}(l) \quad (3.8)$$

We observe that the l -dependence of the T_m operators is governed by commutators. The first term on the right-hand side is responsible for the nested structure of the commutators. Using the initial conditions (determined by the unperturbed system), one can recursively solve these equations order by order, and then take the limit $l \rightarrow \infty$ to obtain H_{eff} . However, at this point we already achieved our goal to show that H_{eff} must depend on nested commutators of T_m .

3.3 Series expansions on finite graphs

Let us consider a model on a lattice Λ , described by the Hamiltonian

$$H = \sum_{\langle \nu_1 \dots \nu_n \rangle} h_{\nu_1 \dots \nu_n}, \quad (3.9)$$

where each $h_{\nu_1 \dots \nu_n}$ acts on a local set of n (typically neighboring) sites, and generally consists of a diagonal part, as well as a non-diagonal part (the perturbation), weighted by a small parameter. The local nature of (3.9) allows for a linked-cluster expansion. A linked cluster is defined by a set of lattice sites connected by bonds (see Figure (3.1) for an example). We are interested in a series expansion of an extensive quantity P per lattice site. Following the notation of Gelfand et al. [106], we write P as a function of connected clusters c :

$$P(\Lambda)/N = \sum_c L(\Lambda, c) W(c), \quad (3.10)$$

$$W(c) = P(c) - \sum_{c' \subset c} W(c'). \quad (3.11)$$

Here, N is the number of sites, $L(\Lambda, c)$ is the number of embeddings of a cluster c per lattice site, usually referred to as the 'lattice constant'. $W(c)$ is the (reduced) weight of a cluster c . One computes $W(c)$ by first calculating the series expansion of P on cluster c , and then subtracting the weights of all subclusters $c' \neq c$ which can be embedded in c (denoted by $c' \subset c$).

Specifically in the present work, P represents a matrix element of the effective Hamiltonian, corresponding to the ground-state energy or hopping amplitudes of n particles in the n -particle Hilbert space. Alternatively to using pCUT, the series expansion of P

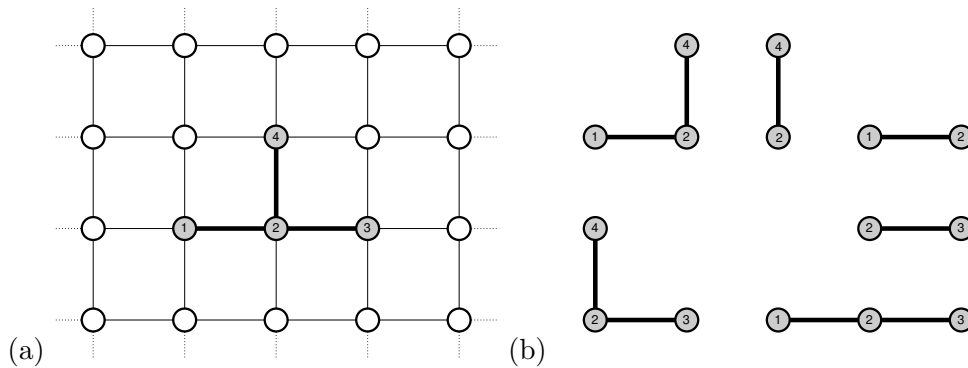


FIGURE 3.1: (a) An example of a connected four-site cluster on a square lattice for a local Hamiltonian, where each term acts on pairs of nearest neighbors [this corresponds to $n = 2$ in (3.9)]. (b) Distinct subclusters associated with the cluster in (a). Each subcluster contains at least two sites, due to $n = 2$.

can be computed with any perturbative method, e.g., the standard Rayleigh-Schrödinger perturbation theory [107, 112], or the efficient formalism developed by Kato and Takahashi [113, 114] for systems with degeneracy. All of the above methods yield the same result for scalar-valued P . However, when P is a matrix, the quasi-particle picture provided by pCUT turns out to be quite powerful because in contrast to many other methods, it allows to directly compute individual hopping amplitudes, even for multi-particle states.

Usually one is free to choose between different strategies to tackle the linked-cluster part of the problem, each having its own advantages and downsides as listed below.

(i) **Linked-cluster expansion**

As a first step, one has to determine all contributing clusters c , as well as their (relative) embedding numbers. One can use, for example, the 'pegs in holes' algorithm by Oitmaa et al. [107] to perform this task efficiently. Next, perturbation theory is performed on each graph. Finally, the series expansion of P is obtained by an appropriate summation of the results, using equations (3.11) in order to obtain the reduced weights $W(c)$. This seems to be the most efficient method since no redundant calculations are performed. However, the number of relevant graphs increases severely with perturbation order (especially for differently colored bonds or sites) so that even when using symmetries to reduce the number of graphs, the actual computation can become rather challenging.

(ii) **Single periodic cluster**

A kind of opposite approach, compared to (i), is to perform a one-step calculation. As can easily be followed from the linked-cluster theorem, a finite-order series expansion can be computed on a single piece of the lattice, as long as it is big enough. The minimal size of the cluster depends on the lattice structure, the Hamiltonian,

and the perturbation order. One of the simplest strategies is therefore to use a finite cluster with with periodic boundary conditions, thereby realizing exactly (for a fixed perturbation order) the translational symmetry of a system in the thermodynamic limit. Although this is an elegant way to incorporate the linked-cluster theorem in order to avoid dealing with a plethora of graphs, one is usually limited to relatively low perturbation orders, due to the rapidly increasing system size, and finite hardware resources. Still, this is a useful approach to compute the first few terms of a series and use it as an independent check for the more involved graph-based calculations.

(iii) Finite-lattice method

For square lattices, the so-called 'finite-lattice method' has been developed by de Neef and Enting [115] in the context of the classical Ising model, and applied for the first time to a quantum system by Dusuel et al. [102]. If applicable, this is a very efficient approach since it optimally combines the advantages of (i) and (ii). The basic idea is to consider only rectangular subclusters $\mathbf{C}_{m \times n}$ with $m \times n$ sites. These can be easily constructed and, more importantly, their embedding numbers can be found algebraically so that no combinatorial tasks have to be performed. Furthermore, the total amount of graphs is dramatically decreased. The equations (3.10) and (3.11) simplify to

$$P(\Lambda)/N = \sum_{m \leq n} L(\Lambda, \mathbf{C}_{m \times n}) W(\mathbf{C}_{m \times n}), \quad (3.12)$$

$$W(\mathbf{C}_{m \times n}) = P(\mathbf{C}_{m \times n}) - \sum_{\substack{m' \leq m \\ n' < n}} \sum_{\substack{m' < m \\ n' = n}} (m - m' + 1)(n - n' + 1) W(\mathbf{C}_{m' \times n'}), \quad (3.13)$$

where the last sum is constructed to run through all m' and n' , such that $\mathbf{C}_{m' \times n'}$ can be embedded in $\mathbf{C}_{m \times n}$, with $\mathbf{C}_{m' \times n'} \neq \mathbf{C}_{m \times n}$. The lattice constant in (3.12) equals to one, for square-shaped subclusters, and to two, for other rectangular shapes. This can be verified by counting the number of embeddings N_{emb} of a rectangular cluster $\mathbf{C}_{m \times n}$ in a square lattice. Generally

$$N_{\text{emb}} = \begin{cases} 2mn, & \text{if } m \neq n \\ m^2, & \text{if } m = n \end{cases}. \quad (3.14)$$

Dividing N_{emb} by the number of sites (mn for $m \neq n$ and m^2 for $m = n$) yields the lattice constant³. The relations (3.12) and (3.13) are valid in the thermodynamic

³The factor two for cases with $m \neq n$ can be understood, by realizing that non-square shapes have less symmetries, e.g., contrary to square clusters, they are not invariant under a mirror transformation on their diagonal.

limit. However, due to the linked-cluster theorem, in a finite-order calculation maximal m and n can be found so that the above sums become limited. This step is problem dependent, and we refer to Chapter 5 for an explicit example where we will demonstrate the finite-lattice method (more precisely its generalized quantum version) by applying it to the toric code in a field. It should be mentioned that this method can also be used similarly for triangular lattices [116]; however, the subclusters and their embeddings are then less trivial. It is possible to extend the finite-lattice method to higher dimensions [117], as well as other lattices (checkerboard lattice in Section 5.1.1), as long as one is able to find an algebraic expression for the embedding numbers of subclusters. In practice, calculations are limited by the perturbation order dependent size of the largest cluster. While the largest $\mathbf{C}_{m \times n}$ has generally less sites than the largest cluster from (ii), it is clearly bigger than any cluster from (i). Nevertheless, this disadvantage [compared to (i)] is compensated by a significantly lower total number of graphs, as well as an almost trivial subtraction scheme.

The toric code

In this chapter, the toric code and its exact solution are presented. We address the properties of the topologically-ordered ground states as well as of elementary excitations which are static non-interacting anyons or bosons. When exposed to a magnetic field, the anyons generally become dispersive and start to interact. Certain limiting cases of the toric code in a magnetic field can be mapped onto known models and we are able to resort to literature in order to learn about basic properties of the critical behavior of the model.

4.1 Model and ground-state properties

The toric code [28] is a two-dimensional spin-1/2 quantum system. Following Kitaev's convention, the spins are located at bonds of a square lattice [see Figure 4.1 (a)] and their interaction is governed by the Hamiltonian

$$H_{\text{TC}} = -J \sum_s A_s - J \sum_p B_p, \quad (4.1)$$

$$A_s = \prod_{i \in s} \sigma_i^x, \quad (4.2)$$

$$B_p = \prod_{i \in p} \sigma_i^z, \quad (4.3)$$

with $J > 0$. Here, s stands for 'star', or equivalently vertex of the square lattice in Figure 4.1 (a), p denotes elementary (square) plaquettes, and σ_i^α are $SU(2)$ Pauli operators, acting at site i . Within this notation, A_s (B_p) is defined as a product of Pauli operators along the boundaries of a star (plaquette), thus H consists entirely of four-body interactions. Note that throughout this work we will use the same amplitude J for the

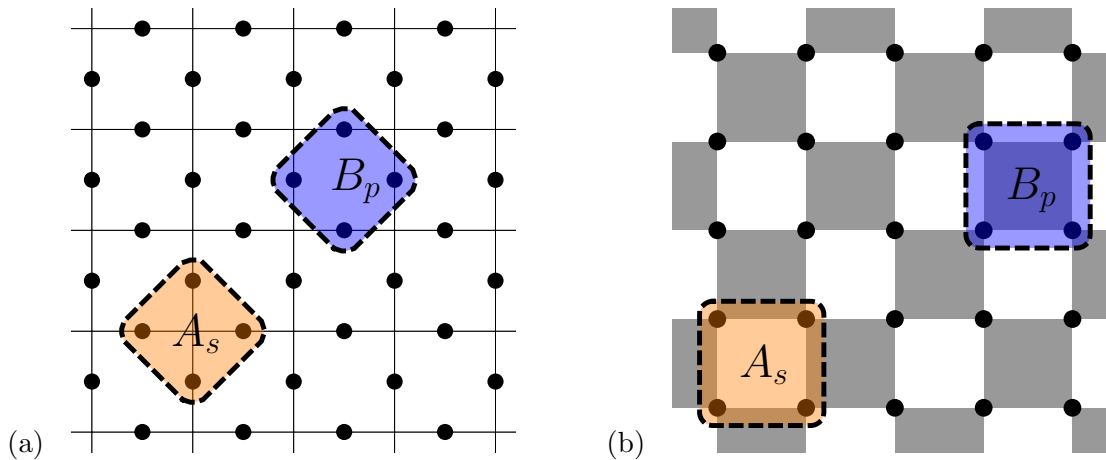


FIGURE 4.1: Two possible ways to define the toric code on a lattice. (a) Following Kitaev's convention, spins are placed on bonds of a square lattice, the operators A_s (B_p) act on vertices (plaquettes). (b) An equivalent representation of the toric code. Here spins are positioned on vertices of a checkerboard lattice, the operators A_s (B_p) act on white (gray) plaquettes.

two types of interactions. Sometimes, it is convenient to consider an equivalent picture of the toric code where the system is geometrically rotated by $\pi/4$ so that spins can be placed on vertices of a checkerboard lattice and interact through A_s on white, and B_p on gray plaquettes, as shown in Figure 4.1 (b). Generally, the spin lattice can be embedded on various two-dimensional manifolds. However, it should be clear that the topological properties of the toric code strongly depend on the boundary conditions. In order to function as a quantum memory, the system should be able to carry various topologically-protected sectors which, in the toric code, are characterized by non-contractible loops directly related to the genus g of the manifold. Therefore, one is often led to define the spin lattice on closed and orientable surfaces with $g > 0$. The simplest representative of such a manifold (with $g = 1$) is a torus. Nevertheless, it is also useful to consider the toric code on an open infinite plane, in order to compute *local* properties of H_{TC} (such as eigenenergies) which do not depend on boundary conditions. It should be mentioned that for an experimental realization it might also be useful to consider this model on a finite perforated plane, where instead of non-contractible loops around the whole system topological invariants are constructed by strings around holes, or strings connecting distant edges of the system, as suggested by Ioffe et al. [45] and Douçot et al. [46, 118] for an implementation in Josephson junction arrays. In the present manuscript, however, we will focus mainly on properties of the model, valid in the thermodynamical limit, where the influence of system edges can safely be neglected.

There is an extensive number of conserved quantities in the toric code. For all s and p , the A_s and B_p commute with each other and consequently with the Hamiltonian.

$$[A_s, A_{s'}] = 0 = [B_p, B_{p'}], \quad (4.4)$$

$$[A_s, B_p] = 0. \quad (4.5)$$

This follows directly from the commutation relations of Pauli operators and the fact that any star-plaquette pair has either two or zero spins in common. It is helpful to realize that due to

$$A_s^2 = \mathbf{1} = B_p^2, \quad (4.6)$$

the local spectrum of each A_s and B_p has two energy levels with eigenvalues ± 1 . On a torus (but not on an open plane) these degrees of freedom are, further, subject to the global constraint

$$\prod_s A_s = \mathbf{1} = \prod_p B_p. \quad (4.7)$$

Since in a lattice with N spins there are $N/2$ stars and $N/2$ plaquettes, we have so far $N - 2$ conserved quantities. There are two additional conserved quantities on a torus. We will find them by considering products of σ^x or σ^z along certain closed paths, called 'loops' in the following. One has to distinguish between contractible and non-contractible loops. Figure 4.2 exemplifies, how a product of overlapping A_s is equivalent to a product of σ^x along a closed loop (same holds for B_p and loop products of σ^z) because spins inside the area enclosed by the loop are acted upon twice by the same Pauli operator. It can be argued that in the thermodynamic limit, products of A_s and B_p can only be related to *contractible* loops (and vice versa). Thus it is obvious that loops of this kind also commute with the Hamiltonian. However, they are not independent degrees of freedom since they are isospectral to the product of enclosed A_s or B_p respectively.

On the contrary, non-contractible loops, as depicted in Figure 4.3, cannot be represented by products of star or plaquette operators and therefore are independent conserved quantities. Let us consider the non-contractible loop operators

$$\mathcal{X}_\mu = \prod_{i \in \mathcal{C}_\mu} \sigma^x, \quad (4.8)$$

$$\mathcal{Z}_\mu = \prod_{i \in \mathcal{C}_\mu} \sigma^z, \quad (4.9)$$

with $\mu \in \{1, 2\}$, and \mathcal{C}_μ are contours defined in Figure 4.3. While \mathcal{X}_μ and \mathcal{Z}_μ commute with the Hamiltonian they generally do not commute with each other so that on the

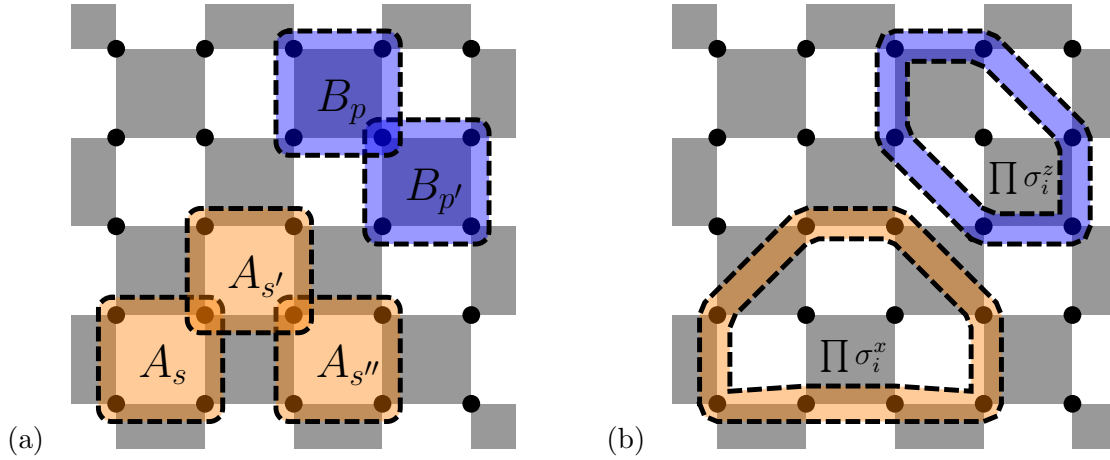


FIGURE 4.2: Contractible loops in the toric code. A product of A_s (B_p) [for instance the one shown in (a)] can be represented by a product of σ^x (σ^z) on the outermost sites of the enclosed region, as shown in (b). Loop operators of this kind by construction commute with the Hamiltonian.

torus only two of them can be chosen independently.

$$[\mathcal{X}_\mu, \mathcal{X}_\nu] = 0, \quad (4.10)$$

$$[\mathcal{Z}_\mu, \mathcal{Z}_\nu] = 0, \quad (4.11)$$

$$[\mathcal{X}_\mu, \mathcal{Z}_\nu] = 2\mathcal{X}_\mu \mathcal{Z}_\nu (1 - \delta_{\mu\nu}). \quad (4.12)$$

This way we recover two additional independent degrees of freedom which compensate for the constraints in (4.7), and thus maintain the exact solvability of the toric code (in total there are N conserved quantities in a system with N spins). As previously, it is easy to check that $\mathcal{X}_\mu^2 = \mathbb{1} = \mathcal{Z}_\mu^2$. Consequently, the eigenvalues of each of these loop operators are limited to ± 1 so that each configuration of A_s - and B_p -degrees of freedom is four-fold degenerate. Thus, the Hilbert space of H separates in topologically-protected subspaces which, in the thermodynamic limit, cannot be connected by a local perturbation. The number of non-contractible loops and consequently the degeneracy of each state scales as 2^{2g} with the genus g of the manifold, on which the model is defined. Thus, we obtain the interesting result that the ground-state degeneracy depends on the topology of the system, which is an important attribute of topological order. Note that on an infinite open plane all loops are contractible, hence the ground state is unique.

We proceed by constructing the exact ground state $|g\rangle$ where all A_s and B_p should have positive eigenvalues (+1), due to (4.1) and $J > 0$:

$$A_s |g\rangle = |g\rangle, \quad (4.13)$$

$$B_p |g\rangle = |g\rangle. \quad (4.14)$$

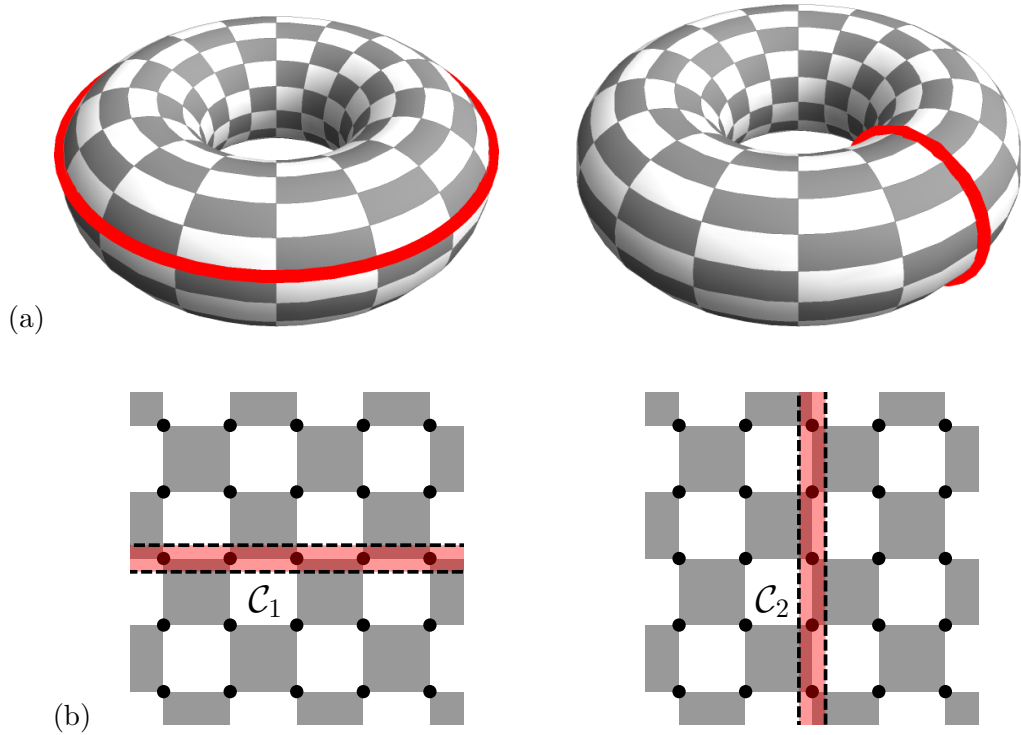


FIGURE 4.3: Non-contractible loops on a torus: a closed, orientable $g = 1$ manifold. (a) Two different non-contractible loops exist on the surface of a torus. (b) In two dimensions a torus can be represented by a plane with the following periodic boundary conditions: the lower edge of the plane is identified with the top edge and the right edge with the left. In the toric code, loop operators are defined as products of Pauli operators along the highlighted sites, denoted by \mathcal{C}_1 and \mathcal{C}_2 .

Furthermore, we use the operators \mathcal{Z}_1 and \mathcal{Z}_2 (this choice is, however, not unique), with respective eigenvalues z_1 and z_2 , to unambiguously identify the subspace of non-contractible loops. Due to (4.12), the $z_i \in \{\pm 1\}$ can be set independently. They will be used as quantum numbers labeling the ground state $|g, z_1, z_2\rangle$. Let us now consider an arbitrary reference state $|\text{ref}\rangle$. We will work with local projectors $(\mathbb{1} + A_s)/2$ and $(\mathbb{1} + B_p)/2$, in order to build an eigenstate of H with the minimal energy, where all eigenvalues of A_s and B_p are set to +1:

$$|g, z_1, z_2\rangle = \mathcal{N}_{\text{ref}} \left(\frac{\mathbb{1} + z_1 \mathcal{Z}_1}{2} \right) \left(\frac{\mathbb{1} + z_2 \mathcal{Z}_2}{2} \right) \prod_s \left(\frac{\mathbb{1} + A_s}{2} \right) \prod_p \left(\frac{\mathbb{1} + B_p}{2} \right) |\text{ref}\rangle, \quad (4.15)$$

where \mathcal{N}_{ref} is a normalization constant. Provided that the above state is non zero, it is an exact four-fold degenerate ground state of the toric code. With this technique one can build any eigenstate of the toric code, as will be shown in an explicit example in the next section.

At this point, it can be instructive to consider the specific reference spin state $|\uparrow\rangle$ where all spins point upward (in the z -direction). This state is already an eigenstate of the

B_p -ground-state projector, so we obtain

$$|g, z_1, z_2\rangle = \mathcal{N} \left(\frac{\mathbb{1} + z_1 \mathcal{Z}_1}{2} \right) \left(\frac{\mathbb{1} + z_2 \mathcal{Z}_2}{2} \right) \prod_s \left(\frac{\mathbb{1} + A_s}{2} \right) |\uparrow\rangle, \quad (4.16)$$

where \mathcal{N} is a normalization constant. Expanding the remaining projector yields

$$|g, z_1, z_2\rangle = \mathcal{N} \left(\frac{\mathbb{1} + z_1 \mathcal{Z}_1}{2} \right) \left(\frac{\mathbb{1} + z_2 \mathcal{Z}_2}{2} \right) \left(\frac{1}{2} \right)^{N/2} \left(\mathbb{1} + \sum_s A_s + \sum_{s,s'} A_s A_{s'} + \dots \right) |\uparrow\rangle, \quad (4.17)$$

where we accounted for (4.7), and the fact that a system of N spins has $N/2$ stars. As has been already shown (Figure 4.2), each product of A_s corresponds to a closed loop of flipped spins. Thus the ground state of the toric code can be considered as an equal-weight superposition of all possible loops and combination of loops (this is sometimes referred to as 'loop gas') within the four topologically separated sectors fixed by z_1 and z_2 . We point out that on an open plane the ground state can be constructed in exactly the same way as a product of local projectors, but since all loops are contractible, there are no topologically distinct sectors, and the ground state is unique.

4.2 Properties of elementary excitations

Elementary excitations (also referred to as 'particles' in the following) of the toric code are obtained by changing the eigenvalues of the star and plaquette degrees of freedom from +1 to -1. Due to the special structure of the model, any local operator flips eigenvalues of A_s (as well as B_p) pairwise. Such elementary flips can be realized by acting with σ^α operators on the ground state. Consider, for example, the operator σ_i^x (σ_i^z) which acts on a site i . While this operator anticommutes with each of the two neighboring p (s) sharing the site i , it commutes with every remaining term in the Hamiltonian. With the same argument, $\sigma_i^y = i\sigma_i^x\sigma_i^z$ anticommutes with two p and two s , connected to the site i . Consider Figure 4.4 for an intuitive picture of the discussed commutator relations. For convenience, we will call excitations on stars s , 'charges', and the ones on plaquettes p , 'fluxes'. The naming is motivated by actual charges and fluxes from electrodynamics since, as in the Aharonov-Bohm effect, moving a charge around a flux yields a phase shift in the corresponding wave function, as will be discussed in more detail below.

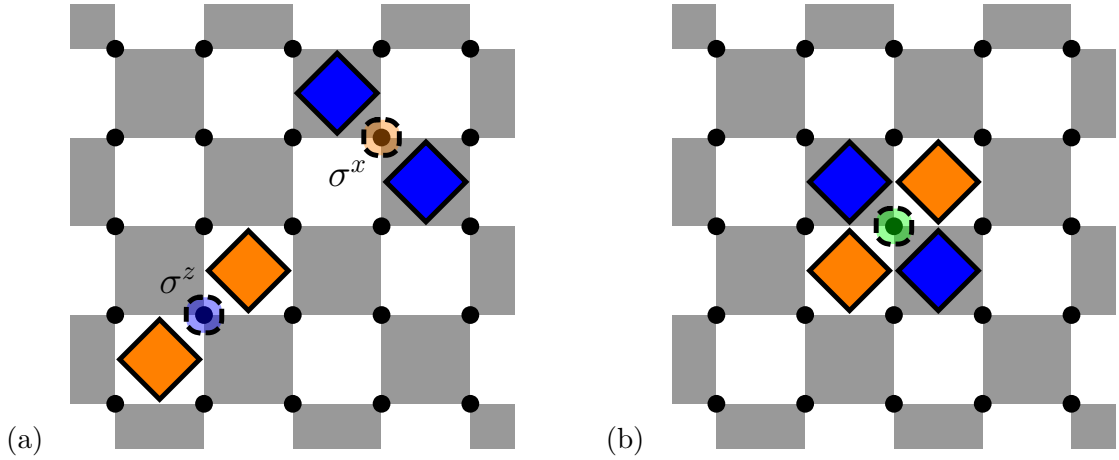


FIGURE 4.4: Examples of how local excitations of the toric code are created by acting with Pauli operators. White and gray squares correspond to the eigenvalue $+1$ (the local ground-state energy) of A_s and B_p respectively. s (p) with eigenvalues -1 are illustrated by orange (blue) shapes, referred to as charges (fluxes) in the text. (a) A σ^z flips two neighboring charges, and a σ^x flips to neighboring fluxes. (b) A σ^y simultaneously flips a pair of charges and fluxes.

By construction, charges and fluxes are static excitations which do not interact. The energy of an excited state can thus simply be obtained by counting the number of particles in the system. On the torus, the particle vacuum is protected by a gap of $4J$, corresponding to the energy cost of creating a particle pair. Let us consider a case, where σ^z operators act on certain neighboring spins, as illustrated in Figure 4.5. Obviously,

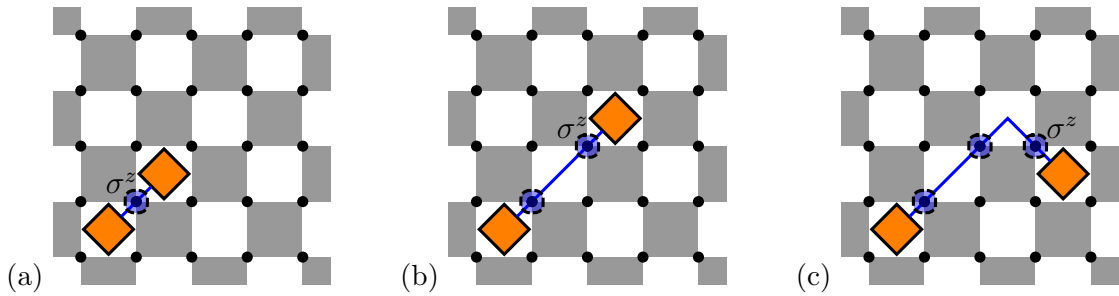


FIGURE 4.5: Through successive application of σ^z operators a pair of charges is created and moved apart. Alternatively, one can consider charges as ends of open strings highlighted by blue lines in the figure. All of the presented states have the same energy.

when the eigenvalue of an A_s is flipped from -1 to $+1$, the charge it carries is destroyed. In the particular case shown in Figure 4.5 (b)-(c), the charge is simultaneously created on a previously 'empty' neighboring star. This process does not change the energy of the state because the number of particles in the system is constant. One can observe two important properties of these elementary excitations. Firstly, a pair of charges is always connected by a 'string' of σ^z (one can alternatively consider the elementary excitations as end points of open strings). Secondly, the string is free of energy, it does not produce

any 'tension' between particles. This fact enables us to study single charges, by driving a pair of particles sufficiently far apart. Due to the finite excitation gap, all correlations vanish exponentially and the charge is indeed deconfined. Locally, an isolated charge (with its partner at infinity) is equivalent to a single charge on an infinite open plane, whereas one end of the string is connected to the charge and the other one to the plane edge at infinity. This will be essential for series expansions we perform with pCUT in the one-quasi-particle subspace of the effective Hamiltonian. All of the above considerations can, *mutatis mutandis*, be applied to fluxes. Figure 4.6 illustrates what we will call a 'single particle'. Formally, it is possible to define single particle states on an infinite

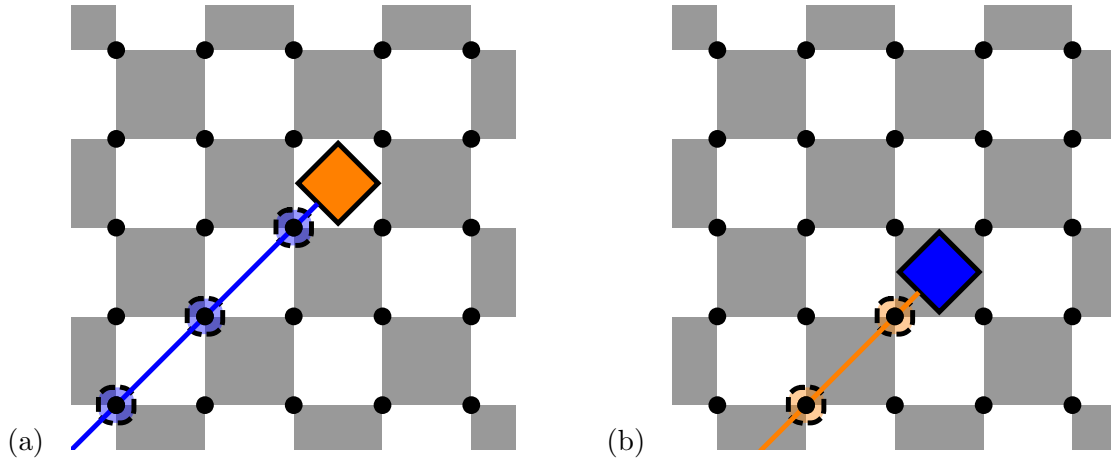


FIGURE 4.6: Single particles in the toric code. (a) A single charge with a string of σ^z operators. (b) A single flux with a string of σ^x operators. There are two ways to consider these figures. (i) On the one hand they can be regarded as local views of a torus in the thermodynamic limit, then the shown particles are connected by a string with their respective partner at infinity. (ii) Alternatively one can view the lattices in (a) and (b) as finite open planes, where only fully shown stars and plaquettes are part of the model. Because edge-spins of the plane are connected to single stars and plaquettes, the model admits the creation of single particles which, however, are always attached to an edge by a string. In the thermodynamic limit, where edges of the open plane are at infinity, the local properties of single particles are equivalent in (i) and (ii).

open plane, where the unique ground state can be denoted by

$$|g\rangle_{\text{plane}} = \mathcal{N} \prod_s \left(\frac{\mathbb{1} + A_s}{2} \right) |\uparrow\rangle. \quad (4.18)$$

A single-charge state with a charge positioned at star s can be written as

$$|s\rangle = \left(\prod_{i \in \mathcal{C}_s} \sigma_i^z \right) |g\rangle_{\text{plane}} = \mathcal{N} \left(\frac{\mathbb{1} - A_s}{2} \right) \prod_{s' \neq s} \left(\frac{\mathbb{1} + A_{s'}}{2} \right) |\uparrow\rangle, \quad (4.19)$$

where \mathcal{C}_s is a one-dimensional semi-infinite path on the lattice, with one endpoint at s and the other one at the edge of the infinite plane. Similarly, we define a single-flux

state as

$$|p\rangle = \left(\prod_{i \in \mathcal{C}_p} \sigma_i^x \right) |g\rangle_{\text{plane}} = \mathcal{N} \prod_s \left(\frac{\mathbb{1} + A_s}{2} \right) |\mathcal{C}_p\rangle, \quad (4.20)$$

where the flux is positioned at p and \mathcal{C}_p is defined analogically. The notation of the state $|\mathcal{C}_p\rangle$ symbolizes that all spins are up, except the ones belonging to \mathcal{C}_p . Multi-particle states can easily be defined in the same fashion. We point out that the lack of symmetry in the notation of single charges and fluxes is the consequence of our explicit choice of the basis, where the reference state $|\uparrow\rangle$ denotes a state with all spins up. Also, it should be stressed that while the presented construction of single-particle states might be difficult to implement in an experiment, it is legitimated by the fact that perturbation theory is a 'local' approach.

Certainly, one of the most remarkable features of the toric code is the unusual statistics of the quasi-particles. While two charges behave as hard-core bosons¹ (same holds for two fluxes), a charge and a flux are mutual Abelian anyons. Sometimes they are called 'semions' since braiding a single flux around a single charge (or vice versa) yields the initial state multiplied by a minus sign. This corresponds to a phase of π and is one *half* of the phase one would get for fermions. To prove this, we will profit from the simplicity of the toric code where braiding operations can be performed by acting with Pauli operators and where the mutual statistics of the elementary excitations can be explicitly demonstrated in a more or less trivial way.

Let us consider a state $|\psi\rangle$ where two distinct pairs of particles are aligned as shown in Figure 4.7 (a). We will now perform two independent operations:

- (i) Move a flux along the contour $\mathcal{C}_{\text{flux}}$ highlighted in Figure 4.7 (b), by applying the operator $\mathcal{O}_{\text{braid}} = \prod_{i \in \mathcal{C}_{\text{flux}}} \sigma_i^x$.
- (ii) Move a charge inside the area enclosed by the path of the flux, by acting with σ_i^z on site i .

Algebraically, it is clear that since $\mathcal{O}_{\text{braid}}$ and σ_i^z do not commute, the order in which they are applied matters. Physically, $\mathcal{O}_{\text{braid}} \sigma_i^z |\psi\rangle = |\psi'\rangle_{\text{braid}}$ [Figure 4.7 (b)] corresponds to a braid of the flux around a charge. The case $\sigma_i^z \mathcal{O}_{\text{braid}} |\psi\rangle = |\psi'\rangle$ [Figure 4.7 (c)] yields an identical final state, however, no braiding has been performed.

¹These particles are so-called 'hard-core' bosons because the local Hilbert space allows for an occupation of at most one particle per star or plaquette.

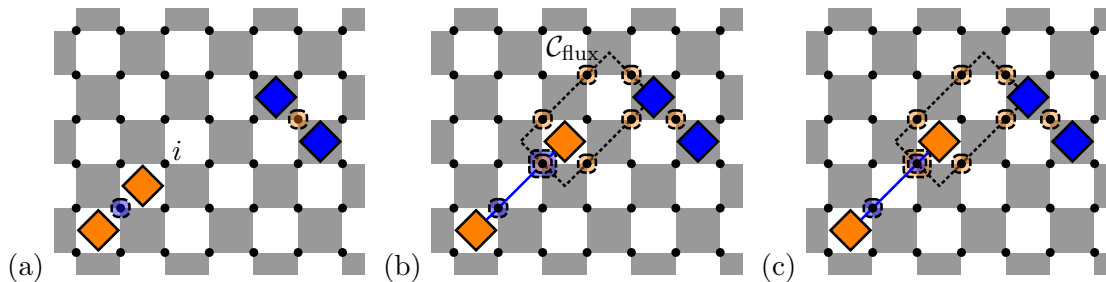


FIGURE 4.7: Braiding a flux (blue) around a charge (orange) reveals the anyonic character of elementary excitations in the toric code. (a) The initial state $|\psi\rangle$. (b) First, a charge is displaced into the area enclosed by $\mathcal{C}_{\text{flux}}$, then a flux hops along a loop path around the charge and back to its initial position. The resulting state is $|\psi'\rangle_{\text{braid}}$. (c) First, a flux moves along $\mathcal{C}_{\text{flux}}$, then the charge hops to its final position. Effectively no braiding has been performed and we obtain $|\psi'\rangle$.

Thus, we obtain

$$\mathcal{O}_{\text{braid}}\sigma_i^z|\psi\rangle = -\sigma_i^z\mathcal{O}_{\text{braid}}|\psi\rangle, \quad (4.21)$$

$$|\psi'\rangle_{\text{braid}} = -|\psi'\rangle = e^{i\pi}|\psi'\rangle. \quad (4.22)$$

We conclude that the performed braid yields a non-trivial global phase of $2\theta = \pi$, contrary to what is expected for fermions ($2\theta = 2\pi$) or bosons ($2\theta = 0$) under the same operations. It should be emphasized that the anyonic behavior is the direct consequence of the non-local structure of the elementary excitations (due to strings). In order to demonstrate that charges are mutual bosons one can proceed in a similar fashion by braiding a charge around another charge. But, one can also simply argue that strings of charges commute so that braiding has no effect. Consequently, a state where two charges exchange positions (half a braid) yields a global phase of $\theta = 0$ which is a signature of bosons. Same considerations can be carried out for fluxes. In the same spirit as for single particles, one can straightforwardly show that *pairs* of charges (or fluxes) form a boson, while a charge-flux pair is a fermion.

4.3 Toric code in a magnetic field: limiting cases

The exactly solvable toric code is one of the few known models one can use to study quantum phase transitions in a topologically-ordered system. Furthermore, the robustness of the topological phase against external perturbations is relevant to determine its potential usability as a quantum memory. In this section, we will discuss known results about the toric code perturbed by a magnetic field which is one of the simplest uniform perturbations in a quantum spin system. The toric code in an arbitrary uniform

magnetic field is defined as

$$H_{\text{TCF}} = \underbrace{-J \sum_s A_s - J \sum_p B_p}_{H_{\text{TC}}} - h_x \sum_i \sigma_i^x - h_y \sum_i \sigma_i^y - h_z \sum_i \sigma_i^z, \quad (4.23)$$

where sums over index i run through all lattice spins, σ_i^α are the usual Pauli operators, and h_α the respective field amplitudes. Motivated by the structure of A_s and B_p , in literature, one usually refers to the h_x - and h_z fields as 'parallel' and to the h_y field as 'transverse'. We argue that H_{TCF} features at least two distinct phases. In the zero-field limit we obtain the topologically-ordered H_{TC} with anyonic elementary excitations, as discussed in the previous section. For $J = 0$, the ground state is unique (whatever the system topology) and polarized in the field direction, so there must be a quantum phase transition. Interestingly, in certain limits of (4.23), exact mappings to already known models can be found and will be presented below. These models are usually easier to tackle numerically and unravel important properties of the toric code in a magnetic field. Furthermore, the connection to known results provides an additional check for our own studies (see Chapter 6).

We begin with the simplest case of a *single* parallel magnetic field. This perturbation is sufficient to drive the toric code out of its topological phase. In Refs. [65, 119] it has been found that the spectrum of the toric code in a single parallel field is equivalent (up to degeneracies) to the one of the ferromagnetic transverse-field Ising model

$$H_{\text{TFIM}} = -J_I \sum_{\langle i,j \rangle} \sigma_i^z \sigma_j^z - h_I \sum_i \sigma_i^x, \quad (4.24)$$

where quantum spins are placed on vertices i of a square lattice and $\langle i, j \rangle$ stands for nearest neighbors. In what follows, we will adapt the notation of Ref. [102]. Each term of the Ising-interaction corresponds to a two-level system one can mimic by a pseudo-spin

$$\tilde{\sigma}_\beta^z = \sigma_i^z \sigma_j^z, \quad (4.25)$$

where β represents a bond connecting neighboring sites i and j . Note that this mapping conserves neither the degeneracy nor the dimension of the Hilbert space, but only the spectrum. The field term is slightly more intricate. We recall that a vertex on a square lattice with four attached bonds is called 'star'. The operator σ_i^x flips a spin at site i , thus inverting the eigenvalues of our new bond variables $\tilde{\sigma}_\beta^z$ on such a star

$$\tilde{A}_s = \prod_{\beta \in s} \tilde{\sigma}_\beta^x = \sigma_i^x, \quad (4.26)$$

where the product runs over four bonds attached to site i . We obtain

$$\tilde{H}_{\text{TFIM}} = -J_I \sum_{\beta} \tilde{\sigma}_{\beta}^z - h_I \sum_s \tilde{A}_s. \quad (4.27)$$

In a single h_z field, the B_p degrees of freedom are still conserved. This means that their local eigenvalues and can be fixed to a constant value, in other words we consider fluxes as 'frozen out' at low energies. This way \tilde{H}_{TFIM} is isospectral to the toric code, adjusted by a global energy shift that depends on the B_p eigenvalues. Since we are interested in low-energy physics, we choose the local eigenvalues of each B_p to be +1. Note that low-field limit of \tilde{H}_{TFIM} (low h_I) corresponds to the high-field limit of the toric code and vice-versa. H_{TFIM} is known to display a second-order phase transition from the ordered, polarized ($J_I \gg h_I$) phase to a disordered phase at $(J_I/2h_I)_c = 0.32847(2)$ computed by mapping the H_{TFIM} onto its three-dimensional classical analogue and applying the continuous-time Monte Carlo technique [120]. The natural order parameter for H_{TFIM} is the magnetization per site $\langle \sum_i \sigma_i^z \rangle / N$. However, from this it cannot be concluded that a *local* order parameter exists in the toric code. It has been checked by Monte Carlo calculations [65, 67] and also derived from series expansions [68, 121, 122] that the magnetization per bond² $\tilde{\sigma}_{\beta}^z / 2N$ of the toric code is non-zero throughout the whole parameter range (except in the trivial zero-field limit). As Kitaev aptly remarks: "a hidden long-range order [...] cannot be described by any local order parameter" [28]. Note also that \tilde{H}_{TFIM} and H_{TFIM} are truly different at finite temperatures where the degeneracy of energy levels becomes important in the partition function. Finally, we remark that the toric code in a single h_x field can be treated in an analogue way. One has to perform a basis rotation $\sigma^x \rightarrow \sigma^z$, $\sigma^z \rightarrow -\sigma^x$ and obtains again (4.27) (the A_s -degrees of freedom are frozen out).

Tupitsyn et al. [66] found a way to map the toric code including *both* parallel fields h_x and h_z onto the anisotropic \mathbb{Z}_2 gauge Higgs model [123] which again can be studied using its classical counterpart. The rather technical procedure will be sketched only briefly, more details can be found in Ref. [66]. The mapping relies on artificial spin degrees of freedom which are centered on stars s and are denoted by μ_s^x and μ_s^z . After the transformation

$$\sigma_i^z \rightarrow \mu_{s_i}^z \sigma_i^z \mu_{s'_i}^z, \quad (4.28)$$

$$\sigma_i^x \rightarrow \sigma_i^x, \quad (4.29)$$

where s and s' are neighboring stars sharing the site i , the Hilbert space is enlarged, but the physical states $|\psi\rangle$ can be projected out with $\mu_s^x |\psi\rangle = |\psi\rangle$. The additional degrees

²Note that on the square lattice the number of bonds is twice the number of sites.

of freedom generate a local symmetry and thus impose a gauge invariant transformation for the physical states

$$\mu_s^x A_s |\psi\rangle = |\psi\rangle. \quad (4.30)$$

In the next step, one considers the evolution in imaginary time of the resulting effective Hamiltonian H_{phys} which preserves the physical subspace of the enlarged Hilbert space

$$H_{\text{phys}} = -J_x \sum_s \mu_s^x - J_z \sum_p B_p - h_x \sum_i \sigma_i^x - h_z \sum_i \mu_{s_i}^z \sigma_i^z \mu_{s'_i}^z \quad (4.31)$$

When H_{phys} is mapped onto (2+1) dimensional classical model, one recovers the anisotropic \mathbb{Z}_2 -gauge Higgs model. The anisotropy results from the fact that the coupling in the imaginary-time direction is different from the one in spatial directions. However, Tupitsyn et al. considered the isotropic case which fixes a certain ratio of the four free parameters of (4.31). Note also that in contrast to (4.1), here generally $J_x \neq J_z$. In consequence, one cannot compare the obtained phase diagram quantitatively to the one of the toric code, considered in this manuscript. Minor parameter changes, however, do not affect the critical behavior so that the phase diagram discussed in Ref. [66] contains all main features of the toric code in a parallel field. Indeed, this phase diagram is in agreement with series expansions results by Vidal et al. [68], as well as recent quantum Monte Carlo simulations [performed directly in (2+1) dimensions] by Wu et al. [67] (see Figure 4.8).

Let us discuss this phase diagram in more detail. On the axes $h_x = 0$ and $h_z = 0$ one recovers a second-order phase transition in the 3d Ising universality class at $h/J = 0.32847(2)$. The phase transition along red curves belongs to the same universality class, this has been shown generally in the context of the isotropic \mathbb{Z}_2 Higgs model [123] and also by comparing critical exponents [68]. For $h_x < h_z$, the transition into a magnetically-ordered phase (spins are polarized in the direction of the field) is triggered by condensation of charges, whereas for $h_x > h_z$, fluxes condense first. Interestingly, the charge-condensed phase is separated from the flux-condensed one by a first-order phase transition line which terminates at the second-order transition point P_2 . The exact connection of the phase boundaries around P_1 is still under debate but, according to Tupitsyn et al. [66], the scenario where all three lines meet at one point is rather likely. Assuming this is indeed the case, P_1 is a multicritical point since it borders three critical manifolds. This picture is consistent with pCUT calculations in Ref. [68], where the value of the critical exponent $z\nu$ at P_1 was found to be different from the Ising one, indicating a distinct universality class. From the physical point of view, it is also expected that the critical behavior at $h_x = h_z$, where the Hamiltonian has an increased \mathbb{Z}_2 -symmetry, is truly different compared to $h_x \neq h_z$. While along the

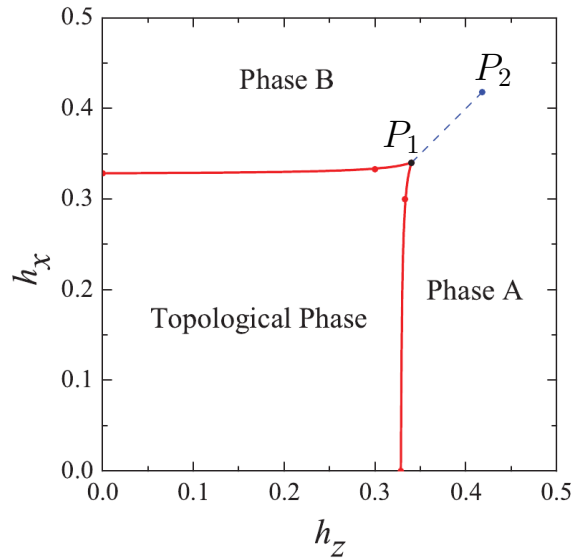


FIGURE 4.8: Phase diagram of the toric code (with $J = 1$) perturbed by the parallel fields h_x and h_z . The figure is taken from Ref. [67], where the phase boundaries were computed with continuous-time quantum Monte Carlo and are precise up to the third digit. Red lines denote a continuous Ising-type phase transition, while the dotted blue line marks a first-order phase transition. On the symmetric line $h_x = h_z$ the Ising-type boundaries of the topological phase meet a first-order phase transition line at the point $P_1 : h_x = h_z = 0.340(2)$. The discontinuous transition line connects the multicritical point P_1 with a second-order transition point $P_2 : h_x = h_z = 0.418(2)$. The low-field phase corresponds to the topological phase of the toric code, while regions A and B are charge-condensed and respectively flux-condensed phases, smoothly connected at the high-field limit where elementary excitations are magnons.

red line the phase transition occurs when bosonic particles condense (either charges *or* fluxes), at P_1 the two kinds of elementary excitations condense simultaneously so that their anyonic character may become relevant for the phase transition.

Another limiting case of interest is the toric code in a transverse magnetic field, investigated by Vidal et al. in Ref. [69].

$$H_{\text{TF}} = -J \sum_s A_s - J \sum_p B_p - h_y \sum_i \sigma_i^y, \quad (4.32)$$

Here, the system is governed by an utterly different physics, e.g., elementary excitations can combine into bound states and show dimensional reduction in their kinetics, contrary to 'freely' dispersive fluxes and charges in the parallel field case [69]. We shall discuss bound states in detail in Chapter 7. However, one can already understand the dimensional reduction of the kinetics, by considering Figure 4.4. The operator σ^y flips eigenvalues of two stars, as well as two plaquettes, surrounding a site. Thus, the action of the particle conserving effective Hamiltonian can shift a vertically (horizontally) adjacent charge-flux pair into horizontal (vertical) direction. Movements in any other

direction are forbidden since they always involve a creation of additional particles. Similarly, two neighboring particles of the *same* type are not dispersive because the only particle conserving action of σ^y is the transformation of the charge pair into a flux pair (and vice versa), without moving the center of mass of the particle pair. Analogue arguments can be used to explain the dimensional reduction of bound states with more than two particles.

Using a non-local mapping, the model (4.32) can be transformed onto a self-dual model proposed by Xu and Moore [124, 125].

$$H_{\text{XM}} = -J \sum_i \sigma_i^x - h_y \sum_p \prod_{i \in p} \sigma_i^z, \quad (4.33)$$

where quantum spins-1/2 are placed at *vertices* i of a square lattice and $i \in p$ denotes, as usual, the four sites around a square plaquette p . In order to transform H_{TF} , we consider the toric code on an infinite open plane with spins positioned on bonds of Λ . We will use illustrations in order to guide through this somewhat sophisticated mapping. First, the \mathbb{Z}_2 degrees of freedom on stars and plaquettes are replaced by effective spin variables

$$\tilde{\sigma}_{j_s}^z = A_s, \quad (4.34)$$

$$\tilde{\sigma}_{j_p}^z = B_p, \quad (4.35)$$

so that sites j lie on a rhombic superlattice $\tilde{\Lambda}$, represented by gray squares in Figure 4.9 (a). The magnetic field is subject to a non-local mapping via

$$\tilde{\sigma}_j^x = \prod_{i < j} \sigma_i^y, \quad (4.36)$$

where the sum on the right runs through all $i \in \Lambda$, relatively to $j \in \tilde{\Lambda}$ as depicted in Figure 4.9 (b). Finally, we argue that the toric code in a transverse magnetic field is isospectral to

$$\tilde{H}_{\text{XM}} = -J \sum_j \tilde{\sigma}_j^z - h_y \sum_{\tilde{p}} \prod_{j \in \tilde{p}} \tilde{\sigma}_j^x, \quad (4.37)$$

where $j \in \tilde{p}$ is a product along the boundary sites $j \in \tilde{\Lambda}$ of the plaquette \tilde{p} of the lattice $\tilde{\Lambda}$. Note that this mapping is not exact concerning degeneracies (also we end up with a tilted square lattice, but this has no physical effect). However, the first sum counts the number of charges and fluxes and its spectrum is equivalent to the one of the unperturbed toric code. Considering a single term from the second sum, we illustrate the action of $\prod_{j \in \tilde{p}} \tilde{\sigma}_j^x$ in Figure 4.9 (c). Since acting an even number of times with a Pauli

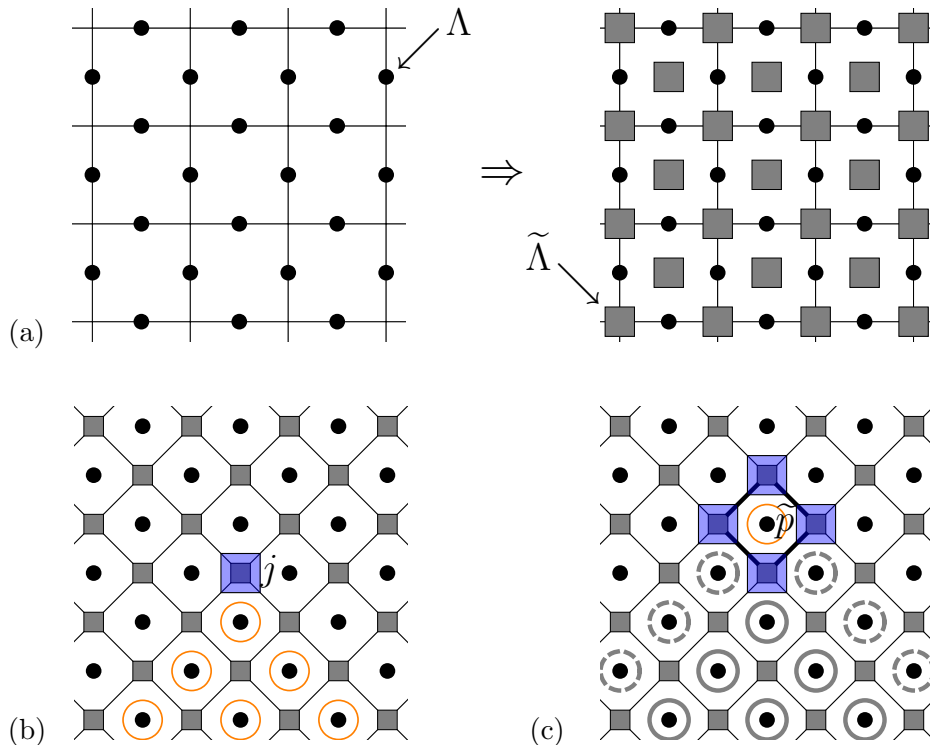


FIGURE 4.9: Illustration of the mapping of the toric code in a transverse field (4.32) onto the Xu-Moore model (4.37). (a) In addition to the initial spins of the toric code, positioned on lattice Λ , effective spins on stars and plaquettes are introduced. They are depicted by gray squares which assemble into a rhombic lattice $\tilde{\Lambda}$. (b) Action of $\tilde{\sigma}_j^x = \prod_{i < j} \sigma_i^y$. The site j is highlighted by a blue square, while the sites $i < j$ are encircled with an orange color, covering a quarter of the infinite open plane. (c) Action of $\prod_{j \in \tilde{p}} \tilde{\sigma}_j^x$, \tilde{p} is marked by a thick border. The spins acted upon twice (four times) are highlighted by dashed (solid), gray circles. The spin inside the plaquette \tilde{p} is acted upon only once.

operator is equivalent to unity, the non-local part of this term is canceled out and what is left is a single σ_i^y with $i \in \Lambda$. Thus, the second sum can be identified with $\sum_{i \in \Lambda} \sigma_i^y$ and \tilde{H}_{XM} has indeed the same spectrum as H_{TF} .

The Xu-Moore model itself can also be mapped onto the quantum compass model [126] which in turn can be mapped onto the so-called cluster-state Hamiltonian [127–129], relevant for measurement-based quantum computing. The quantum compass model has been known for a fairly long time in the context of frustrated magnetism [130] and received intensive interest through the last decade [118, 126, 131–134]. Several of these studies have argued that the system undergoes a discontinuous phase transition at the self-dual point $J = h_y$. This has also been clarified by series expansions (with pCUT) as well as exact diagonalizations in Ref. [69]. Additionally, in Ref. [69] it has been shown that the low-energy physics of the toric code in a transverse field is very different from the one in a parallel field. In a presence of pure transverse field a single charge (or equivalently a single flux) is dispersionless, while multi-particle composites hop in a

correlated way along typical one-dimensional paths. This is in deep contrast to what is found in the toric code with a parallel magnetic field, where the dispersion of charges and fluxes is truly two-dimensional. In the following section, we will show how the quasi-particle picture provided by pCUT naturally explains these phenomena.

We summarize that exact mappings of the toric code in a solely parallel as well as a solely transverse magnetic field to well known models provide us with a rich phase diagram. In the parallel field with $h_x \neq h_z$ condensation of either fluxes or charges yields a quantum phase transitions of second-order with critical exponents from 3d Ising universality class. For $h_x = h_z$, charges and fluxes condense simultaneously so that their mutual anyonic character directly influences the critical behavior. Indeed, it has been found that the critical exponents for this case differ from the 3d Ising universality class. Furthermore, the phase transition point for $h_x = h_z$ is multicritical since it is very likely connected to a first-order phase transition line outside the topological phase. Due to the sign problem, quantum Monte Carlo simulations cannot be performed efficiently for the general field case so that perturbative expansions and variational methods are the only available tools to tackle the problem. We have seen that in the transverse field the topological phase of the toric code undergoes a discontinuous phase transition. Low-energy series expansions in one phase are, by construction, blind to level-crossings, and are therefore unable to detect first-order phase transitions. Therefore, we have been led to combine pCUT with a variational method (see Section 5.3.3 for more details) in order to obtain the full phase diagram.

pCUT method for the toric code in a field

Our goal in this chapter is to demonstrate how the pCUT technique is applied in practice. In the low-field limit of the toric code, the system is topologically ordered, and we face the challenge of deriving a quasi-particle picture for anyons, which is a non-trivial task in a highly-entangled system. Furthermore, in order to profit from the finite-lattice method, it has to be adapted to the specific lattice of the toric code, where elementary graphs are more complex than the ones of a square lattice. Subsequently, we draw our attention to the limit of high magnetic fields. In this case, the system is polarized in the field direction and the pCUT approach is applied to compute the gap of a dressed magnon. Finally, we discuss the general structure of the algorithm used in our computer-aided analysis, and we explain extrapolation methods essential to determine the phase boundaries from high-order series expansions.

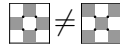
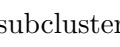
5.1 Applying pCUT to a topological phase

5.1.1 First steps: effective operators, finite clusters

In order to apply the pCUT method to a model of interest, one first needs to make sure that the conditions (i)-(iii) listed in Section 2.1 are fulfilled. We have already seen that the spectrum of the unperturbed toric code (4.1) is discrete and equidistant. Let us focus on open-plane boundary conditions. The ground-state energy of a system with N spins is then exactly $-NJ$, and the distance between neighboring energy levels¹ is constantly $4J$. We set once and for all $J = 1/2$ so that the excitation energy of each

¹We point out that the equidistant spectrum is realized as long as the cost of creating charges and fluxes is the same. Introducing individual coupling amplitudes $J_s \neq J_p$ would destroy this feature and hereby the applicability of pCUT.

state above the ground state coincides with the number of particles in the system. Thus, we meet already the conditions (i) and (ii). Next, we reformulate the perturbation by the magnetic field in terms of operators T_m that change the number of fluxes and charges by m . While in Section 4.2 we considered the action of Pauli operators on the ground state (see in particular Figure 4.4), we now generalize their action to an arbitrary quasi-particle sector.

It is important to note that the perturbing operators always act on *single* spins and thus affect the \mathbb{Z}_2 eigenvalues of a pair of stars and a pair of plaquettes surrounding the spin. Therefore it is legitimate to consider an elementary piece $\mathbf{C}_{2 \times 2}^s$ of the lattice to fully determine the action of each Pauli operator. We adopt the notation of rectangular subclusters from Section 3.3, taking into account the specific characteristics of the toric code: firstly, particles live on stars and plaquettes instead of sites, and secondly p and s form a checkerboard lattice, where subclusters, in addition to their dimension, are characterized by tile symmetry. Inversion of tile colors yields generally a cluster not related to the initial one by any rotational or mirror symmetry. For example:  \neq  (formally $\mathbf{C}_{3 \times 3}^s \neq \mathbf{C}_{3 \times 3}^p$). The two possible colorings for each checkerboard subcluster are distinguished by an upper index s or p depending on the type of the lower left tile. In what follows, we will use the graphical notation according to Table 5.1, in order to denote physical states on a given cluster.

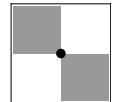
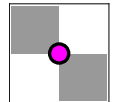
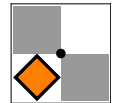
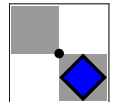
zero particles, spin up		zero particles, spin down	
single charge, spin up		single flux, spin up	

TABLE 5.1: Illustration of the graphical notation of the \mathbb{Z}_2 degrees of freedom of the toric code, exemplified on an elementary piece of the lattice. Spins are represented by round shapes: the black dot stands for spin up and the purple circle for spin down. An s (p) not carrying a particle will be represented by a white (gray) square. Particles are shown as colored rectangular shapes. Although it is unambiguous whether a particle is a charge or a flux, we find it helpful to distinguish them additionally by color: orange stands for charges and blue for fluxes.

With the introduced graphical language at hand, the action of Pauli operators can now be summarized as it is done in Table 5.2. In principle, we have to consider the action of every Pauli operator on each of the 2^5 possible states on the clusters $\mathbf{C}_{2 \times 2}^s$, as well as $\mathbf{C}_{2 \times 2}^p$ (and this is actually done in our computer-aided analysis). However, at this point, we find it useful to only show basic non-trivial processes, characteristic for the toric code in a magnetic field (see Table 5.2) and refer to Appendix A.1 for the complete list.

	T_0	$T_{\pm 2}$	$T_{\pm 4}$
σ^z			
σ^x			
σ^y			

TABLE 5.2: Action of Pauli matrices on eigenstates of the toric code. Only representatives of non-zero processes are shown. The table should be viewed as follows. Acting with T_0 , T_{+2} or T_{+4} on a state to the left of the double arrow (in each respective column) yields the state on the right. In the same spirit, acting with T_0 , T_{-2} or T_{-4} on a state to the right of the double arrow yields the state on the left. Note that some operations may involve a change of amplitude (to ± 1 or $\pm i$), this is not shown here in order to keep a clear overview. See Appendix A.1 for more details.

Thereby, we have shown that the perturbing magnetic field can be represented by T_m operators, and the last criterion (iii) is met. This is sufficient to run the pCUT machinery on the given problem. The performance of our computations will, however, be significantly improved when making use of the finite-cluster approach (see Section 3.3). In the next step we will present a generalized version of the finite-cluster method, by updating (3.12) and (3.13) to the formalism of quantum mechanics, and also the somewhat unusual toric code subclusters (in the sense that in addition to a square lattice of spins we have two tilted square sublattices (a checkerboard) of stars and plaquettes).

The above considerations allow us to establish the notion of 'linked' for clusters of the toric code. Let us remind that the effective Hamiltonian H_{eff} at order k is a superposition of $T(\mathbf{m})$, with $|\mathbf{m}| = k$. Incorporating relation (3.1), one can expand all terms in H_{eff} and obtains generally a superposition of $\mathcal{T}(\mathbf{m}, i_1, i_2 \dots i_k)$ (referred to as 'processes' later on) constructed as follows:

$$\mathcal{T}(\mathbf{m}, i_1, i_2 \dots i_k) = \mathcal{T}_{m_1, i_1} \mathcal{T}_{m_2, i_2} \dots \mathcal{T}_{m_k, i_k}. \quad (5.1)$$

These are k -fold products of operators with $m_j \in \{0, \pm 2, \pm 4\}$ and $\sum_j m_j = 0$. An operator \mathcal{T}_{m_j, i_j} changes the number of particles by m_j , by acting on site i_j . The question is, what is the maximal distance between two sites of this k -fold product so that the resulting process can be linked? This is crucial for determining the maximal cluster size and thus the bounds of the sum in (3.12). At order one, $\mathcal{T}(\mathbf{m}, i_1)$ consists of a single operator, acting on exactly one site. In this case, trivially, there are no linked processes

involving more than one site. At order two, we have to consider the operator $\mathcal{T}(\mathbf{m}, i_1, i_2)$. This operator generates linked processes, if the sites i_1 and i_2 are neighboring sites on the vertical, horizontal, or diagonal. In this sense, a site on the square lattice is surrounded by 8 direct neighbors, 16 secondary neighbors and $8(k-1)$ k -degree neighbors. Using this definition we conclude that $\mathcal{T}(\mathbf{m}, i_1, i_2 \dots i_k)$ can only be linked, if any two sites $i_j, i_{j'}$ are neighbors of degree k or less. Therefore, at order k , the biggest clusters to consider are $\mathbf{C}_{m \times n}^s$ and $\mathbf{C}_{m \times n}^p$ (as well as $\mathbf{C}_{n \times m}^s$ and $\mathbf{C}_{n \times m}^p$) with $m = k + 1$ and $n \in \{2, 3, \dots, k + 1\}$, see Table 5.3 for an example. The total number of contributing clusters grows quadratically with order.

order 1	
order 2	
order 3	

TABLE 5.3: Toric code clusters relevant for computations at a given order. For the sake of clarity we show only $\mathbf{C}_{m \times n}^s$. The contributing $\mathbf{C}_{m \times n}^p$ can be obtained through tile-color inversion.

Let us generally denote a quantum state living on a cluster $\mathbf{C}_{m \times n}$ by $|\mathbf{C}_{m \times n}, \varphi\rangle$, where φ is a set of quantum numbers fully characterizing the state. We define a matrix element of a Hamiltonian H acting in the Hilbert space of the finite cluster as

$$P(\mathbf{C}_{m \times n}; \varphi'; \varphi) = \langle \mathbf{C}_{m \times n}, \varphi' | H | \mathbf{C}_{m \times n}, \varphi \rangle. \quad (5.2)$$

On the toric code lattice Λ_{TC} , the matrix element at order k is, in the thermodynamic limit, found to be

$$P(\Lambda_{\text{TC}}; \varphi'; \varphi)^{(k)}/N = \sum_{m=2}^{k+1} \sum_{n=2}^{k+1} \widetilde{W}^+(\mathbf{C}_{m \times n}; \varphi'; \varphi), \quad (5.3)$$

$$\widetilde{W}^{\pm}(\mathbf{C}_{m \times n}; \varphi'; \varphi) = \frac{W(\mathbf{C}_{m \times n}^s; \varphi'; \varphi) \pm W(\mathbf{C}_{m \times n}^p; \varphi'; \varphi)}{2}, \quad (5.4)$$

where W are subtracted weights to be defined below, \widetilde{W}^+ is symmetrized and \widetilde{W}^- is antisymmetrized with respect to s and p . Note that in contrast to (3.12), we dropped the condition $m \leq n$ in the double sum. While this is irrelevant for $m = n$, the lattice constant of non-square subclusters has to be multiplied with $1/2$, thus the lattice constant dependent prefactor of all \widetilde{W} is set to one. Let us now define the reduced

weights:

$$\begin{aligned}
W(\mathbf{C}_{m \times n}^s; \varphi'; \varphi) = \\
P(\mathbf{C}_{m \times n}^s; \varphi'; \varphi) - \sum_{\substack{m' \leq m \\ n' < n}} \sum_{\substack{m' < m \\ n' = n}} \left[\Delta x \Delta y \widetilde{W}^+(\mathbf{C}_{m' \times n'}; \varphi'; \varphi) + \delta x \delta y \widetilde{W}^-(\mathbf{C}_{m' \times n'}; \varphi'; \varphi) \right],
\end{aligned} \tag{5.5}$$

$$\begin{aligned}
W(\mathbf{C}_{m \times n}^p; \varphi'; \varphi) = \\
P(\mathbf{C}_{m \times n}^p; \varphi'; \varphi) - \sum_{\substack{m' \leq m \\ n' < n}} \sum_{\substack{m' < m \\ n' = n}} \left[\Delta x \Delta y \widetilde{W}^+(\mathbf{C}_{m' \times n'}; \varphi'; \varphi) - \delta x \delta y \widetilde{W}^-(\mathbf{C}_{m' \times n'}; \varphi'; \varphi) \right],
\end{aligned} \tag{5.6}$$

where we abbreviated

$$\Delta x = m - m' + 1 \tag{5.7}$$

$$\Delta y = n - n' + 1 \tag{5.8}$$

$$\delta x = (m \bmod 2) + (m' \bmod 2) - 1 \tag{5.9}$$

$$\delta y = (n \bmod 2) + (n' \bmod 2) - 1. \tag{5.10}$$

The basic idea behind the above formulae is the same as in (3.12) and (3.13). We construct reduced weights of each cluster, by subtracting all contributions which would fit on a cluster with a smaller size. On a checkerboard lattice, one has to account for alternating colors, which results in more complicated functions governing the type and the number of subtracted subclusters. In order to exemplify the general expressions (5.2) -(5.10) in a useful context, we will next consider their application in various quasi-particle subspaces of interest.

5.1.2 General procedure

The effective particle-conserving Hamiltonian has been determined model-independently up to a high order [102]. We denote

$$H_{\text{eff}} = \sum_k H_{\text{eff}}^{(k)}, \tag{5.11}$$

where $H_{\text{eff}}^{(k)}$ is the effective Hamiltonian at order k . To be specific, in the case of the toric code model in a magnetic field, the first three orders of H_{eff} read

$$H_{\text{eff}}^{(0)} = -NJ + Q, \tag{5.12}$$

$$H_{\text{eff}}^{(1)} = T_0, \tag{5.13}$$

$$H_{\text{eff}}^{(2)} = \frac{1}{2}T_2T_{-2} - \frac{1}{2}T_{-2}T_2 + \frac{1}{4}T_4T_{-4} - \frac{1}{4}T_{-4}T_4, \quad (5.14)$$

$$\begin{aligned} H_{\text{eff}}^{(3)} = & \frac{1}{16}T_{-4}T_0T_4 + \frac{1}{8}T_{-4}T_2T_2 - \frac{1}{32}T_{-4}T_4T_0 + \frac{1}{8}T_{-2}T_{-2}T_4 + \frac{1}{4}T_{-2}T_0T_2 \\ & - \frac{1}{8}T_{-2}T_2T_0 - \frac{1}{4}T_{-2}T_4T_{-2} - \frac{1}{32}T_0T_{-4}T_4 - \frac{1}{8}T_0T_{-2}T_2 - \frac{1}{8}T_0T_2T_{-2} \\ & - \frac{1}{32}T_0T_4T_{-4} - \frac{1}{4}T_2T_{-4}T_2 - \frac{1}{8}T_2T_{-2}T_0 + \frac{1}{4}T_2T_0T_{-2} + \frac{1}{8}T_2T_2T_{-4} \\ & - \frac{1}{32}T_4T_{-4}T_0 + \frac{1}{8}T_4T_{-2}T_{-2} + \frac{1}{16}T_4T_0T_{-4}, \end{aligned} \quad (5.15)$$

where N is the number of spins and Q the particle-counting operator. The small parameters (fields h_x , h_y and h_z) are included in the definitions of T_m . Note that in the toric code, terms including $T_{\pm 1}$, $T_{\pm 3}$ and $T_{\pm m}$ with $m > 4$ do not exist and are therefore not shown. A further technical remark is that formally the coefficients of any term in $H_{\text{eff}}^{(k)}$ can be rescaled to the ones of an effective Hamiltonian with exclusively T_0 , $T_{\pm 1}$ and $T_{\pm 2}$ operators by the factor $(1/2)^{k-1}$. Next, we will demonstrate the general procedure of applying the pCUT and the finite-cluster methods to the perturbed toric code.

Our general approach is to compute matrix elements of H_{eff} in various (low) quasi-particle subspaces by acting with H_{eff} on appropriate states. In the toric code, this seems to be a non-trivial task because of the 'projector structure' of the eigenstates. Let us begin by considering the ground state (4.16). In the thermodynamic limit, the four-fold degenerate ground states cannot be connected by $H_{\text{eff}}^{(k)}$ with finite k because of the topological order and also due to the linked-cluster theorem. Thus, without loss of generality, one can derive local properties of the model exclusively in the subspace $|\text{gs}, 1, 1\rangle$, i.e., there are no non-contractible loops in the ground state of the system. Note that it is possible to perform calculations using any of the ground states, but the choice must be consistent.

As argued in Section 4.1, the ground state of the toric code can be viewed as an equal-weight superposition of states, each one being characterized by a distinct combination of closed spin-down loops in an all-spins-up reference state $|\uparrow\rangle$ [see (4.17)]. This picture will be useful in the following. An important consequence of the particle-conserving feature of H_{eff} is that instead of a loop-gas state it is sufficient to consider a single representative, namely the reference state $|\uparrow\rangle$. This can be understood by realizing that in the ground state the effective Hamiltonian commutes with the projectors which generate the loop gas because the local eigenvalues of A_s are kept constantly $+1$.

$$H_{\text{eff}} |\text{gs}, 1, 1\rangle = \mathcal{N} H_{\text{eff}} \prod_s \left(\frac{\mathbf{1} + A_s}{2} \right) |\uparrow\rangle = \mathcal{N} \prod_s \left(\frac{\mathbf{1} + A_s}{2} \right) H_{\text{eff}} |\uparrow\rangle. \quad (5.16)$$

Given the fact that for any projector P it follows $P^2 = P$, one gets

$$\langle \text{gs}, 1, 1 | H_{\text{eff}} | \text{gs}, 1, 1 \rangle = \langle \uparrow | \mathcal{N}^2 \prod_s \left(\frac{\mathbb{1} + A_s}{2} \right) H_{\text{eff}} | \uparrow \rangle = \langle \text{gs}, 1, 1 | \mathcal{N} H_{\text{eff}} | \uparrow \rangle. \quad (5.17)$$

In a similar fashion, one can get rid of the loop gas in a one-particle state. For example let us consider the action of H_{eff} on single-particle states, as defined in (4.19) and (4.20).

$$H_{\text{eff}} |s\rangle = \mathcal{N} H_{\text{eff}} \left(\frac{\mathbb{1} - A_s}{2} \right) \prod_{s' \neq s} \left(\frac{\mathbb{1} + A_{s'}}{2} \right) | \uparrow \rangle \quad (5.18)$$

$$= \mathcal{N} \prod_{s' \neq s} \left(\frac{\mathbb{1} + A_{s'}}{2} \right) H_{\text{eff}} \left(\frac{\mathbb{1} - A_s}{2} \right) | \uparrow \rangle, \quad (5.19)$$

$$H_{\text{eff}} |p\rangle = \mathcal{N} H_{\text{eff}} \prod_s \left(\frac{\mathbb{1} + A_s}{2} \right) | \mathcal{C}_p \rangle \quad (5.20)$$

$$= \mathcal{N} \prod_s \left(\frac{\mathbb{1} + A_s}{2} \right) H_{\text{eff}} | \mathcal{C}_p \rangle. \quad (5.21)$$

A matrix element of H_{eff} in the one-particle subspace is thereupon

$$\langle s' | H_{\text{eff}} |s\rangle = \langle s' | \mathcal{N} H_{\text{eff}} \left(\frac{\mathbb{1} - A_s}{2} \right) | \uparrow \rangle, \quad (5.22)$$

$$\langle p' | H_{\text{eff}} |p\rangle = \langle p' | \mathcal{N} H_{\text{eff}} | \mathcal{C}_p \rangle. \quad (5.23)$$

One can straightforwardly generalize this for multi-particle states. Thus, we have shown that if one is interested to compute matrix elements of the effective Hamiltonian, the vacuum of H_{eff} can be represented by the reference state $| \uparrow \rangle$. This is an essential premise to apply pCUT efficiently in the given context.

Finally, we demonstrate how pCUT is performed under use of the finite-lattice method by explicitly calculating the ground-state energy up to order two. After convincing ourselves that the loop-gas can be avoided in our computations, we find that the clusters shown in Table 5.3 actually already carry the ground state (under adherence of the notation in Table 5.1) and can directly be used to compute (5.17). Generally, when acting on the ground state, H_{eff} creates an even number of particles, makes them hop on a square sublattice of s and p and annihilates them again. Since only particles of the same type can annihilate, the geometry of the lattice allows only an *even* number of hoppings before an annihilation. Thus, the series expansion of the ground state contains only even terms. At order zero, we already know the ground-state energy to be $-JN$. Formally, we use (5.12) to write

$$e_0^{(0)} = \frac{-N/2}{N/2 + N/2} = -\frac{1}{2}, \quad (5.24)$$

where, $e_0^{(0)}$ is the zeroth order contribution to the ground-state energy per site in the thermodynamic limit. As usual, J has been set to $1/2$, and $N/2$ is the number of stars and plaquettes in a lattice of N spins.

We compute $e_0^{(2)}$, by first calculating

$$E(\mathbf{C}_{2 \times 2}^s) = E(\mathbf{C}_{2 \times 2}^p) = \langle \mathbf{C}_{2 \times 2}^s | H_{\text{eff}}^{(2)} | \mathbf{C}_{2 \times 2}^s \rangle, \quad (5.25)$$

$$E(\mathbf{C}_{3 \times 2}^s) = E(\mathbf{C}_{3 \times 2}^p) = E(\mathbf{C}_{2 \times 3}^p) = E(\mathbf{C}_{2 \times 3}^s) = \langle \mathbf{C}_{3 \times 2}^s | H_{\text{eff}}^{(2)} | \mathbf{C}_{3 \times 2}^s \rangle, \quad (5.26)$$

$$E(\mathbf{C}_{3 \times 3}^s) = \langle \mathbf{C}_{3 \times 3}^s | H_{\text{eff}}^{(2)} | \mathbf{C}_{3 \times 3}^s \rangle, \quad (5.27)$$

$$E(\mathbf{C}_{3 \times 3}^p) = \langle \mathbf{C}_{3 \times 3}^p | H_{\text{eff}}^{(2)} | \mathbf{C}_{3 \times 3}^p \rangle, \quad (5.28)$$

where the notation from (5.2) has been used to denote the ground state ($|\mathbf{C}_{m \times n}^s\rangle$ or $|\mathbf{C}_{m \times n}^p\rangle$) as well as the (unsubtracted) ground-state energy $E(\mathbf{C}_{m \times n})$ of a cluster $\mathbf{C}_{m \times n}$. Here, we denote energies without the index corresponding to perturbation order because it is clear that we work at order two. The equalities in (5.25) and (5.26) are valid due to rotational symmetry of the concerned clusters. Let us now insert the explicit expression of $H_{\text{eff}}^{(2)}$ from equation (5.14) in order to compute (5.25).

$$\langle \begin{array}{|c|c|} \hline \blacksquare & \blacksquare \\ \hline \blacksquare & \blacksquare \\ \hline \end{array} | H_{\text{eff}}^{(2)} | \begin{array}{|c|c|} \hline \blacksquare & \blacksquare \\ \hline \blacksquare & \blacksquare \\ \hline \end{array} \rangle = \langle \begin{array}{|c|c|} \hline \blacksquare & \blacksquare \\ \hline \blacksquare & \blacksquare \\ \hline \end{array} | \frac{1}{2}T_2T_{-2} - \frac{1}{2}T_{-2}T_2 + \frac{1}{4}T_4T_{-4} - \frac{1}{4}T_{-4}T_4 | \begin{array}{|c|c|} \hline \blacksquare & \blacksquare \\ \hline \blacksquare & \blacksquare \\ \hline \end{array} \rangle. \quad (5.29)$$

Terms annihilating particles on the ground state yield zero by definition. The two remaining terms are now processed as follows

$$\langle \begin{array}{|c|c|} \hline \blacksquare & \blacksquare \\ \hline \blacksquare & \blacksquare \\ \hline \end{array} | T_{-2}T_2 | \begin{array}{|c|c|} \hline \blacksquare & \blacksquare \\ \hline \blacksquare & \blacksquare \\ \hline \end{array} \rangle = \langle \begin{array}{|c|c|} \hline \blacksquare & \blacksquare \\ \hline \blacksquare & \blacksquare \\ \hline \end{array} | T_{-2} \left(-h_z \begin{array}{|c|c|} \hline \color{orange}{\blacksquare} & \color{orange}{\blacksquare} \\ \hline \color{orange}{\blacksquare} & \color{orange}{\blacksquare} \\ \hline \end{array} - h_x \begin{array}{|c|c|} \hline \color{blue}{\blacksquare} & \color{blue}{\blacksquare} \\ \hline \color{blue}{\blacksquare} & \color{blue}{\blacksquare} \\ \hline \end{array} \right) \rangle \quad (5.30)$$

$$= \langle \begin{array}{|c|c|} \hline \blacksquare & \blacksquare \\ \hline \blacksquare & \blacksquare \\ \hline \end{array} | h_z^2 + h_x^2 | \begin{array}{|c|c|} \hline \blacksquare & \blacksquare \\ \hline \blacksquare & \blacksquare \\ \hline \end{array} \rangle = h_z^2 + h_x^2 \quad (5.31)$$

$$\langle \begin{array}{|c|c|} \hline \blacksquare & \blacksquare \\ \hline \blacksquare & \blacksquare \\ \hline \end{array} | T_{-4}T_4 | \begin{array}{|c|c|} \hline \blacksquare & \blacksquare \\ \hline \blacksquare & \blacksquare \\ \hline \end{array} \rangle = -ih_y \langle \begin{array}{|c|c|} \hline \blacksquare & \blacksquare \\ \hline \blacksquare & \blacksquare \\ \hline \end{array} | T_{-4} \begin{array}{|c|c|} \hline \color{orange}{\blacksquare} & \color{blue}{\blacksquare} \\ \hline \color{blue}{\blacksquare} & \color{orange}{\blacksquare} \\ \hline \end{array} \rangle = h_y^2 \langle \begin{array}{|c|c|} \hline \blacksquare & \blacksquare \\ \hline \blacksquare & \blacksquare \\ \hline \end{array} | \begin{array}{|c|c|} \hline \blacksquare & \blacksquare \\ \hline \blacksquare & \blacksquare \\ \hline \end{array} \rangle = h_y^2, \quad (5.32)$$

and we find

$$E(\mathbf{C}_{2 \times 2}^s) = -\frac{1}{2} (h_z^2 + h_x^2) - \frac{1}{4} h_y^2. \quad (5.33)$$

Obviously, *at order two*, all processes in H_{eff} involve exclusively single spins² when acting on the ground state. Therefore, $E(\mathbf{C}_{2 \times 2}^s)$ is already equivalent to the second-order contribution to ground-state energy per site. However, it is the purpose of this exercise to demonstrate the properties of the finite-lattice method and we continue the calculation even though the following results might seem trivial. In the same way as

²Note that this is a model-specific feature, rather than a general feature of H_{eff} .

above, we obtain the remaining terms

$$E(\mathbf{C}_{3 \times 2}^s) = -h_z^2 - h_x^2 - \frac{1}{2}h_y^2, \quad (5.34)$$

$$E(\mathbf{C}_{3 \times 3}^s) = -2(h_z^2 + h_x^2) - h_y^2, \quad (5.35)$$

$$E(\mathbf{C}_{3 \times 3}^p) = -2(h_z^2 + h_x^2) - h_y^2. \quad (5.36)$$

Note that generally $E(\mathbf{C}_{3 \times 3}^s) \neq E(\mathbf{C}_{3 \times 3}^p)$. However, since at order two neighboring spins are not linked, H_{eff} does not feel the different symmetry of $\mathbf{C}_{3 \times 3}^s$ and $\mathbf{C}_{3 \times 3}^p$. Now we apply the subtraction scheme defined in (5.3) and we obtain

$$W(\mathbf{C}_{2 \times 2}^s) = E(\mathbf{C}_{2 \times 2}^s), \quad (5.37)$$

$$W(\mathbf{C}_{2 \times 2}^p) = E(\mathbf{C}_{2 \times 2}^p), \quad (5.38)$$

$$\widetilde{W}^+(\mathbf{C}_{2 \times 2}) = \frac{E(\mathbf{C}_{2 \times 2}^s) + E(\mathbf{C}_{2 \times 2}^p)}{2} = E(\mathbf{C}_{2 \times 2}^s), \quad (5.39)$$

where the last equality is due to (5.25). For the remaining quantities we find

$$W(\mathbf{C}_{3 \times 2}^s) = E(\mathbf{C}_{3 \times 2}^s) - 2\widetilde{W}^+(\mathbf{C}_{2 \times 2}) = E(\mathbf{C}_{3 \times 2}^s) - 2E(\mathbf{C}_{2 \times 2}^s), \quad (5.40)$$

$$W(\mathbf{C}_{3 \times 2}^p) = E(\mathbf{C}_{3 \times 2}^p) - 2\widetilde{W}^+(\mathbf{C}_{2 \times 2}) = E(\mathbf{C}_{3 \times 2}^s) - 2E(\mathbf{C}_{2 \times 2}^s), \quad (5.41)$$

$$W(\mathbf{C}_{2 \times 3}^s) = E(\mathbf{C}_{2 \times 3}^s) - 2\widetilde{W}^+(\mathbf{C}_{2 \times 2}) = E(\mathbf{C}_{3 \times 2}^s) - 2E(\mathbf{C}_{2 \times 2}^s), \quad (5.42)$$

$$W(\mathbf{C}_{2 \times 3}^p) = E(\mathbf{C}_{2 \times 3}^p) - 2\widetilde{W}^+(\mathbf{C}_{2 \times 2}) = E(\mathbf{C}_{3 \times 2}^s) - 2E(\mathbf{C}_{2 \times 2}^s), \quad (5.43)$$

$$\widetilde{W}^+(\mathbf{C}_{3 \times 2}) = \frac{W(\mathbf{C}_{3 \times 2}^s) + W(\mathbf{C}_{3 \times 2}^p)}{2} = E(\mathbf{C}_{3 \times 2}^s) - 2E(\mathbf{C}_{2 \times 2}^s), \quad (5.44)$$

$$\widetilde{W}^+(\mathbf{C}_{2 \times 3}) = \frac{W(\mathbf{C}_{2 \times 3}^s) + W(\mathbf{C}_{2 \times 3}^p)}{2} = E(\mathbf{C}_{2 \times 3}^s) - 2E(\mathbf{C}_{2 \times 2}^s). \quad (5.45)$$

Here we used the relations (5.26) for the energies.

$$W(\mathbf{C}_{3 \times 3}^s) = E(\mathbf{C}_{3 \times 3}^s) - 4\widetilde{W}^+(\mathbf{C}_{2 \times 2}) - 2\widetilde{W}^+(\mathbf{C}_{3 \times 2}) - 2\widetilde{W}^+(\mathbf{C}_{2 \times 3}) \quad (5.46)$$

$$= E(\mathbf{C}_{3 \times 3}^s) - 2E(\mathbf{C}_{3 \times 2}^s) - 2E(\mathbf{C}_{2 \times 3}^s) + 4E(\mathbf{C}_{2 \times 2}^s), \quad (5.47)$$

$$W(\mathbf{C}_{3 \times 3}^p) = E(\mathbf{C}_{3 \times 3}^p) - 4\widetilde{W}^+(\mathbf{C}_{2 \times 2}) - 2\widetilde{W}^+(\mathbf{C}_{3 \times 2}) - 2\widetilde{W}^+(\mathbf{C}_{2 \times 3}) \quad (5.48)$$

$$= E(\mathbf{C}_{3 \times 3}^p) - 2E(\mathbf{C}_{3 \times 2}^s) - 2E(\mathbf{C}_{2 \times 3}^s) + 4E(\mathbf{C}_{2 \times 2}^s), \quad (5.49)$$

$$\widetilde{W}^+(\mathbf{C}_{3 \times 3}) = \frac{W(\mathbf{C}_{3 \times 3}^s) + W(\mathbf{C}_{3 \times 3}^p)}{2}, \quad (5.50)$$

$$= \frac{E(\mathbf{C}_{3 \times 3}^s) + E(\mathbf{C}_{3 \times 3}^p)}{2} - 2E(\mathbf{C}_{3 \times 2}^s) - 2E(\mathbf{C}_{2 \times 3}^s) + 4E(\mathbf{C}_{2 \times 2}^s). \quad (5.51)$$

By inserting the ground-state energies computed for each subcluster in (5.33)-(5.36) we obtain the symmetrized reduced weights

$$\widetilde{W}^+(\mathbf{C}_{2 \times 2}) = -\frac{1}{2}(h_z^2 + h_x^2) - \frac{1}{4}h_y^2, \quad (5.52)$$

$$\widetilde{W}^+(\mathbf{C}_{3 \times 2}) = 0, \quad (5.53)$$

$$\widetilde{W}^+(\mathbf{C}_{2 \times 3}) = 0, \quad (5.54)$$

$$\widetilde{W}^+(\mathbf{C}_{3 \times 3}) = 0. \quad (5.55)$$

Finally, the (trivial) summation (5.3) yields the second-order contribution to the ground-state energy per site

$$e_0^{(2)} = -\frac{1}{2}(h_z^2 + h_x^2) - \frac{1}{4}h_y^2. \quad (5.56)$$

Generally, in a perturbative expansion to higher orders, there are linked processes involving *multiple* sites. So the subtraction is less trivial, in contrast to the presented specific example, where most subtracted symmetrized weights are zero. Furthermore, with higher perturbation orders the number of subclusters grows quadratically, while the number of terms in H_{eff} grows exponentially so that one should tackle the problem with high-performance computing.

Some of the exotic features of the toric code start to appear only beyond order four in perturbation since four is the minimal number of sites necessary for a closed loop. An explicit order four calculation is already beyond the scope of a written manuscript. However, it might be insightful to consider a certain non-trivial process. Let us examine the action of the order four term $T_{-2}T_0T_0T_2$ on the ground state of the cluster $\mathbf{C}_{3 \times 3}^s$. We will focus on the specific process $\mathcal{T}_{-2,4}\mathcal{T}_{0,3}\mathcal{T}_{0,2}\mathcal{T}_{+2,1}$, where sites are numbered according to Figure 5.1. The final state of the process shown in Figure 5.1 is clearly a ground state (because it contains zero particles). Thus we have shown, how a vacuum fluctuation induced by H_{eff} 'leaves a trace' in the form of a closed loop. Obviously, at higher orders

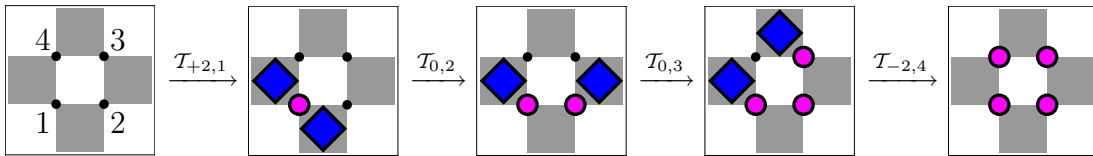


FIGURE 5.1: Action of the process $\mathcal{T}_{-2,4}\mathcal{T}_{0,3}\mathcal{T}_{0,2}\mathcal{T}_{+2,1}$ on the ground state of the cluster $\mathbf{C}_{3 \times 3}^s$. The first index of \mathcal{T} refers to the change of the particle number, while the second one indicates the number of a site. In the shown process, a pair of fluxes is created and, after two hoppings, annihilated again so that the system is back in its ground state. This is a typical example of how closed loops are generated by the particle-conserving Hamiltonian.

in perturbation bigger loops in various shapes can be generated. While in the zero-quasi-particle sector these loops do not play a role because of their zero weight, their appearance becomes particularly important when studying one- or multi-quasi-particle subspaces, where a particle encircled by a loop generally yields a global minus sign originating from the anyonic statistics (see Section 5.1.4).

5.1.3 Multi-particle subspace I: translational invariance

In principle, the computational procedure shown in the previous chapter is the same for any quasi-particle sector. Instead of the single reference state per cluster (the ground state with all spins up) one now has to consider all possible starting positions \mathbf{r}_i of each multi-particle combination on every contributing cluster. Let us denote the set of positions of μ particles relative to their center of mass by $\mathbf{R}_\mu = \{\mathbf{r}_1, \mathbf{r}_2, \dots, \mathbf{r}_\mu\}$ and the set of particle types (charges or fluxes) by $\boldsymbol{\tau}_\mu = \{\tau_1, \tau_2, \dots, \tau_\mu\}$. The particle-conserving Hamiltonian generally shifts the quasi-particles to a set of positions \mathbf{R}'_μ , and it might also change the types to $\boldsymbol{\tau}'_\mu$ so that the quantity of interest in the μ -particle subspace is

$$t_{\mathbf{d}_{\text{cm}}, \mathbf{D}_\mu, \boldsymbol{\tau}'_\mu, \boldsymbol{\tau}_\mu} = \sum_{\mathbf{R}'_\mu - \mathbf{R}_\mu = \mathbf{D}_\mu} P(\Lambda_{\text{TC}}; \mathbf{R}'_\mu, \boldsymbol{\tau}'_\mu; \mathbf{R}_\mu, \boldsymbol{\tau}_\mu), \quad (5.57)$$

where \mathbf{d}_{cm} is the hopping distance of the center of mass, and \mathbf{D}_μ are relative hopping distances of the μ particles. This general formula becomes more transparent after the detailed treatment of specific cases discussed below.

To explore the low-energy physics, we are mainly interested in low quasi-particle subspaces. The Fourier transform of the one-particle sector yields the dispersion of the quasi-particle which can be minimized in order to obtain the series expansion of the gap. The two-particle subspace is also of significant interest since it contains information about the mutual interaction of the quasi-particles. Furthermore, it allows to determine certain correlation functions, e.g., spectral weights, which play a major role in the possible experimental implementation of the model.

The calculations performed with pCUT are valid in the thermodynamic limit, where the system is translationally invariant, so it is natural to consider the action of H_{eff} in momentum space. The structure of H_{eff} as well as its mathematical properties in real and momentum spaces have been widely investigated in Refs. [86, 87, 100, 101]. Here, we focus only on details relevant for computations performed in this thesis. In Chapter 2, it has been shown that the effective Hamiltonian H_{eff} is block-diagonal in real space since it preserves the number of quasi-particles. Let us remind that each block H_μ of the

semi-infinite matrix H_{eff} spans a Hilbert subspace \mathcal{H}_μ with an individual number μ of dressed elementary excitations. In addition, these blocks are sorted in increasing order respectively the number of quasi-particles in their characteristic subspace. Generally, we write

$$H_{\text{eff}}|_{\mu\text{qp}} = \sum_{\mu'=0}^{\mu} H_{\mu'}, \quad (5.58)$$

where $H_{\text{eff}}|_{\mu\text{qp}}$ contains all matrix elements of H_{eff} which contribute in \mathcal{H}_μ .

According to (5.58), in the single-particle sector \mathcal{H}_1 the action of H_{eff} can be reduced to the one of H_0 and H_1 .

$$H_{\text{eff}}|_{1\text{qp}} = H_0 + H_1. \quad (5.59)$$

Let us denote a single-particle state by $|\mathbf{r}\rangle$, where \mathbf{r} is the position of the particle. In the toric code, only particle pairs of the *same* type can be created or annihilated (as can also be verified in Table 5.2). Consequently, in the single-particle sector of our effective Hamiltonian, the particle type is preserved and does not need to be indexed. The action of the effective Hamiltonian on a single-particle state yields

$$H_0 |\mathbf{r}\rangle = E_0 |\mathbf{r}\rangle, \quad (5.60)$$

$$H_1 |\mathbf{r}\rangle = \sum_{\mathbf{r}'} t_{\mathbf{r}'} |\mathbf{r} + \mathbf{r}'\rangle. \quad (5.61)$$

While H_0 is diagonal in the zero-particle subspace, under the action of H_1 , the quasi-particle moves from \mathbf{r} to $\mathbf{r} + \mathbf{r}'$ with a hopping amplitude $t_{\mathbf{r}'}$. In general, the hopping amplitude may also depend on \mathbf{r} , however, this is not the case for a translationally invariant system, so we omit the corresponding index. Given a system with N possible single-particle positions, the Fourier transform of $|\mathbf{r}\rangle$ is defined as

$$|\mathbf{k}\rangle = \frac{1}{\sqrt{N}} \sum_{\mathbf{r}} e^{i\mathbf{k}\mathbf{r}} |\mathbf{r}\rangle. \quad (5.62)$$

We verify that, here, H_{eff} is responsible for single-particle dynamics by considering its action in the momentum space:

$$H_0 |\mathbf{k}\rangle = E_0 |\mathbf{k}\rangle, \quad (5.63)$$

$$H_1 |\mathbf{k}\rangle = \frac{1}{\sqrt{N}} \sum_{\mathbf{r}, \mathbf{r}'} e^{i\mathbf{k}\mathbf{r}} t_{\mathbf{r}'} |\mathbf{r} + \mathbf{r}'\rangle \stackrel{\mathbf{r} \rightarrow \mathbf{r} - \mathbf{r}'}{\equiv} \left(\sum_{\mathbf{r}'} t_{\mathbf{r}'} e^{-i\mathbf{k}\mathbf{r}'} \right) \frac{1}{\sqrt{N}} \sum_{\mathbf{r}} e^{i\mathbf{k}\mathbf{r}} |\mathbf{r}\rangle \quad (5.64)$$

$$= \left[t_0 + \sum_{\mathbf{r}' \in \mathcal{D}_{\text{pos}}} 2 t_{\mathbf{r}'} \cos(\mathbf{k}\mathbf{r}') \right] |\mathbf{k}\rangle \quad (5.65)$$

$$= \omega(\mathbf{k}) |\mathbf{k}\rangle, \quad (5.66)$$

where we used the symmetry of the square sublattice to set $t_{\mathbf{r}'} = t_{-\mathbf{r}'}$. In (5.65) the sum over \mathbf{r}' is limited to 'positive' distances, as defined in the following. Using the unit vectors \mathbf{n}_1 and \mathbf{n}_2 from Figure 5.2, the hopping distance is generally $\mathbf{r}' = p\mathbf{n}_1 + q\mathbf{n}_2$, with $(p, q) \in \mathbb{Z}^2$. We refer to the distance as 'positive', if

$$\left(p = 0 \wedge q > 0 \right) \vee p > 0. \quad (5.67)$$

This is illustrated in Figure 5.2. Note that the dispersion $\omega(\mathbf{k})$ is also a function of the

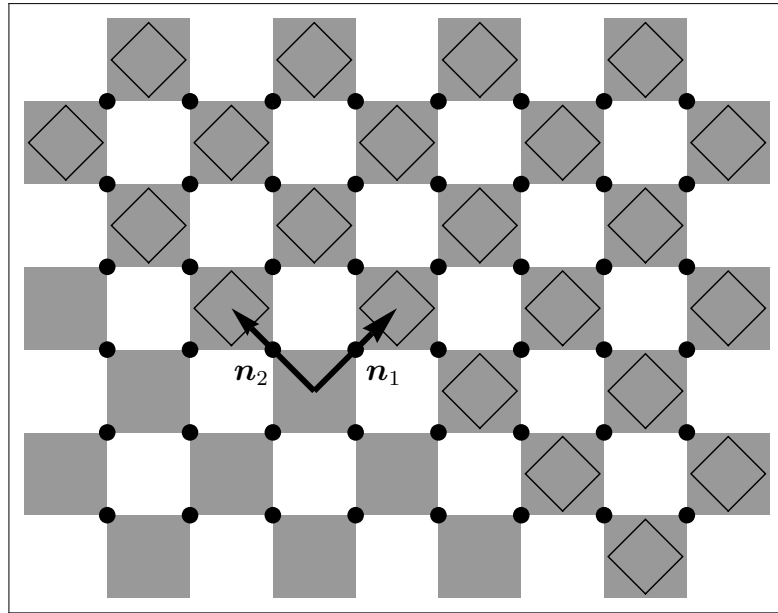


FIGURE 5.2: Set \mathcal{D}_{pos} of distances, relevant for the treatment of the one- and two-particle subspaces of the toric code. \mathbf{n}_1 and \mathbf{n}_2 are unit vectors, placed at the origin of our coordinate system. The rhombic contours highlight possible positions of a flux within a distance $\mathbf{r}' \in \mathcal{D}_{\text{pos}}$ from the origin. We call these distances 'positive' because in the present model the symmetries of the lattice require $t_{\mathbf{r}'} = t_{-\mathbf{r}'}$

perturbation since the hopping amplitudes $t_{\mathbf{r}'}$ are series expansions in the perturbation parameters. The maximal hopping distance is limited by the finite order of perturbation. However, it generally increases with the perturbation order since larger and larger

fluctuations are possible. In the one-particle sector, our goal is to calculate the dispersion

$$\omega(\mathbf{k}) = \langle \mathbf{k} | H_1 | \mathbf{k} \rangle = \langle \mathbf{k} | \left(H_{\text{eff}}|_{\text{1qp}} - H_0 \right) | \mathbf{k} \rangle, \quad (5.68)$$

$$= \langle \mathbf{k} | (H_{\text{eff}} - H_0) | \mathbf{k} \rangle, \quad (5.69)$$

where we used the fact that, due to (5.59), the action of H_{eff} on one-particle states is equivalent to the one of $H_{\text{eff}}|_{\text{1qp}}$. We proceed along similar lines as in Section 5.1.2, by acting with H_{eff} onto every one-particle state of contributing clusters. Note that the contribution from H_0 has to be subtracted, as implied in (5.68). As can be followed from (5.62) this contribution is only non-zero for local hoppings, i.e., initial and final positions of the particle coincide. Formally, using the notation from (5.57), we compute hopping amplitudes

$$t_{\mathbf{r}'} = \sum_{\mathbf{r}} P(\Lambda_{\text{TC}}; \mathbf{r} + \mathbf{r}'; \mathbf{r}), \quad (5.70)$$

with contributions from finite clusters as defined in (5.2) and (5.3)

$$P(\mathbf{C}_{m \times n}; \mathbf{r} + \mathbf{r}'; \mathbf{r}) = \langle \mathbf{C}_{m \times n}, \mathbf{r} + \mathbf{r}' | H_1 | \mathbf{C}_{m \times n}, \mathbf{r} \rangle \quad (5.71)$$

$$= \langle \mathbf{C}_{m \times n}, \mathbf{r} + \mathbf{r}' | H_{\text{eff}} - H_0 | \mathbf{C}_{m \times n}, \mathbf{r} \rangle. \quad (5.72)$$

We now examine the two-particle space which, in the toric code on an infinite plane, separates in two decoupled subspaces. Either a pair of particles is of the same type (i.e., two charges or two fluxes), or we have a pair with unequal types (one charge and one flux). As already argued above, Pauli operators may create or destroy only equal-type pairs of particles. Therefore, under the action of H_{eff} two charges can transform into two fluxes (and vice versa), but never into a charge-flux pair. From this, it can generally be concluded that no local perturbation can couple subspaces with even and odd numbers of either charges or fluxes. At this point, we will concentrate only on particle pairs of the same type since this case is relevant for spectral densities to be computed in Section 7.3. We will use the index τ to denote the type of the pair (either charge-charge or flux-flux). A two-particle state in the toric code can thus generally be denoted by $|\mathbf{r}, \mathbf{r} + \mathbf{d}, \tau\rangle$, where \mathbf{r} and $\mathbf{r} + \mathbf{d}$ are particle coordinates. Let us now consider the action of H_{eff} , or more precisely, its relevant blocks in the subspace \mathcal{H}_2 .

$$H_0 |\mathbf{r}, \mathbf{r} + \mathbf{d}, \tau\rangle = E_0 |\mathbf{r}, \mathbf{r} + \mathbf{d}, \tau\rangle, \quad (5.73)$$

$$H_1 |\mathbf{r}, \mathbf{r} + \mathbf{d}, \tau\rangle = \sum_{\mathbf{r}' \neq \mathbf{d}} t_{\mathbf{r}'} |\mathbf{r} + \mathbf{r}', \mathbf{r} + \mathbf{d}, \tau\rangle + \sum_{\mathbf{r}' \neq -\mathbf{d}} t_{\mathbf{r}'} |\mathbf{r}, \mathbf{r} + \mathbf{r}' + \mathbf{d}, \tau\rangle, \quad (5.74)$$

$$H_2 |\mathbf{r}, \mathbf{r} + \mathbf{d}, \tau\rangle = \sum_{\substack{\mathbf{r}', \mathbf{d}', \tau' \\ \mathbf{d}' \in \mathcal{D}_{\text{pos}}}} t_{\mathbf{r}', \mathbf{d}', \tau'}^{\mathbf{d}, \tau} |\mathbf{r} + \mathbf{r}', \mathbf{r} + \mathbf{r}' + \mathbf{d}', \tau'\rangle, \quad (5.75)$$

H_0 is, again, diagonal in the given basis. While H_1 lets *either one* of the two particles hop, H_2 involves *both* particles and shifts them to new positions generally changing the pair-type from τ to τ' . Note that we accounted for the hard-core constraint of the particles by excluding certain hopping distances in (5.74) and (5.75). In momentum space, two-particle states are constructed as follows

$$|\mathbf{K}, \mathbf{d}, \tau\rangle = \frac{1}{\sqrt{N}} \sum_{\mathbf{r}} e^{i\mathbf{K}(\mathbf{r} + \mathbf{d}/2)} |\mathbf{r}, \mathbf{r} + \mathbf{d}, \tau\rangle, \quad (5.76)$$

where \mathbf{K} is the total momentum of the pair and $\mathbf{r} + \frac{1}{2}\mathbf{d}$ is the position of the center of mass. Here we use the fact that \mathbf{K} is conserved due to translational invariance and is therefore a good quantum number. Now we would like to compute the action of H_{eff} in the Fourier-transformed space.

$$H_0 |\mathbf{K}, \mathbf{d}, \tau\rangle = E_0 |\mathbf{K}, \mathbf{d}, \tau\rangle, \quad (5.77)$$

$$H_1 |\mathbf{K}, \mathbf{d}, \tau\rangle = \frac{1}{\sqrt{N}} \sum_{\mathbf{r}} e^{i\mathbf{K}(\mathbf{r} + \mathbf{d}/2)} \times \left(\sum_{\mathbf{r}' \neq \mathbf{d}} t_{\mathbf{r}'} \underbrace{|\mathbf{r} + \mathbf{r}', \mathbf{r} + \mathbf{d}, \tau\rangle}_{\mathbf{r} \rightarrow \mathbf{r} - \mathbf{r}'} + \sum_{\mathbf{r}' \neq -\mathbf{d}} t_{\mathbf{r}'} |\mathbf{r}, \mathbf{r} + \mathbf{r}' + \mathbf{d}, \tau\rangle \right), \quad (5.78)$$

$$= \frac{1}{\sqrt{N}} \sum_{\mathbf{r}' \neq \mathbf{d}} t_{-\mathbf{r}'} \sum_{\mathbf{r}} e^{i\mathbf{K}(\mathbf{r} - \mathbf{r}' + \mathbf{d}/2)} |\mathbf{r}, \mathbf{r} - \mathbf{r}' + \mathbf{d}, \tau\rangle + \frac{1}{\sqrt{N}} \sum_{\mathbf{r}' \neq -\mathbf{d}} t_{\mathbf{r}'} \sum_{\mathbf{r}} e^{i\mathbf{K}(\mathbf{r} + \mathbf{d}/2)} |\mathbf{r}, \mathbf{r} + \mathbf{r}' + \mathbf{d}, \tau\rangle, \quad (5.79)$$

$$= \sum_{\mathbf{r}'} e^{-i\mathbf{K}\mathbf{r}'/2} \left\{ t_{-\mathbf{r}'} |\mathbf{K}, \mathbf{d} - \mathbf{r}', \tau\rangle [1 - \delta_{\mathbf{r}', \mathbf{d}}] + t_{\mathbf{r}'} |\mathbf{K}, \mathbf{d} + \mathbf{r}', \tau\rangle [1 - \delta_{\mathbf{r}', -\mathbf{d}}] \right\}. \quad (5.80)$$

With the same arguments as above, we now use the relation $t_{\mathbf{r}'} = t_{-\mathbf{r}'}$ to sum up symmetric terms.

$$H_1 |\mathbf{K}, \mathbf{d}, \tau\rangle = \sum_{\mathbf{r}' \in \mathcal{D}_{\text{pos}}} 2 t_{\mathbf{r}'} \cos(\mathbf{K}\mathbf{r}'/2) |\mathbf{K}, \mathbf{d} + \mathbf{r}', \tau\rangle (1 - \delta_{\mathbf{r}', -\mathbf{d}}), \quad (5.81)$$

where \mathbf{r}' is restricted to positive distances. Finally, we consider the action of H_2 onto a momentum state.

$$H_2 |\mathbf{K}, \mathbf{d}, \tau\rangle = \frac{1}{\sqrt{N}} \sum_{\mathbf{r}} e^{i\mathbf{K}(\mathbf{r}+\mathbf{d}/2)} \sum_{\substack{\mathbf{r}', \tau' \\ \mathbf{d}' \in \mathcal{D}_{\text{pos}}}} t_{\mathbf{r}', \mathbf{d}', \tau'}^{\mathbf{d}, \tau} |\mathbf{r} + \mathbf{r}', \mathbf{r} + \mathbf{r}' + \mathbf{d}', \tau'\rangle, \quad (5.82)$$

$$\stackrel{\mathbf{r} \rightarrow \mathbf{r} - \mathbf{r}'}{=} \frac{1}{\sqrt{N}} \sum_{\substack{\mathbf{r}', \tau' \\ \mathbf{d}' \in \mathcal{D}_{\text{pos}}}} t_{\mathbf{r}', \mathbf{d}', \tau'}^{\mathbf{d}, \tau} \sum_{\mathbf{r}} e^{i\mathbf{K}(\mathbf{r} - \mathbf{r}' + \mathbf{d}/2)} |\mathbf{r}, \mathbf{r} + \mathbf{d}', \tau'\rangle, \quad (5.83)$$

$$= \sum_{\substack{\mathbf{r}', \tau' \\ \mathbf{d}' \in \mathcal{D}_{\text{pos}}}} t_{\mathbf{r}', \mathbf{d}', \tau'}^{\mathbf{d}, \tau} e^{i\mathbf{K}\left(\frac{\mathbf{d} - \mathbf{d}'}{2} - \mathbf{r}'\right)} |\mathbf{K}, \mathbf{d}', \tau'\rangle, \quad (5.84)$$

where the particle distance \mathbf{d}' is without loss of generality restricted to \mathcal{D}_{pos} because in the toric code, particles of the same type are indistinguishable. Note that since the action of H_2 must involve *both* particles, in a finite-order calculation the linked-cluster theorem fixes a maximal interaction distance, $|\mathbf{d}_{\text{max}}| < L_{\text{const}}$, where L_{const} is a positive constant that depends on the order. The two-particle hopping amplitudes $t_{\mathbf{r}', \mathbf{d}', \tau'}^{\mathbf{d}, \tau}$ of particles at a distance beyond \mathbf{d}_{max} must be zero. In contrast, there is no such restriction of the *mutual distance* concerning the action of H_1 . According to (5.81), only the hopping radius of an individual particle is limited, while the distance \mathbf{d} can take any value. Therefore, in the basis $|\mathbf{K}, \mathbf{d}, \tau\rangle$, the matrix elements of the effective Hamiltonian in the subspace \mathcal{H}_2 can be grouped into two parts. For distances within the range of \mathbf{d}_{max} , the matrix elements are determined by $\langle \mathbf{K}, \mathbf{d}, \tau | H_1 + H_2 | \mathbf{K}, \mathbf{d}', \tau' \rangle$, outside this range we have $\langle \mathbf{K}, \mathbf{d}, \tau | H_1 | \mathbf{K}, \mathbf{d}', \tau' \rangle$. We do not include H_0 in this matrix because in experiments usually energies *relatively* to the ground-state energy are accessible. Note that in practice one has to introduce a finite cutoff for the mutual distance (lets say $|\mathbf{d}| < L_{\text{cutoff}}$ with $L_{\text{cutoff}} \gg L_{\text{const}}$) in order to be able to diagonalize the matrix. The full spectrum of the system with two quasi-particles is thus obtained approximately, but, of course, we try to make this cutoff as large as possible to enhance the numerical precision and check the convergence of the calculation.

Matrix elements for distances beyond \mathbf{d}_{max} can be easily reconstructed using the single-particle hopping amplitudes obtained in a preceding calculation of the one-particle sector. So that, in the two-particle sector, our primary goal is to obtain two-particle hopping amplitudes, by letting H_{eff} act on every two-particle configuration on each contributing cluster. Similarly as for (5.70)-(5.72), we compute

$$t_{\mathbf{r}', \mathbf{d}', \tau'}^{\mathbf{d}, \tau} = \sum_{\mathbf{r}} P(\Lambda_{\text{TC}}; \mathbf{r} + \mathbf{r}', \mathbf{r} + \mathbf{r}' + \mathbf{d}', \tau'; \mathbf{r}, \mathbf{r} + \mathbf{d}, \tau), \quad (5.85)$$

with the following contributions from finite clusters

$$P(\mathbf{C}_{m \times n}; \mathbf{r} + \mathbf{r}', \mathbf{r} + \mathbf{r}' + \mathbf{d}', \tau'; \mathbf{r}, \mathbf{r} + \mathbf{d}, \tau) = \langle \mathbf{C}_{m \times n}; \mathbf{r} + \mathbf{r}', \mathbf{r} + \mathbf{r}' + \mathbf{d}', \tau' | H_2 | \mathbf{C}_{m \times n}; \mathbf{r}, \mathbf{r} + \mathbf{d}, \tau \rangle \quad (5.86)$$

$$= \langle \mathbf{C}_{m \times n}; \mathbf{r} + \mathbf{r}', \mathbf{r} + \mathbf{r}' + \mathbf{d}', \tau' | H_{\text{eff}} - H_1 - H_0 | \mathbf{C}_{m \times n}; \mathbf{r}, \mathbf{r} + \mathbf{d}, \tau \rangle. \quad (5.87)$$

We point out that the subtraction in (5.87) is non-trivial, especially in view of the fact that single-particle hoppings in the two-particle subspace cannot be compared to the ones in the one-particle subspace. Due to their hard-core character, the presence of a second particle prohibits certain hopping paths of the first. One can tackle this problem by tracing the action of H_{eff} and keeping only processes, where each of the particles has been acted upon at least once. However, the complexity of this task is comparable to the one of a linked-cluster expansion. It turns out to be much cheaper to act with H_{eff} onto a two-particle state and perform a subtraction using our explicit knowledge about the particle behavior. To be more precise, if both particles have changed their position, we know that exclusively H_2 has been involved so that nothing has to be subtracted. If the position of only one of the particles has changed we subtract the contribution of H_1 acting on one of the particles in presence of the other. If the final positions of the particle pair correspond to their initial positions, we subtract the local single-particle hopping of *each* of the particles in presence of the other as well as the contribution of H_0 .

All of the above considerations can simply be extended to the case of particles with different types (on an open plane) by dropping the hard-core constraint and the index τ . We recall that charges and fluxes live, by definition, on different sublattices and the pair-type of the charge-flux composite is conserved. Of course, for particles with different types one has in addition to account for semi-infinite strings which generally have an effect on the single-particle hopping independent of the distance \mathbf{d}_{max} , as will be discussed in more detail in the next section.

5.1.4 Multi-particle subspace II: non-locality

In the toric code on an infinite plane, single particles are defined as ends of semi-infinite strings (see Figure 4.6). The formalism developed in the preceding section does not account for strings explicitly, but they can be included in the definition of quasi-particles as long as we follow certain conventions introduced below.

(i) Fixed string-gauge

A single particle is connected to infinity (or to an edge of a finite system) by a string. There are infinitely many possibilities to shape this string, without changing the particles position and energy. In order to construct a complete basis in one-quasi-particle subspace, we incorporate the semi-infinite string into our definition of a fixed spin background, by following the convention that on any finite lattice the particle string should point down left, as shown in Figure 5.3 (a) and (c). Other conventions are also possible. However, it is crucial to keep a fixed convention since a consistent single-particle picture is necessary to keep track of braiding signs in the two-particle subspace. When under

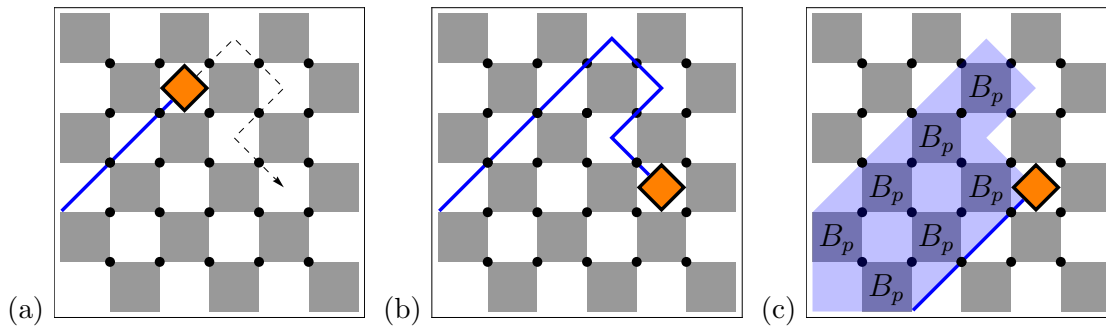


FIGURE 5.3: Including the semi-infinite string into the spin background. Our convention is that any semi-infinite string should point down left as shown in (a) and (c). (b) illustrates a common final state resulting after the action of H_{eff} on the state in (a). Generally the particle changes its initial position so that the semi-infinite string is deformed. By acting with B_p on p inside the highlighted area, or more generally, on p enclosed by the strings in (a) and (c) as well as the hopping path of the particle, the deformed string is gauged to our convention. For single fluxes the situation is analogous, except that instead of B_p (gray plaquettes), A_s (white plaquettes) are enclosed.

the action of H_{eff} a particle is displaced, our string convention requires a kind of gauge transformation of the string, depicted in Figure 5.3. The transformation is realized by acting with a contractible loop operator assembled by the particle-string in the initial state, the path of the particle, and the correctly shaped string of the final state. According to Section 4.1 (see also Figure 4.2) this is equivalent to an action of B_p operators for charges and A_s operators for fluxes on p (or s respectively) inside the enclosed area of the loop. Using this approach, one automatically collects a minus sign, if there is an odd number of particles (of opposite type), inside the enclosed area.

(ii) Counting of loops

A closed loop of a charge around a flux (and vice versa) yields a global minus sign which, in an algebraic computation, would simply result from the non-commuting operators on the site, where the infinite string of the single particle crosses the loop. However, in our representation of states, strings of charges are 'invisible', contrary to strings belonging to

fluxes (see Figure 5.4). This is a purely technical issue, resulting from our choice of the basis of Pauli operators. Even though it is possible to choose a basis where both kinds of strings can be treated on equal terms, the advantage of the current basis is that it provides an intuitive graphical language, directly implementable in a computer program (see Section 5.3.1). The consequence of 'hidden' σ^z -strings is that loops around charges

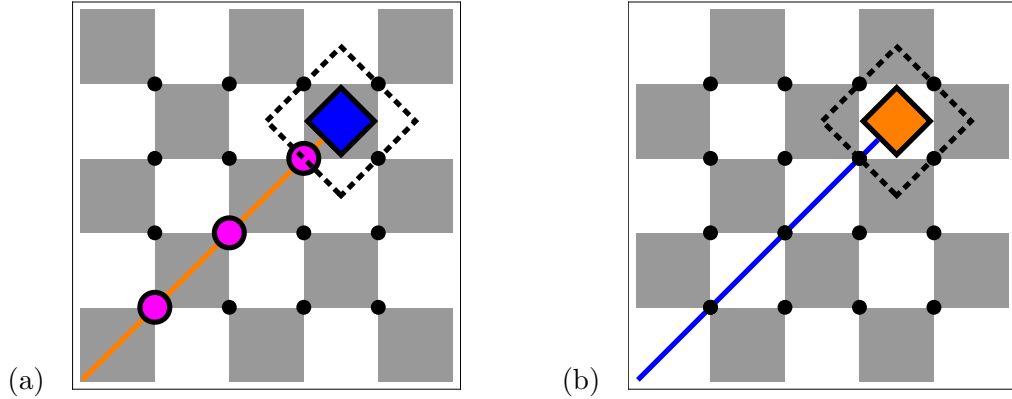


FIGURE 5.4: Loops around single particles in the σ^z -basis. (a) A single flux is attached to a string of σ^x operators (connected by an orange line as a guide to the eye). Given our choice of the ground state (all spins are up) and basis of Pauli operators, the string of a flux is 'visible' as a string of spins pointing down. A loop of σ^z operators along the dashed line, yields a global minus sign which results from the action on the down-spin belonging to the flux-string. (b) A single charge with a string of σ^z operators (highlighted by a blue line), is invisible in our graphical language because of our choice of the basis. A loop of σ^x operators along the dashed line does not produce the required minus sign so that our algorithm has to explicitly detect loops around charges and impose the correct sign onto the final state.

and fluxes have to be treated differently. While, in our computer program, σ^z -loops around a single flux 'automatically' yield the required minus sign [see Figure 5.4 (a)], σ^x -loops around a single charge have to be detected explicitly, in order to set the sign to its physically correct value. Note that at higher orders in perturbation theory one has to account for cases where there is more than one loop around a particle, or where multiple particles are encircled by a loop and so forth. The braiding rules of semions are such that only an odd number of σ^z -loops around an odd number of charges yields a minus sign.

Finally, we remark that in the one-quasi-particle subspace it is sufficient to study exclusively the single-flux case. There is a flux-charge symmetry in the problem, which allows us to reconstruct charge hopping-amplitudes from flux hopping-amplitudes through a basis rotation: $\sigma^x \rightarrow \sigma^z$, $\sigma^z \rightarrow -\sigma^x$, $\sigma^y \rightarrow \sigma^y$. However, it is a good test of our string-detection procedure to compute both dispersions independently and then check that they are equivalent under the above rotation.

5.2 Applying pCUT to the high-field phase

In the limit $J = 0$, the Hamiltonian (4.23) becomes

$$H_{\text{HF}} = - \sum_i \mathbf{h} \cdot \boldsymbol{\sigma}_i, \quad (5.88)$$

where on each site i we have a scalar product of the field amplitudes and the corresponding Pauli operators

$$\mathbf{h} = \{h_x, h_y, h_z\}, \quad (5.89)$$

$$\boldsymbol{\sigma}_i = \{\sigma_i^x, \sigma_i^y, \sigma_i^z\}. \quad (5.90)$$

In the ground state, the system is fully polarized in the field direction. Hence, it is natural to rotate the basis of the local Hilbert space of the spins-1/2 so that the z -axis points into the field direction \mathbf{h} . The basis transformation yields

$$\tilde{\boldsymbol{\sigma}} = R \boldsymbol{\sigma}, \quad (5.91)$$

where R is the following rotation matrix

$$R = \begin{pmatrix} \cos \phi \cos \theta & -\sin \theta & \cos \theta \sin \phi \\ \cos \phi \sin \theta & \cos \theta & \sin \phi \sin \theta \\ -\sin \phi & 0 & \cos \phi \end{pmatrix}, \quad (5.92)$$

and angles ϕ and θ parametrize the three-dimensional magnetic field as shown in Figure 5.5.

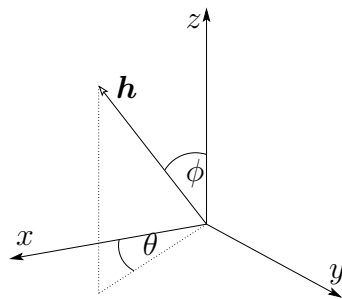


FIGURE 5.5: Parametrization of the three-dimensional magnetic field \mathbf{h} in spherical coordinates. For $\phi = 0$ and $\theta = 0$, we obtain the original basis of (5.88).

In the new basis, we have on each site a two-level system with eigenvalues $\pm \sqrt{h_x^2 + h_y^2 + h_z^2}$. For brevity we introduce $\tilde{h}_z = \sqrt{h_x^2 + h_y^2 + h_z^2}$. In a system with N spins, the ground-state energy is thus $-N\tilde{h}_z$. Elementary excitations are local spin flips, hence \tilde{H}_{HF} has

an equidistant spectrum with a constant gap of $2\tilde{h}_z$ between the energy levels. Obviously, the system meets constraints (i) and (ii) (see Section 2), necessary for a treatment with pCUT. To make sure that (iii) is also fulfilled, we examine the system under perturbation, where for finite J the perturbing operators are the well-known toric code interactions, rotated into the optimal basis.

$$\tilde{H}_{\text{TCF}} = -\tilde{h}_z \sum_i \tilde{\sigma}_i^z - J \sum_s \tilde{A}_s - J \sum_p \tilde{B}_p, \quad (5.93)$$

$$\tilde{A}_s = \prod_{i \in s} \tilde{\sigma}_i^x, \quad (5.94)$$

$$\tilde{B}_p = \prod_{i \in p} \tilde{\sigma}_i^z. \quad (5.95)$$

The expressions of the four-spin interactions \tilde{A}_s and \tilde{B}_p are generally superpositions of four-fold products of Pauli operators with all possible combinations of σ^x , σ^y and σ^z . Due to R , every term has a θ - and ϕ -dependent amplitude. In other words, all matrix elements of the 2^4 -dimensional Hilbert space of the four spins on a star (or a plaquette) are non-zero, and depend on the direction of the field. Consequently, the action of \tilde{A}_s as well as \tilde{B}_p contains every possible change in number of spin flips and can be represented by particle creation and annihilation operators T_m with $m \in \{0, \pm 1, \pm 2, \pm 3, \pm 4\}$, as illustrated in Table 5.4. Thus, the condition (iii) from Section 2.3 is fulfilled, and we can

	T_0	$T_{\pm 1}$	$T_{\pm 2}$	$T_{\pm 3}$	$T_{\pm 4}$

TABLE 5.4: Action of the perturbing (toric code) operators in the polarized phase. Entries with dots show only a subset of possible states, all of which can be reconstructed by rotational symmetry. The table should be viewed as follows. Acting with T_0 , T_{+1} , T_{+2} , T_{+3} or T_{+4} on a state in the most left column yields the state on the right. The reverse process corresponds to an action of T_0 , T_{-1} , T_{-2} , T_{-3} or T_{-4} respectively. Note that all of these operations have generally unique amplitudes which depend on the tile color (here only white tiles are shown) and the direction of the magnetic field. The complete list of operators and the corresponding amplitudes is given in Appendix A.2.

apply pCUT also to the high-field limit of the toric code. Note that while the matrix elements of \tilde{A}_s and \tilde{B}_p are the same concerning the change in particle number, they differ in their ϕ - and θ -dependence so that the action of the perturbation is different on stars and plaquettes. Therefore, we have to consider similar subclusters (depicted in Table 5.5) as in the low-field limit. In order to perform the finite-cluster method

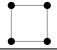
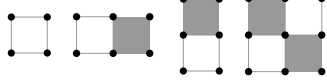
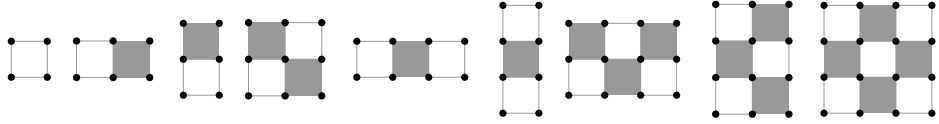
order 1	
order 2	
order 3	

TABLE 5.5: Subclusters relevant for computations at a given order in the high-field limit of the toric code. Here we show only $\mathbf{C}_{m \times n}^s$ to keep a clear overview. The contributing $\mathbf{C}_{m \times n}^p$ can be obtained through tile-color inversion. In contrast to the low-field limit (see Table 5.3), quasi-particles live on sites instead of stars and plaquettes. However, due to the structure of the perturbation, one has to consider checkerboard-like clusters.

one can still apply the general formulas (5.3)-(5.10), accounting for the fact that here quasi-particles are located at sites instead of plaquettes.

To give a simple example, we present a calculation of the ground-state energy up to order one. As in the previous chapter, the effective Hamiltonian in the rotated basis can be written as

$$H_{\text{eff}}^{(0)} = -N\tilde{h}_z + 2\tilde{h}_z Q, \quad (5.96)$$

$$H_{\text{eff}}^{(1)} = T_0, \quad (5.97)$$

where Q counts the number flipped spins. We set $\tilde{h}_z = 1/2$ so that the cost of a single particle in the unperturbed system is one. The ground state corresponds to a particle vacuum with $Q = 0$ so that, at order zero, the ground-state energy per site is

$$e_0^{(0)} = -\tilde{h}_z = -\frac{1}{2}. \quad (5.98)$$

At order one, we first compute the reduced weights

$$W(\mathbf{C}_{2 \times 2}^s) = \langle \begin{array}{|c|c|} \hline \bullet & \bullet \\ \hline \bullet & \bullet \\ \hline \end{array} \left| T_0 \right| \begin{array}{|c|c|} \hline \bullet & \bullet \\ \hline \bullet & \bullet \\ \hline \end{array} \rangle = -J \cos^4 \phi \langle \begin{array}{|c|c|} \hline \bullet & \bullet \\ \hline \bullet & \bullet \\ \hline \end{array} \left| \begin{array}{|c|c|} \hline \bullet & \bullet \\ \hline \bullet & \bullet \\ \hline \end{array} \right\rangle = -J \cos^4 \phi, \quad (5.99)$$

$$W(\mathbf{C}_{2 \times 2}^p) = \langle \begin{array}{|c|c|} \hline \blacksquare & \blacksquare \\ \hline \blacksquare & \blacksquare \\ \hline \end{array} \left| T_0 \right| \begin{array}{|c|c|} \hline \blacksquare & \blacksquare \\ \hline \blacksquare & \blacksquare \\ \hline \end{array} \rangle = -J \cos^4 \theta \sin^4 \phi \langle \begin{array}{|c|c|} \hline \blacksquare & \blacksquare \\ \hline \blacksquare & \blacksquare \\ \hline \end{array} \left| \begin{array}{|c|c|} \hline \blacksquare & \blacksquare \\ \hline \blacksquare & \blacksquare \\ \hline \end{array} \right\rangle = -J \cos^4 \theta \sin^4 \phi. \quad (5.100)$$

The order one contribution to the ground-state energy is thus

$$e_0^{(1)} = \widetilde{W}^+(\mathbf{C}_{2 \times 2}) = \frac{1}{2} \left[W(\mathbf{C}_{2 \times 2}^s) + W(\mathbf{C}_{2 \times 2}^p) \right] \quad (5.101)$$

$$= -\frac{J}{2} \left[\cos^4 \phi + \cos^4 \theta \sin^4 \phi \right]. \quad (5.102)$$

It is instructive to consider a special direction of the magnetic field $\mathbf{h} = (0, 0, h_z)$, or equivalently $R = \mathbb{1}$. This leads to $\tilde{A}_s = A_s$ and $\tilde{B}_p = B_p$. The toric code in a single parallel field can be mapped onto the Ising model in a transverse field, as we have learned in Section 4.3. An interesting property of the model is that with increasing J , the *four*-quasi-particles gap is the first one to close, as will be shown explicitly in Section 6.5. There are two equivalent explanations for this behavior. On the one hand, one can argue that the high-field limit of the toric code corresponds to the low-field limit of the Ising model. In this mapping, the toric code is constructed by effective \mathbb{Z}_2 -variables on bonds of a square lattice so that single spin flips in the Ising model correspond to a simultaneous flipping of four effective spins on the surrounding bonds. At the same time, there is no local operator which flips the eigenvalue of a *single* interaction term in the Ising model³. Therefore, local elementary excitations of the toric code in a large σ^z field are flips of four spins on a star. On the other hand, operators B_p commute with the Hamiltonian, which means that the number of fluxes is conserved. States with open loops of flipped spins (including the one with a single flipped spin) generally belong to a 2μ -flux sector (with $\mu \in \mathbb{N}$ and $\mu \geq 1$) so that for finite J their energy is lifted up, proportionally to μ . This is similar for states which contain closed loops; however, here it is possible to construct states which belong to the zero-flux sector, e.g., a loop around a single star (so at least four flipped spins are necessary).

It is reasonable to assume that at least for small deviations from the Ising line [field direction $\mathbf{h} = (0, 0, h)$], the true elementary excitations are still of four-particle type. However, at least in the field direction $\mathbf{h} = (h, 0, h)$ the transformed operators \tilde{A}_s and \tilde{B}_p allow single spin flips, and none of them commutes with the Hamiltonian so that the flux sector is not preserved. Therefore, we have a strong hint that here the one-particle gap is the relevant one.

Let us close this section with the remark that there is a major difference between the situation we encounter here compared to the one in the low-field limit. While processes listed in Table 5.2 have an amplitude which is either ± 1 or $\pm i$, every process shown in Table 5.4 has an individual amplitude, depending on the type of the tile (star or plaquette) and on rotation angles ϕ and θ . This together with the fact that the number of T_m operators is larger than in the low-field case make the computation numerically heavier. Therefore, while in the high-field limit the quasi-particle picture seems to be less challenging than in the topological phase, only relatively low orders in perturbation can be reached.

³Note that this is consistent with the unmapped toric code, where in the high-field limit, none of the perturbing operators A_s and B_p can flip single spins.

5.3 Numerical tools

5.3.1 Computer program

As has been already discussed in previous sections, our strategy to compute series expansions of matrix elements of the effective particle-conserving Hamiltonian H_{eff} is to consider each quasi-particle subspace separately, and to let H_{eff} act on every state from the corresponding Hilbert space. We emphasize that it is important to reach a significantly high perturbation order so that extrapolations of the series can be used efficiently for a quantitative study of the critical properties of the model (see the upcoming section for more details). In this section, we estimate the magnitude of the computational task and introduce a computational algorithm to tackle this problem. The basic ideas of the algorithm can also be found in Refs. [83, 100, 101].

The number of terms in H_{eff} grows exponentially, and (in two dimensions) the number of relevant subclusters grows quadratically with order so that the computational task is intensive in time and memory, especially at high perturbation orders. In Table 5.6, we list the number N_{terms} of terms in the effective Hamiltonian. Even though a few

Order	$N_{\text{terms}}, m_{\text{max}} = 2$	$N_{\text{terms}}, m_{\text{max}} = 4$
1	1	1
2	4	8
3	18	60
4	84	488
5	380	3950
6	1750	32660
7	8134	273126
8	38164	
9	180324	
10	856944	

TABLE 5.6: Number of terms in the particle-conserving effective Hamiltonian H_{eff} , where operators T_m are characterized by $m \in \{0, \pm 1, \pm 2, \dots, \pm m_{\text{max}}\}$. Each row lists the number of individual same-order terms. These terms are model-independent and are available up to a high order (see Ref. [102]). Here, we refer only to terms actually used in our computations, where we have reached order 10 for the low-field limit ($m_{\text{max}} = 2$) and order 7 for the high-field limit ($m_{\text{max}} = 4$) of the toric code.

terms have vanishing coefficients, and at subspaces with a low particle number many terms yield zero by definition, the growth of N_{terms} is still exponential. Therefore, the computational demands at order $(r + 1)$ are usually about an order of magnitude higher than in order r . Every term of order r consists of r -fold products of T_m operators which, in turn, are sums over local particle creation and annihilation operators. Expanding this r -fold product yields generally $(pq)^r$ processes (as the one discussed in Figure 5.1) *per*

term on the cluster $\mathbf{C}_{p \times q}$. Note that not all of these processes are linked. However, by construction, only the linked ones yield a non-zero contribution at the end. In the low- as well as in the high-field limit of the toric code, clusters with $(p, q) \in \{2, 3, \dots, r+1\}^2$ contribute at order r . As illustrated in Figure 5.6, the computation of each matrix element in the μ -particle subspace is performed by acting with H_{eff} on every possible μ -particle state which lives on the contributing subclusters, and collecting the final states.

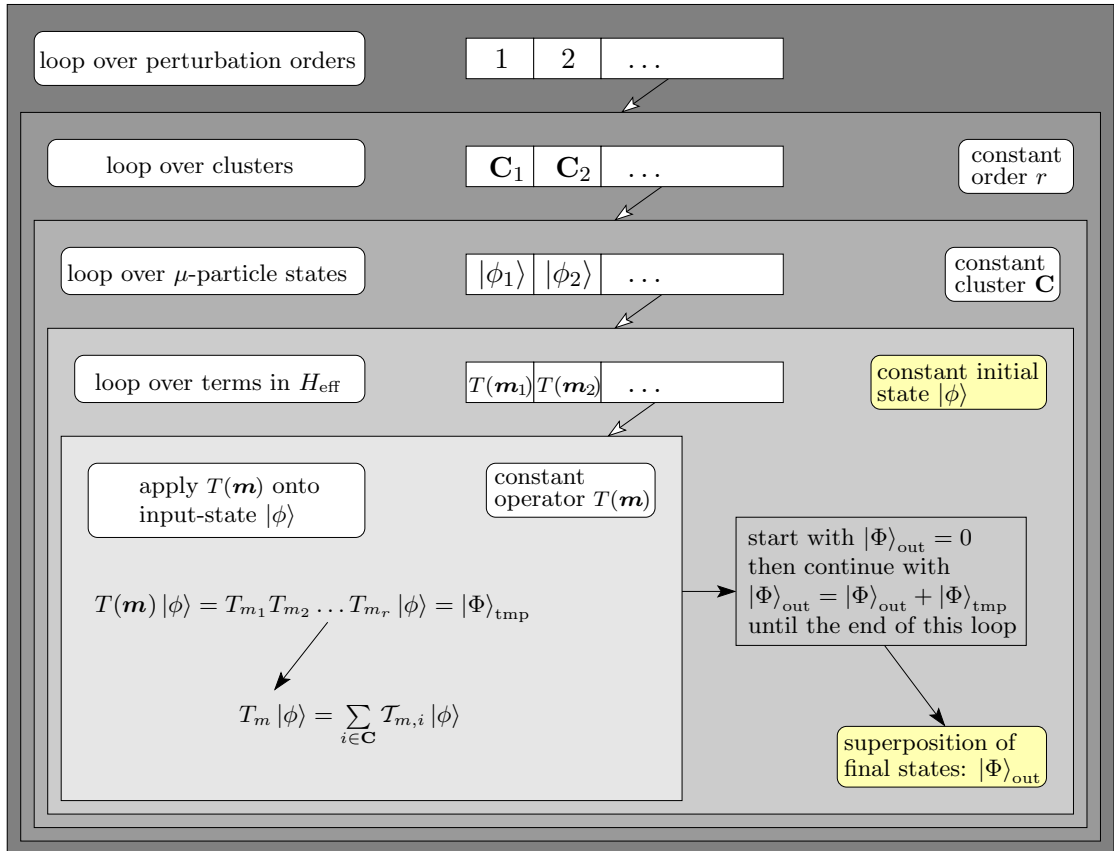


FIGURE 5.6: Scheme of the algorithm to compute matrix elements of the effective particle-conserving Hamiltonian H_{eff} . Arrows with white heads indicate iterations. In each shaded block, the algorithm performs operations according to the description in the upper left corner. The remarks on the upper right of each shaded area are comments used to fix the notation of a general operation, carried out in the most inner loop. Yellow areas contain the input and output information of the program. Matrix elements (as defined in (5.2)) are obtained by performing the scalar product $\langle \phi | \Phi \rangle_{\text{out}}$.

Next, let us discuss how the necessary objects are realized in the computer program. A local \mathbb{Z}_2 -degree of freedom can be represented by a bit which is either zero or one. The Hilbert space of a state on a finite cluster, with n \mathbb{Z}_2 -degrees of freedom (and therefore 2^n energy levels), can be mapped onto n bits. A state is thus constructed by a set of bits and is characterized by a fixed configuration of all degrees of freedom. Consider Figure 5.7 for a concrete example. The central part of our code is the action of a $\mathcal{T}_{m,i}$

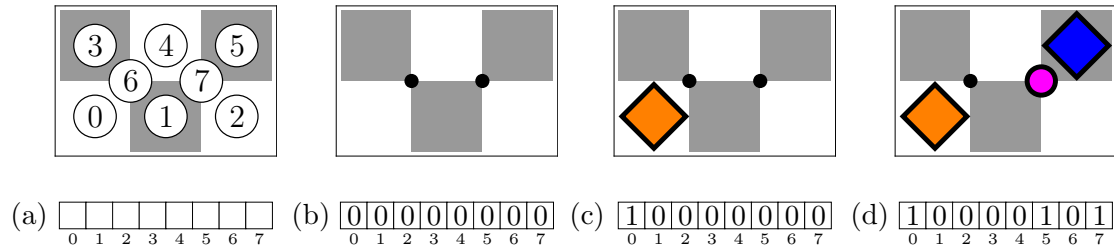


FIGURE 5.7: Representing a toric code state by a set of bits. In the topological phase of the toric code, a state is characterized by \mathbb{Z}_2 -degrees of freedom on stars and plaquettes and through a spin background, where spins $1/2$ can be either up or down. The eigenvalues of A_s and B_p are either $+1$ or -1 , depending on whether a particle is present or not. Our convention is that an absent particle is represented by bit 0, otherwise the bit is set to 1. Bits representing spin- $1/2$ degrees of freedom will be set to 0 (1) if the correspondent spin is up (down). (a) All degrees of freedom on the cluster $\mathbf{C}_{3 \times 2}^s$ are numbered in an arbitrary but consistent way and mapped onto a set of bits. (b) Zero-particle state on the cluster $\mathbf{C}_{3 \times 2}^s$. (c) An example of a single-charge state. (d) A typical two-particle state.

operator on a state (see most inner area in Figure 5.6). It is realized through a function which selects a set of neighboring degrees of freedom and modifies them according to Table 5.2 in the topological phase or Table 5.4 in the polarized phase. Note that in addition to the bit configuration our state is characterized by an amplitude which is, generally, a polynomial in the perturbation parameters.

Finally, we remark that the loop structure of our algorithm is suitable for parallelization so that, in practice, the biggest computational barrier is the finite memory resource, rather than computing time. Nevertheless, the computation⁴ of the relevant quantities has consumed in total roughly $5 \cdot 10^4$ CPU-hours. Of course, we have also made use of model-specific optimizations, e.g., symmetries between certain clusters and matrix elements.

5.3.2 Extrapolation methods

Perturbative series approximate an analytic function well for small perturbation parameters. Usually, it is possible to extrapolate a finite-order series, in order to capture certain analytic properties in the non-perturbative regime. To the best of our knowledge, Domb and Sykes [135, 136] were the first to determine critical exponents using perturbative series, more than half a century ago. This approach regained popularity in the 1970's and various series analysis methods were introduced and successively optimized for specific cases, as is summarized in a review by Guttman [137]. Generally, there is no extrapolation technique which is optimal for *any* series so that one usually has to try different methods and test their convergence. In this section, we introduce a

⁴To cope with the high demand on RAM memory and CPU time, we have used computer clusters cl1, PhiDO and LiDOng in Dortmund.

few series analysis methods which are standard in our field of research and have been applied successfully in the past for similar problems [42, 81, 83, 102, 104, 121, 122, 138].

Let us consider an analytical function $f(x)$ and its Taylor series at order N around $x = 0$

$$S_N(x) = \sum_{i=0}^N a_i x^i. \quad (5.103)$$

A widely known approach is to extrapolate $S_N(x)$ by a rational function, the so-called *Padé approximant* [139], defined as

$$P[L(x), M(x)] = \frac{P_L(x)}{Q_M(x)}, \quad (5.104)$$

where $P_L(x)$ and $Q_M(x)$ are polynomials in x , of degree L and M respectively.

$$P_L(x) = \sum_{i=0}^L p_i x^i, \quad (5.105)$$

$$Q_M(x) = \sum_{i=0}^M q_i x^i. \quad (5.106)$$

In order to keep notations short, we will write $P[L, M]$ as well as S_N without the explicit x -dependence. The series expansion of the Padé approximant $P[L, M]$ at order N must be equivalent to S_N . Comparing coefficients leads to a set of N linear equations for p_i , q_i and a_i , with a unique solution for $L + M \leq N$. In our context, the coefficients a_i are exactly known. While in the perturbative limit the Padé approximants are, by construction, very close to $f(x)$, for large L and M they are expected to give a better representation of $f(x)$ than the bare series; even though $P[L, M]$ can have up to M poles in the complex plane, which are usually not physical poles. For a rigorous discussion of convergence of Padé approximants we refer to Ref. [140].

If $f(x)$ is a quantity with an algebraic divergence at the critical point x_c

$$\lim_{x \rightarrow x_c} f(x) = A (x_c - x)^{-\theta}, \quad (5.107)$$

it is common to approximate its logarithmic derivative:

$$\frac{d}{dx} \ln[f(x)] = \frac{f'(x)}{f(x)} = \lim_{x \rightarrow x_c} \frac{\theta}{x_c - x}, \quad (5.108)$$

With this trick a Padé extrapolation of the left-hand side of (5.108) (referred to as $\text{DlogP}[L, M]$) can be used to approximate the critical point x_c through its poles and the critical exponent θ through its residues. Generally a $\text{DlogP}[L, M]$ yields up to M pole-residue pairs. In order to identify the physical one, a detailed knowledge about

the model is needed. Here, we are interested in real-valued functions $f(x)$ with positive x . If the approximant $\text{DlogP}[L, M]$ (or $\text{P}[L, M]$) features real poles closer to the origin than the physical singularity, it is called defective. The existence of spurious poles is quite common in the Padé analysis and can lead to an impression of pseudo-convergence. As it is shown in Ref. [137], a defective approximant $[L, M]$ can be related to a non-defective approximant $[L - 1, M - 1]$ so that effectively a higher-order series yields no new information. The usual practice is to gather results from all approximants $\text{DlogP}[L, M]$ with $L + M \leq N - 1$ in a so-called Padé table and try to find sequences of stable approximations to estimate the accuracy of the extrapolation. Often the best approximants are $[L - 1, L]$, $[L, L]$ and $[L, L - 1]$.

The method of Padé approximations has been generalized in various ways [137], a certain class of generalizations is known under the name *differential approximants* (DA). Consider the Padé approximation of the left-hand side of (5.108)

$$\frac{d}{dx} \ln [f(x)] = \frac{f'(x)}{f(x)} = \frac{P_L(x)}{Q_M(x)}. \quad (5.109)$$

Rearranging terms yields

$$Q_M(x)f'(x) - P_L(x)f(x) = 0. \quad (5.110)$$

Guttman and Joyce generalized (5.110) by adding a higher derivative of $f(x)$, weighted by a polynomial [141]. An alternative approach is to add an inhomogeneous term instead or to combine both types of generalizations [142–144]. However, here, we focus on the approach by Guttman, where the approximation problem can be reformulated to finding polynomials $T_M(x)$, $R_M(x)$ and $S_M(x)$ with $M \leq \lfloor (N - 1) / 3 \rfloor$ ($\lfloor r \rfloor$ denotes the floor function which selects the highest integer not greater than r) so that the Taylor expansion of $f(x)$ satisfies

$$T_M(x) \frac{d^2}{dx^2} f(x) + R_M(x) \frac{d}{dx} f(x) + S_M(x) f(x) = 0. \quad (5.111)$$

Similarly as above, the Taylor expansion of $f(x)$ provides sufficient information to determine the coefficients of $T_M(x)$, $R_M(x)$ and $S_M(x)$. We refer the interested reader to Ref. [141] for an explicit algorithm. Let us now insert (5.107) into the above equation

$$T_M(x) \frac{\theta(1 + \theta)}{(x_c - x)^2} + R_M(x) \frac{\theta}{x_c - x} + S_M(x) = 0, \quad (5.112)$$

$$T_M(x)\theta(1 + \theta) + R_M(x)\theta(x_c - x) + S_M(x)(x_c - x)^2 = 0. \quad (5.113)$$

Assuming that all polynomials have distinct zeroes and $\theta \neq -1$, in the limit $x \rightarrow x_c$ the equation (5.113) can only be fulfilled if $T(x) = 0$. Thus the roots of $T(x)$ approximate

the location x_c of the pole. The critical exponent θ is then determined through

$$\theta = \lim_{x \rightarrow x_c} \left[1 + \frac{R_M(x)}{T_M(x)} (x_c - x) \right]. \quad (5.114)$$

Guttman argues that this method is superior to the DlogPadé approximation since it is robust for a wider spectrum of types of singularities [141]. However, one has to keep in mind that the number of possible approximants decreases when derivatives of higher orders are required.

Consider one more time the relation (5.110). If $Q_M(x)$ does not have zeros with multiplicity greater than one, then for $p \leq M$ and $p \leq L + 1$ the general solutions of (5.110) are the functions

$$f(x, p) = \prod_{i=1}^p (1 - A_i x)^{n_i}. \quad (5.115)$$

Yukalov et al. [145–147] developed an extrapolation scheme, based on (5.115); however, with complex-valued A_i and n_i . The so-called *self-similar factor approximants* (SSFA) are thus more general than the Padé or DlogPadé approximations [148] which are kind of a subset of SSFA. As usual, the constants A_i and n_i are determined by comparison of coefficients of the Taylor-expanded $f(x)$ with S_N , which yields $2p$ equations constructed below.

$$\sum_{i=1}^p n_i A_i^m = \frac{(-1)^{m-1}}{(m-1)!} \lim_{x \rightarrow 0} \left(\frac{d^m}{dx^m} \ln S_N \right), \quad \text{with } m \in \{1, 2, \dots, 2p\} \quad (5.116)$$

Since the number of free parameters in $f(x, p)$ is always even, for odd N one of them must be set to a constant (a convenient choice is $A_1 = 1$). After solving (5.116), the critical value x_c can be obtained from the roots of $f(x, p)$. In the region of the pole, $f(x, p)$ diverges with the critical exponent

$$\theta = \sum_{i=1}^p n_i. \quad (5.117)$$

Finally, let us mention that the Padé approximants can be generalized to treat series in more than one variable [149, 150]. However, for our purposes, it will be sufficient to scan the multi-variable space in fixed directions, and apply the single-variable methods introduced above.

5.3.3 iPEPS

We recall that while it is possible to extrapolate the series expansions obtained with pCUT, in order to find second-order phase transitions, the finite series do not capture a first-order transition. Therefore, in this last subsection, we would like to briefly discuss a variational method which, in our context, is specifically used to detect discontinuous (first-order) phase transitions in the perturbed toric code. The idea is to use a network of interconnected tensors as a variational ansatz for the ground state of a quantum system [151]. In particular the *projected entangled-pair state* (PEPS), as well as its translationally invariant version *infinite* PEPS (iPEPS) have proved to be well suited to simulate ground states of strongly-correlated quantum systems in two dimensions [75–77]. Here, we will only present basic concepts of the method, which are reviewed in more detail in Ref. [152].

Generally, the Hilbert space of an N -body quantum system is constructed by a tensor product of the N local Hilbert spaces. A state can then generally be written as

$$|\psi_N\rangle = \sum_{s_1, s_2, \dots, s_N} C_{s_1, s_2, \dots, s_N} |s_1, s_2, \dots, s_N\rangle, \quad (5.118)$$

where a basis $\{s_i\}$ is assigned to each local degree of freedom and C_{s_1, s_2, \dots, s_N} are complex-valued coefficients. Let d_i be the dimension of the local Hilbert space at site i . Then, the state $|\psi_N\rangle$ can be represented through its coefficients stored in an N -dimensional tensor with d_i elements in each dimension, as depicted in Figure 5.8 (a). A reasonable approximation for the ground state of local Hamiltonians on a lattice is to assume that the entanglement in the system is short-ranged [153, 154], as illustrated in Figure 5.8 (b). Due to this simplification, the number of coefficients (and thus the computational complexity) grows only polynomially with N , in contrast to an exponential growth for an exact representation of a quantum many-body state. Of course, the approximation of a general state by a PEPS becomes better with increasing dimension D of shared indices (referred to as 'bond dimension') since then a spatially wider entanglement is taken into account⁵. However, in practice, a low bond dimension is used and for $D \ll N$, this approach fails to describe a system close to criticality because of the diverging correlation length.

The PEPS approach is well suited to treat the perturbed toric code model. It can be shown that the ground state of the unperturbed toric code is *exactly* a PEPS with $D = 2$ [153]. In the high-field limit, where the toric code interactions can be neglected, the ground state is simply a state, where all spins point into the polarization direction. This exactly corresponds the fully disentangled PEPS with $D = 1$. In between these two

⁵In the limit $D = N$, we recover exactly the general quantum state ψ_N .

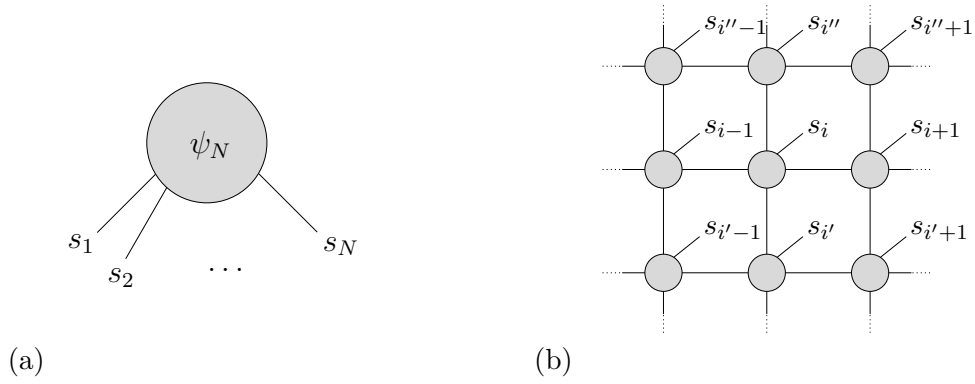


FIGURE 5.8: Representing a quantum state through a tensor network. (a) An N -dimensional tensor can be illustrated as an object with N legs, where each leg is labeled by an index running from 1 to d_i , the dimension of the local Hilbert space at site i . (b) Excerpt of a tensor network. Interconnecting bonds represent shared indices of neighboring tensors. In addition, a tensor at site i is assigned an index s_i to label the local Hilbert space.

limiting cases, the ground state $|\psi_{\text{gs}}\rangle$ is approached variationally through an evolution in imaginary time

$$|\psi_{\text{gs}}\rangle = \lim_{\tau \rightarrow \infty} \frac{e^{-\tau H} |\psi_0\rangle}{\|e^{-\tau H} |\psi_0\rangle\|}, \quad (5.119)$$

where H is the Hamiltonian, and $|\psi_0\rangle$ is some reference state which must have a finite overlap with the ground state. Using the Suzuki-Trotter decomposition, τ is discretized so that the operator action on the right-hand side of (5.119) can be written as a product of so-called gates $e^{-\delta\tau H_i}$, where $\delta\tau$ is a finite step in imaginary time and H_i a local term of the Hamiltonian. After an action of each gate on a set of neighboring sites (or equivalently neighboring tensors) of the PEPS $|\psi(\tau)\rangle$, the state is updated to $|\psi(\tau + \delta\tau)\rangle$ where the coefficients of the tensors, comprised by the gate, are chosen to minimize

$$\begin{aligned} \left\| |\tilde{\psi}(\tau + \delta\tau)\rangle - |\psi(\tau)\rangle \right\|^2 &= \langle \psi(\tau) | \psi(\tau) \rangle + \langle \tilde{\psi}(\tau + \delta\tau) | \tilde{\psi}(\tau + \delta\tau) \rangle \\ &\quad - \langle \tilde{\psi}(\tau + \delta\tau) | \psi(\tau) \rangle - \langle \psi(\tau) | \tilde{\psi}(\tau + \delta\tau) \rangle, \end{aligned} \quad (5.120)$$

where

$$|\tilde{\psi}(\tau + \delta\tau)\rangle = e^{-\delta\tau H_i} |\psi(\tau)\rangle. \quad (5.121)$$

Note that the computation of (5.120) involves a contraction of the tensor network or, in other words, a summation over all shared bonds. There are different strategies to perform the contraction efficiently and we refer to literature for details [76, 77]. However, it should be mentioned that the contraction method chosen in the present study involves a further approximation, controlled by the so-called environment bond dimension χ .

Summarizing, we have an efficient numerical tool at hand, which allows to approximate the ground-state energy of the toric code in a variational manner. This method is especially sensitive to first-order phase transitions. Sources of errors are the finite bond dimension D and the environment bond dimension χ as well as the discrete step size in imaginary time $\delta\tau$. The parameters χ and $\delta\tau$ can be varied until the precision reaches certain limits, but it is (computationally) much harder to increase D .

Phase diagram of the toric code in a uniform magnetic field

In this chapter, we present and analyze the exact perturbative expansions of the ground-state energy and the one-particle gap of the toric code in a uniform magnetic field. Some of the most important results of this chapter have been published in Ref. [99]. Our main focus lies on the study of the topological phase of the toric code (low-field limit), where the obtained series confirm known results for the purely parallel field [68] as well as a single transverse field [69], and in the case of the parallel field upgrade the expansion to higher orders. Most importantly, our series expansions allow for the first time to study the toric code and its critical behavior under a simultaneous effect of the parallel and transverse magnetic fields in order to answer questions concerning the structure of the phase diagram as well as critical behaviors for this general case.

Furthermore, we introduce a new approach [42, 99] where iPEPS, a variational method, is combined with series expansions, obtained by pCUT. This technique is well suited to precisely determine the boundaries of a phase, where first- as well as second-order phase transitions are expected to occur.

6.1 Preliminaries

We begin by presenting series expansions of the ground-state energy and the gap of the lowest-lying excitation in the topological phase. Then, we discuss our strategy to determine the boundaries of the topological phase, where we have to cope with continuous as well as discontinuous phase transitions. If the transition is continuous, our series are used to compute certain critical exponents of the model.

6.1.1 Series expansion results

The results presented in this chapter, are based on perturbative series, we have computed with pCUT, as described in Section 5.1. The ground-state energy per site e_0 , has been obtained up to order 10 in the limit $h_x, h_y, h_z \ll J = 1/2$. There are certain symmetries in the expression of e_0 which reflect a symmetry between charges and fluxes. Thus, we introduce auxiliary variables $S_k = h_x^k + h_z^k$ and $P_{2k} = h_x^k h_z^k$ and write the series expansion of ground-state energy as

$$\begin{aligned}
e_0 = & -\frac{1}{2} - \frac{1}{2}S_2 - \frac{1}{4}h_y^2 - \frac{15}{8}S_4 - \frac{7}{32}S_2h_y^2 + \frac{1}{4}P_4 - \frac{13}{192}h_y^4 - \frac{147}{8}S_6 - \frac{371}{128}S_4h_y^2 \\
& + \frac{113}{32}S_2P_4 - \frac{1045}{3456}S_2h_y^4 + \frac{2003}{384}P_4h_y^2 - \frac{197}{3072}h_y^6 - \frac{18003}{64}S_8 - \frac{1954879}{36864}S_6h_y^2 \\
& + \frac{6685}{128}S_4P_4 - \frac{34054175}{3981312}S_4h_y^4 + \frac{146861}{2304}S_2P_4h_y^2 - \frac{15343549}{26542080}S_2h_y^6 + \frac{20869}{384}P_8 \\
& + \frac{5020085}{497664}P_4h_y^4 - \frac{163885}{1769472}h_y^8 - \frac{5420775}{1024}S_{10} - \frac{1563459523}{1327104}S_8h_y^2 + \frac{39524033}{36864}S_6P_4 \\
& - \frac{1115105409427}{5733089280}S_6h_y^4 + \frac{10058235445}{7962624}S_4P_4h_y^2 - \frac{4219640835497}{191102976000}S_4h_y^6 \\
& + \frac{5650925}{6912}S_2P_8 + \frac{20854097563}{143327232}S_2P_4h_y^4 - \frac{483890940281}{382205952000}S_2h_y^8 + \frac{1202498305}{1990656}P_8h_y^2 \\
& + \frac{1994817656221}{71663616000}P_4h_y^6 - \frac{186734746441}{1146617856000}h_y^{10}. \tag{6.1}
\end{aligned}$$

The matrix elements of the effective Hamiltonian in the one-particle sector correspond to hopping amplitudes $t_{\mathbf{r}}$ of a single quasi-particle [see (5.61)]. As argued in Section 5.1.3 the index \mathbf{r} is limited to a finite range which depends on the perturbation order. We computed all relevant $t_{\mathbf{r}}$ up to order 8. The lengthy expressions are listed in the Appendix B.1. With Fourier transformation, we obtain the one-quasi-particle dispersion $\omega(\mathbf{k})$ [see (5.66)]. For a single dressed charge and $\mathbf{k} = (k_x, k_y)$, the dispersion at order three reads

$$\begin{aligned}
\omega(\mathbf{k}) = & 1 - 2h_z(\cos k_x + \cos k_y) - h_y^2 + 2h_z^2 - h_z^2(\cos 2k_x + 4\cos k_x \cos k_y + \cos 2k_y) \\
& \frac{1}{8}h_z(\cos k_x + \cos k_y)[8h_x^2 + 11h_y^2 + 48h_z^2 - 16h_z^2(\cos 2k_x + 4\cos k_x \cos k_y + \cos 2k_y)]. \tag{6.2}
\end{aligned}$$

The series expansion of the dispersion of a single dressed flux can be simply constructed by exchanging h_x and h_z in the above expression (for $h_z = h_x$ both dispersions are equivalent). In Figure 6.1, we plot $\omega(\mathbf{k})$ of a charge along the conventional symmetry lines in the Brillouin zone. We find that the dispersion has a minimum at $\mathbf{k} = (0, 0) = \mathbf{k}_0$, a maximum at $\mathbf{k} = (\pi, \pi)$, and a saddle point at $\mathbf{k} = (\pi, 0)$ (as well as at $\mathbf{k} = (0, \pi)$, due to rotational symmetry). These specific points play a major role in understanding the structure of the two-quasi-particle continuum which we discuss in Section 7.3. For

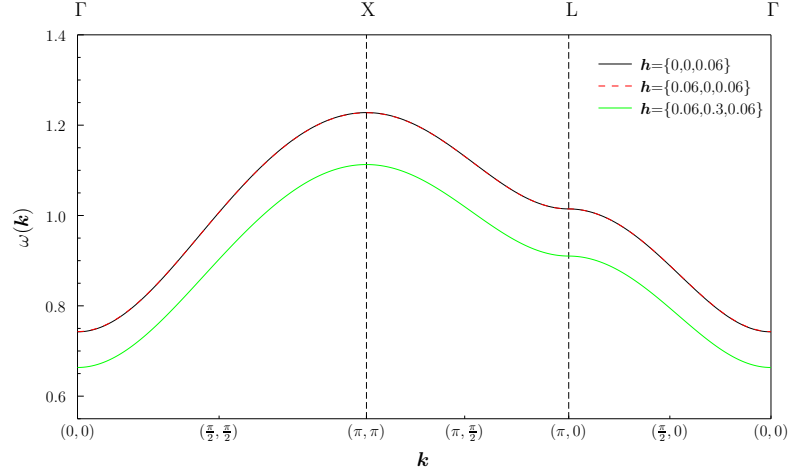


FIGURE 6.1: Dispersion $\omega(\mathbf{k})$ of a single charge in the magnetic field $\mathbf{h} = (h_x, h_y, h_z)$, for three typical parameter configurations. As will be shown below, the values of the magnetic field are chosen such that the system is topologically ordered and far away from the phase transition. The difference between the black and the red, dashed curve is less than 10^{-3} , due to the small amplitude of the parallel field.

the remainder of the current chapter, however, we concentrate on the one-quasi-particle gap $\Delta = \omega(\mathbf{k}_0)$. For the case of a single dressed charge, we obtain the series

$$\begin{aligned}
\Delta = & 1 - 4h_z - h_y^2 - 4h_z^2 + 2h_x^2h_z + \frac{11}{4}h_y^2h_z - 12h_z^3 + 5h_x^4 + 17h_x^2h_y^2 - \frac{15}{16}h_y^4 + 3h_x^2h_z^2 \\
& - 9h_y^2h_z^2 - 36h_z^4 + \frac{27}{2}h_x^4h_z + \frac{17}{4}h_y^4h_z + \frac{9}{4}h_x^2h_y^2h_z + \frac{83}{4}h_x^2h_z^3 + \frac{473}{64}h_y^2h_z^3 - 176h_z^5 \\
& + 92h_x^6 + \frac{14267}{96}h_y^2h_x^4 + 71h_z^2h_x^4 + \frac{13621}{1152}h_y^4h_x^2 + 63h_z^4h_x^2 + \frac{1305}{8}h_y^2h_z^2h_x^2 - \frac{575}{384}h_y^6 \\
& - \frac{2625}{4}h_z^6 - \frac{7971}{64}h_y^2h_z^4 - \frac{135619}{3456}h_y^4h_z^2 + \frac{495}{2}h_x^6h_z + \frac{1142149}{4608}h_x^4h_y^2h_z \\
& - \frac{3031}{13824}h_x^2h_y^4h_z + \frac{799973}{110592}h_y^6h_z + \frac{925}{4}h_x^4h_z^3 + \frac{13807}{48}h_x^2h_y^2h_z^3 + \frac{1782929}{20736}h_y^4h_z^3 \\
& + \frac{28633}{64}h_x^2h_z^5 - \frac{238621}{1152}h_y^2h_z^5 - \frac{14771}{4}h_z^7 + \frac{35649}{16}h_x^8 + \frac{7715431}{3072}h_x^6h_y^2 \\
& + \frac{3032191}{31104}h_x^4h_y^4 + \frac{98263727}{3981312}h_x^2h_y^6 - \frac{26492351}{7962624}h_y^8 + \frac{80999}{96}h_x^6h_z^2 + \frac{2199571}{4608}h_x^4h_y^2h_z^2 \\
& + \frac{24547709}{165888}h_x^2h_y^4h_z^2 - \frac{1495320677}{19906560}h_y^6h_z^2 + \frac{19263}{16}h_x^4h_z^4 + \frac{5186533}{1728}h_x^2h_y^2h_z^4 \\
& - \frac{1760584999}{1990656}h_y^4h_z^4 + \frac{118029}{64}h_x^2h_z^6 - \frac{4663837}{1728}h_y^2h_z^6 - \frac{940739}{64}h_z^8. \tag{6.3}
\end{aligned}$$

This expression is valid for $h_z \geq h_x$. At $h_x \geq h_z$ one has to consider the gap of a single dressed flux. As already discussed for the general case of a single-particle dispersion, the series expansion of the flux gap is constructed by exchanging h_x and h_z in the above expression (for $h_z = h_x$ both gaps are equivalent).

The parallel-field case is numerically easier to tackle so that setting $h_y = 0$, we are able to obtain an additional order of the expansion:

$$\begin{aligned}
\Delta_{\text{par}} = & 1 - 4h_z - 4h_z^2 - 12h_z^3 + 2h_x^2h_z - 36h_z^4 + 3h_x^2h_z^2 + 5h_x^4 - 176h_z^5 + \frac{83}{4}h_x^2h_z^3 \\
& + \frac{27}{2}h_x^4h_z - \frac{2625}{4}h_z^6 + 63h_x^2h_z^4 + 71h_x^4h_z^2 + 92h_x^6 - \frac{14771}{4}h_z^7 + \frac{28633}{64}h_x^2h_z^5 \\
& + \frac{925}{4}h_x^4h_z^3 + \frac{495}{2}h_x^6h_z - \frac{940739}{64}h_z^8 + \frac{118029}{64}h_x^2h_z^6 + \frac{19263}{16}h_x^4h_z^4 \\
& + \frac{80999}{96}h_x^6h_z^2 + \frac{35649}{16}h_x^8 - \frac{11472297}{128}h_z^9 + \frac{14650547}{1152}h_x^2h_z^7 + \frac{918461}{144}h_x^4h_z^5 \\
& + \frac{18372481}{4608}h_x^6h_z^3 + \frac{162525}{32}h_x^8h_z, \tag{6.4}
\end{aligned}$$

where Δ_{par} is the gap of the toric code in a parallel field for $h_z \geq h_x$.

6.1.2 Combining pCUT and iPEPS

The series expansions of the single-particle gap from one phase, do not allow to capture a discontinuous transition. However, if the system becomes critical, we can use various extrapolation methods (see Section 5.3.2) in order to determine the position of the critical point with remarkable precision. In this regard, iPEPS is a kind of antipodal method. Here, the ground-state energy is computed in a variational manner, and the precision depends rather on the amount of entanglement in the ground state than on the ratio of the interaction J and the perturbation parameters h_x, h_y , and h_z . While iPEPS is sensitive to discontinuous phase transitions, the detection of a second-order phase transition is significantly less accurate because of the finite bond dimension and the fact that with each derivation of the minimized energy the influence of numerical noise is increased.

As discussed in Section 4.3, the toric code undergoes a second-order phase transition for $h_y = 0$ and a first-order phase transition for $h_x = h_z = 0$. Apart from these limiting cases, the type of phase transition is a priori not known. By combining pCUT and iPEPS methods, we develop a powerful criterion to decide whether the phase transition outside the limiting cases is continuous or not. Figure 6.2 shows a typical behavior of the ground-state energy per site e_0 and the gap Δ in a certain direction of the magnetic field, parametrized by the (one-dimensional) variable h . The ground-state energy computed with pCUT and iPEPS is dubbed $e_0^{\text{pCUT}}(h)$ and $e_0^{\text{iPEPS}}(h)$ respectively. In the perturbative regime, where h is close to 0, we typically find that $e_0^{\text{iPEPS}}(h)$ is slightly above $e_0^{\text{pCUT}}(h)$, due to the approximations listed in Section 5.3.3, as well as numerical errors (however, the Figure 6.2 shows an idealized example). The perturbative expansions are valid up to the point h^* , where a variationally-computed energy minimum

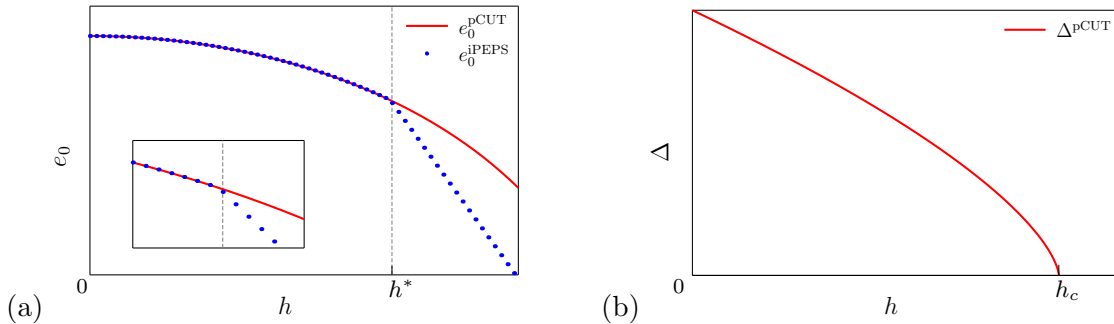


FIGURE 6.2: A qualitative sketch of the ground-state energy and the single-particle gap dependence on the magnetic field h . (a) The variational energy $e_0^{\text{iPEPS}}(h)$ undershoots the perturbatively computed energy $e_0^{\text{pCUT}}(h)$ at the point h^* , enlarged in the inset. (b) A typical shape of the one-particle gap extrapolated from a perturbative series. The gap closes at h_c .

below $e_0^{\text{pCUT}}(h)$ is found:

$$e_0^{\text{pCUT}}(h) - e_0^{\text{iPEPS}}(h) \leq 0 \quad \text{for } h \leq h^*, \quad (6.5)$$

$$e_0^{\text{pCUT}}(h) - e_0^{\text{iPEPS}}(h) > 0 \quad \text{for } h > h^*. \quad (6.6)$$

As shown in Figure 6.2 (b), Δ vanishes at $h = h_c$, thus the critical field h_c is implicitly defined through

$$\Delta(h < h_c) > 0, \quad (6.7)$$

$$\Delta(h_c) = 0. \quad (6.8)$$

If the gap vanishes inside the perturbative validity range ($h_c < h^*$), then the system indeed undergoes a continuous phase transition at h_c , while in the opposite case ($h_c > h^*$) we interpret h^* as a first-order transition point. We point out that our perturbative treatment tracks exclusively the single quasi-particle gap and is blind to the scenario, where *multi*-particle modes (e.g., bound states condense), or, generally, a level crossing of a high-energy mode with the ground-state energy occurs before the gap is fully closed. Note that alternatively one can identify h^* with the position of the kink in $e_0^{\text{iPEPS}}(h)$ (or its derivation). However, unlike in the illustration 6.2 (a), the kink is usually less pronounced so that, in practice, its position cannot be determined as sharply as the criterion (6.5)-(6.6) allows us to do.

6.1.3 Critical exponents

One of our main goals in this chapter is to find the critical field h_c where the topological phase breaks down. In general, when a system is close to criticality, the correlation

length ξ diverges with the critical exponent ν

$$\xi \propto (h - h_c)^{-\nu}. \quad (6.9)$$

The correlation length should be proportional to $1/\Delta$, where Δ is the mass gap which behaves as

$$\Delta \propto (h - h_c)^{z\nu}. \quad (6.10)$$

The condensation of elementary excitations is a clear signal of a phase transition. Therefore we are interested to determine the critical field h_c where the gap becomes zero. By means of extrapolation methods, introduced in Subsection 5.3.2, we are also able to obtain the critical exponent $z\nu$ from the gap series. In addition, we will compute the dynamical exponent z which links the characteristic time and length scales through

$$\tau \propto \xi^{-z}, \quad (6.11)$$

where τ is the correlation time. This exponent can be obtained from the dispersion of the lowest excited state at h_c with

$$\omega(h_c, \mathbf{k}) \propto |\mathbf{k} - \mathbf{k}_0|^z, \quad (6.12)$$

where \mathbf{k}_0 minimizes the dispersion [155]. We calculate the quantity $z\nu$ by extrapolating the series expansion of Δ , as discussed in Section 5.3.2. However, we cannot use this approach to compute z because we do not have the series expansion of ω in \mathbf{k} . Instead, in order to determine the dynamical exponent, we use a trick. For fixed momenta \mathbf{k} with $|\mathbf{k} - \mathbf{k}_0| \ll 1$, we extrapolate $\omega(\mathbf{k})$ and evaluate the gap at the critical point h_c . Thus one can track the \mathbf{k} -dependence of the extrapolated gap at the point h_c and perform a logarithmic fit, to obtain z . As we will see below, this approach is less precise than 'direct' extrapolation methods.

6.2 Low-field limit: Ising line

As a first check, we verify that our results for the parallel field case are consistent with series expansions by He et al. [121] for the (2+1)-dimensional transverse-field Ising model. We denote the magnetic field vector by $\mathbf{h} = (h_x, h_y, h_z)$. Setting $\mathbf{h} = (0, 0, h)$ [or alternatively $\mathbf{h} = (h, 0, 0)$], we compare the series coefficients of the ground-state energy per site, as well as the one-particle gap (see Table 6.1). Note that the series are rescaled, due to $J = 1/2$. We find an exact correspondence, as can be verified by representing our

order	e_0 (He et al.)	e_0 (this work)	Δ (He et al.)	Δ (this work)
0	0	0	2	2
1	0	0	-4	-4
2	-0.5	$-\frac{1}{2}$	-2	-2
3	0	0	-3	-3
4	-0.46875	$-\frac{15}{32}$	-4.5	$-\frac{9}{2}$
5	0	0	-11	-11
6	-1.1484375	$-\frac{147}{128}$	-20.5078125	$-\frac{2625}{128}$
7	0	0	-57.69921875	$-\frac{14771}{256}$
8	-4.395263671875	$-\frac{18003}{4096}$	-114.83630371	$-\frac{940739}{8192}$
9	0	0	-350.106719971	$-\frac{11472297}{32768}$
10	-20.6786155701	$-\frac{5420775}{262144}$	-730.535977681	$-\frac{287258435}{393216}$

TABLE 6.1: Coefficients of high-temperature series for the (2+1)-dimensional Ising model and the low-field series expansion of the toric code in the direction $\mathbf{h} = (0, 0, h)$. The floating point coefficients for the ground-state energy per site e_0 and the one-particle gap Δ were obtained by He et al. [121] with a full graph expansion. The coefficients in form of rational numbers were computed with pCUT using the finite-lattice method, and have been rescaled to the $J = 1$ case for comparison reasons.

rational coefficients as floats. While He et al. reach a higher order in perturbation [121], due to a superior method (full graph expansion) and a simpler model, our series feature *exact* coefficients and are, in addition, obtained from a special case of a multi-variable expansion.

We point out that there is no standard method to estimate the error of series extrapolations. Fortunately, we are able to test the accuracy of our method in the limiting case where the toric code in a field is isospectral to the Ising model. Note that, here, higher orders of the series expansion are available [121, 122] and lead to more accurate results. However, our goal is to determine the order of magnitude of the precision, when using *our* expansion. Specially because this is relevant to estimate the accuracy of our calculations outside this limiting case.

Let us now compute the position of the critical point h_c where the Ising model undergoes a second-order phase transition. Table 6.2 shows that the DlogPadé approximants capture the first three digits of the most accurately known value of the critical field $h_c = 0.164235(10)$ [120]. The (2+1)-dimensional Ising model is characterized by the critical exponent $\nu = 0.630$ [156] and the dynamical exponent $z = 1$ [157]. Note that most reliable methods seem to agree on the first three digits of ν (which is sufficient for our purposes), while the precise value of this critical exponent is under debate, as

$L \setminus M$	1	2	3	4	5	6	7	8
1	0.162162	0.164716	0.165169	0.164830	0.164564	0.164501	0.164471	0.164415
2	0.168182	0.165165	0.164986	0.162453	0.164485	0.164441	0.164540*	-
3	0.162242	0.164836	0.161609	0.164602	0.164457	0.164502*	-	-
4	0.166905	0.164563	0.164477	0.164454	0.164311	-	-	-
5	0.162267	0.164496	0.164444	0.164489*	-	-	-	-
6	0.166615	0.164467	0.164531*	-	-	-	-	-
7	0.162424	0.164413	-	-	-	-	-	-
8	0.166252	-	-	-	-	-	-	-

(a)

$L \setminus M$	1	2	3	4	5	6	7	8
1	0.631118	0.655552	0.660874	0.655370	0.650053	0.648568	0.647738	0.646000
2	0.704042	0.660812	0.658256	0.550128	0.648094	0.646692	0.649284*	-
3	0.609726	0.655478	0.492657	0.651404	0.647264	0.648487*	-	-
4	0.702536	0.650009	0.647874	0.647155	0.641474	-	-	-
5	0.593233	0.648413	0.646815	0.648151*	-	-	-	-
6	0.713861	0.647612	0.649081*	-	-	-	-	-
7	0.582253	0.645905	-	-	-	-	-	-
8	0.718074	-	-	-	-	-	-	-

(b)

TABLE 6.2: DlogPadé approximants $\text{DlogP}[L, M]$. (a) Estimate of the critical value h_c . (b) The corresponding critical exponent νz . Values highlighted by an asterisk correspond to defective approximants. While the critical value is approximated well up to the third digit, the critical exponent νz seems to be overestimated by a few percent.

summarized in Ref. [156]. Considering Table 6.2 we observe that our approach yields a rather precise estimate of the critical value of the field, while the critical exponent ν is slightly overestimated, which is typical for series expansions [68, 122]. Additionally, we determine the dynamical exponent to be approximately $z \approx 1.3$, which is rather far off the literature value. As explained in the previous section, we cannot extrapolate ω directly in \mathbf{k} . Furthermore, by construction, the momentum dependence in our dispersion enters only in cosines (due to $t_{\mathbf{r}} = t_{-\mathbf{r}}$, see Section 5.1.3). Since these are even functions, the convergence towards a linear vanishing of the gap around $\mathbf{k} = 0$ is conceivably bad. On the contrary, for cases where $z = 2$, our extrapolation should become much more precise. Even though our series seem to be not well suited to determine the dynamical exponent of the transverse field Ising model, we find a value which is significantly closer to one than two, therefore at least a qualitative agreement can be reached.

Next, we compute the differential approximants (DA) for $M \in \{1, 2, 3\}$ which extrapolate series of orders 4, 7, and 10 respectively. Note that this extrapolation cannot be used to compute z because the approximated function enters only implicitly, but its explicit form is necessary in order to study the momentum dependence. As shown in Table 6.3, the differential approximants seem to converge towards values obtained with DlogPadé approximants. The self-similar factor approximants (SSFA) are also in agreement with DlogPadé approximants (see Table 6.4).

order	4	7	10
h_c	0.172414	0.163924	0.164098
$z\nu$	0.737940	0.643978	0.644724

TABLE 6.3: Critical field h_c and critical exponent $z\nu$ computed with differential approximants [141]. The approximation is governed by the integer parameter M which restricts the contributing orders of a series to $1 + 3M$.

order	2	4	6	8	10
h_c	0.166667	0.164716	0.164986	0.164602	0.164311
$z\nu$	0.666667	0.653061	0.661396	0.628658	0.656814
z	1.33398	1.31058	1.31634	1.30207	

TABLE 6.4: Critical field h_c , and exponents $z\nu$ and z computed with self-similar approximants. Note that $z\nu$ and z have been computed independently, in the sense that $z\nu$ is obtained by extrapolating the gap at \mathbf{k}_0 and z is determined by the behavior of the dispersion at h_c in the vicinity of \mathbf{k}_0 .

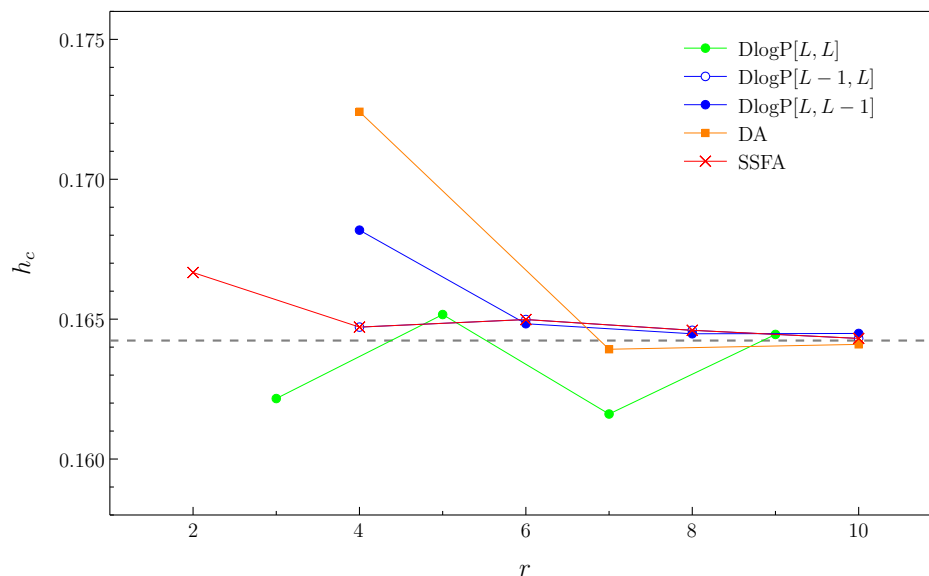


FIGURE 6.3: Transition point h_c of the (2+1)-dimensional Ising model extrapolated from finite-order series with different methods. The 'best' literature value $h_c = 0.164235(10)$ [120] is highlighted by the dashed line, r is the order of the series. To keep a clear overview, only the standard Padé approximants $[L, L]$, $[L - 1, L]$ and $[L, L - 1]$ are shown, with $L = [r - (r \bmod 2)] / 2$.

Summarizing, we observe that different extrapolation schemes yield consistent results with high precision (roughly 0.2%) for the critical point of the (2+1)-dimensional Ising model (see Figure 6.3). The computed critical exponent ν is close to the literature value, but less accurate (the deviation is approximately 3%, as shown Figure 6.4). Each extrapolation method shows a tendency to converge towards the known value for higher orders. Our result for the dynamical exponent appears to be closer to the correct value $z = 1$ than for example $z = 2$, which of course is only a qualitative statement. It is reasonable to assume that the accuracy of our calculations does not change significantly

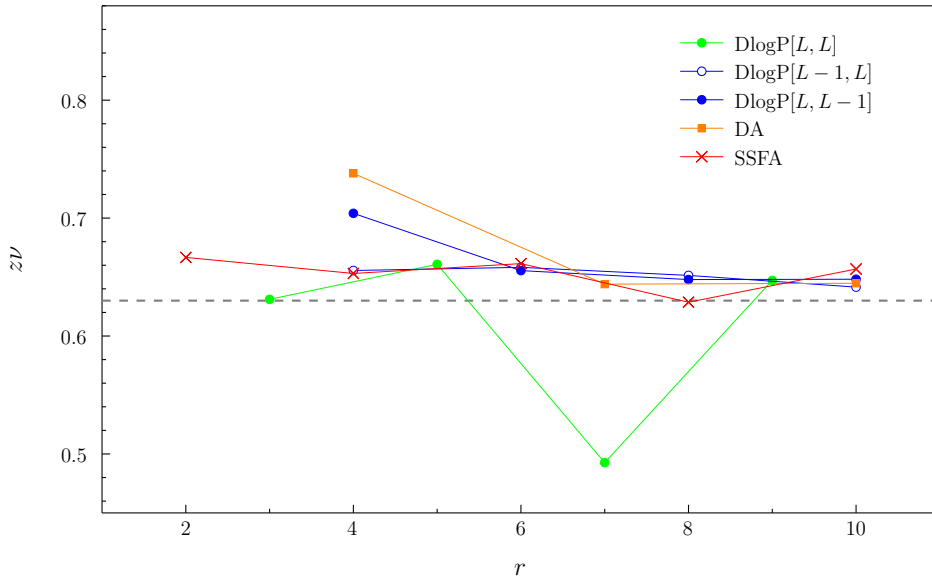


FIGURE 6.4: Critical exponent $z\nu$ of the (2+1)-dimensional Ising model, extrapolated with different methods, using perturbative expansions of the gap. The literature values of the critical exponents are $z = 1$ and $\nu = 0.630$ (highlighted by the dashed line), r is the order of the polynomial used in the extrapolations. To keep a clear overview only the standard Padé approximants $[L, L]$, $[L - 1, L]$ and $[L, L - 1]$ are included, where $L = \lceil r - (r \bmod 2) \rceil / 2$.

in the vicinity of the Ising point studied in this section. Therefore, the presented results should provide an intuition for the precision of our results away from the direction of the magnetic field $\mathbf{h} = (0, 0, h_z)$.

6.3 Low-field limit: parallel fields

The toric code in a two-dimensional parallel magnetic field has been studied with pCUT in Refs. [68, 99] and has already been the subject of several publications (see the discussion in Section 4.3). In the recent Ref. [67], the boundaries of the topological phase were computed by means of continuous-time Monte Carlo simulations. The high-precision calculations confirm the pCUT (low-field expansions based) predictions with great accuracy. In this chapter, we discuss these pCUT results in more detail, updating the series expansions to a higher order and including additional extrapolation methods.

One of the strength of our approach is that the obtained perturbative series allow to study each point in the three-dimensional parameter space of the magnetic field with a relatively low cost. This is in contrast with, for example, quantum Monte Carlo, where heavy numerics have to be performed for every constant set of variables (an even more crucial difference is the fact that quantum Monte Carlo cannot be applied efficiently to the toric code in a non-zero transverse magnetic field, due to the sign problem). The

parallel magnetic field can be parametrized by $\mathbf{h} = (h \sin \varphi, 0, h \cos \varphi)$, where $\varphi = 0$ corresponds to the Ising direction studied in the previous section. We obtain $h_c(\varphi)$, by successively fixing φ to a constant (which sets a certain direction of the magnetic field) and performing different extrapolations in order to compute h_c for the given direction of the field. Due to the charge-flux symmetry, it is sufficient to consider the parameter range $\varphi \in [0, \pi/4]$. In the case $\varphi = \pi/4$, the amplitudes of both parallel fields are equivalent and, as shown in the phase diagram in Figure 4.8, the phase boundary is multicritical.

In Figure 6.5, we report how the value of the critical magnetic field h_c changes when φ is tuned between these two significant points. First, and most importantly, we observe that all approximants are in a very good agreement on at least two digits of the critical field. Since it is not known how to specify exact error bars when extrapolating finite series,

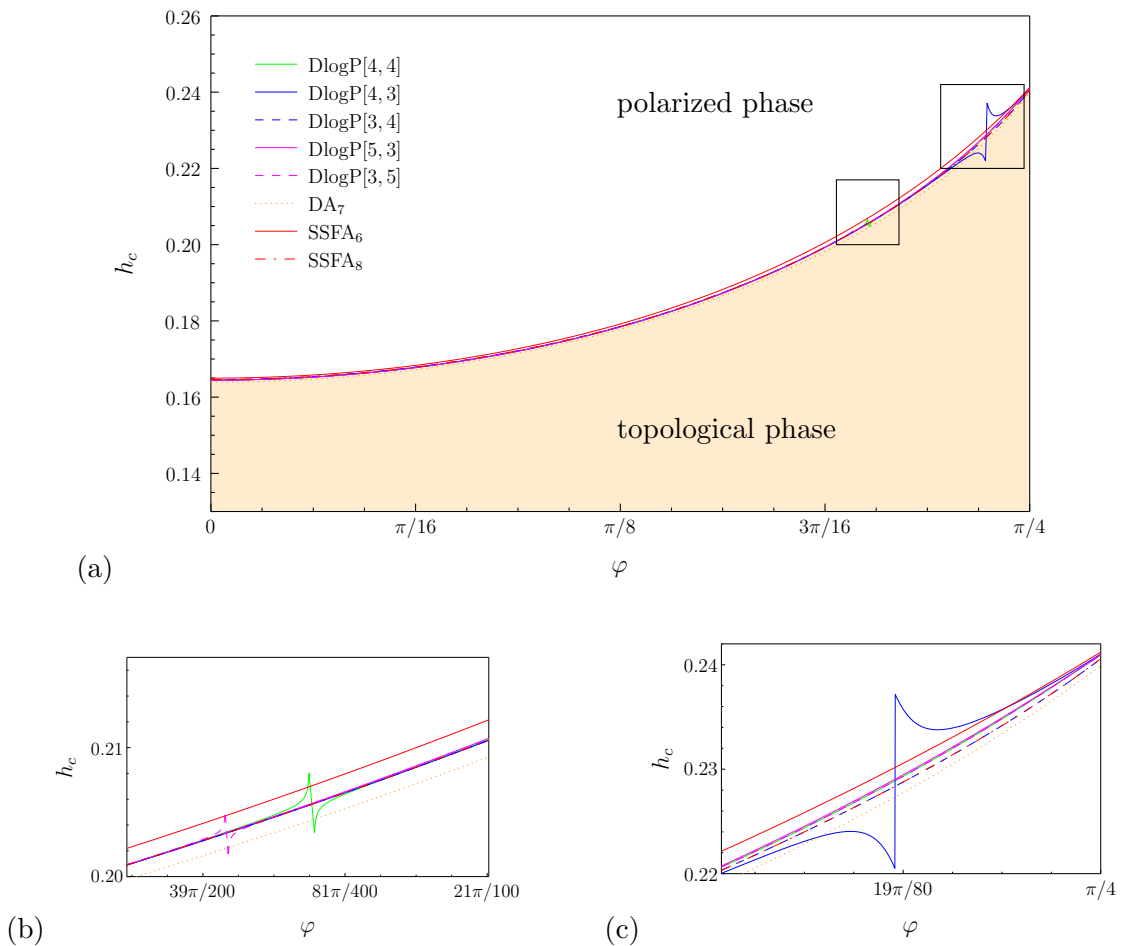


FIGURE 6.5: Boundary of the topological phase of the toric code in a parallel magnetic field. (a) Dependence of the critical value of the field on the angle φ between h_x and h_z . To keep a clear overview, the bundle of Padé approximants is represented by a few high-order extrapolations. The lower index of the differential approximants (DA) as well as the self-similar factor approximants (SSFA) denotes the order of the extrapolated series. (b) and (c) zoom on regions where a local failure of certain approximants is compensated by the set of remaining approximants.

it is common to consider the variation of h_c computed with various approximations, as a rough measure of accuracy. We will perform more concrete accuracy checks below by comparing our results with quantum Monte Carlo data. Furthermore, we notice that some approximants seem to diverge at certain directions of the magnetic field. This feature is an extrapolation artifact, as can be best understood by considering the denominator of a DlogPadé. Zeroes of this quantity determine the position of poles and thus define the phase transition point. In Figure 6.6 we consider the behavior of a specific DlogPadé extrapolation in proximity of its divergence. The analytic form of the

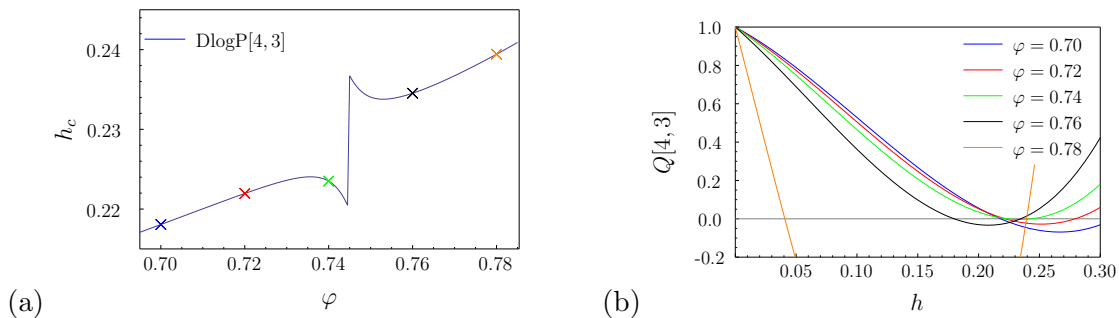


FIGURE 6.6: Example of how the non-physical behavior of the critical field is an extrapolation artifact. (a) The DlogP[4,3] approximant yields a diverging h_c in the shown parameter range. Since h_c is computed from poles of DlogP[4,3], it is useful to consider the zeroes of the *denominator* of DlogP[4,3]. We refer to this denominator as $Q[4,3]$. (b) Behavior of $Q[4,3]$ for certain fixed angles φ (highlighted in (a) by crosses). With increasing φ the real zeroes move closer to the origin and make the approximant defective at some point. The extrapolation fails and yields non-physical results when the minimum of the local parabola either touches the horizontal axis (so that the multiplicity of the pole becomes two) or moves above the zero axis, making the pole disappear.

denominator of this approximant is such that with increasing φ the real-valued zeroes are shifted to the left. Exactly at the position of the divergence, the multiplicity of the lowest zero goes from one to two, violating one of the premises of our extrapolation scheme¹. Further increasing of φ makes the extrapolation defective. Obviously, in the parameter domain where an approximant is diverging it has to be considered non-physical so that in order to describe the phase boundary smoothly, one has to take into account the whole set of approximations.

Let us consider the resulting phase diagram in convenient coordinates (as in Figure 4.8). Figure 6.7 shows that the boundary of the topological phase is obtained in a precise and consistent way. In regions where certain approximants diverge, others are smooth. Furthermore, the critical values obtained from various approximants are considerably close to each other. Indeed, as we will show below, the accuracy of our method is comparable to the one of quantum Monte Carlo (see Figure 6.9). With perturbative

¹We recall that a DlogPadé, approximates the function $\frac{\theta}{(x_c-x)}$ where the multiplicity of the pole is explicitly one (see Section 5.3.2 for details).

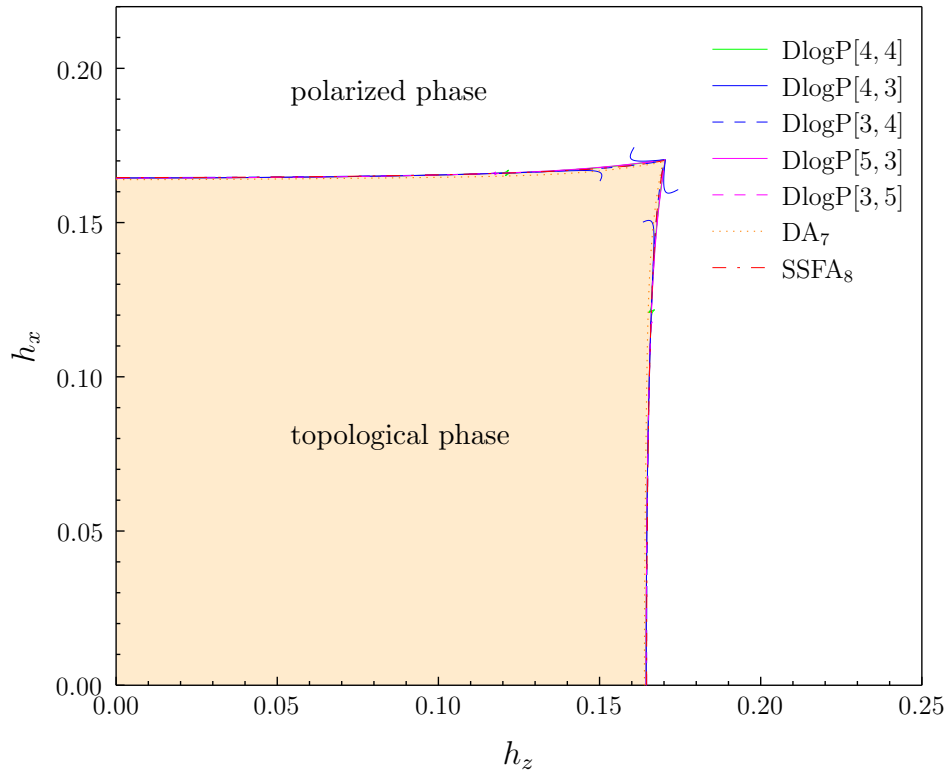


FIGURE 6.7: Phase diagram of the toric code in a parallel magnetic field. The plot is based on the same data as shown in Figure 6.5, except that here we use Cartesian coordinates. In contrast to Figure 4.8, we do not show the finite first-order transition line on the symmetry axis $h_x = h_z$, but only the boundary of the topologically-ordered phase. In addition to the known results from Ref. [68], the boundary has been computed with various DlogPadé approximations as well as other extrapolation methods, using a series expansion of the one-particle gap of order 9. Note that since we set $J = 1/2$, there is a factor 2 difference in our coordinates, when compared with the ones from Ref. [67].

series it is not possible to access directly the first-order phase transition line, attached to the multicritical point at $h_x = h_z = 0.170$. However, we will tackle this problem using high-field series expansions in Section 6.5.

Next, we investigate how the critical exponent $z\nu$ changes in the interval $0 < \varphi < \pi/4$. Figure 6.8 shows that, as anticipated in Section 4.3, the critical exponent remains constant for $\varphi > 0$, except in the region close to the multicritical point. We observe that apart from the negligible (since non-physical) divergences, the DlogPadé approximants are remarkably converged. Thus, we find that the universality class of the model is still compatible with the one of the (2+1)-dimensional Ising model (provided $z = 1$), even when φ is varied. The significant increase of the critical exponent at $\varphi = \pi/4$ indicates that here the universality class is likely different from the (2+1)-dimensional Ising model. Since our analysis is based on finite-order series which are extrapolated by rational functions, we do not observe a discontinuous change in $z\nu$, but rather a smooth increase near the multicritical point.

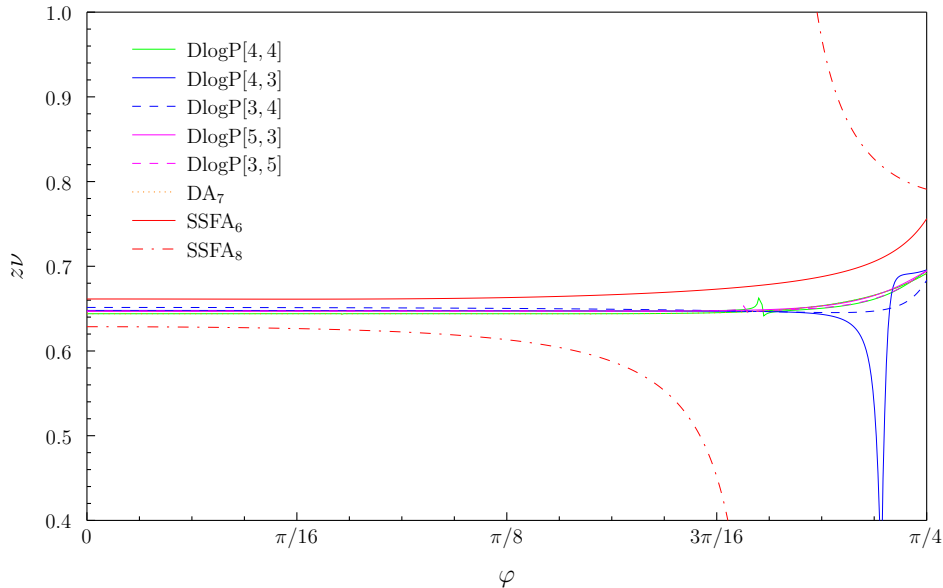


FIGURE 6.8: Critical exponent $z\nu$, obtained from the vanishing one-particle gap of the toric code in a two-dimensional parallel magnetic field. The lower index of the differential approximants (DA) as well as the self-similar factor approximants (SSFA) denotes the order of the extrapolated series. While the best DA extrapolation agrees with the Padé results, the highest-order SSFA approximation seems to fail for $\varphi > \pi/8$. Here, we show only a subset of DlogPadé approximants which give reliable results in the Ising point. For example, we do not show DlogPadé[8,1] because it clearly is an outlier, as shown in Table 6.2.

The quantum Monte Carlo calculations of the critical field in Ref. [67] allow us to compare the series results quantitatively in two distinct points of the phase diagram. Figure 6.9 confirms the notable accuracy of our results for the phase boundary. Note that in Figure 6.9 (a) the QMC simulation is performed for a constant $h_x = 0.15$ so that in order to compare with our parametrization of the problem, we had to find a φ such that the h_x -component of extrapolated h_c corresponds (up to numerical noise) precisely to the QMC value.

Let us take a closer look at the multicritical point, where $h_x = h_z$ and consequently $\varphi = \pi/4$. In analogy to our study of the Ising point, Table 6.5 lists DlogPadé approximants for the critical field h_c and the critical exponents $z\nu$. We find that the critical exponent is approximately $z\nu \approx 0.69$, which is significantly different from the Ising value (0.630).

The differential approximants at order 7, listed in Table 6.6, seem to be close to values from DlogPadé approximants. While the self-similar factor approximation yields consistent result for the critical field, it fails to approximate the critical exponent. As also shown in Figure 6.8, the SSFA results at the highest available order of the series are not reliable at the multicritical point.

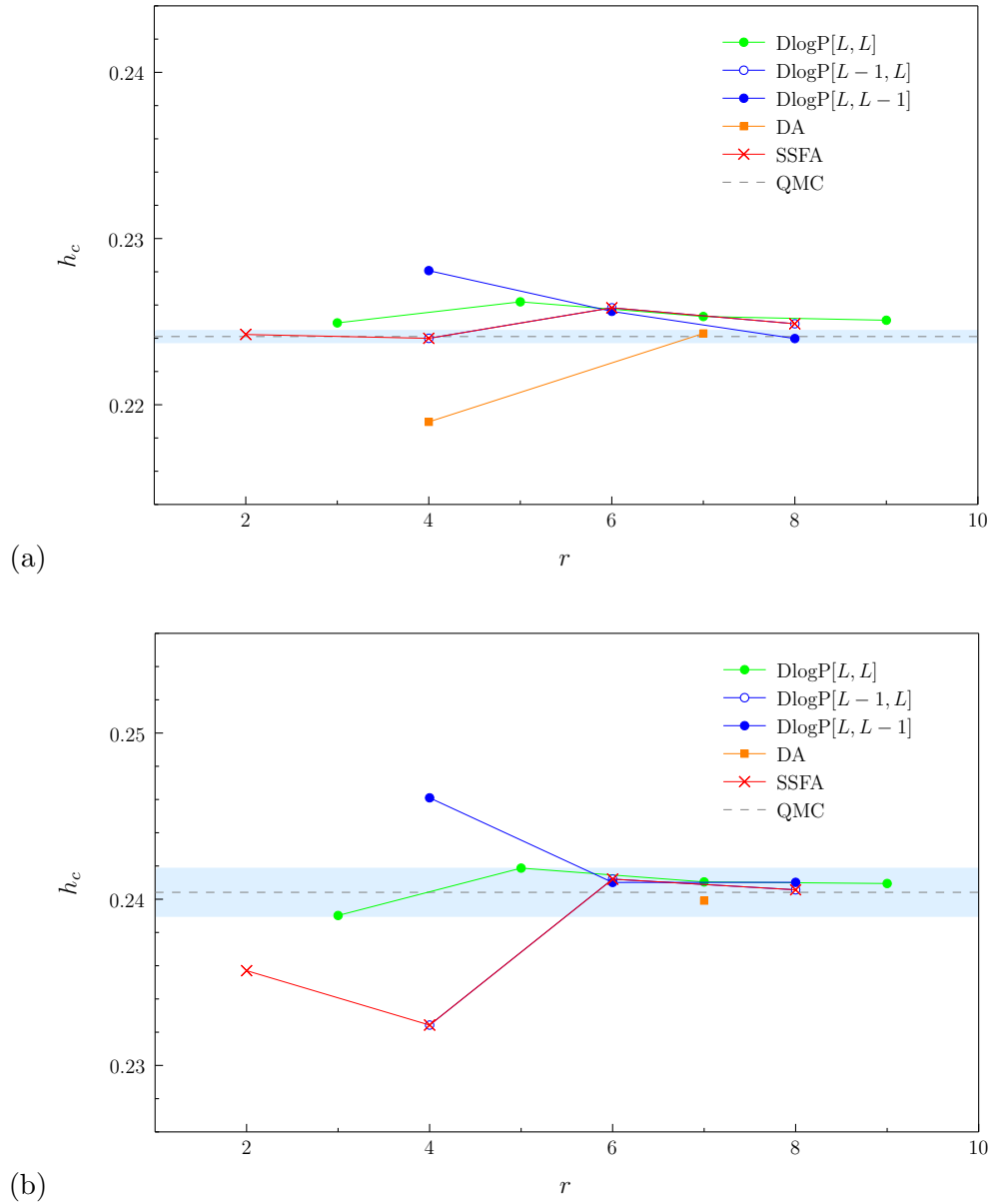


FIGURE 6.9: Comparison of the critical field h_c (computed with different series extrapolation methods at order r) with numerically precise values obtained by QMC simulations in Ref. [67]. The error of the QMC result is highlighted by a blue stripe. (a) Critical point for the direction of the magnetic field $\varphi \approx 0.73$. Here, the system is found to be critical at $h_z = 0.1665(5)$, which corresponds to $h_c \approx 0.2241$. (b) h_c at the critical point $\varphi = \pi/4$ (see also Table 6.5). The QMC simulation yields $h_c \approx 0.2404$, and is in remarkable agreement with extrapolations from finite-order series.

$L \setminus M$	1	2	3	4	5	6	7
1	0.239022	0.232428*	0.241975	0.240962	0.241057	0.240892	0.240998
2	0.246101	0.241872	0.241210	0.241047	0.240997	0.240956	-
3	0.235859	0.241010	0.241042	0.240568	0.240950	-	-
4	0.246457	0.241043	0.241017	0.240946	-	-	-
5	0.235639	0.240903	0.240955	-	-	-	-
6	0.246113	0.240988	-	-	-	-	-
7	0.236273	-	-	-	-	-	-

(a)

$L \setminus M$	1	2	3	4	5	6	7
1	0.685578	0.666935*	0.706586	0.695017	0.696391	0.693521	0.695686
2	0.748312	0.705431	0.698410	0.696227	0.695462	0.694744	-
3	0.631304	0.695680	0.696133	0.683496	0.694608	-	-
4	0.786467	0.696158	0.695758	0.694530	-	-	-
5	0.600786	0.693723	0.694727	-	-	-	-
6	0.814576	0.695446	-	-	-	-	-
7	0.587719	-	-	-	-	-	-

(b)

TABLE 6.5: DlogPadé approximants $\text{DlogP}[L, M]$ at the multicritical point $h_x = h_z$. (a) Estimate of the critical value h_c . (b) The corresponding critical exponent $z\nu$. Values highlighted by an asterisk correspond to defective approximants.

order	4	7
h_c	0.216291	0.239916
$z\nu$	0.352024	0.691748

TABLE 6.6: Critical field h_c and critical exponent $z\nu$ at the multicritical point $h_x = h_z$, computed with differential approximants. The approximation is governed by the integer parameter M which restricts the contributing orders of a series to $1 + 3M$.

order	2	4	6	8
h_c	0.235702	0.232428	0.241210	0.240568
$z\nu$	0.666667	0.662069	0.756161	0.790959
z	1.33392	-	1.39665	1.36378

TABLE 6.7: Critical field h_c and critical exponents $z\nu$ and z at the multicritical point $h_x = h_z$, computed with self-similar approximants. Note that $z\nu$ and z have been computed independently, in the sense that $z\nu$ is obtained by extrapolating the gap at \mathbf{k}_0 and z is determined by the behavior of the dispersion at h_c in the vicinity of \mathbf{k}_0 .

Figure 6.10 summarizes our estimates for the critical exponents $z\nu$ of the multicritical point. From our study of the Ising point in Section 6.2, we know that the resulting extrapolations typically tend to overestimate the critical exponent. However, because of the fact that in the field $h_x = h_z$ and $h_y = 0$ the Hamiltonian has an additional symmetry, and taking into account the accuracy of the presented results, we are confident that the point $h_x = h_z = 0.170$ indeed belongs to a universality class distinct from the (2+1)-dimensional Ising model.

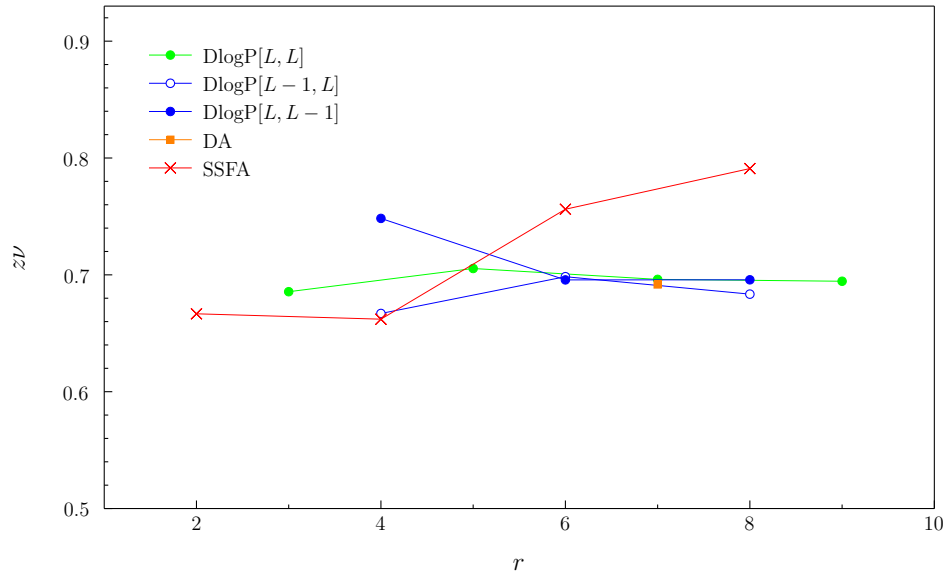


FIGURE 6.10: Critical exponents $z\nu$ of the multicritical point $h_x = h_z$ computed with various approximants at order r . Except the SSFA results (which are non-physical, as shown in Figure 6.8), the extrapolations seem to agree on $z\nu \approx 0.69$, which is clearly distinct from the value of the (2+1)-dimensional Ising model. The DlogPadé approximations seem to be more converged than other extrapolation methods at this point.

6.4 Low-field limit: arbitrary fields

After the close examination of the toric code in a parallel magnetic field, we consider the simultaneous perturbation by parallel *and* transverse fields. Note that here no Monte Carlo data is available since the simulations suffer from the sign problem². However, we have seen in the previous section that the perturbative approach gives accurate results for the critical values of the parallel magnetic field, thus we expect a similar precision in our calculations for the case where a transverse magnetic field is present. As it has been discussed in Section 4.3, the transition from the topological phase into the polarized phase can be either of first or of second order. We tackle this problem by including the variational iPEPS method in addition to our perturbative analysis. Let us remind that

²In the special case of a pure transverse field, the toric code can be mapped to the quantum compass model where the sign problem can be avoided [133].

the ground-state energies computed with pCUT and iPEPS are denoted via e_0^{pCUT} and e_0^{iPEPS} , the critical field h_c is determined by extrapolations of the perturbative series of the gap, and h^* is found by comparing e_0^{pCUT} and e_0^{iPEPS} , as discussed in Section 6.1.2. In order to give a demonstrative example, we consider two specific directions of the field where our approach of combining these two methods allows to decide clearly about the nature of the phase transition. As shown in Figure 6.11, we distinguish two cases. While in Figure 6.11 (a) the critical field h_c is smaller than h^* , we find the opposite scenario in

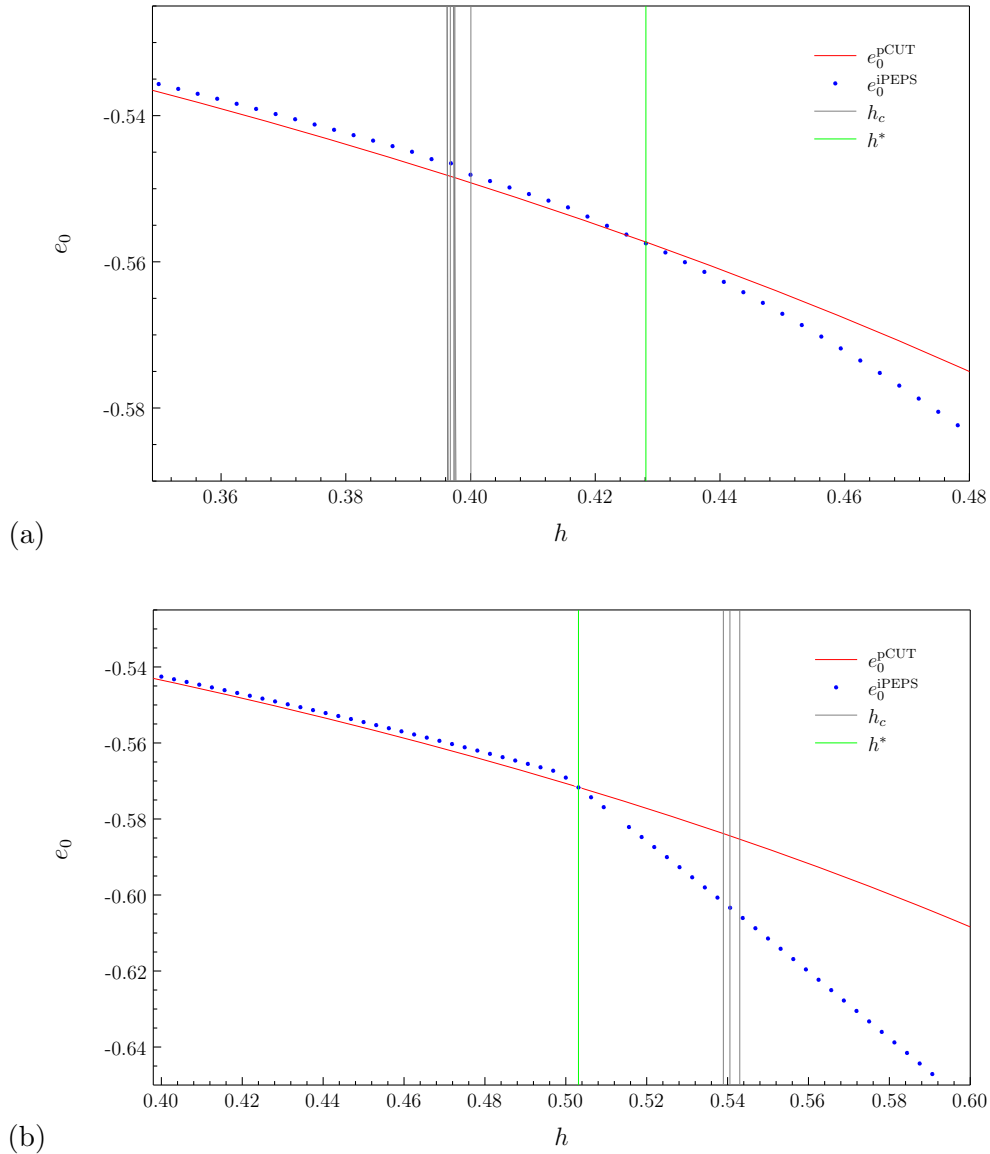


FIGURE 6.11: Ground-state energy of the toric code exposed to the magnetic field $\mathbf{h} = (0, h \sin \theta, h \cos \theta)$. The notation in the legend has been introduced in Section 6.1.2. The critical field h_c has been computed with various DlogPadé approximants, not specified here. (a) For $\theta = 0.38125 \pi$, the one-particle gap seems to close in a region where the numerically minimized ground-state energy is clearly above the perturbative one, which indicates a second-order phase transition. (b) At $\theta = 0.44375 \pi$, we find $h^* < h_c$. In this case, a first-order phase transition occurs before the gap vanishes.

Figure 6.11 (b). Using our definition from Section 6.1.2, we identify a continuous phase transition at h_c in the first case and a discontinuous transition at h^* in the second. In the pCUT validity range (at magnetic field $h < h^*$), e_0^{iPEPS} is always slightly above e_0^{pCUT} because the iPEPS ground-state energy has been computed variationally. An additional cause could be the finite bond dimension $D = 2$ of the iPEPS. Increasing D to 3, however, does not lead to a significant improvement of the results (not shown). Note that the field directions discussed in Figure 6.11 correspond to two points from the phase diagram in Figure 6.12 that will be discussed next.

Similarly to the previous section, we parametrize the magnetic field \mathbf{h} with the following spherical coordinates: $\mathbf{h} = h(\sin \varphi \cos \theta, \sin \theta, \cos \varphi \cos \theta)$. For fixed angles $\varphi = 0, \pi/8$, and $\pi/4$ we compute the critical values h_c and h^* while varying θ in small discrete steps. Let us begin by considering the case $\varphi = 0$ in Figure 6.12. One has to keep in mind that the vertical axis at constant θ corresponds to a certain direction of the magnetic field. The system undergoes a phase transition from a topologically-ordered phase at low fields, to a polarized phase. The critical values h_c , shown as continuous lines (which actually consist of a dense set of discrete points), are determined by the vanishing of the one-particle gap, extrapolated with various methods. The critical value h^* is computed by comparing e_0^{pCUT} and e_0^{iPEPS} , as described in Section 6.1.2. In Figure 6.12 (a), we distinguish three distinct domains separated by vertical dashed lines. According to the criteria of Section 6.1.2, in the left (right) region, the phase transition is of second (first) order, while in the intermediate region a clear conclusion is not possible. The discontinuities in the curvature of h_c are attributed to the already familiar numerical artifacts, discussed in the previous section. Note that at certain points our calculations can be checked with known results. The transition point at $\theta = 0$ (or equivalently $h_y = 0$), corresponds to the Ising point, already discussed in Figure 6.9, where we confirm the second-order phase transition at $h_z \approx 0.164$, as found for the transverse-field Ising model. At $\theta = \pi/2$ (or equivalently $h_z = 0$), it is known from Ref. [69] that the point $h_y = 1/2$ is a self-dual point where the system undergoes a first-order phase transition. Figure 6.12 confirms that also at this point our approach yields the correct result with significant precision.

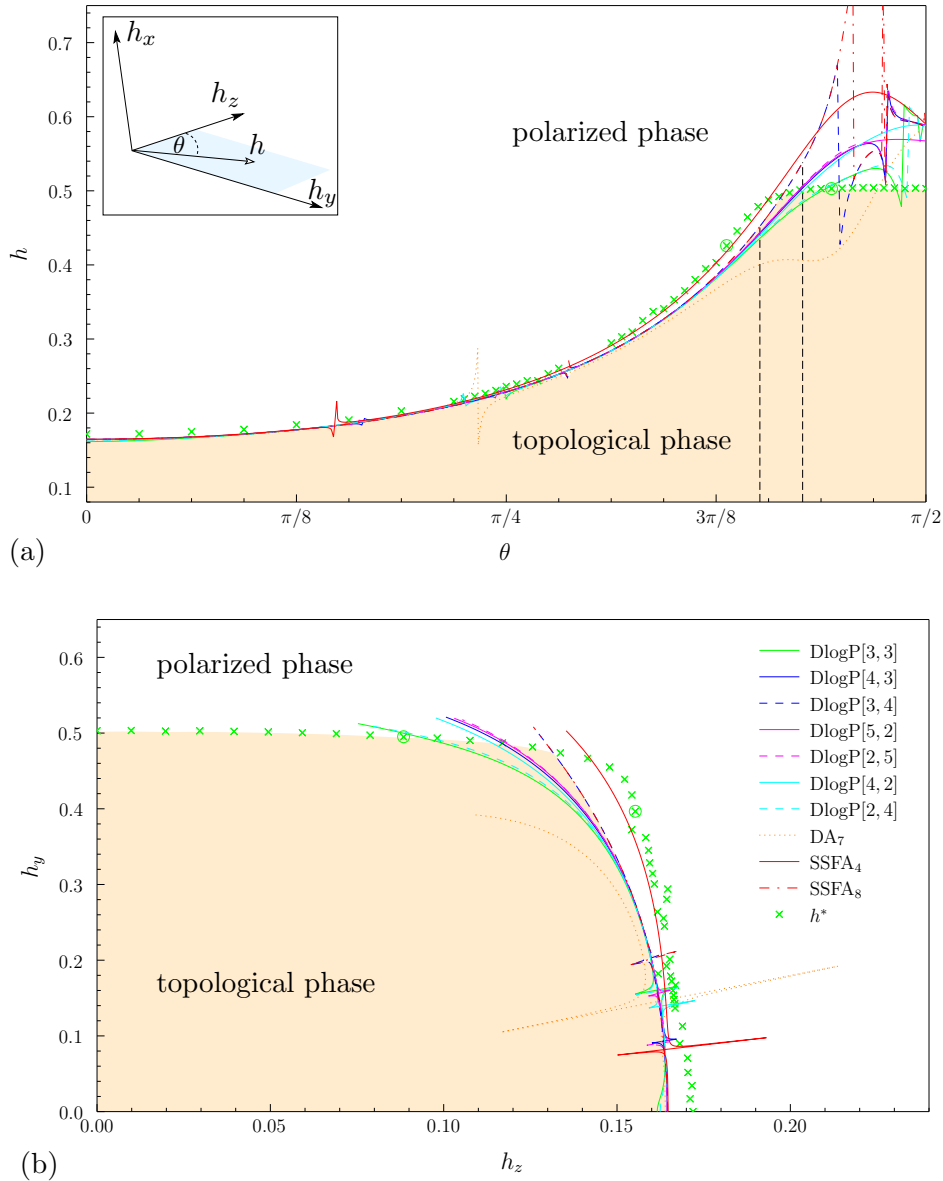


FIGURE 6.12: Phase diagram of the toric code (in polar and Cartesian coordinates) perturbed by the magnetic field $\mathbf{h} = h(0, \sin\theta, \cos\theta)$. (a) As visualized in the inset, we scan the $h_z - h_y$ plane of the three-dimensional orientation of the magnetic field. Colored curves correspond to h_c , computed with extrapolation methods as listed in the legend of (b). Vertical dashed lines at $\theta = 1.26$ and $\theta = 1.34$ delimit an uncertainty region which begins approximately at the point where the value of h_c starts to strongly depend on the extrapolation method (leading to a spreading of the colored curves), and ends where h^* , denoted by a green crosses, become smaller than the predominant subset of h_c 's. The two distinct field directions, discussed in Figure 6.11 are highlighted by encircled crosses. (b) Phase boundary of the topological phase as a function of h_y and h_z . It seems that in the region $0.08 < h_y < 0.2$ most approximants undergo a non-physical divergence.

Now, we perform the same considerations for a fixed $\varphi = \pi/8$ on a plane parallel to the h_y -axis, as shown in the inset of Figure 6.13. We find a very similar picture of the phase diagram, where to the left (right) of the uncertainty region $1.252 < \theta < 1.316$ the system undergoes a second-order (first-order) phase transition. At $\theta < 5\pi/16$, the iPEPS calculations do not yield conclusive results due to numerical problems. However, it is reasonable to assume that close to $\theta = 0$ (or equivalently $h_y = 0$), where the phase transition is known to be of second order, the 'missing' iPEPS points would yield $h_c \lesssim h^*$. This scenario is supported by the behavior of the critical exponents (see Figure 6.16) which do not indicate a phase transition for $\theta < 5\pi/16$, as will be discussed below.

In the preceding section we have given special attention to the symmetry line $h_x = h_z$ (with $h_y = 0$) where the Hamiltonian has an enhanced symmetry. Moreover, both types of elementary excitations, charges as well as fluxes, condense simultaneously so that their non-conventional mutual statistics might become relevant when the system approaches criticality. Indeed, we have shown that while the phase transition of the toric code for $h_x \neq h_z$ is known to be in the universality class of the transverse-field Ising model, the universality class of the phase transition in the distinguished symmetry point is clearly different. Thus, one of the most intriguing questions for the phase diagram of the toric code in a field concerns the transition properties on the symmetry line $h_x = h_z$ and $h_y > 0$. Figure 6.14 reveals the phase diagram on this line for finite h_y . In contrast to the previous cases, the extrapolated h_c are consistently close to each other even beyond the point $\theta = 1.082$, where the nature of the phase transition changes from second order (at $\theta < 1.082$) to first order. Similarly to the phase diagram discussed in Figure 6.13, the minimization procedure of the iPEPS ground-state energy suffers from numerical difficulties around a certain parameter region, where, remarkably, also the series approximants yield non-physical divergences. It seems that in this parameter domain the system is especially difficult to handle. In Figure 6.14 (b), we observe that the first-order transition line at the top of the phase diagram has a linear dependence in h_z (which is equivalent to h_x for the current parametrization) up to the crossing point with the second-order transition line. Thus, instead of an uncertainty region, we are able to give precise coordinates of this crossing point $\mathcal{P}_{\text{crit}} = (0.175, 0.465, 0.175)$.

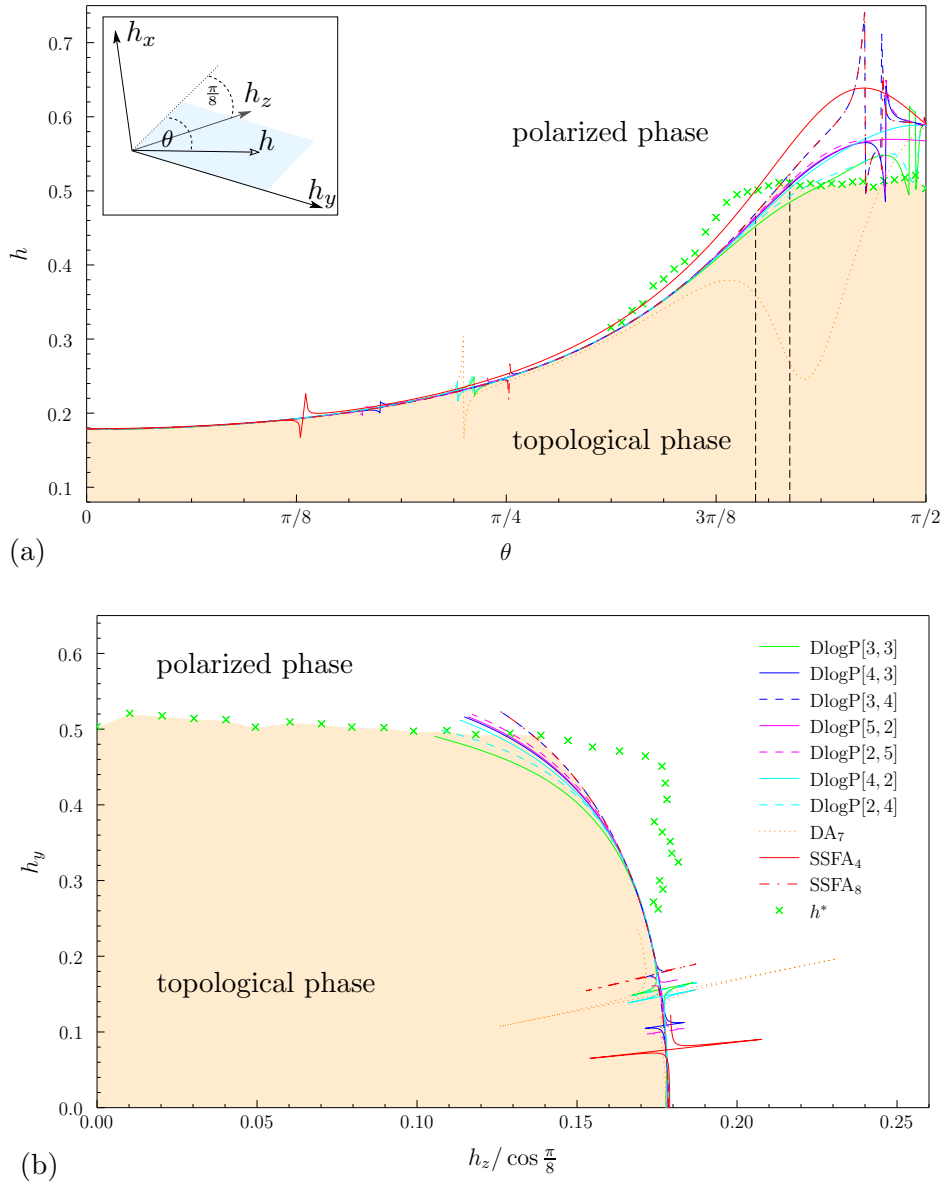


FIGURE 6.13: Phase diagram of the toric code (in polar and Cartesian coordinates) perturbed by the magnetic field $\mathbf{h} = h (\sin \frac{\pi}{8} \cos \theta, \sin \theta, \cos \frac{\pi}{8} \cos \theta)$. (a) The shaded area of the inset corresponds to the investigated parameter range. Colored curves represent h_c , computed with extrapolation methods as listed in the legend in (b). Vertical, dashed lines at $\theta = 1.252$ and $\theta = 1.316$ delimit an uncertainty region which begins approximately at the point where the value of h_c starts to strongly depend on the extrapolation method (leading a spreading of the colored curves) and ends where h^* , denoted by green crosses, become smaller than the predominant subset of h_c 's. (b) Phase boundary of the topological phase as a function of h_x , h_y and h_z , where the horizontal axis corresponds to the bottom of the shaded plane in the inset of (a) (so that $h_x = h_z \tan \pi/8$). It seems that in the region $0.08 < h_y < 0.2$ most approximants undergo a non-physical divergence. Furthermore, in this parameter range the iPEPS method fails to provide reliable results for h^* .

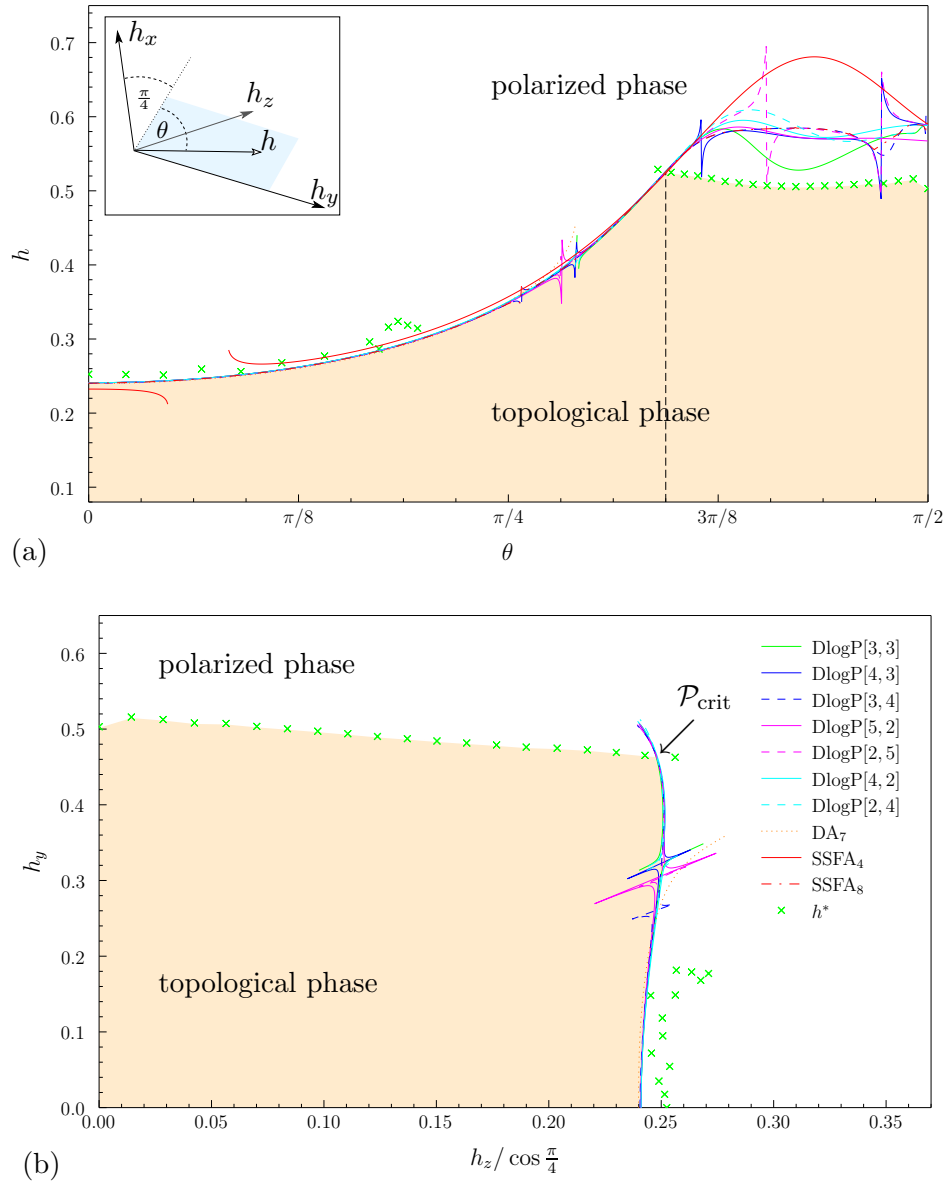


FIGURE 6.14: Phase diagram of the toric code (in polar and Cartesian coordinates) in the magnetic field parametrized by $\mathbf{h} = h (\sin \frac{\pi}{4} \cos \theta, \sin \theta, \cos \frac{\pi}{4} \cos \theta)$. (a) The shaded area of the inset corresponds to the investigated parameter range. Colored curves represent h_c , computed with extrapolation methods as listed in the legend of (b). The vertical dashed line at $\theta = 1.082$ separates two domains of the phase diagram, where the system undergoes a second-order ($\theta < 1.082$) or a first-order ($\theta > 1.082$) phase transitions. (b) Phase boundary of the topological phase as a function of h_x , h_y and h_z , where the horizontal axis corresponds to the bisection of the h_x - h_z -plane. In the region around $h_y = 0.3$, all approximants feature non-physical divergences. In the same parameter range, the iPEPS method fails to provide reliable results for h^* . The crossing point $\mathcal{P}_{\text{crit}}$ of the first-order and the second-order transition lines is highlighted by the arrow.

After the detailed analysis of the phase diagram at three distinct angles φ , we complete this study by performing extrapolations in the intermediate regions, which yields the full phase diagram of the toric code in a uniform magnetic field, presented in Figure 6.15. We find that the first-order transition point at $\mathbf{h} = (0, 1/2, 0)$ belongs to a first-order transition sheet \mathcal{S}_1 , while the well-known second-order transition lines on the h_x - h_z -plane become second-order sheets \mathcal{S}_2 at finite h_y . \mathcal{S}_2 highlights the parameter range where the topologically-ordered phase breaks down, due to the condensation of charge-quasi-particles (in the range $h_z \geq h_x$), or flux-quasi-particles (in the range $h_z \leq h_x$). The sheet \mathcal{S}_1 is rather flat for small parallel magnetic fields so that the h_y -coordinate of the intersection lines (green in Figure 6.15) of the sheets \mathcal{S}_1 and \mathcal{S}_2 is approximately $h_y \approx 0.49$. Due to the large value of the magnetic field, the perturbative expansions are not reliable enough for an accurate estimation of the corresponding h_x and h_z coordinates (see also Figures 6.12-6.13). However, the remarkably converged results on the symmetry line $h_x = h_z$ allow us to determine the precise location of the point $\mathcal{P}_{\text{crit}}$, shown in Figure 6.15.

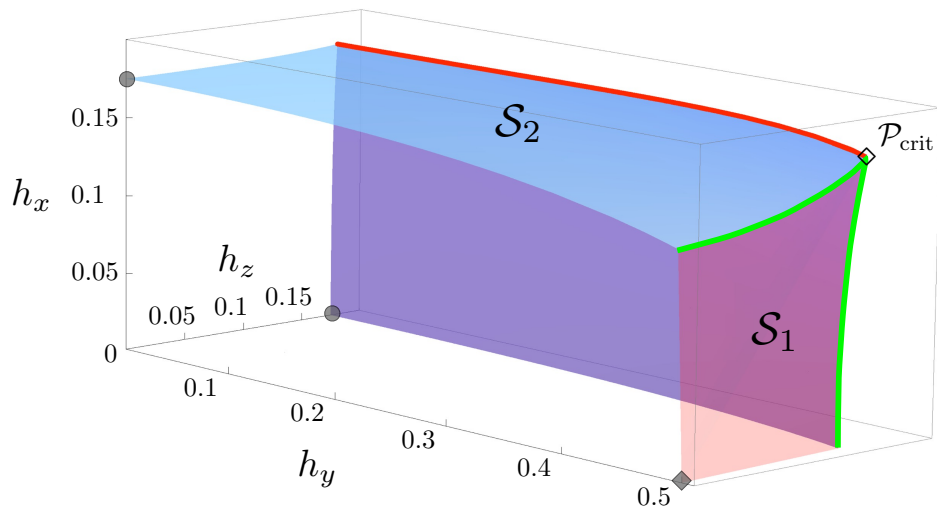


FIGURE 6.15: Sketch of the phase diagram of the toric code in a uniform magnetic field. The topologically-ordered phase is delimited by a first-order transition sheet \mathcal{S}_1 and a second-order transition sheet \mathcal{S}_2 . On the h_x - as well as h_z -axis the model can be mapped onto the transverse-field Ising model, where the location of the second-order phase transition point (denoted by filled circles) is well known. The self-dual point at $\mathbf{h} = (0, 1/2, 0)$ (denoted by a filled rhomb) features a first-order phase transition, as discussed in Ref. [69] (as well as Section 4.3). The intersection lines of \mathcal{S}_1 and \mathcal{S}_2 are pointed out by a green color, while the charge-flux symmetry line with $h_x = h_z$ is colored red. The red line ends at a the point $\mathcal{P}_{\text{crit}}$ at $\mathbf{h} = (0.175, 0.465, 0.175)$ which is highlighted by an empty rhomb.

Let us now consider the critical exponent $z\nu$. In Figure 6.16 we observe that while θ is increased, $z\nu$ stays constant except near the first-order transition domain, where it is not defined. As expected, here the extrapolations from finite series become less

reliable, in accordance with previously obtained results of the critical field. Outside the uncertainty region, defined in Figure 6.12 and Figure 6.13, the system seems to remain in the universality class of the transverse-field Ising model.

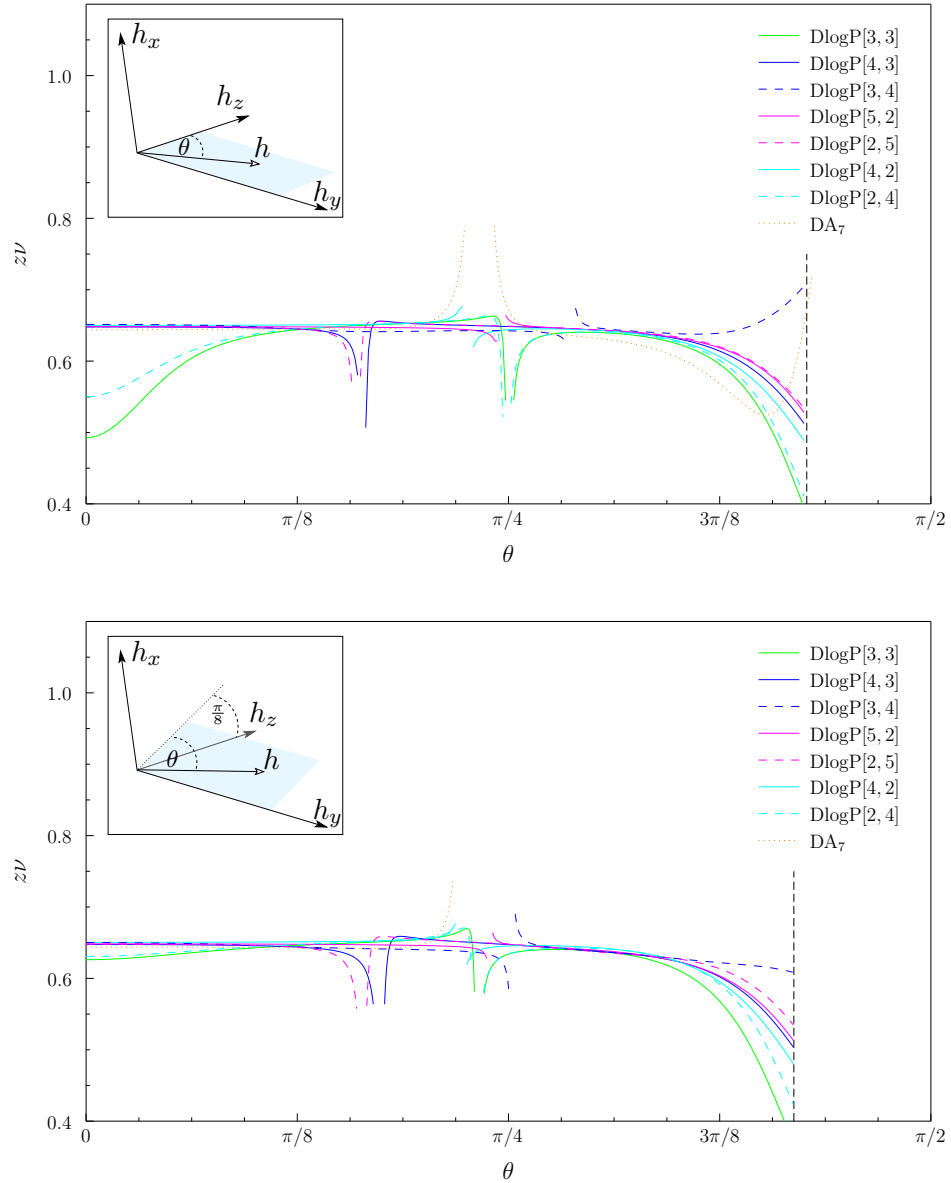


FIGURE 6.16: Critical exponent $z\nu$ for the parameter range highlighted in the top left inset. The vertical dashed line marks the beginning of the first-order phase transition domain, where the low-field expansion fails to describe the correct physics. Besides the non-physical divergences in the range $\pi/8 < \theta < \pi/4$, we observe that $\text{DlogP}[3,3]$ and $\text{DlogP}[2,4]$ vary strongly around $\theta = 0$. Since $\theta = 0$ corresponds to the Ising line, where we already have a precise result (see Table 6.2), the values of $\text{DlogP}[3,3]$ and $\text{DlogP}[2,4]$ in this range must be considered as unphysical. The remaining approximants yield a consistent picture of a constant critical exponent, except near the first-order phase transition domain, where $z\nu$ starts to decrease. This effect, however, becomes weaker for extrapolation of higher orders and probably disappears when very high perturbation orders are taken into account.

Our computation of the dynamical critical exponent z yields, as discussed previously, only a rough estimate. We recall that, on the Ising line, the expected value $z = 1$ is overestimated by almost 30 percent. Nevertheless, Figure 6.17 seems to confirm our observation that, in the considered parametrization, the critical exponents do not depend on θ . As in previous figures, the extrapolations become non-reliable when θ is close the first-order transition domain. Interestingly, the gap exponents on the intersection line of the second-order transition plane and the first-order transition plane might be compatible with the ones of a tricritical 3d-Ising point (where $\nu = 1/2$) [158, 159]. While

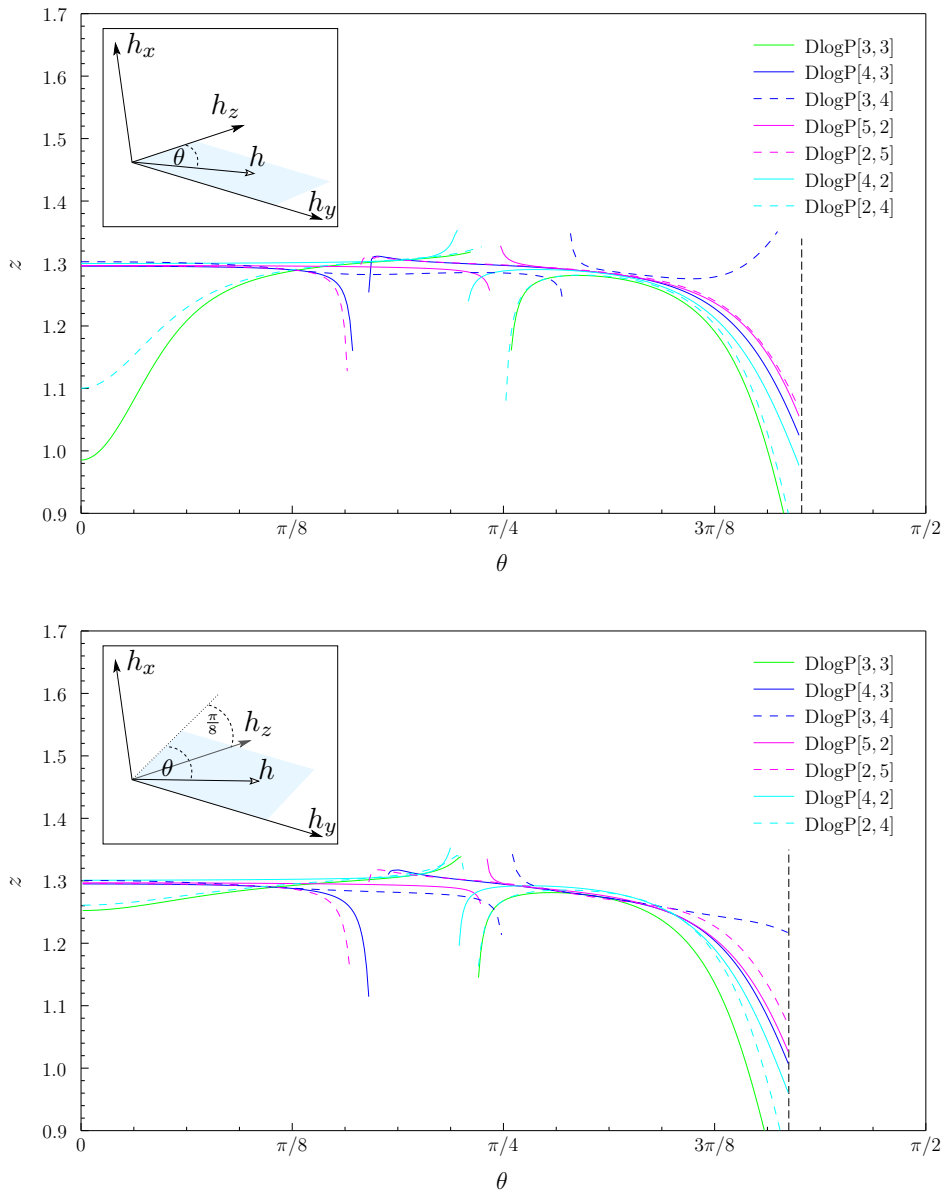


FIGURE 6.17: Critical exponents z for the parameter range highlighted in the top left inset. The vertical dashed line marks the beginning of the first-order phase transition domain. Interestingly, the behavior of $z\nu$ (Figure 6.16), although computed independently, yields to qualitatively same behavior of the approximants.

this remains to be checked, our results from Figure 6.16 and Figure 6.17 tend to support this scenario ($z \approx 1$ and $z\nu \approx 0.5$).

The situation is rather different on the symmetric plane $h_x = h_z$. It is shown in Figure 6.18 that we obtain a continuously increasing $z\nu$ with a maximum precisely around $\theta = 1.08$, which is the location of $\mathcal{P}_{\text{crit}}$. Only for $\theta > 1.08$, where, as we already know, the system undergoes a first-order phase transition *before* the charge (or equivalently the flux) gap vanishes, the approximants start to spread out. This is an additional

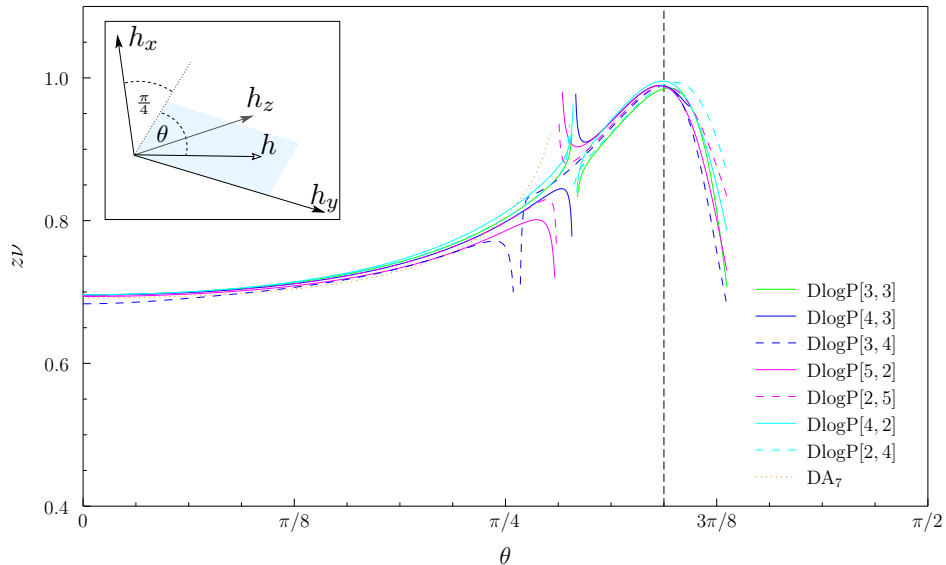


FIGURE 6.18: Critical exponent $z\nu$ on the symmetry plane $h_x = h_z$. Various approximants yield a consistent picture of a continuously varying critical exponent with a maximum at $\mathcal{P}_{\text{crit}}$, denoted by a dashed vertical line. Beyond the critical line, the extrapolations do not have a physical meaning. This is in agreement with the fact that here, at a fixed θ , one obtains strongly varying results depending on the extrapolation.

argument that the validity range of the perturbative expansions ends at $\mathcal{P}_{\text{crit}}$. Note that all approximation methods we have used yield the same continuous increase of the critical exponent with θ . This is very different from the cases $\varphi = 0$ and $\varphi = \pi/8$, shown in Figure 6.16. There, the exponent deviates from its *constant* value only in the parameter domain where the approximants are not reliable anymore (since the results start to depend strongly on the extrapolation method). A continuously varying critical exponent is an interesting feature found only in a few known 2d quantum theories, with prominent examples being the Ashkin-Teller model and the eight-vertex model [160–162]. However, one has to keep in mind that we approximate polynomials of finite order by rational functions. Their residua can, by construction, only be continuous functions of θ . In other words, using only a finite order perturbation theory, our method does not allow to distinguish a continuously varying critical exponent from a scenario where there is a discrete jump. Thus the results shown in Figure 6.18 admit the interpretation that the critical exponent is constantly $z\nu \approx 0.69$ for $\theta > 0$, and discontinuously changes to

$z\nu = 1$ at the point $\mathcal{P}_{\text{crit}}$. Or, alternatively, the jump of the critical exponent could be at an intermediate θ value; for example, close to the point where most of the approximants seem to diverge.

Finally, we compute the dynamical exponent z , shown in Figure 6.19. We recover a similar behavior of a continuously varying critical exponent, or alternatively, a discontinuous change with a jump at the point $\mathcal{P}_{\text{crit}}$. Let us recall that, by construction, our method of computing the dynamical critical exponent is more precise when z is close to 2 rather than to 1 (see Section 6.2). Independently of how the continuous change of the critical exponents is interpreted, we find that the model is in a distinct universality class at the point $\mathcal{P}_{\text{crit}}$, with $z = 2$ and correspondingly $\nu = 1/2$. Interestingly, the toric code is known to feature a so-called conformal quantum critical point [157, 163], with the exotic characteristic that all equal-time correlators in the quantum ground state are equivalent to correlation functions of a local two-dimensional classical model. Even though the relation between the deformed toric code studied in Ref. [157] and the toric code in a magnetic field is not yet clear, $\mathcal{P}_{\text{crit}}$ might be compatible with a conformal quantum critical point in the universality class of a certain limit of the eight-vertex model [157].

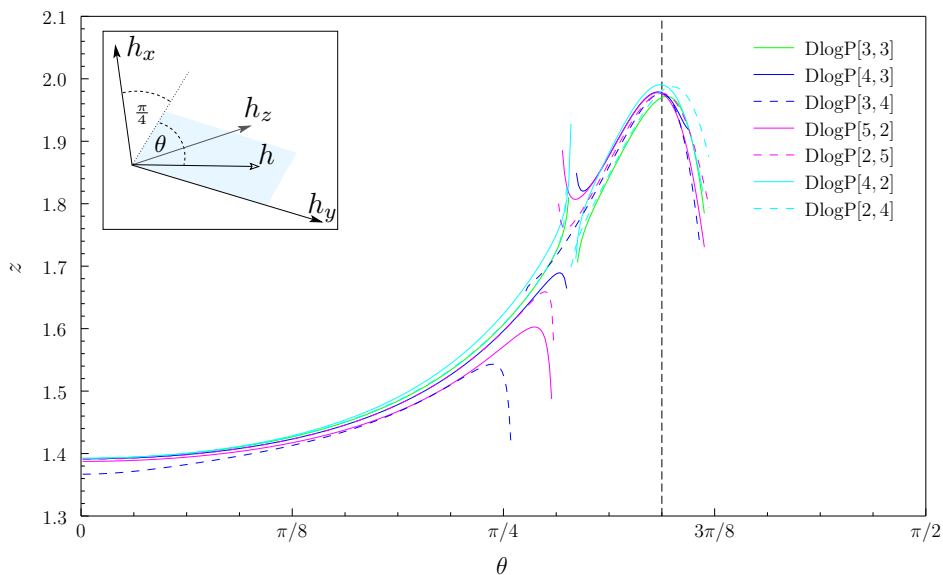


FIGURE 6.19: Critical exponent z on the symmetry plane $h_x = h_z$. Various approximants yield a consistent picture of a continuously varying z with a maximum at $\mathcal{P}_{\text{crit}}$, denoted by a dashed vertical line. The divergences around $\theta = 9\pi/32$ are extrapolation artifacts. Beyond the dashed line, our approximants do not have a physical meaning, which is in agreement with the fact that here, at a fixed θ , one obtains strongly varying results, depending on the extrapolation.

In order to learn more about the fascinating properties of the critical line on the charge-flux symmetry plane $h_z = h_x$, we shall perform series expansions in the opposite limit of high magnetic fields in the following chapter.

6.5 High-field limit

In the limit $J \ll |\mathbf{h}|$, we have computed the ground-state energy and the one-quasi-particle gap up to order 5. For the lengthy expressions, we refer to the Appendix B.3. As has been discussed in Section 5.2, the derivation of an effective model with pCUT is much more challenging in the high-field limit than in the low-field case. Thus the maximally feasible order of perturbative expansions is relatively low. First, we examine the system gap at $\theta = 0$. Following up our discussion on page 69, we regard the vanishing of the one-particle gap Δ_1 as an indicator for a phase transition, only at the critical point $h_x = h_z$. Let us recall that on the Ising line [$\mathbf{h} = (0, 0, h_z)$] the ground state cannot be excited into a single-particle state by any local operator. Consequently, in the effective language of the toric code, the four-particle gap Δ_4 is the relevant one. The perturbative expansion of Δ_4 has been computed using pCUT in Ref. [102] and is in precise agreement with the low-temperature series of the Ising model in a transverse field [122].

$$\Delta_4(\varphi = 0) = 4 - \frac{3}{2}\tilde{J}^2 + \frac{43}{96}\tilde{J}^4, \quad (6.13)$$

$$\Delta_1(\varphi = 0) = 1 + 4\tilde{J} - \frac{1}{2}\tilde{J}^2 + \frac{3}{32}\tilde{J}^4, \quad (6.14)$$

$$\begin{aligned} \Delta_1(\varphi = \pi/4) = & 1 - \tilde{J} - \frac{11}{48}\tilde{J}^2 + \frac{71}{256}\tilde{J}^3 - \frac{1101497}{552960}\tilde{J}^4 + \frac{13570006967}{1300561920}\tilde{J}^5 \\ & - \frac{721074550661327}{16387080192000}\tilde{J}^6 + 175.70719\tilde{J}^7, \end{aligned} \quad (6.15)$$

where we parametrize $\tilde{J} = J/2\tilde{h}_z$ in order to be able to compare with the low-field limit results (where $J = 1/2$). Furthermore, we choose $\tilde{h}_z = \sqrt{h_x^2 + h_y^2 + h_z^2} = 1/2$ so that the energy scale is set to natural units, such that the energy of the unperturbed system is given by the number of excitations. We stress that Δ_1 has been calculated for general angles up to order 5. However, for $\theta = 0$ and $\varphi = 0$ the order 5 contribution is exactly zero [see (6.14)]. Therefore, although higher orders of the polynomial 6.13 are available, they are obsolete in our comparison of Δ_4 and Δ_1 at $\varphi = 0$. At angles $\theta = 0$ and $\varphi = \pi/4$, we were able to push the calculation to higher orders [see (6.15)]. However, due to numerical optimizations, the order 7 coefficient is obtained as a float. Most importantly, on the Ising line ($\varphi = 0$), Δ_4 vanishes at finite \tilde{J} , in contrast to Δ_1 , as shown in Figure 6.20. We observe that, here, the energy of Δ_1 increases with J , obviously due to the linear term which is the direct consequence of two 'frozen' fluxes, created by a single spin flip. While on the symmetry line $\varphi = \pi/4$ (where B_p is not a conserved quantity) the one-particle gap vanishes relatively close to the phase transition point predicted by quantum Monte Carlo simulations [67]. The Padé table (Table 6.8) at $\varphi = \pi/4$ does not show the convergent behavior, we have observed in the low-field limit in the previous chapter.

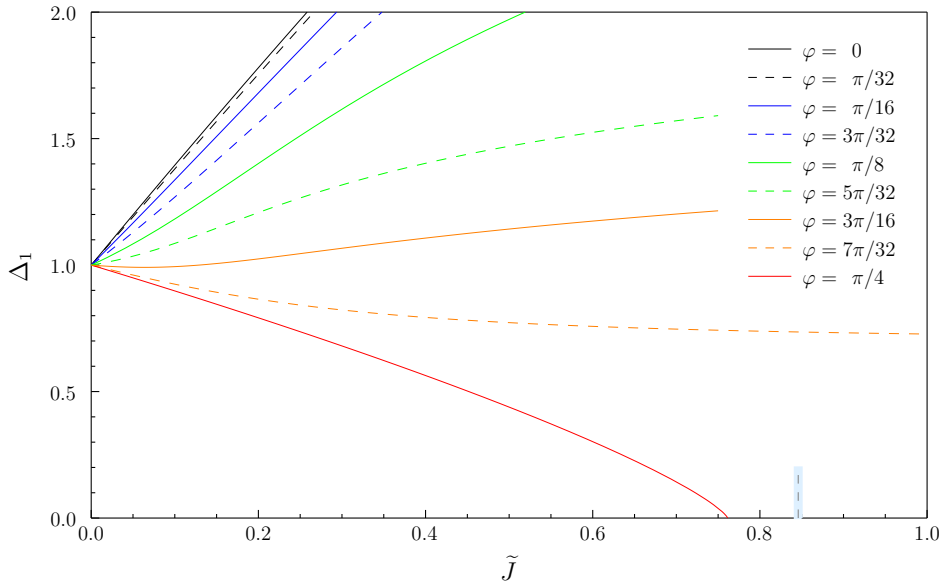


FIGURE 6.20: One-particle gap Δ_1 for $\theta = 0$. Here we show SSFA extrapolations of order 4; however, other extrapolation schemes yield similar results. Δ_1 does not show a tendency to close, except at φ near $\pi/4$. The QMC value of the phase transition point at $\varphi = \pi/4$ is $\tilde{J}_c = 2^{-3/2}/0.418(2) \approx 0.846$, as denoted by a vertical dashed line, where the blue region highlights the error margin. The factor $2^{-3/2}$ accounts for the renormalization of the gap.

$L \setminus M$	1	2	3	4	5
1	0.207397	0.464383	0.477246		0.580899
2	3.67012	0.477746	0.464972		-
3		0.120621	0.346677	-	-
4		2.02746	-	-	-
5		-	-	-	-

TABLE 6.8: DlogPadé approximants $\text{DlogP}[L, M]$ of the critical field for $\theta = 0$ and $\varphi = \pi/4$. Note that, as in the previous tables, cases where the order N series cannot be extrapolated because the condition $L + M \leq N - 1$ is not fulfilled are denoted by '-'. Empty entries indicate that, although an extrapolation exists, no real positive solutions are found. Physically relevant approximants are highlighted by a gray background.

$L \setminus M$	2	3
1	0.774118	0.727404
2	0.724905	0.772795

TABLE 6.9: DlogPadé approximants $\text{DlogP}[L, M]$ of the critical exponent $z\nu$ for $\theta = 0$ and $\varphi = \pi/4$. Here, we show results from the physically meaningful approximants, highlighted in Table 6.8.

In addition to the relatively low order of the series, we find that most approximants do not have poles near the phase transition point $h_c = 0.418(2)$, determined with QMC. The solely four approximants with physically relevant poles, highlighted in Table 6.8, yield an h_c which is 10 to 15 percent off the QMC value. Obviously, we do not reach an adequate precision to estimate critical exponents. As we already saw in the previous sections, the accuracy of the extrapolated critical exponent $z\nu$ is smaller than the one of the critical

field. Nevertheless, we give the corresponding approximants in Table 6.9 which, however, should be taken into account with caution. Integrated differential approximants yield no physical results, while with self-similar approximants (at higher orders) we find poles at precisely the same location as with DlogPadé, this is shown in Table 6.10.

order	2	4	6
h_c	0.515599	0.464383	0.464972
$z\nu$	0.685714	0.776411	0.774984

TABLE 6.10: Critical field h_c and critical exponents $z\nu$, computed with self-similar approximants for $\theta = 0$ and $\varphi = \pi/4$. Interestingly, at order 2 and 4 these approximants are found to be equivalent to DlogP[1,2] and DlogP[2,3], respectively. The corresponding critical exponents are slightly different though.

Even though the high-field expansion does not yield high-precision results, it is interesting to perform a further study, and to see what happens on the plane $\varphi = \pi/4$ for $\theta > 0$, or in other words: how does the endpoint of the first-order line evolve, when the field h_y is switched on? Despite the obvious extrapolation difficulties, we expect to capture at least the qualitative behavior of this unexplored part of the phase diagram. Figure 6.21

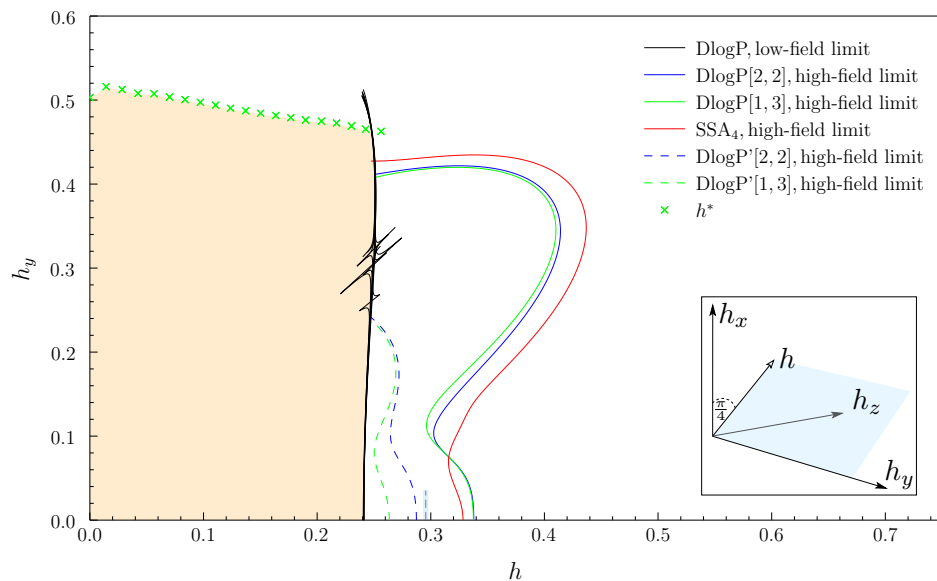


FIGURE 6.21: Phase diagram of the toric code on the $h_x = h_z$ -plane. The boundaries of the topological phase (shaded area) have been computed in the previous chapter. On the horizontal axis it is known that there is a first-order transition line, connecting the boundary of the topological phase to a second-order transition point, highlighted by a vertical gray line. This point has been computed with quantum Monte Carlo simulations in Ref. [67]. In addition to the commonly used series extrapolations, which do not show a conclusive behavior for $h_y > 0.1$, we extrapolate the high-field series using a variable transformation $J = \lambda$, $h = 1 - \lambda$. The resulting series (highlighted by dashed lines) contain the infinite-field limit ($\lambda = 1$), but can be extrapolated around $\lambda = 1/2$. This approach yields directly the critical field in the parameters of the low-field expansion.

shows that indeed the high-field limit approximants cannot reach the accuracy of the low-field limit, studied in the previous chapter. Unfortunately, there are only a few approximants with real and positive poles. Especially at finite h_y the computed critical value of the field depends strongly on the extrapolation method. Although the high-field approximants do not give reliable results, they indicate that the end-point of the first-order phase transition line is likely shifted towards the boundary of the topological phase for $h_y > 0$. This would lead to a mitt-shaped (∇) first-order transition plane. The point where an upper boundary of this plane meets the second-order transition line of the topologically-ordered phase could have a different criticality, then the rest of the line. A possible scenario is that this point is located around $h_y = 0.3$ which appears to be the most difficult point to tackle numerically. But, one can also not exclude the possibility that the end point of the mitt coincides with the point $\mathcal{P}_{\text{crit}}$.

6.6 Chapter summary

In order to investigate the phase diagram of the toric code in a uniform magnetic field, we have joined two distinct methods into a powerful tool to detect phase transitions of first and second orders. While the purely numerical approach (iPEPS) is sensitive to first-order phase transitions, the analytical, perturbative series, obtained with pCUT, are ideally suited to detect continuous phase transitions. This strategy allowed us to determine the precise boundaries of the topological phase of the perturbed toric code. In addition, we were able to make qualitative predictions concerning the structure of the first-order cusp inside the polarized phase, by means of high-field series expansions. In principle, iPEPS is well suited to investigate the precise shape of this cusp. Therefore, this part of the phase diagram might be subject to future studies.

As illustrated in Figure 6.15, the topological phase of the perturbed toric code is bounded by two second-order and one first-order phase transition planes. The second-order planes are adiabatically connected to the Ising points of the model, where the perturbation consists of a single h_z field (or equivalently a single h_x field). The first-order plane is adiabatically connected to the self-dual point, where the perturbation is a single h_y field. Using series resummation techniques, we have computed critical exponents and were able to identify the universality class of the second-order planes to be equivalent to the one of the 3d Ising model. The intersection lines between the first- and second-order planes seem to correspond to tricritical 3d Ising points. Most interestingly, the intersection line of the two second-order transition planes (which is the symmetry line $h_x = h_z$) shows clearly a distinguished critical behavior which supports the idea that on this special line the system is in a separate universality class. This is likely because here the Hamiltonian

has an additional \mathcal{Z}_2 symmetry. Furthermore, the one-quasi-particle gaps of charges and of fluxes are degenerate, consequently both types of particles condense simultaneously and their semionic statistics possibly plays a role at the phase transition point. The intersection point $\mathcal{P}_{\text{crit}}$ of all three planes, just discussed, might be compatible with a conformal quantum critical point which has unusual critical characteristics and is therefore of particular interest. We have determined the precise location of this point and found critical exponents very close to $z = 2$ and $\nu = 1/2$. While we have shown that $\mathcal{P}_{\text{crit}}$ belongs to a different universality class than the multicritical point at $h_x = h_z$ and $h_y = 0$, our study does not allow to clearly decide, whether for intermediate values of the transverse field, the critical exponents vary continuously, or not.

So far, we have considered the zero- and one-quasi-particle subspaces of the effective Hamiltonian. From this study alone, it is not clear whether bound states (of two or more particles) can drive the phase transition for certain directions of the field. A first step to answer this question is the analysis of the two-particle subspace of the toric code in a field, which we perform in the next chapter.

Bound states and spectral properties of the perturbed toric code

In the previous chapter, we have investigated the phase diagram of the toric code in a field by considering the one-quasi-particle subspace of the effective low-energy model. In the present chapter, we analyze the spectrum of the toric code's two-quasi-particle subspace, following up and extending the study in Ref. [69]. We determine specific areas inside the topological phase of the toric code where there are bound states or, in other words, collective states with two interacting particles, energetically favored over a pair of 'free' particles (without interaction). The energy gain is commonly interpreted as a result of an attractive interaction which leads to binding effects. As shall be discussed in detail, the pCUT technique allows to perform a quantitative analysis of the low-energy properties of spectral densities. This are a dynamical structure factors most likely to be measured spectroscopically in a potential experimental realization of the toric code.

7.1 Spectrum of the two-quasi-particle subspace

In Section 5.1, we have discussed how to compute matrix elements of the two-quasi-particle subspace of the effective Hamiltonian H_{eff} . We recall that in the toric code one has to consider two distinct subspaces which in the following shall be denoted by \mathcal{H}^f and \mathcal{H}^b . Here, the indices point out the (bosonic or fermionic) statistics of the particle-pair composite. As we have argued in Section 4.2, charge-flux pairs are fermions while charge-charge and flux-flux pairs are bosons. Note that states with an odd number of charges or fluxes can only be constructed within a system with open boundary conditions. In contrast, the subspace \mathcal{H}^b , which contains only particle pairs of the same type (so either

charge-charge or flux-flux), is compatible with any boundary condition (in addition, the subspace \mathcal{H}^b is particularly relevant for the computation of local observables, as shall be discussed below). Thus, there are two different sets of quantum numbers for the two-particle subspace. While in \mathcal{H}^f , a state is fully characterized¹ by the relative position of the two particles and the position of their center of mass, in \mathcal{H}^b the particle *type* has to be specified in addition. In the limit of small magnetic fields, we compute the two-particle hopping amplitudes $t_{\mathbf{r}', \mathbf{d}', \tau'}^{\mathbf{d}, \tau}$, defined in (5.75), as series in the three field variables h_x , h_y , and h_z up to order 6. One must keep in mind that for a finite perturbation order, there is a maximal distance \mathbf{d}_{\max} below which two particles can directly interact. Beyond \mathbf{d}_{\max} , the remaining matrix elements of $H_{\text{eff}}|_{2\text{qp}}$ can be constructed from one-quasi-particle hopping amplitudes. However, in the charge-flux subspace, where the two particles are *mutual* semions, the sign of the hopping has to be adjusted so that it is consistent with the global string gauge. Since the Hilbert space \mathcal{H}^f is only accessed in a system with open boundary conditions, the two particles are connected to the edge of the system by semi-infinite strings. This means that even if a charge and a flux are very far apart, a hopping in a local region can lead to a sign change of the global wave function. This non-locality is the main difficulty (and interest) of the present work. The hopping amplitudes of particle pairs at distances $|\mathbf{d}| \leq |\mathbf{d}_{\max}|$ are listed in the Appendix B.2.

7.1.1 First steps

Before we investigate the two-quasi-particle spectrum of the perturbed toric code inside the topological phase, there are a few technical remarks to be made. Since the total momentum of a particle pair is a conserved quantity, it is useful to switch to center of mass coordinates with unit vectors $\mathbf{m}_1 = (\mathbf{n}_1 - \mathbf{n}_2)/2$ and $\mathbf{m}_2 = (\mathbf{n}_1 + \mathbf{n}_2)/2$, where \mathbf{n}_i are defined in Figure 5.2. The rhombic structure of the reciprocal lattice allows to limit our considerations to a few symmetry lines connecting the points $\Gamma = (0, 0)$, $\mathbf{X} = (0, \pi)$ and $\mathbf{L} = (\pi/2, \pi/2)$. For a fixed set of field variables h_i and a total momentum \mathbf{K} of a particle pair, we diagonalize a *finite* $n \times n$ -matrix. This corresponds to a finite system where only states $|\mathbf{K}, \mathbf{d}, \tau\rangle$ with $|\mathbf{d}| \leq |\mathbf{d}_m|$ are taken into account. For $\mathbf{d}_m = m\mathbf{n}_1$, the order n of the matrix is a simple function of m

$$n = 2m(m + 1). \quad (7.1)$$

This function can be understood by considering the specific example presented in Figure 7.1. In order to eliminate finite-size effects, we increase n until the energy levels converge up to the third digit, which occurs typically at $n \approx 10^4$. It should be stressed

¹Once again, we follow our convention of the gauge choice, as introduced in Section 5.1.4.

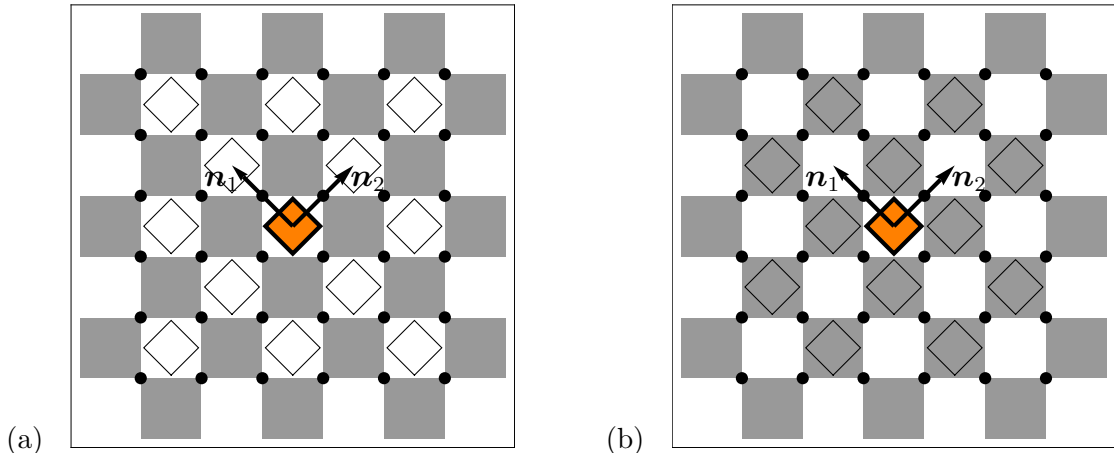


FIGURE 7.1: Examples of possible two-particle distances for $m = 2$ so that one obtains $n = 12$ with (7.1). Without loss of generality, we fix the position of one of the particles (the charge) to the origin. The rhombic contours highlight possible positions of the second particle which must be a charge in the Hilbert space \mathcal{H}^b shown in (a), or a flux in the Hilbert space \mathcal{H}^f shown in (b). Note that in the subspace \mathcal{H}^b particles are indistinguishable so that only one half of the depicted two-particle distances are taken into account in the calculation. However, the factor one half is exactly compensated by the fact that (unlike in \mathcal{H}^f) in \mathcal{H}^b charge pairs can transmute to flux pairs.

that such numerical precision is one of the benefits of the pCUT method which allows to decouple the two-particle sector from the rest of the Hilbert space.

We expect that in a two-particle system where single particles are dispersive the asymptotic behavior leads to a spectrum with a continuous band limited by an upper and a lower band edge $\epsilon_{\text{ub}}(\mathbf{K})$ and $\epsilon_{\text{lb}}(\mathbf{K})$. These can be computed from the single-particle dispersion relations as follows. All energy levels of the two-particle continuum can be obtained from

$$\omega_{\text{cont}}^{\tau\tau'}(\mathbf{K}, \mathbf{q}) = \omega_1^\tau\left(\frac{\mathbf{K}}{2} + \mathbf{q}\right) + \omega_1^{\tau'}\left(\frac{\mathbf{K}}{2} - \mathbf{q}\right), \quad (7.2)$$

where ω_1 is the dispersion of a single particle, \mathbf{q} is the relative momentum and τ the particle type. This definition implies that $\tau = \tau'$ in \mathcal{H}^b and $\tau \neq \tau'$ in \mathcal{H}^f . Energies at the boundaries of the continuum can then be obtained via

$$\epsilon_{\text{ub}}(\mathbf{K}) = \max_{\mathbf{q}} \left[\omega_{\text{cont}}^{\tau\tau'}(\mathbf{K}, \mathbf{q}) \right], \quad (7.3)$$

$$\epsilon_{\text{lb}}(\mathbf{K}) = \min_{\mathbf{q}} \left[\omega_{\text{cont}}^{\tau\tau'}(\mathbf{K}, \mathbf{q}) \right]. \quad (7.4)$$

The one-particle dispersion of a charge and a flux has been computed in the thermodynamic limit up to high orders (see Section 6.1.1), thus we have an additional convergence check of the finite-size diagonalizations.

Let us consider the simple case of a charge-flux pair in a parallel magnetic field ($h_y = 0$), shown in Figure 7.2. For $h_x = 0$ and finite h_z , the flux is 'frozen', which means that its energy distribution in momentum space is constant. Consequently, the boundaries of the continuum do not depend on \mathbf{K} [see Figure 7.2 (a)]. For $h_x > 0$ both particles are dispersive, and the band edges depend on \mathbf{K} as well as on the ratio of h_x and h_z [see Figure 7.2 (b)]. The gap at $\mathbf{K} = (0, 0)$ decreases when the total field strength $|\mathbf{h}|$ is enlarged [see Figure 7.2 (c)]. In the special case of $h_x = h_z$, shown in Figure 7.2 (d), both types of particles have the same dispersion so that boundaries of the continuum are equivalent to the ones obtained for charge-charge (or flux-flux) pairs from the sector \mathcal{H}^b . In the subspace \mathcal{H}^b , the continuum edges do not depend so strongly on the ratio of h_x and h_z , as shall be explained in the following. For $h_z > h_x$, the extremal energies of the continuum must be dominated by charge dispersions because the dependence of the dispersion of a single charge (single flux) on h_z starts at order one (three), while h_x begins to contribute at order three (one) [see (6.2)]. Thus, when h_x is varied the energy of the continuum edges changes in leading order by $4h_z^2 h_x$, which for the parameter range from Figure 7.2 is at most $\approx 10^{-3}$. This energy difference cannot be seen with the naked eye on the scale of Figure 7.2.

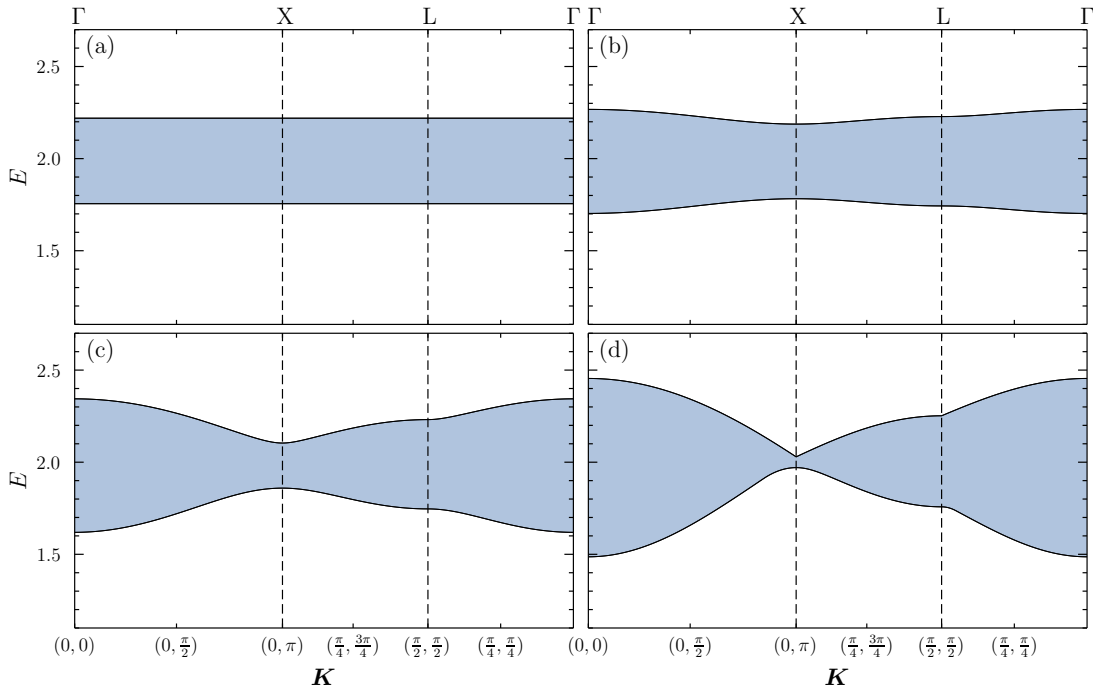


FIGURE 7.2: Synoptic view of the spectrum of the toric code in the two-particle subspace \mathcal{H}^f with $h_y = 0$, $h_z = 0.06$ and (a) $h_x = 0$, (b) $h_x = 0.01$, (c) $h_x = 0.03$, and (d) $h_x = 0.06$.

In the limit $h_x = h_z = 0$ and $h_y > 0$, there is no continuum because single particles are not dispersive. This can be best understood by considering the parity operators $\prod_{i \in \mathcal{C}_1} \sigma_i^y$ and $\prod_{i \in \mathcal{C}_2} \sigma_i^y$, where the \mathcal{C}_1 and \mathcal{C}_2 are contours (referred to as 'diagonal')

and antidiagonal) shown in Figure 4.3 (b). In absence of a parallel field, these parity operators are conserved quantities because they commute with every A_s and B_p , as well as (trivially) with the transverse field. Here, 'parity' refers to the number of flipped spins along each \mathcal{C}_i . Since this number is conserved, we have a strong restriction on the mobility of elementary excitations, e.g., single particles can only hop locally². Similarly, this effect of *dimensional reduction* is also found for two-particles states since the mutual distance of two particles cannot be changed without altering the eigenvalues of the parity operators. As it has been shown in Ref. [69] there are two types of two-particle states. The first type characterizes states, where pairs of particles are positioned in a vertical or horizontal direction. These states have a one-dimensional dispersion since they are mobile only in the spatial direction perpendicular to their relative distance vector. All other two-particle states are not dispersive. In the next step, we will have a closer look at the energy spectrum of the two-particle subspace of the toric code in a transverse field. Moreover, we analyze how the spectrum is influenced by the simultaneous presence of transverse as well as parallel fields.

7.1.2 Bound states in \mathcal{H}^b

Let us begin by considering the subspace \mathcal{H}^b which is of special interest since, as shall be discussed in the following section, it dominates the low-energy physics in a system with periodic boundary conditions. Two-particle states are characterized by distances $\mathbf{d} = p\mathbf{m}_1 + q\mathbf{m}_2$ and shall therefore be labeled by $|\Psi_{pq}^b\rangle$ where the upper index refers to the respective subspace. We find the exact eigenstates $|\Psi_{pq}^b\rangle$, and the corresponding two-particle excitation energies e_{pq}^b , listed in the following.

$$e_{11}^b = 2 \mp h_y - \frac{5}{4}h_y^2 \pm \frac{1}{8}h_y^3 - \frac{353}{192}h_y^4 \pm \frac{1355}{2304}h_y^5 - \frac{247511}{55296}h_y^6, \quad (7.5)$$

$$e_{02}^b = 2 - 2h_y^2(1 \pm \cos k_x) - h_y^4 \left(\frac{1}{48} \mp \frac{1}{2} \cos k_x + \frac{13}{16} \cos 2k_x \right) - h_y^6 \left(\frac{32527}{13824} + \frac{77}{128} \cos 2k_x \pm \frac{871}{1728} \cos 3k_x \pm \frac{167}{1152} \cos k_x \right), \quad (7.6)$$

$$e_{20}^b = 2 - 2h_y^2(1 \pm \cos k_y) - h_y^4 \left(\frac{1}{48} \mp \frac{1}{2} \cos k_y + \frac{13}{16} \cos 2k_y \right) - h_y^6 \left(\frac{32527}{13824} + \frac{77}{128} \cos 2k_y \pm \frac{871}{1728} \cos 3k_y \pm \frac{167}{1152} \cos k_y \right), \quad (7.7)$$

$$e_{04}^b = 2 - 2h_y^2 - h_y^4 \left(\frac{15}{8} \pm 2 \cos k_x \right) - h_y^6 \left(\frac{575}{192} \pm \frac{21}{16} \cos k_x \right), \quad (7.8)$$

$$e_{40}^b = 2 - 2h_y^2 - h_y^4 \left(\frac{15}{8} \pm 2 \cos k_y \right) - h_y^6 \left(\frac{575}{192} \pm \frac{21}{16} \cos k_y \right), \quad (7.9)$$

²As it is common in literature, with 'local hopping' we refer to a zero-momentum hopping, realized through a process, where the final position of a particle corresponds to its initial one. This should not be confused with the definition of 'local' in the context of operators.

$$e_{06}^b = 2 - 2h_y^2 - \frac{15}{8}h_y^4 - h_y^6 \left(\frac{575}{192} \pm 2 \cos k_x \right), \quad (7.10)$$

$$e_{60}^b = 2 - 2h_y^2 - \frac{15}{8}h_y^4 - h_y^6 \left(\frac{575}{192} \pm 2 \cos k_y \right), \quad (7.11)$$

$$e_{22}^b = 2 - 2h_y^2 - h_y^4 \left(\frac{49}{24} \pm \frac{5}{3} \right) - h_y^6 \left(\frac{116851}{27648} \pm \frac{487}{432} \right), \quad (7.12)$$

$$e_{31}^b = 2 - 2h_y^2 \pm h_y^3 - \frac{15}{8}h_y^4 \pm \frac{13}{64}h_y^5 - \frac{122227}{55296}h_y^6, \quad (7.13)$$

$$e_{33}^b = 2 - 2h_y^2 - \frac{15}{8}h_y^4 - \frac{166501}{55296}h_y^6, \quad (7.14)$$

$$e_{52}^b = 2 - 2h_y^2 - \frac{15}{8}h_y^4 \pm h_y^5 - \frac{575}{192}h_y^6, \quad (7.15)$$

$$e_{\text{rest}}^b = 2 - 2h_y^2 - \frac{15}{8}h_y^4 - \frac{575}{192}h_y^6. \quad (7.16)$$

Here we use a symmetrized notation in order to combine energies of symmetric and antisymmetric eigenstates into the same expression. Obviously, more distant particles become dispersive at a higher order, which is clearly a consequence of the local nature of the perturbation. With e_{rest}^b , we denote all remaining eigenenergies in the thermodynamic limit. They are degenerate up to order 6 in a perturbative expansion, but the degeneracy is lifted at higher orders. Our result for the minimal energy of e_{11}^b and e_{20}^b is in agreement with the series expansion in Ref. [69]. The full spectrum is plotted in Figure 7.3 (a), where the lowest-energy branch is two-fold degenerate. The corresponding eigenstates are

$$|\Psi_{11}^b\rangle = \frac{1}{\sqrt{2}} \left(|\mathbf{K}, \mathbf{m}_1 + \mathbf{m}_2, \tau\rangle + i |\mathbf{K}, \mathbf{m}_1 - \mathbf{m}_2, \tau'\rangle \right), \quad (7.17)$$

$$|\Psi_{1-1}^b\rangle = \frac{1}{\sqrt{2}} \left(|\mathbf{K}, \mathbf{m}_1 - \mathbf{m}_2, \tau\rangle + i |\mathbf{K}, \mathbf{m}_1 + \mathbf{m}_2, \tau'\rangle \right). \quad (7.18)$$

Dispersive states with the lowest energies are

$$|\Psi_{20}^b\rangle = \frac{1}{\sqrt{2}} \left(|\mathbf{K}, 2\mathbf{m}_1, \tau\rangle - |\mathbf{K}, 2\mathbf{m}_1, \tau'\rangle \right), \quad (7.19)$$

$$|\Psi_{02}^b\rangle = \frac{1}{\sqrt{2}} \left(|\mathbf{K}, 2\mathbf{m}_2, \tau\rangle - |\mathbf{K}, 2\mathbf{m}_2, \tau'\rangle \right). \quad (7.20)$$

When, in addition to the transverse field, the parallel field is switched on the spectrum develops two significant features, shown in Figure 7.3. Firstly, a continuum evolves around e_{rest} and becomes wider with increasing h_x and h_z , and secondly, there are energy branches *below* the continuum. These energies are associated with collective bound states. The structure of these bound states is more complicated than the one discussed for the case of a pure transverse field because in an arbitrary magnetic field charges and fluxes are dispersive quasi-particles, as shown in Figure 7.4. We point out,

however, that bound states with the lowest energy are the ones connected adiabatically to $\Psi_{1,\pm 1}^b$.

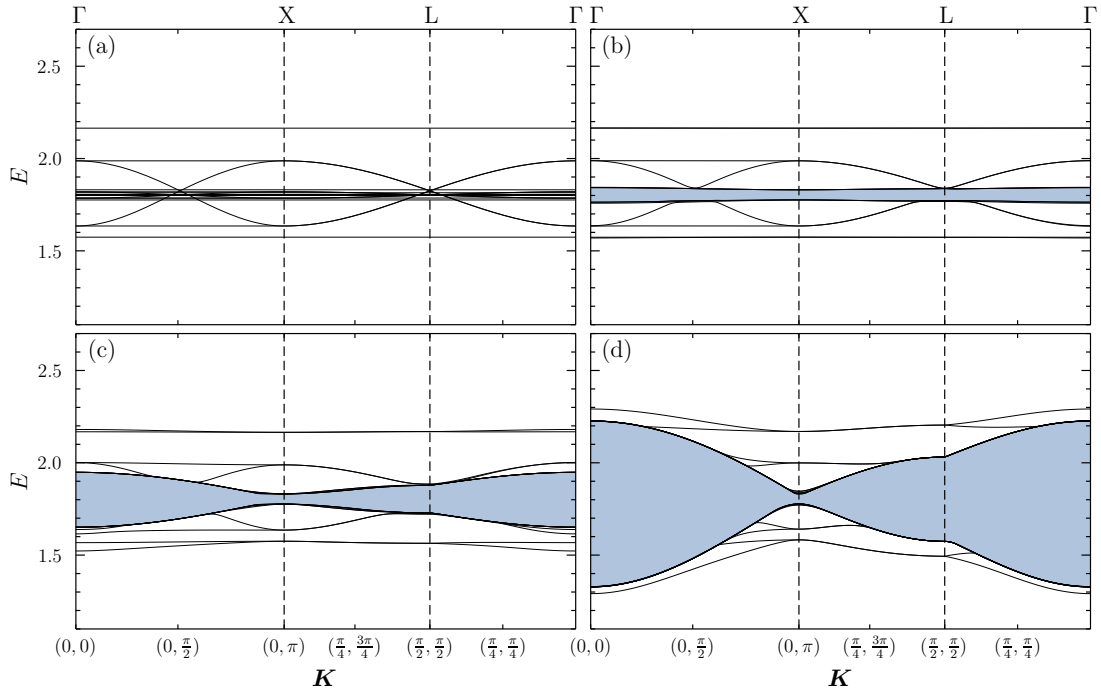


FIGURE 7.3: Synoptic view of the spectrum of the toric code in the two-particle subspace \mathcal{H}^b with $h_y = 0.3$, $h_x = h_z$ and (a) $h_x = 0$, (b) $h_x = 0.005$, (c) $h_x = 0.02$, and (d) $h_x = 0.06$. While (a) shows the analytic functions (7.5)-(7.16), the remaining plots result from numerical diagonalizations.

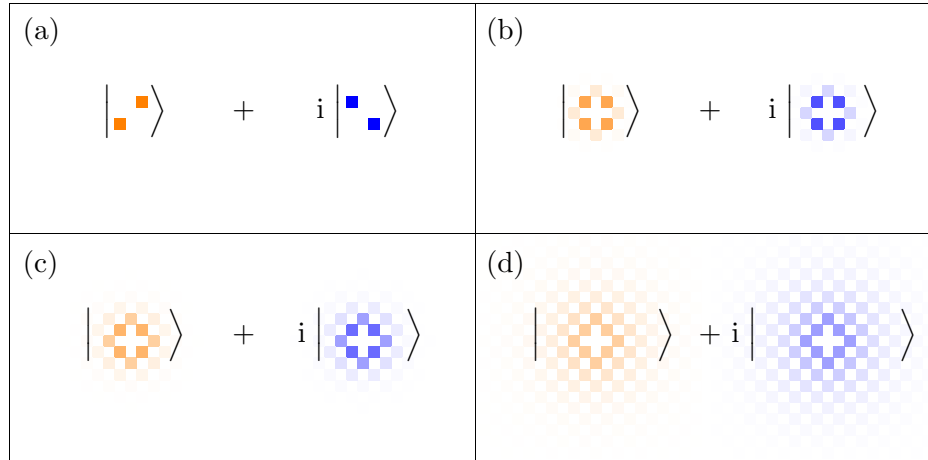


FIGURE 7.4: Wave function of a bound state. We show the real-space representation of the eigenstate with the lowest energy at the Γ -point in absolute values. For overview, the superposition of charge-pairs (orange) is represented by the ket on the left, and, similarly, superpositions of flux-pairs (blue) is shown as a ket on the right of each subfigure. The field parameters are chosen as follows: $h_y = 0.3$, $h_x = h_z$ and (a) $h_x = 0$, (b) $h_x = 0.005$, (c) $h_x = 0.02$, (d) $h_x = 0.06$. While charges and fluxes have unique positions in (a) (in our notation it is the state $|\Psi_{1,1}^b\rangle$), in an additional parallel field, quasi-particles and two-particle states are delocalized in real space.

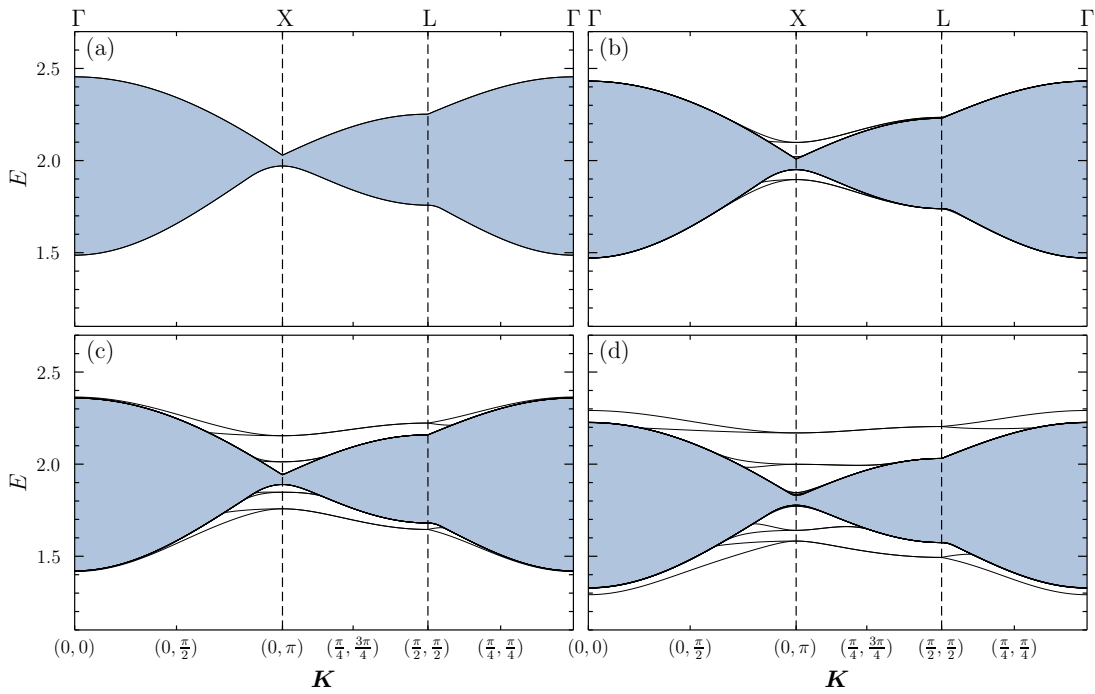


FIGURE 7.5: Synoptic view of the spectrum of the toric code in the two-particle subspace \mathcal{H}^b with $h_x = h_z = 0.06$ and (a) $h_y = 0$, (b) $h_y = 0.1$, (c) $h_y = 0.2$, and (d) $h_y = 0.3$.

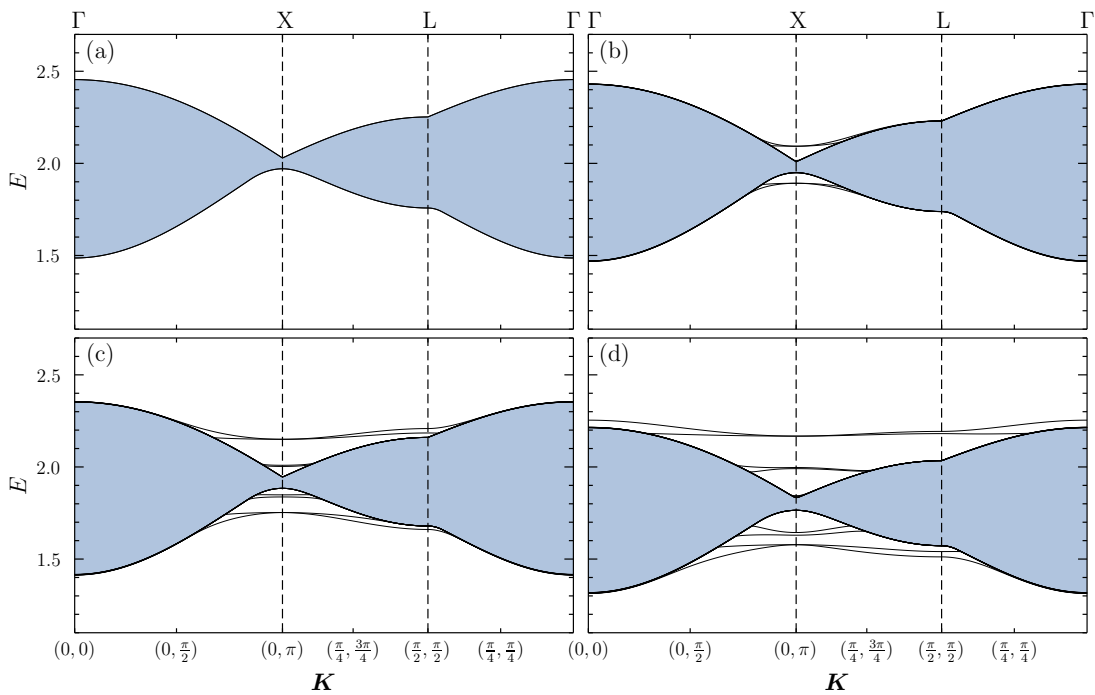


FIGURE 7.6: Synoptic view of the spectrum of the toric code in the two-particle subspace \mathcal{H}^b with $h_x = 0$, $h_z = 0.06$ and (a) $h_y = 0$, (b) $h_y = 0.1$, (c) $h_y = 0.2$, and (d) $h_y = 0.3$.

To give an idea about how the spectrum depends on the direction of the magnetic field, we fix the value of the parallel field strength and compute the spectrum at different h_y values. As it is shown in Figure 7.5 and Figure 7.6, the continuum is hardly affected by the transverse field. Because, as can be verified from the single-particle dispersion in (6.2), the transverse field starts to contribute to a hopping of a single particle only at order two. Therefore, its effect on the boundaries of the continuum is an order of magnitude below the one of the parallel field. On the contrary, the transverse field has a much stronger effect on the bound states (and also antibound states, above the continuum), e.g., two neighboring particles can interact already in order one. If two particles are not adjacent, then the leading-order difference to non-interacting single particles is an order two contribution to the local hopping by the operator $T_{-2}T_{+2}$ (see the effective action of σ_y in Table 5.2). Furthermore, we observe that changing the ratio h_x/h_z , lifts some degeneracies of the low-energy modes (for example between the X- and Γ -points). Setting h_x to zero eliminates certain interaction terms. Therefore bound states have lower energies at $h_x > 0$, as can be clearly observed, for example, at the Γ -point in Figure 7.5 (d) and in Figure 7.6 (d).

7.1.3 Bound states in \mathcal{H}^f

Similarly to the previous subsection, we have computed the series expansions of two-quasi-particle excitation energies in the subspace \mathcal{H}^f , for $h_x = h_z = 0$.

$$\begin{aligned}
e_{01}^f &= 2 \pm 2h_y \sin k_x + \frac{1}{2}h_y^2 (\cos 2k_x - 1) \mp \frac{1}{4}h_y^3 (\sin 3k_x + 2 \sin k_x) \\
&\quad - h_y^4 \left(\frac{109}{96} - \frac{1}{8} \cos 2k_x + \frac{5}{32} \cos 4k_x \right) \\
&\quad - h_y^5 \left(\pm \frac{1379}{1152} \sin k_x \pm \frac{121}{576} \sin 3k_x - \frac{7}{64} \sin 5k_x \right) \\
&\quad - h_y^6 \left(\frac{6337}{2304} - \frac{289}{864} \cos 2k_x + \frac{425}{3456} \cos 4k_x - \frac{21}{256} \cos 6k_x \right), \quad (7.21)
\end{aligned}$$

$$\begin{aligned}
e_{10}^f &= 2 \pm 2h_y \sin k_y + \frac{1}{2}h_y^2 (\cos 2k_y - 1) \mp \frac{1}{4}h_y^3 (\sin 3k_y + 2 \sin k_y) \\
&\quad - h_y^4 \left(\frac{109}{96} - \frac{1}{8} \cos 2k_y + \frac{5}{32} \cos 4k_y \right) \\
&\quad - h_y^5 \left(\pm \frac{1379}{1152} \sin k_y \pm \frac{121}{576} \sin 3k_y - \frac{7}{64} \sin 5k_y \right) \\
&\quad - h_y^6 \left(\frac{6337}{2304} - \frac{289}{864} \cos 2k_y + \frac{425}{3456} \cos 4k_y - \frac{21}{256} \cos 6k_y \right), \quad (7.22)
\end{aligned}$$

$$\begin{aligned}
e_{03}^f &= 2 - 2h_y^2 \pm 2h_y^3 \sin k_x - \frac{15}{8}h_y^4 \pm \frac{13}{32}h_y^5 \sin k_x \\
&\quad + h_y^6 \left(\frac{1523}{1024} \cos 2k_x - \frac{12071}{13824} \right), \quad (7.23)
\end{aligned}$$

$$e_{30}^f = 2 - 2h_y^2 \pm 2h_y^3 \sin k_y - \frac{15}{8}h_y^4 \pm \frac{13}{32}h_y^5 \sin k_y + h_y^6 \left(\frac{1523}{1024} \cos 2k_y - \frac{12071}{13824} \right), \quad (7.24)$$

$$e_{05}^f = 2 - 2h_y^2 - \frac{15}{8}h_y^4 \pm 2h_y^5 \sin k_x - \frac{575}{192}h_y^6, \quad (7.25)$$

$$e_{50}^f = 2 - 2h_y^2 - \frac{15}{8}h_y^4 \pm 2h_y^5 \sin k_y - \frac{575}{192}h_y^6, \quad (7.26)$$

$$e_{21}^f = 2 - h_y^2 (2 \pm 1) - h_y^4 \left(\frac{107}{96} \mp \frac{1}{4} \right) - h_y^6 \left(\frac{33295}{9216} \pm \frac{35}{36} \right), \quad (7.27)$$

$$e_{41}^f = 2 - 2h_y^2 - h_y^4 \left(\frac{15}{8} \pm 1 \right) - h_y^6 \left(\frac{575}{192} \pm \frac{21}{32} \right), \quad (7.28)$$

$$e_{61}^f = 2 - 2h_y^2 - \frac{15}{8}h_y^4 - h_y^6 \left(\frac{575}{192} \pm 1 \right), \quad (7.29)$$

$$e_{32}^f = 2 - 2h_y^2 - \frac{15}{8}h_y^4 - h_y^6 \left(\frac{90893}{27648} \pm \frac{16181}{6912} \right), \quad (7.30)$$

$$e_{\text{rest}}^f = 2 - 2h_y^2 - \frac{15}{8}h_y^4 - \frac{575}{192}h_y^6. \quad (7.31)$$

As in (7.5), we use a short notation to denote energies of symmetric as well as antisymmetric states with the same expression. In contrast to the previously discussed two-particle sector \mathcal{H}^b , the lowest-energy modes are dispersive. We find their exact expressions to be

$$|\Psi_{10}^f\rangle = \frac{1}{\sqrt{2}} \left(|\mathbf{K}, \mathbf{m}_1, \tau\rangle - |\mathbf{K}, -\mathbf{m}_1, \tau'\rangle \right), \quad (7.32)$$

$$|\Psi_{01}^f\rangle = \frac{1}{\sqrt{2}} \left(|\mathbf{K}, \mathbf{m}_2, \tau\rangle - |\mathbf{K}, -\mathbf{m}_2, \tau'\rangle \right). \quad (7.33)$$

These are two-particles states, where a charge and a flux are direct neighbors and can therefore hop together already in order one (as can be easily verified in Table 5.2). All other modes feature momentum dependence exclusively at even orders in perturbation. Once again, we are able to check that the series expansion of e_{01}^f at its minimum is in agreement with the gap computed in Ref. [69]. The minimal energy is found at $\mathbf{K} = (0, \pi/2), (\pi/2, 0)$ and $(\pi/2, \pi/2)$, see also Figure 7.7 (a). The lowest non-dispersive energy mode is four-fold degenerate

$$|\Psi_{2\pm 1}^f\rangle = \frac{1}{\sqrt{2}} \left(|\mathbf{K}, \pm 2\mathbf{m}_1 \pm \mathbf{m}_2, \tau\rangle \pm |\mathbf{K}, -2\mathbf{m}_1 \pm \mathbf{m}_2, \tau'\rangle \right), \quad (7.34)$$

$$|\Psi_{\pm 12}^f\rangle = \frac{1}{\sqrt{2}} \left(|\mathbf{K}, \pm \mathbf{m}_1 - 2\mathbf{m}_2, \tau\rangle \pm |\mathbf{K}, \pm \mathbf{m}_1 + 2\mathbf{m}_2, \tau'\rangle \right). \quad (7.35)$$

We observe that, as in the previous discussion, a continuum is present for a finite parallel magnetic field. However, a major difference here is that the total gap of the system is not necessarily at the Γ -point. The momentum \mathbf{K} which minimizes the energy rather depends on the amplitude of the perturbation.

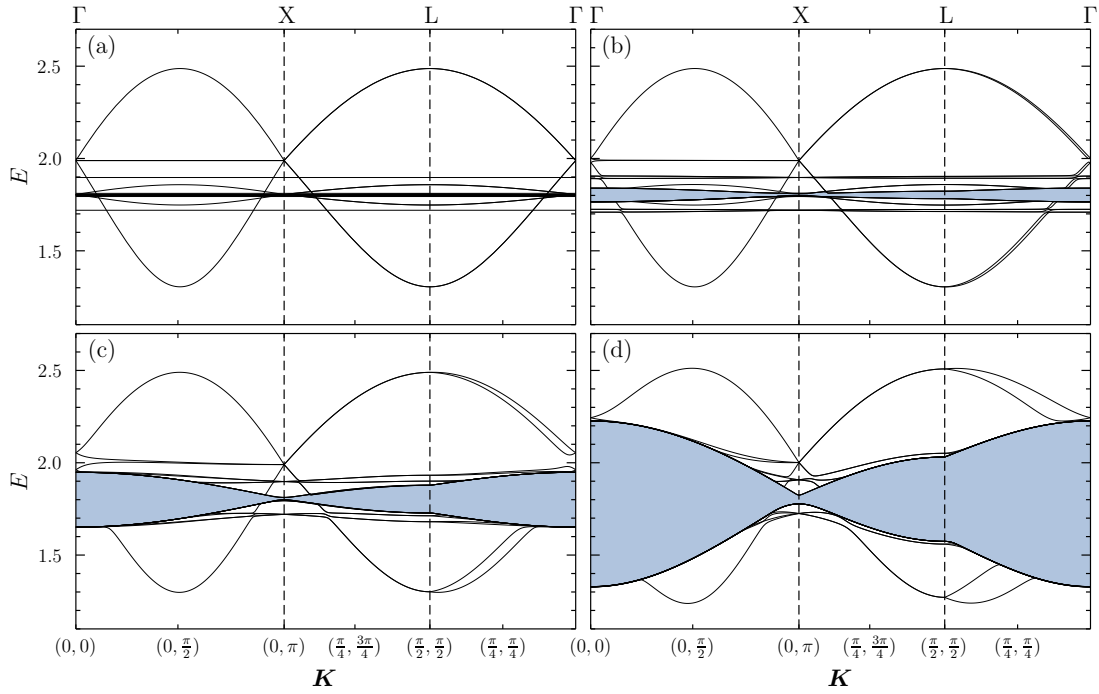


FIGURE 7.7: Synoptic view of the spectrum of the toric code in the two-particle subspace \mathcal{H}^f with $h_y = 0.3$, $h_x = h_z$ and (a) $h_x = 0$, (b) $h_x = 0.005$, (c) $h_x = 0.02$, and (d) $h_x = 0.06$. While (a) shows the analytic functions (7.21)-(7.31), the remaining plots result from numerical diagonalizations.

Now, let us consider the effect of the transverse magnetic field, when the strength of the parallel field is fixed (see Figure 7.8 and Figure 7.9). We observe the same mechanism as in the subspace \mathcal{H}^b . Bound states arise with increasing h_y , while the continuum boundaries hardly depend on the transverse field. It is, however, a peculiarity of the charge-flux subspace that the spectrum heavily depends on the h_x/h_z -ratio. We find that in any case, bound states with the lowest energy are the ones adiabatically connected to $|\Psi_{01}^f\rangle$ and $|\Psi_{10}^f\rangle$.

An important question is whether bound states can close the gap inside the boundaries of the topological phase, computed in Chapter 6, and drive the transition in this case. We recall that the phase boundaries were determined by considering the one-particle sector of H_{eff} , where, by definition, no binding effects are present. However, we argue that a crossing between a two-quasi-particle bound-state energy level and the energy of a single-particle mode, inside the topological phase is unlikely. As it is shown in Figure 7.5 and Figure 7.8, even at relatively large magnetic fields, the lowest energy of the two-quasi-particle subspace are clearly above the one-particle gap at zero field ($E = 1$). A numerical diagonalization of the two-quasi-particle sector much closer on the phase boundary is challenging because in contrast to the one-quasi-particle calculation, one cannot extrapolate via Padé approximations. Still, our numerics suggest that higher-order corrections would not be sufficient for a condensation of bound states to occur before the one-particle gap has vanished.

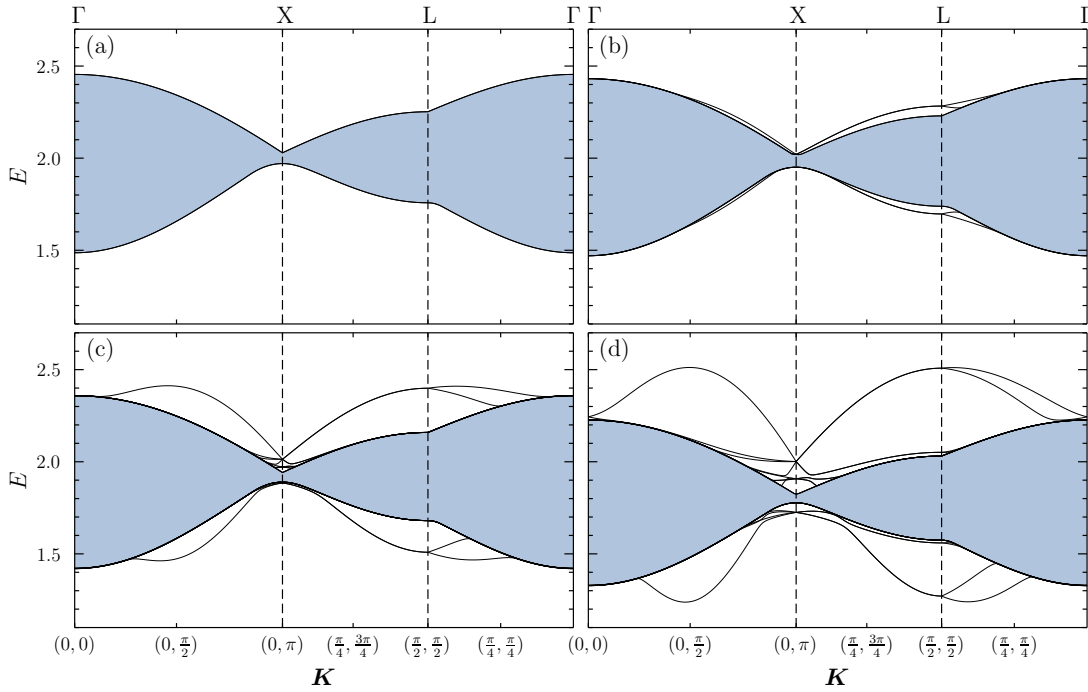


FIGURE 7.8: Synoptic view of the spectrum of the toric code in the two-particle subspace \mathcal{H}^f with $h_x = h_z = 0.06$ and (a) $h_y = 0$, (b) $h_y = 0.1$, (c) $h_y = 0.2$, and (d) $h_y = 0.3$.

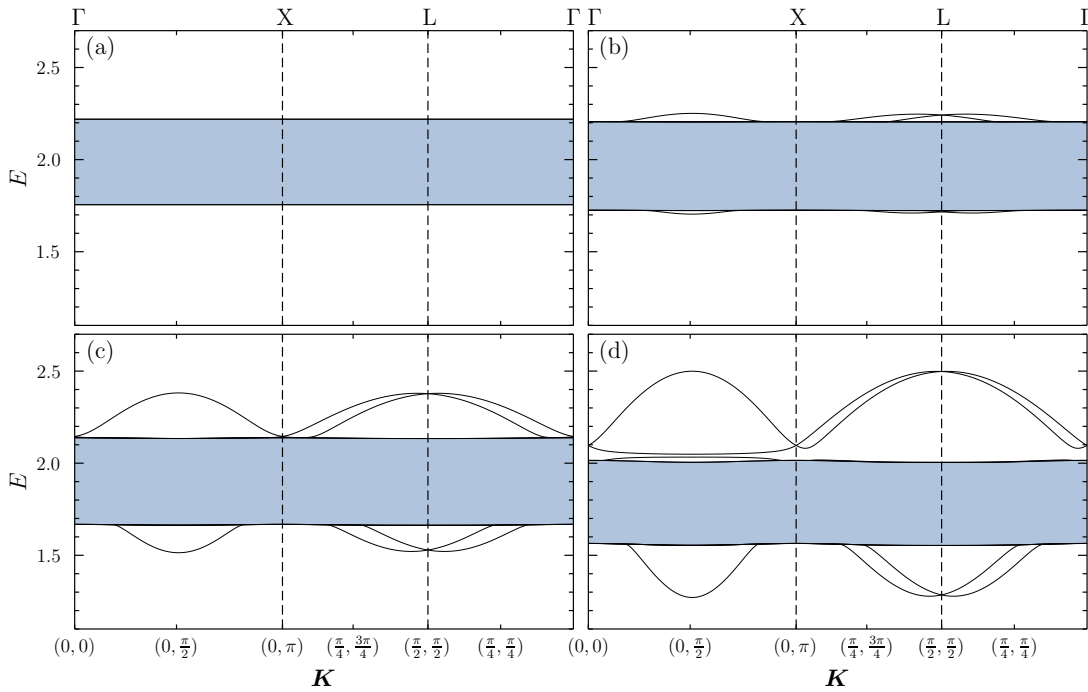


FIGURE 7.9: Synoptic view of the spectrum of the toric code in the two-particle subspace \mathcal{H}^f with $h_x = 0$, $h_z = 0.06$ and (a) $h_y = 0$, (b) $h_y = 0.1$, (c) $h_y = 0.2$, and (d) $h_y = 0.3$. Note that the edges of the continuum band in (b)-(c) have a weak dispersion. The reason is that the frozen flux becomes dispersive at order 4 in h_y , an effect only sufficiently pronounced in (d), where h_y is large.

7.2 Density of states

So far, the density of states [to be denoted as $D(E)$ in the following] in the toric code model has been an unstudied issue. Beside being an interesting topic in itself, $D(E)$ as well as its dependence on the magnetic field, should play a major role in understanding certain features of the spectral densities to be discussed in the next section. As we recall, the two-particle subspace of the toric code can be divided into a fermionic and a bosonic channels. We are interested to observe the differences as well as similarities of the density of states in these two sectors. Furthermore, we will try to understand certain features of the momentum dependence of $D(E)$ by using one-particle properties, first for conceptual clarity, and second as a check of the numerical results with analytical series.

7.2.1 Subspace \mathcal{H}^b

As has been discussed in Chapter 4, elementary excitations of the toric code with periodic boundary conditions are two-particle states where both particles have the same flavor. Therefore the subspace \mathcal{H}^b , where charges and fluxes only appear in pairs, is of specific interest. Using the energy spectra calculated in the previous section we compute the density of states $D(E) \propto N(E + \delta E)$, where $N(E + \delta E)$ is the number of energy levels inside the energy interval $[E + \delta E]$.

In order to understand some distinct features of $D(E)$, let us begin by considering the dispersion of a single charge in the center of mass coordinate system. With (6.2) and $\mathbf{K} = (K_x, K_y)$, the expression at order one reads

$$\omega(\mathbf{K}) = 1 - 2h_z [\cos(K_x + K_y) + \cos(K_x - K_y)], \quad (7.36)$$

as can also be derived from the hopping elements $t_{1,0} = t_{0,1}$ given in the Appendix B.1. Using (7.2), we find the energy of a two-particle mode at order one to be

$$\omega_{\text{cont}}^b(\mathbf{K}, \mathbf{q}) = 2 - 8h_z \left(\cos \frac{K_x}{2} \cos \frac{K_y}{2} \cos q_x \cos q_y + \sin \frac{K_x}{2} \sin \frac{K_y}{2} \sin q_x \sin q_y \right), \quad (7.37)$$

where $\mathbf{q} = (q_x, q_y)$, is the relative momentum of the two particles. For any \mathbf{K} , $q_x = n\pi$, and $q_y = m\pi$ with $(n, m) \in \mathbb{N}^2$, this function is minimized by $n - m \in \mathbb{N}_{\text{even}}$, and has a maximum at $n - m \in \mathbb{N}_{\text{odd}}$. The corresponding energy levels are thus exactly the boundaries of the two-particle continuum at order one. Obviously, the energy of the system is minimized (maximized) for relative momenta, where *each* particle is at its energetic minimum (maximum) according to the single-particle dispersion. We point out

that this somewhat trivial statement is only valid at order one in perturbation theory. Higher-order corrections involve antisymmetric terms in the single-particle dispersion so that, generally, the momenta of the two particles at the extremal energies of the continuum do not necessarily correspond to the ones at the minimum (or maximum) of the single-particle dispersion. Besides the minimum and the maximum, the dispersion of a single charge features a saddle point. As we shall see below, for a constant \mathbf{K} , $D(E)$ is maximal, when both particles are at a saddle point of their dispersion because here $\omega_{\text{cont}}^{\text{b}}(\mathbf{K}, \mathbf{q})$ is locally flat. This is realized when the relative momentum is $\mathbf{q} = 1/2(n\pi, m\pi)$. Note that due to rotational symmetry, there are actually two distinct saddle points, identified by whether $n - m$ is even or odd. This behavior is qualitatively similar to what is known for certain spin-ladder models [87, 95, 164, 165].

In Figure 7.10, we consider the density of states computed at order six on the 'Ising'-line of the toric code, as well as characteristic two-particle modes with relative momentum $\mathbf{q} = (q_x, q_y)$ and eigenenergy $E(\mathbf{K}, \mathbf{q})$ (see Subsection 7.1.1 for notation). As expected, we find maxima of $D(E)$ at momenta, where the two-particle continuum is flat. However, as already anticipated, in contrast to order one, the energy of the two-particle continuum is not necessary minimized for the relative momentum $\mathbf{q} = (0, 0)$, e.g., at $\mathbf{K} = (0, \pi)$ the energy minimum is obtained for $\mathbf{q} = (0, \pi/2)$. Furthermore, we observe a constant, sharp maximum of $D(E)$ at the energy $E = 2$. These are the energies of flux-pairs which are frozen out on the 'Ising'-line. This means that the flux-pairs are non-dispersive and cannot lower their energy, due to the field. Consequently, their $D(E)$ is a delta function at the two-particle creation energy.

How is the density of states affected by finite h_x and h_y fields, moving away from the 'Ising'-line? In Figure 7.11 we present our results based on the spectra computed in the previous chapter. Once again, these numerical results are in agreement with the continuum boundaries, calculated from series expansions of the single-particle dispersions. First, let us consider the effect of a finite h_x field (keeping $h_y = 0$) shown in Figure 7.11 (a)-(b). For $h_x > 0$, the flux-pairs become dispersive and for $h_x < h_z$ we observe two overlapping structures, each one similar to the one shown in Figure 7.10. As long as the transverse magnetic field is zero, there is no matrix element connecting the subspace of charge pairs with the subspace of flux pairs. Thus, one can consider $D(E)$ of charge-pairs, as well as flux-pairs separately. There is an obvious symmetry between the density of states of these two subspaces. This is the consequence of the fact that the one-quasi-particle dispersions a charge and a flux are related by the exchange of h_x - and h_z -variables. The range of the spectrum (the difference between the maximal and minimal energy), as well as the position of the maxima of the density of states are proportional to the ratio h_z/h_x for charges and to h_x/h_z for fluxes. Once again, we find the local maxima of $D(E)$ for two-particle modes with relative momenta as in Figure 7.10.

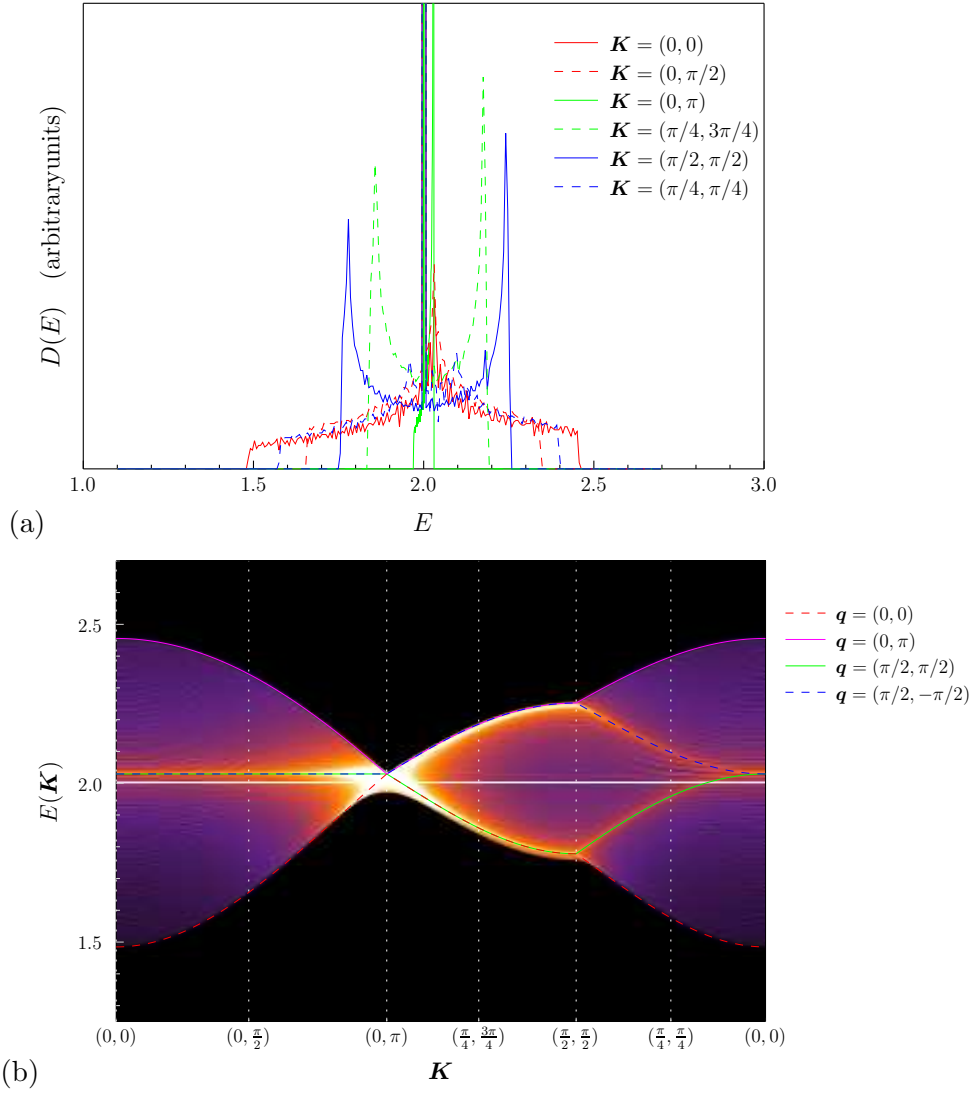


FIGURE 7.10: Density of states $D(E)$ at the 'Ising'-line of the toric code. These results have been obtained at order 6 perturbation theory for the toric code in the magnetic field $\mathbf{h} = (h_x, h_y, h_z) = (0, 0, 0.06)$. $D(E)$ is a function of energy E and momentum \mathbf{K} . We have used energy intervals of $\delta E = 0.006$, to determine $D(E)$. The noisy structures for low $D(E)$ are due to the finite size of the diagonalized matrix. (a) Density of states for certain fixed values of \mathbf{K} . (b) Alternative illustration of $D(E)$, where \mathbf{K} is varied along the symmetry lines of the Brillouin zone. The amplitude of $D(E)$ is indicated by the color gradient, where dark (bright) colors stand for low (high) density. The fixed \mathbf{K} -values from (a) are highlighted by vertical dotted lines. Significant modes of the two-particle continuum where \mathbf{q} refers to the relative momentum of a particle pair, are represented by colored lines.

However, here one must consider two-charge modes as well as two-flux modes. When $h_x = h_z$ [Figure 7.11 (b)], the dispersions of charges and fluxes are equivalent and we obtain a similar plot as in Figure 7.10, except that here, there is obviously no distinctive maximum at $E = 2$ because both types of particles are dispersive.

When in addition to the parallel field, a transverse field is switched on, one expects to find bound states, as has been demonstrated in the previous chapter. However, since the number of two-particle modes in the interval δE inside the two-particle continuum is extensively larger than the degeneracy of the discrete bound states, the density of bound states is too small to be visible in our illustrations. The most pronounced effect of the transverse field on the two-particle continuum is a global shift to lower energies while the local minima and maxima of $D(E)$ are hardly affected. The strong, almost constant peak of $D(E)$ in Figure 7.11 (c), at approximately $E \approx 1.8$, appears because a finite transverse field introduces a small dispersion to the otherwise 'frozen' fluxes so that the sharp peak observed in Figure 7.10 is slightly broadened for certain \mathbf{K} -values.

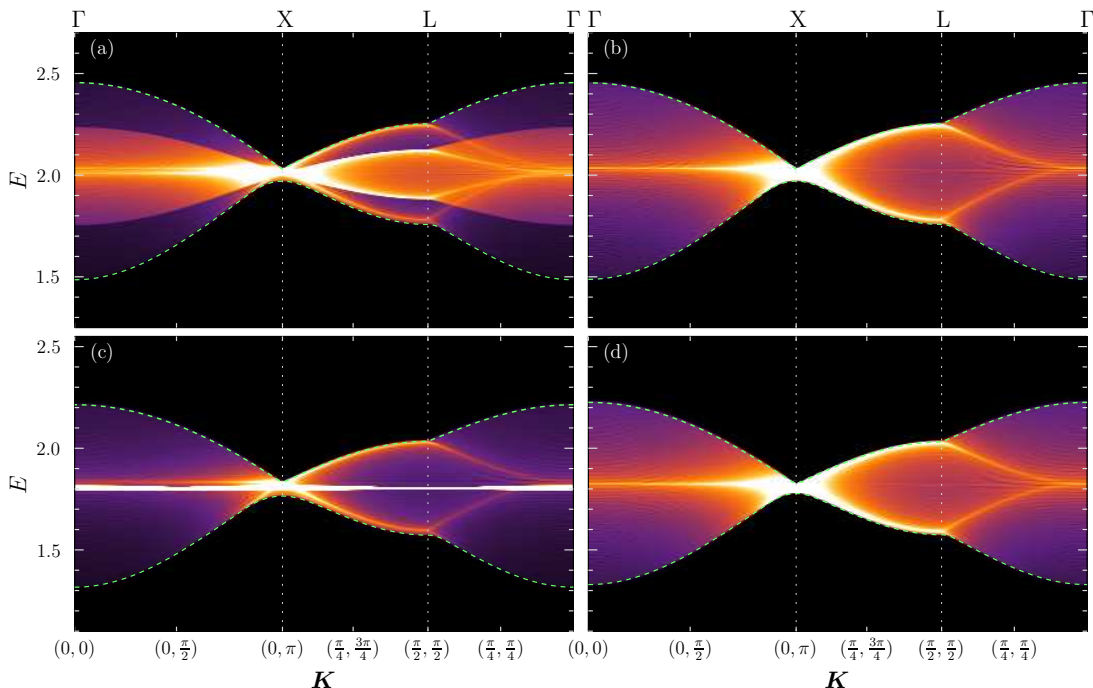


FIGURE 7.11: Density of states $D(E)$ of the toric code in the subspace \mathcal{H}^b , perturbed by the magnetic field (a) $\mathbf{h} = (0.03, 0, 0.06)$, (b) $\mathbf{h} = (0.06, 0, 0.06)$, (c) $\mathbf{h} = (0, 0.3, 0.06)$ and (d) $\mathbf{h} = (0.06, 0.3, 0.06)$. The amplitude of $D(E)$ is indicated by the color gradient, where dark (bright) colors stand for low (high) density. The continuum boundaries, computed from single-particle dispersions, are highlighted by cyan lines.

7.2.2 Subspace \mathcal{H}^f

The fermionic sector of the two-particle subspace is relevant for open systems, where single charges and/or fluxes are created at the boundary and stay connected to this boundary by a string, while propagating through the system. However, our considerations concern only the scenario, where in the thermodynamic limit, the particle pair is far away from any boundary. Furthermore, the subspace \mathcal{H}^f provides us with the unique

possibility to study a two-anyon composite, where, in contrast to the bosonic sector, the anyon pair has a non-trivial mutual statistics.

We apply the same technique as in the previous subsection, and compute $D(E)$ by counting energy levels inside the interval $E + \delta E$. Consider the Figure 7.12, where we present the density of states of the toric code, when subjected to a magnetic field with various field configurations computed at order 6. As already argued in Subsection 7.1.3,

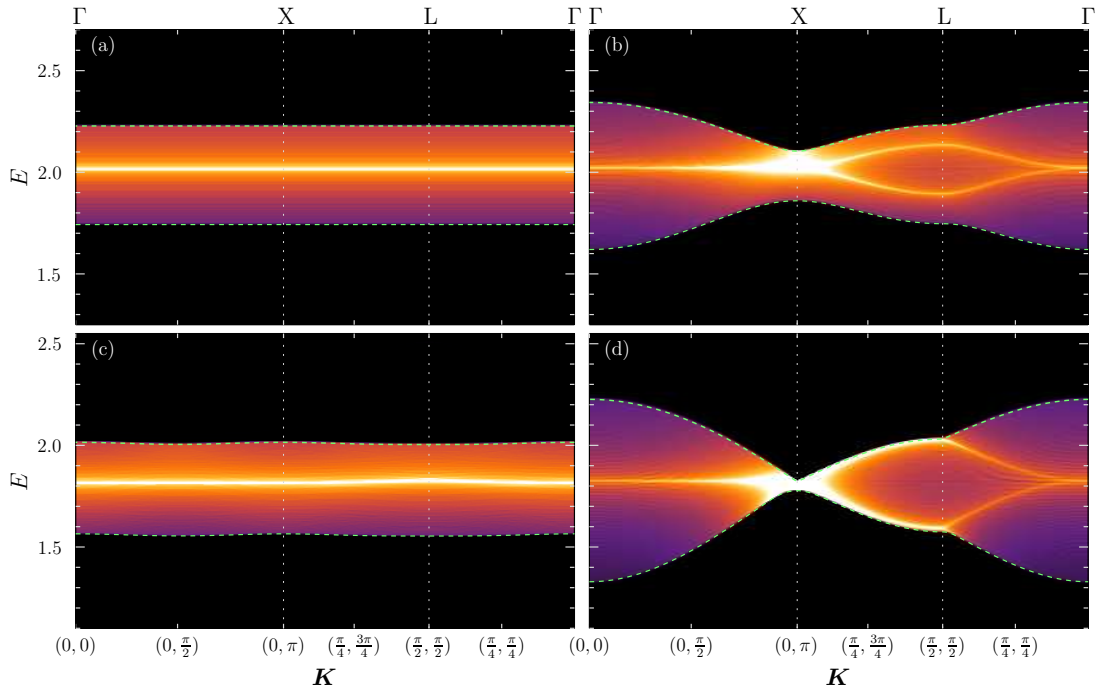


FIGURE 7.12: Density of states $D(E)$ of the toric code in the subspace \mathcal{H}^f , perturbed by the magnetic field (a) $\mathbf{h} = (0, 0, 0.06)$, (b) $\mathbf{h} = (0.03, 0, 0.06)$, (c) $\mathbf{h} = (0, 0.3, 0.06)$ and (d) $\mathbf{h} = (0.06, 0.3, 0.06)$. The amplitude of $D(E)$ is indicated by the color gradient, where dark (bright) colors stand for low (high) density. The continuum boundaries, computed from single-particle dispersions, are highlighted by cyan lines.

on the 'Ising'-line with $h_z > 0$ and $h_x = h_y = 0$, the two-particle states are built from a single 'frozen' flux and a dispersive charge. Thus, the dispersion of the two-particle continuum consists of a constant energy sheet at $E = 1$ plus the dispersion of the charge which, as can be verified in Figure 6.2, has a saddle point at $E = 1$. This has the effect that the saddle points of the continuum are close to $E = 2$, which is consistent with a maximal $D(E)$ at this energy [see Figure 7.12 (a)]. Note that in contrast to the bosonic case, the relative momenta of two-particle modes with energies, where $D(E)$ is maximal, can depend on \mathbf{K} . This is also the case beyond the 'Ising'-line, e.g., in Figure 7.12 (b), where for the same parameters of the field as in Figure 7.11 (a), we find the maxima of the $D(E)$ not for relative two-particle momenta $\mathbf{q} = (\pi/2, \pm\pi/2)$, but at some \mathbf{K} -dependent values. This interesting behavior is the consequence of the fact that when two

particles with different dispersion relations are combined, the position of saddle points of the resulting two-particle mode generally depends on the total momentum.

While the behavior of the $D(E)$ in the bosonic, as well as the fermionic subspace is similar for $h_x = h_z$ [compare Figure 7.11 (d) and Figure 7.12 (d)], due to degenerate dispersion relations of charges and fluxes, the case of $h_x = 0$ and finite h_z and h_y fields is substantially different [see Figure 7.12 (c)]. As in the preceding discussion, here, the $D(E)$ is almost constant for fixed values of E . However, a close look at Figure 7.12 (c) reveals that the boundaries of the continuum are slightly dispersive. This is due to the fact that with finite h_y , the flux acquires a finite dispersion. Since the dependence of the continuum boundaries on the total momentum starts only at order four, the amplitude of the two-particle dispersion is rather small.

After inspecting the spectrum of the two-particle subspace we aim to determine observables, which are more natural to be accessed by experiments than the spectrum itself. As shall be seen later, the information gathered from the density of states is essential to understand certain features of the continuum when the system is probed by an observable.

7.3 Spectral densities

In this section, we discuss how spectral densities can be computed in the pCUT formalism, and present results for the toric code in a magnetic field. To be more specific, we compute the equal-time propagator of a bosonic two-charge composite which should provide valuable information for potential spectroscopic experiments.

As we already learned in Chapter 4, as well as in the previous section, a local perturbation of the toric code in its ground state will excite pairs of particles of the same type (charge-charge or flux-flux). Thus, typically, a scattering experiment will probe the bosonic channel of the model. Note that this lack of one-particle physics in the spectral response is a general feature of spin liquids and in particular of topologically-ordered \mathbb{Z}_2 spin liquids, as the toric code [29, 32, 166].

7.3.1 Preliminaries

A common experimental procedure to investigate spectral properties of a physical system are scattering experiments. The scattered particles, prevalently neutrons or photons, provide information on the dynamical³ correlation functions, modeled in linear response

³Here, we refer to zero-temperature dynamics in momentum space, rather than to time evolution.

theory by the retarded Green's function $\mathcal{G}(\mathbf{K}, \omega)$. At zero temperature, this function is defined as

$$\mathcal{G}^{T=0}(\mathbf{K}, \omega) = \lim_{\epsilon \rightarrow 0^+} \langle 0 | \mathcal{O}^\dagger(\mathbf{K}) \frac{1}{\omega - [H(\mathbf{K}) - E_0] + i\epsilon} \mathcal{O}(\mathbf{K}) | 0 \rangle, \quad (7.38)$$

where E_0 is the eigenenergy of the ground state $|0\rangle$, ω is the frequency, and \mathbf{K} the total momentum of an excitation created by the observable $\mathcal{O}(\mathbf{K})$, when it acts on the ground state. To give an intuitive picture of the above expression, the operator $\mathcal{O}(\mathbf{K})$ 'injects' a two-particle excitation into the vacuum, the resolvent makes the excited state propagate in momentum space, and finally the excitation is destroyed by $\mathcal{O}^\dagger(\mathbf{K})$. The imaginary part of the propagator (7.38) is proportional to the so-called spectral density

$$\mathcal{S}(\mathbf{K}, \omega) = -\frac{1}{\pi} \text{Im} \mathcal{G}^{T=0}(\mathbf{K}, \omega). \quad (7.39)$$

While $\mathcal{S}(\mathbf{K}, \omega)$ is invariant under unitary transformations, it is important to apply the same unitary transformation to the Hamiltonian *and* the observable. In a general fashion, a unitary transformation can be performed by inserting several $UU^\dagger = \mathbb{1}$ into (7.38). We may then simply replace the Hamiltonian by the effective Hamiltonian H_{eff} , and the observables by effective observables \mathcal{O}_{eff} . In the following, we consider exclusively effective observables and therefore drop the corresponding index, to keep a light notation. Note that the ground state $|0\rangle$ is now represented in a unitary transformed basis. Here, we also spare a corresponding index since we will work only in the transformed basis from now on.

Let us introduce the standard approach to compute $\mathcal{S}(\mathbf{K}, \omega)$. Using an algorithm based on the Lanczos method [167, 168], one can write the resolvent (7.38) as

$$\mathcal{G}^{T=0}(\mathbf{K}, \omega) = \lim_{\epsilon \rightarrow 0^+} \frac{\langle 0 | \mathcal{O}^\dagger(\mathbf{K}) \mathcal{O}(\mathbf{K}) | 0 \rangle}{\text{CF}(\omega + i\epsilon)} = \lim_{\epsilon \rightarrow 0^+} \frac{\sum_{\mathbf{d} \in \mathcal{D}_{\text{pos}}} \sum_{\tau} |A_{\mathbf{K}\mathbf{d}\tau}|^2}{\text{CF}(\omega + i\epsilon)}, \quad (7.40)$$

where the coefficients $A_{\mathbf{K}\mathbf{d}\tau}$ shall be defined below [see (7.57)], and $\text{CF}(\omega + i\epsilon)$ is a continued fraction

$$\text{CF}(\omega + i\epsilon) = \omega + i\epsilon - a_0 + \frac{b_1}{\omega + i\epsilon - a_1 + \frac{b_2}{\omega + i\epsilon - a_2 + \dots}}. \quad (7.41)$$

The continued fraction is constructed from the tridiagonalized effective Hamiltonian. Here, the a_i are matrix elements on the diagonal, and b_i on the second diagonal of the tridiagonalized form. They are computed through a successive assembling of the Lanczos basis $\{|\psi\rangle_i\}$ with

$$a_i = {}_i\langle\psi| H_{\text{eff}} |\psi\rangle_i , \quad (7.42)$$

$$b_i = {}_i\langle\psi|\psi\rangle_i , \quad (7.43)$$

$$|\psi\rangle_{i+1} = \frac{1}{b_i} \left(H_{\text{eff}} |\psi\rangle_i - a_i |\psi\rangle_i - b_i |\psi\rangle_{i-1} \right) , \quad (7.44)$$

and the initial conditions

$$|\psi\rangle_{i<0} = 0 , \quad (7.45)$$

$$|\psi\rangle_{i=0} = \frac{1}{\langle 0 | \mathcal{O}^\dagger(\mathbf{K}) \mathcal{O}(\mathbf{K}) | 0 \rangle} \mathcal{O}(\mathbf{K}) | 0 \rangle . \quad (7.46)$$

Generally [167], at $i \rightarrow \infty$, the a_i and b_i converge to

$$a_\infty = \frac{\epsilon_{\text{ub}}(\mathbf{K}) + \epsilon_{\text{lb}}(\mathbf{K})}{2} , \quad (7.47)$$

$$b_\infty = \frac{\epsilon_{\text{ub}}(\mathbf{K}) - \epsilon_{\text{lb}}(\mathbf{K})}{2} , \quad (7.48)$$

where $\epsilon_{\text{ub}}(\mathbf{K})$ and $\epsilon_{\text{lb}}(\mathbf{K})$ are the continuum boundaries, defined in (7.3)-(7.4). In practice, however, the coefficients of the continued fraction converge already after a relatively small number of recursions because we work in an orthogonal basis, set up by the Lanczos-procedure. On the one hand, we use the coefficients a_∞ and b_∞ , computed from the one-particle dispersions, as a consistency check as well as convergence check of our results. On the other hand, one of the standard methods to terminate the continued fraction is to insert a large number of a_∞ and b_∞ in its tail. Another technical remark is that it is common to work with a small but finite ϵ , especially in order to give distinct resonances of $\mathcal{G}^{T=0}(\mathbf{K}, \omega)$ a finite width. The trick is to choose ϵ small enough so that the artificial broadening does not distort the general features of the spectral density. It should also be mentioned that typically, in an actual experiment, the finite resolution leads effectively to a non-zero ϵ .

In Section 2.4, we have shown how to obtain the effective observable in the same basis as the effective Hamiltonian H_{eff} . The action of the effective observable in real space is given by the expansion (2.49). The coefficients of this series have been computed model-independently up to a high order in Ref. [86]. We have argued that at zero temperature, the effective observable can be written as a superposition of operators $\mathcal{O}_{d,0}(\mathbf{r})$ [see (2.51)] which connect the zero-particle subspace with a d -particle subspace. One of the simplest observables to consider in a quantum spin model are the Pauli operators σ^α . Since the action of σ^x or σ^z on the ground state of the toric code yields a two-particle excitation and the action of σ^y a four-particle excitation (see Figure 4.4), an effective observable

for the toric code in a magnetic field can be generally expressed as

$$\mathcal{O}_{\text{eff}}(\mathbf{r}) = \mathcal{O}_{2,0}(\mathbf{r}) + \mathcal{O}_{4,0}(\mathbf{r}) + \mathcal{O}_{6,0}(\mathbf{r}) + \dots \quad (7.49)$$

As already explained above, the low-energy physics of the perturbed toric code is governed by two-particle excitations so that we are interested in the observables σ^x and σ^z . In principle, an investigation of spectral densities in the four-particle subspace would also be interesting as a follow-up study. However, it should be clear that one must, in addition, obtain the effective Hamiltonian in the corresponding subspace. To give an idea about the structure of effective observables in the toric code, we give the expression of $\mathcal{O}^{2,0}(\mathbf{r})$ for the observable σ^z up to order one

$$\mathcal{O}^{2,0}(\mathbf{r}) = T'_2(\mathbf{r}) - \frac{1}{2}T'_0(\mathbf{r})T_2 - \frac{1}{4}T'_{-2}(\mathbf{r})T_4, \quad (7.50)$$

where the T_m are the operators defined in Table 5.4 and $T'_m(\mathbf{r})$ correspond to the effective action of σ^z at site \mathbf{r} (note that the operator structure of σ^x is the same, up to a charge-flux inversion). Here, we see explicitly that unlike H_{eff} , the effective observable is not particle-conserving. We will refer to the first term on the right-hand side of (7.50) as the zeroth-order contribution, the following two terms are the order one contribution, corresponding to the power of the expansion parameter 'hidden' in the definition of T_m (without prime). For the observable σ^z we have $\mathcal{O}_{\text{eff}}(\mathbf{r}) = \mathcal{O}_{2,0}(\mathbf{r})$ at order zero. Due to $\sigma^z\sigma^z = \mathbb{1}$, the total spectral weight must be 1. At higher orders in perturbation there is generally a finite contribution by $\mathcal{O}_{d,0}(\mathbf{r})$ with $d > 2$. However, at low magnetic fields these high-order corrections can be neglected, as will be shown in the following. In order to find out the relative amount of the spectral weight contained in $\mathcal{O}^{2,0}$, we calculate the series expansion of the numerator in (7.40). The resulting expression at order four reads

$$\begin{aligned} \langle 0 | (\mathcal{O}^{2,0})^\dagger \mathcal{O}^{2,0} | 0 \rangle &= 1 - (h_x^2 + h_z^2) - \frac{3}{8}h_y^2 - \frac{1}{2}(13h_x^4 + 33h_z^4) + \frac{13}{8}h_x^2h_z^2, \\ &\quad - \frac{1}{64}(425h_x^2h_y^2 + 354h_y^2h_z^2) - \frac{3445}{2304}h_y^4. \end{aligned} \quad (7.51)$$

As has been discussed above, we see that for zero magnetic fields *all* of the spectral weight is concentrated in the channel governed by $\mathcal{O}_{2,0}(\mathbf{r})$. In this case, the resolvent in (7.38) yields $1/(\omega - 2 + i\epsilon)$ because the Hamiltonian simply measures the excitation energy of the particle-pair. Consequently, the spectral density features a momentum-independent sharp resonance at $\omega = 2$. At finite magnetic fields, the right-hand side of (7.51) gradually decreases [at the same time the resolvent in (7.38) becomes less trivial]. However, even at the largest magnetic fields where the spectral density is analyzed in the following ($h_y = 0.3$, $h_x = h_z = 0.06$) the relative amount of the spectral weight captured by $\mathcal{O}_{2,0}(\mathbf{r})$ is above 94%.

Let us gather some general considerations from Ref. [86] concerning the action of the effective observable. When acting on the particle vacuum, the operator $\mathcal{O}^{2,0}(\mathbf{r})$ generally creates a superposition of particle pairs with mutual distances \mathbf{d} and flavor τ

$$\mathcal{O}^{2,0}(\mathbf{r})|0\rangle = \sum_{\mathbf{r}'\mathbf{d}\tau} \omega_{\mathbf{r}'\mathbf{d}\tau} |\mathbf{r} + \mathbf{r}', \mathbf{r} + \mathbf{r}' + \mathbf{d}, \tau\rangle. \quad (7.52)$$

The Fourier transform of this operator is

$$\mathcal{O}^{2,0}(\mathbf{K}) = \frac{1}{\sqrt{N}} \sum_{\mathbf{r}} e^{i\mathbf{K}\mathbf{r}} \mathcal{O}^{2,0}(\mathbf{r}), \quad (7.53)$$

where N is the total number of sites. Now, we can construct the general expression of the observable action in momentum space, necessary to evaluate (7.40).

$$\mathcal{O}^{2,0}(\mathbf{K})|0\rangle = \frac{1}{\sqrt{N}} \sum_{\mathbf{r}} e^{i\mathbf{K}\mathbf{r}} \sum_{\mathbf{r}'\mathbf{d}\tau} \omega_{\mathbf{r}'\mathbf{d}\tau} |\mathbf{r} + \mathbf{r}', \mathbf{r} + \mathbf{r}' + \mathbf{d}, \tau\rangle, \quad (7.54)$$

$$\stackrel{\mathbf{r} \rightarrow \mathbf{r} - \mathbf{r}'}{=} \sum_{\mathbf{r}'\mathbf{d}\tau} e^{-i\mathbf{K}(\mathbf{r}'+\mathbf{d}/2)} \omega_{\mathbf{r}'\mathbf{d}\tau} \frac{1}{\sqrt{N}} \sum_{\mathbf{r}} e^{i\mathbf{K}(\mathbf{r}+\mathbf{d}/2)} |\mathbf{r}, \mathbf{r} + \mathbf{d}, \tau\rangle, \quad (7.55)$$

$$= \sum_{\mathbf{r}'\mathbf{d}\tau} e^{-i\mathbf{K}(\mathbf{r}'+\mathbf{d}/2)} \omega_{\mathbf{r}'\mathbf{d}\tau} |\mathbf{K}, \mathbf{d}, \tau\rangle, \quad (7.56)$$

$$= \sum_{\mathbf{d} \in \mathcal{D}_{\tau\text{pos}}} A_{\mathbf{K}\mathbf{d}\tau} |\mathbf{K}, \mathbf{d}, \tau\rangle, \quad (7.57)$$

where $|\mathbf{K}, \mathbf{d}, \tau\rangle$ is a two-particle state in momentum space, defined in (5.76), and the distances are limited to the set \mathcal{D}_{pos} , defined in Subsection 5.1.3, accounting for the fact that two charges (or two fluxes) are indistinguishable. We compute the series expansions of amplitudes $A_{\mathbf{K}\mathbf{d}\tau}$ up to order four (see Appendix B.4). This is the minimal order where the anyonic character of the elementary excitations contributes to the matrix elements of the effective Hamiltonian. It might be not so obvious at this point that the bottleneck of this computation is actually (7.46). Since our $\mathcal{O}^{2,0}(\mathbf{K})$ creates *two* particles, the minimal size of an open cluster, to compute (7.46) up to order r is $2(r+1) \times 2(r+1)$ plaquettes. In addition to the big cluster, one has to deal with more coefficients, in the case of the *non-particle-conserving* effective observable than for the computation of the effective Hamiltonian.

It is specific to the toric code that the effective action of σ^x and σ^z is essentially the same, up to a charge-flux inversion. Above all, this is the consequence of (4.1), where we choose the weight of A_s and B_p to be equal. Thus, we argue that the spectral density one obtains from the observable σ^z , when the toric code is exposed to a magnetic field with $h_z \geq h_x$ (and arbitrary h_y) is the same as for σ^x and a magnetic field $h_x \geq h_z$. From here we will therefore only focus on the observable σ^z . Note that when acting on the ground state, at order zero, the operator σ^z creates a pair of neighboring charges,

with an orientation, depending on \mathbf{r} . This is visualized in Figure 7.13. We will refer to $\mathcal{O}_b^{2,0}(\mathbf{K})$ (or equivalently to $\mathcal{O}_r^{2,0}(\mathbf{K})$) as non-symmetric, to $[\mathcal{O}_b^{2,0}(\mathbf{K}) + \mathcal{O}_r^{2,0}(\mathbf{K})] / \sqrt{2}$ as symmetric, and to $[\mathcal{O}_b^{2,0}(\mathbf{K}) - \mathcal{O}_r^{2,0}(\mathbf{K})] / \sqrt{2}$ as antisymmetric, where the indices r and b refer to the sublattices shown in Figure 7.13. We assume that the non-symmetric observables are not relevant for experiments since in a scattering experiment one can hardly control on which sublattice the scattering takes place. It is more likely that one observes an equal-weight superposition of scattering on both sublattices. Therefore we are mostly interested in the symmetric observable.

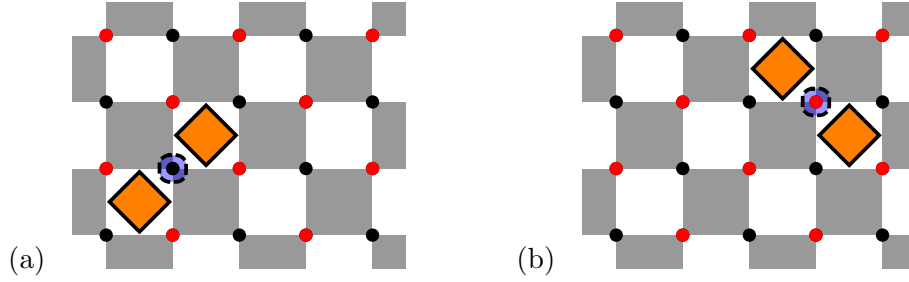


FIGURE 7.13: Effective action of the observable σ^z at order zero. Depending on the lattice site, two charges are created with a different mutual orientation. Translational invariance is fulfilled, if one considers an equal-weight superposition of operators, acting on the black sublattice (a) and the red sublattice (b).

7.3.2 Examples and checks

To provide a better understanding of our computational algorithm, we present the outset of the calculation of $A_{\mathbf{K}d\tau}$. Furthermore, we show that on the Ising line our results for the spectral density are supported by an independent calculation.

We begin by letting the effective observable (7.50) act in real space, in order to compute the $\omega_{\mathbf{r}'d\tau}$. Note that, once again, we use the coordinate system defined in Section 7.1. At order zero we obtain

$$T_2'(\mathbf{r}_b) |0\rangle = \left| \mathbf{r} - \frac{1}{2}(\mathbf{m}_1 + \mathbf{m}_2), \mathbf{r} + \frac{1}{2}(\mathbf{m}_1 + \mathbf{m}_2), c \right\rangle, \quad (7.58)$$

$$T_2'(\mathbf{r}_r) |0\rangle = \left| \mathbf{r} - \frac{1}{2}(\mathbf{m}_1 - \mathbf{m}_2), \mathbf{r} + \frac{1}{2}(\mathbf{m}_1 - \mathbf{m}_2), c \right\rangle, \quad (7.59)$$

where the lower index of \mathbf{r} refers to the sublattice, and we use the letters 'c' and 'f' (for charges and fluxes) to identify the flavor of the particle pair.

At order one, we will only concentrate on the sublattice \mathbf{r}_b ; the procedure on \mathbf{r}_r is very similar. We obtain

$$\begin{aligned}
-\frac{1}{2}T'_0(\mathbf{r}_b)T_2|0\rangle &= \frac{1}{2}h_z \left(\left| \mathbf{r} - \frac{3}{2}(\mathbf{m}_1 + \mathbf{m}_2), \mathbf{r} + \frac{1}{2}(\mathbf{m}_1 + \mathbf{m}_2), \mathbf{c} \right\rangle \right. \\
&\quad + \left| \mathbf{r} - \frac{3}{2}(\mathbf{m}_1 + \mathbf{m}_2), \mathbf{r} + \frac{1}{2}(\mathbf{m}_1 - 3\mathbf{m}_2), \mathbf{c} \right\rangle \\
&\quad + \left| \mathbf{r} - \frac{3}{2}(\mathbf{m}_1 + \mathbf{m}_2), \mathbf{r} - \frac{1}{2}(3\mathbf{m}_1 - \mathbf{m}_2), \mathbf{c} \right\rangle \\
&\quad + \left| \mathbf{r} - \frac{1}{2}(\mathbf{m}_1 + \mathbf{m}_2), \mathbf{r} + \frac{3}{2}(\mathbf{m}_1 + \mathbf{m}_2), \mathbf{c} \right\rangle \\
&\quad + \left| \mathbf{r} - \frac{1}{2}(\mathbf{m}_1 + \mathbf{m}_2), \mathbf{r} + \frac{1}{2}(3\mathbf{m}_1 - \mathbf{m}_2), \mathbf{c} \right\rangle \\
&\quad \left. + \left| \mathbf{r} - \frac{1}{2}(\mathbf{m}_1 + \mathbf{m}_2), \mathbf{r} - \frac{1}{2}(\mathbf{m}_1 - 3\mathbf{m}_2), \mathbf{c} \right\rangle \right), \quad (7.60)
\end{aligned}$$

$$-\frac{1}{4}T'_{-2}(\mathbf{r}_b)T_4|0\rangle = -\frac{i}{4}h_y \left| \mathbf{r} - \frac{1}{2}(\mathbf{m}_1 - \mathbf{m}_2), \mathbf{r} + \frac{1}{2}(\mathbf{m}_1 - \mathbf{m}_2), \mathbf{f} \right\rangle. \quad (7.61)$$

Now, we can construct the coefficients $A_{\mathbf{K}\mathbf{d}\tau}$ by using the formula (7.57), where coefficients $\omega_{\mathbf{r}'\mathbf{d}\tau}$ acquire a phase factor proportional to the shift of the center of mass of the particle pair in respect to \mathbf{r} .

$$\begin{aligned}
\mathcal{O}_b^{2,0}(\mathbf{K})|0\rangle &= |\mathbf{K}, \mathbf{m}_1 + \mathbf{m}_2, \mathbf{c}\rangle \\
&\quad + h_z \cos\left(\frac{K_x - K_y}{2}\right) |\mathbf{K}, 2\mathbf{m}_1, \mathbf{c}\rangle \\
&\quad + h_z \cos\left(\frac{K_x - K_y}{2}\right) |\mathbf{K}, 2\mathbf{m}_2, \mathbf{c}\rangle \\
&\quad - \frac{i}{4}h_y |\mathbf{K}, \mathbf{m}_1 - \mathbf{m}_2, \mathbf{f}\rangle, \quad (7.62)
\end{aligned}$$

where we used the notation $\mathbf{K} = (K_x, K_y)$. This is consistent with coefficients of the non-symmetric observable $\mathcal{O}^{2,0}(\mathbf{r}_b)$ listed in Table B.9 (see Appendix B.4).

Certainly, it is very helpful to have a direct check of the spectral density computed with the recursive method described in the previous subsection. In the following, we argue that on the Ising line our results can be compared to the simple case of hard-core bosons on a square lattice. As we have shown in (7.58), at order zero, the observable σ^z injects a pair of adjacent charges. We consider their propagation under influence of the effective Hamiltonian at order *one*, where the toric code is perturbed by a single h_z field. In other words, we choose a configuration of our effective model such that it solely contains charge hoppings to neighboring sites. Given the general considerations from Section 4.2, one should see that, in this scenario, the physics is equivalent to the one of two hard-core bosons on a square lattice, described by the Ising Hamiltonian which at

order one reads

$$H_{\text{b,sq}} = -J \sum_i n_i - h_z \sum_{\langle i,j \rangle} (b_i^\dagger b_j + b_j^\dagger b_i), \quad (7.63)$$

where i and j are neighboring vertices of a square lattice, and b_i^\dagger (b_i) is the bosonic creation (annihilation) operator. Note that in our scenario the counterpart of the observable $\sigma^z(\mathbf{r}_b)$ in the toric code is the operator $b_i^\dagger b_{i+1}^\dagger$ which creates a pair of neighboring bosons in the horizontal. We computed the corresponding propagator for the model $H_{\text{b,sq}}$ and indeed find numerically exactly coinciding coefficients of the continued fraction (7.41), when comparing to the toric code in a single h_z field at order one⁴.

In Figure 7.14 we show the resulting spectral density as a function of the total momentum $\mathbf{K} = (K_x, K_y)$ and the energy ω . There is a striking similarity with the density of states, calculated in the preceding subsection (see Figure 7.10) for the toric code on the 'Ising'-line. We recall that one can find two-particle modes with relative momentum $\mathbf{q} = (q_x, q_y)$, and eigenenergy $\omega(\mathbf{K}, \mathbf{q})$, corresponding exactly to the energy at the continuum boundaries. Furthermore, the maxima of spectral density are found for two-particle modes with energies, where the density of states is also maximal. However, in contrast to Figure 7.10, we consider an order one calculation, which is special since there are no antisymmetric terms in the single-quasi-particle dispersions. Another important difference is that the spectral density lacks the strong, constant peak at the energy $E = 2$ because we consider an observable which only probes the two-charge sector of \mathcal{H}^{b} so that no frozen fluxes are excited.

Not surprisingly, the weight distribution depends on the type of the observable, as shown in Figure 7.15. Note that the only difference between the non-symmetric observables is the orientation of the injected particle pair (see Figure 7.13). While physically these two cases are identical, Figure 7.15 (a)-(b) shows a difference which simply stems from the fact that the L-point is only a symmetry point for the symmetrized observables. In the following, we will therefore mostly focus on the symmetric observable [shown in Figure 7.15 (c)] which preserves the initial symmetry of the problem. In all cases presented in Figure 7.15 it seems that the maxima of the density of states, at saddle points of the two-particle dispersion (discussed in the previous subsection), are related to the characteristic features inside the continuum.

⁴The calculation of the spectral density of two hard-core bosons has been performed with an independently written computer code, which is a further check of our computational procedure.

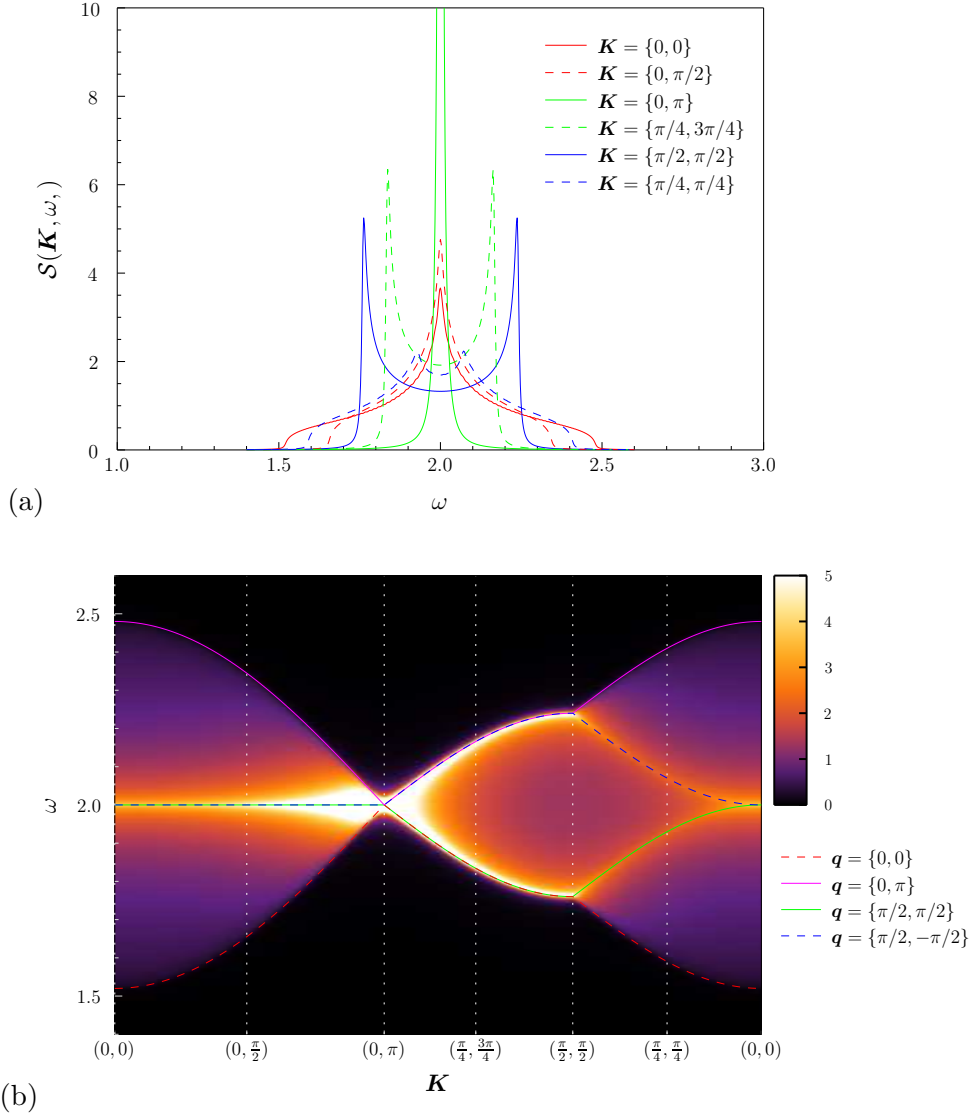


FIGURE 7.14: Spectral density of the non-symmetric observable $\mathcal{O}_b = \sigma^z$ at order zero, for the toric code in the magnetic field $\mathbf{h} = (h_x, h_y, h_z) = (0, 0, 0.06)$ at perturbation order one. This spectral density is the same as the one of the observable $\mathcal{O}_b = b_i^\dagger b_{i+1}^\dagger$ for the model $H_{b,\text{sq}}$. The spectral density $S(\mathbf{K}, \omega)$ is a function of the energy ω and the total momentum $\mathbf{K} = (K_x, K_y)$. We have used $\epsilon = 0.005$, to give the energy peaks a finite width. Consequently, the boundaries of the continuum are artificially smoothed out, most drastically for the case $\mathbf{K} = (0, \pi)$ where the total weight is concentrated in a single two-particle mode. (a) Spectral density for certain fixed values of \mathbf{K} . (b) Alternative illustration of the spectral density, where \mathbf{K} is varied along the symmetry lines of the Brillouin zone. The color gradient corresponds to the amplitude of $S(\mathbf{K}, \omega)$. The fixed \mathbf{K} values from (a) are highlighted by vertical dotted lines; \mathbf{q} refers to the relative momentum of a particle pair.

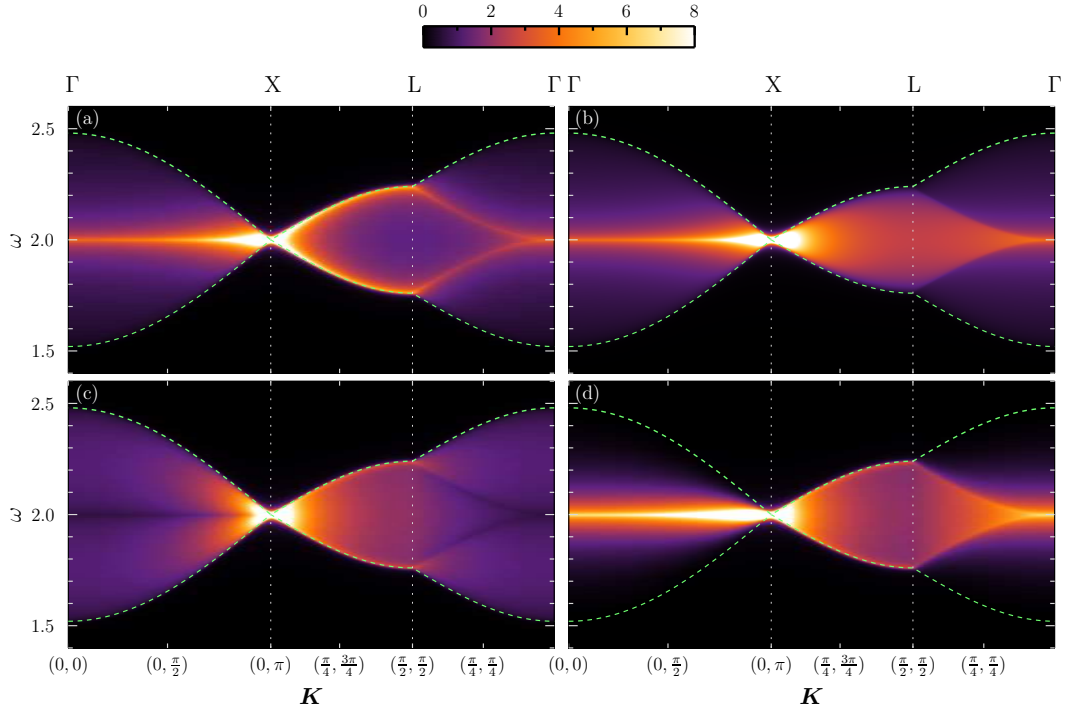


FIGURE 7.15: Spectral density of the toric code in the magnetic field $\mathbf{h} = (0, 0, 0.06)$, at order 1 with $\epsilon = 0.005$ and (a) the non-symmetric observable \mathcal{O}_b , (b) the non-symmetric observable \mathcal{O}_r , (c) the symmetric observable, and (d) the antisymmetric observable. The amplitude of $\mathcal{S}(\mathbf{K}, \omega)$ corresponds to the color scale at the top. In (a) and (b) $\mathcal{S}(\mathbf{K}, \omega)$ has been re-normalized by a factor two, in order to compare to the symmetrized cases. The boundaries of the continuum are highlighted by green dashed lines.

7.3.3 Results

In this subsection, we present our results on the spectral density of the toric code in a general magnetic field using the symmetric version of the observable σ^z (denoted by $[\mathcal{O}_b^{2,0}(\mathbf{K}) + \mathcal{O}_r^{2,0}(\mathbf{K})] / \sqrt{2}$ in previous discussions). Analogue plots for the non-symmetric as well as the antisymmetrized cases can be found in the Appendix C. The computations are based on our findings from previous chapters, where we were able to obtain the effective observable up to order four and the effective Hamiltonian up to order six with pCUT. We will follow the strategy from Section 7.1 where the influence of the magnetic field on the two-quasi-particle spectrum was studied by scanning the parameter space along representative symmetry lines. Thus, one can directly match the spectra computed in Section 7.1 with the weight distribution among the corresponding energy levels to be presented below. For the remainder of this chapter, a broadening $\epsilon = 0.002$ is used, unless stated otherwise. Furthermore, we have checked that in the considered parameter regions the spectral densities are converged with perturbation order, which means that there are no significant changes at higher orders.

We begin by considering the case of a pure transverse field in Figure 7.16 (a). Here, the total weight of the spectral density is concentrated in the non-dispersive bound states $|\Psi_{11}^b\rangle$ and $|\Psi_{1-1}^b\rangle$ [see (7.17)]. The reason is simply that these are the only states generated by the effective observable when $h_x = h_z = 0$. Formally, the amplitudes $A_{\mathbf{K}d\tau}$ of any other state are zero in the thermodynamic limit (see also Table B.11). The physical explanation is that due to dimensional reduction in this special point of the parameter space, single charges and single fluxes are non-dispersive. Thus, the only possible two-particle states which can be generated by a *local* observable are two neighboring charges or two-neighboring fluxes which are the exact constituents of $|\Psi_{11}^b\rangle$ and $|\Psi_{1-1}^b\rangle$. As can be observed in Figure 7.16 (b)-(d), at finite parallel fields the two-particle continuum carries some spectral weight. However, clearly, the bound states (as well as antibound states above the continuum) are dominating the spectral density. Note that a four-particle continuum should appear at higher energies ($\omega = 4$). Considering the lowest two-particle energy ($\omega \approx 1.3$) in Figure 7.16 (d), we estimate that the lowest energy of *four*-particle bound states is close to $\omega \approx 2.6$ so that in the discussed parameter region there is no 'interference' with the two-particle physics.

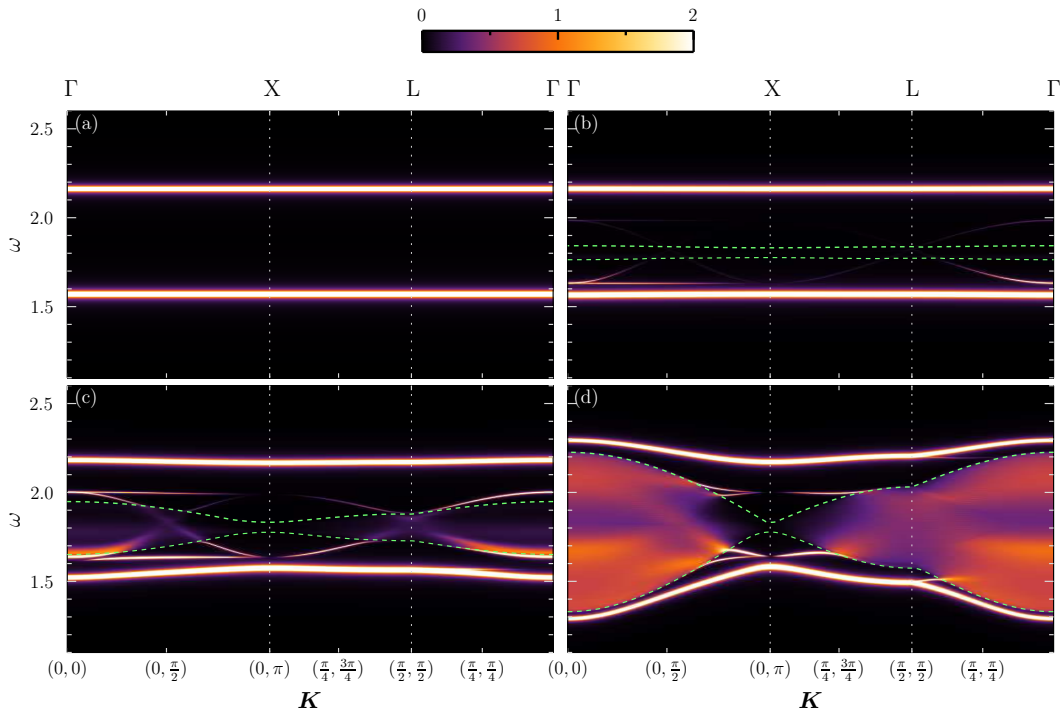


FIGURE 7.16: Spectral density of the toric code in the magnetic field $h_y = 0.3$, $h_x = h_z$ and (a) $h_x = 0$, (b) $h_x = 0.005$, (c) $h_x = 0.02$, (d) $h_x = 0.06$. See Figure 7.3 for a comparison with the corresponding energy spectrum. The amplitude of $\mathcal{S}(\mathbf{K}, \omega)$ corresponds to the color scale at the top. The boundaries of the continuum are highlighted by green dashed lines.

A compelling feature in the discussed plots is the decay of bound states that one can observe in regions where the bound-state dispersions enter the two-particle continuum. Apparently, bound states 'survive' even inside the continuum, at least when the parallel field strength is small, see for example the continuum in Figure 7.16 (c) around $\mathbf{K} = (0, \pi/2)$ and $\mathbf{K} = (\pi/2, \pi/2)$. For a larger parallel field 'resonances' remain from bound states inside the continuum [see Figure 7.16 (d)]. The weight agglomeration inside the continuum can be understood as a combined effect of 'saddle point'-modes which seem to play a role even with high-order corrections and several decaying bound states. We shall discuss these points in more detail by considering Figure 7.17, where at fixed values of \mathbf{K} we show the spectral density between the L- and Γ -points of Figure 7.16 (d). This parameter region allows us to observe more closely how the dispersion of a bound state changes after entering the continuum band. First, let us comment on some of the rich features of the two-particle continuum. The two-particle modes with a relative momentum $\mathbf{q} = (0, 0)$ and $\mathbf{q} = (0, \pi)$ have the exact energy of the lower and respectively upper boundary of the continuum. The saddle-point modes, indicated by green dashed lines in Figure 7.17, flag significant points (kinks of the otherwise smooth curvature) of the continuum. These modes correspond to two-particle states where the relative momenta of the two particles are either $\mathbf{q} = (-\pi/2, \pi/2)$ (left vertical line) or $\mathbf{q} = (\pi/2, \pi/2)$ (right vertical line). This behavior is typical since it is known that at saddle-modes frequencies one usually finds discontinuities or zeroes of the spectral density, at least in (quasi-) one-dimensional systems [87, 95, 164, 165].

Next, we focus on the bound state represented by the sharp peak in spectral density close to the lower boundary of the continuum highlighted in Figure 7.17 (a). With decreasing total momentum [moving from left to right in Figure 7.16 (d)], the bound state enters the continuum and its spectral density is strongly lowered. However, the remaining resonance can still be clearly identified inside the continuum. By tracking the maximum of its amplitude, the decay of a bound state can be observed even more clearly in Figure 7.18. After entering the continuum the spectral weight of the bound state drops by an order of magnitude and then slowly continues to decrease.

Let us one more time draw our attention to Figure 7.16 in order to discuss an interesting property of $\mathcal{S}(\mathbf{K}, \omega)$, found when comparing with the corresponding energy spectrum in Figure 7.3. The most striking difference is the absence of spectral weight for certain bound states. This is related to interference effects which, depending on the symmetry of eigenstates and the observable, can be constructive or destructive. Indeed, as can be verified in Figure 7.19, modes suppressed in the case of the symmetric observable are dominant for the antisymmetric observable. We shall specify this statement by examining the lowest energy branch, which is degenerate in the limit $\mathbf{h} = (0, h_y, 0)$ and corresponds to eigenstates $|\Psi_{11}^b\rangle$ and $|\Psi_{1-1}^b\rangle$ in this limit [see (7.17)-(7.18) for

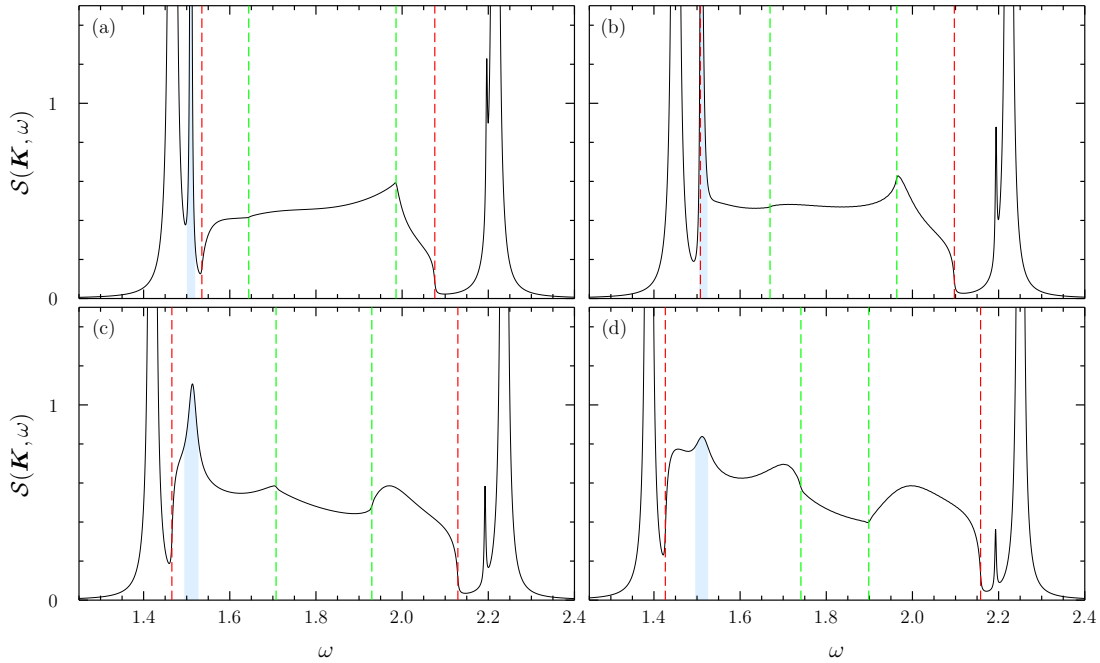


FIGURE 7.17: Decay of a bound state. Here we consider the spectral density ($\epsilon = 0.001$) of the toric code, subjected to the magnetic field $\mathbf{h} = (h_x, h_y, h_z)$ with $h_y = 0.3$ and $h_x = h_z = 0.06$. The particle pair has a total momentum of $\mathbf{K} = (K, K)$ and (a) $K = 3\pi/7 \approx 0.43\pi$, (b) $K = 11\pi/28 \approx 0.39\pi$, (c) $K = 47\pi/140 \approx 0.34\pi$ and (d) $K = 39\pi/140 \approx 0.28\pi$, which corresponds to the region between the L- and Γ -points, plotted in Figure 7.16 (d). Red (green) dashed lines are boundaries of the continuum (saddle modes), computed from one-particle dispersions. The bound state of interest is identified by a peak in the spectral density, highlighted by a light blue color.

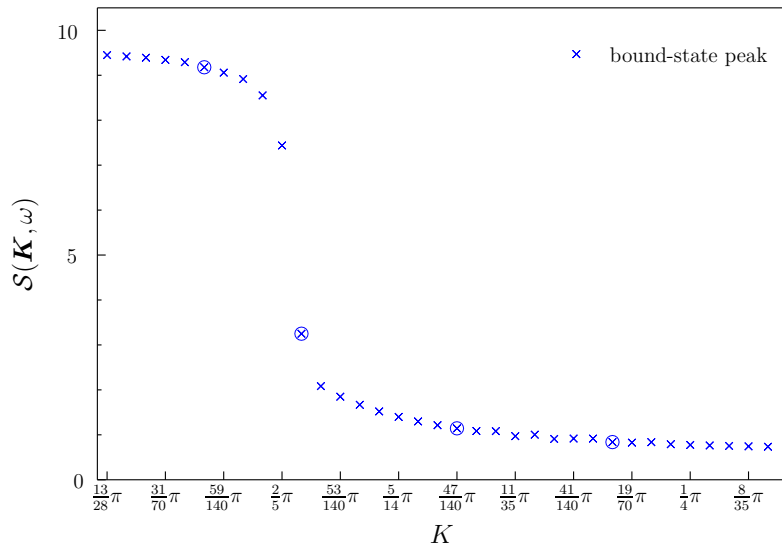


FIGURE 7.18: Dependence of the maximal amplitude of the bound-state peak, highlighted in Figure 7.17 on the total momentum $\mathbf{K} = (K, K)$ of the quasi-particle pair. Encircled data points correspond to values of K discussed in Figure 7.17. A strong decrease of the amplitude occurs as soon as the bound state enters the continuum, thus characterizing the decay of this bound state.

the definition]. At finite parallel fields, the degeneracy is lifted for certain momenta and the eigenenergies of states connected adiabatically to the symmetric wave function $|\Psi_{11}^b\rangle$ as well as the antisymmetric wave function $|\Psi_{1-1}^b\rangle$ can be dealt with separately. Figure 7.19 clearly indicates that the symmetric observable allocates the spectral weight mostly into the symmetric bound state, while the antisymmetric observable preferably collects the most weight in the antisymmetric bound state. Obviously, the symmetry of eigenstates does not play a role for non-symmetric observables, where the spectral density is distributed equally among states with different symmetry. Analogue behavior can be observed for 'antibound' states above the two-particle continuum.

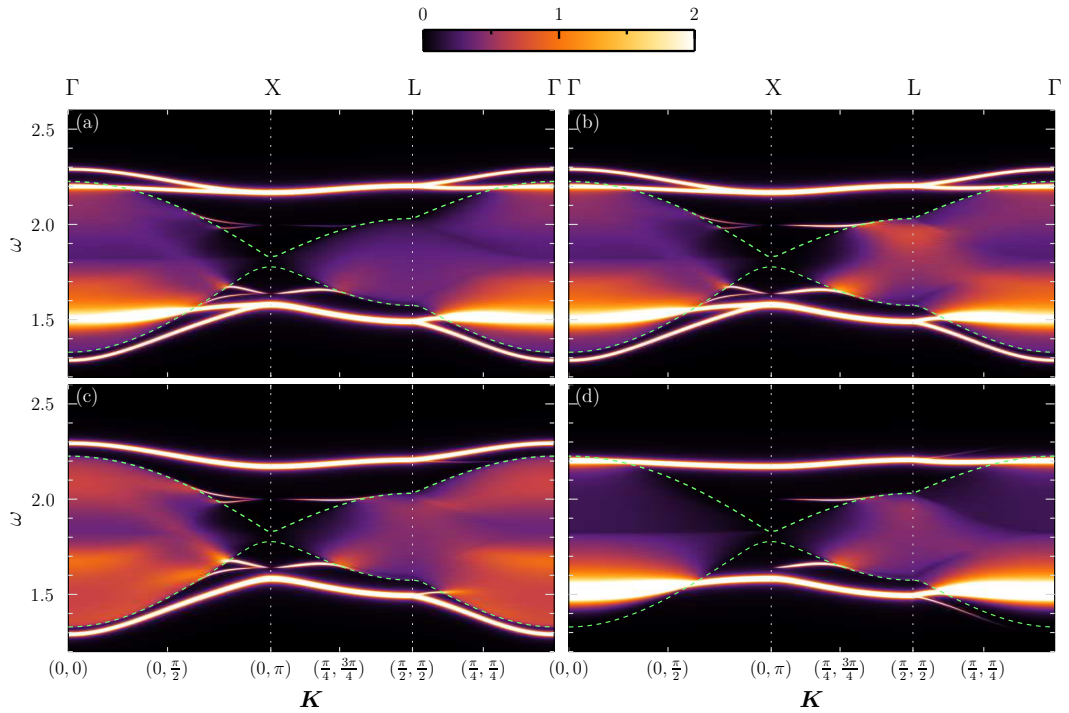


FIGURE 7.19: Spectral density of the toric code in the magnetic field $h_y = 0.3$ and $h_x = h_z = 0.06$ for (a) the non symmetric observable \mathcal{O}_b , (b) the non symmetric observable \mathcal{O}_r , (c) the symmetric observable $(\mathcal{O}_b + \mathcal{O}_r)/\sqrt{2}$, and (d) the antisymmetric observable $(\mathcal{O}_b - \mathcal{O}_r)/\sqrt{2}$.

We now return to the symmetric observable and regard the spectral density for a *constant* parallel field and an increasing transverse field. Figure 7.20 illustrates how, starting from a continuum band without bound states at zero transverse field h_y , a finite h_y causes bound states to arise and progressively pick up spectral weight. More weight is shifted from the two-particle continuum into the bound states, as the transverse field is turned up. Similarly to previous cases, we find that the spectral weight inside the continuum displays significant features at saddle-modes energies. In contrast to the order one calculation presented in Figure 7.15, the symmetry of the continuum with regard to the diagonal energy is distorted due to higher order corrections, as it is also the case

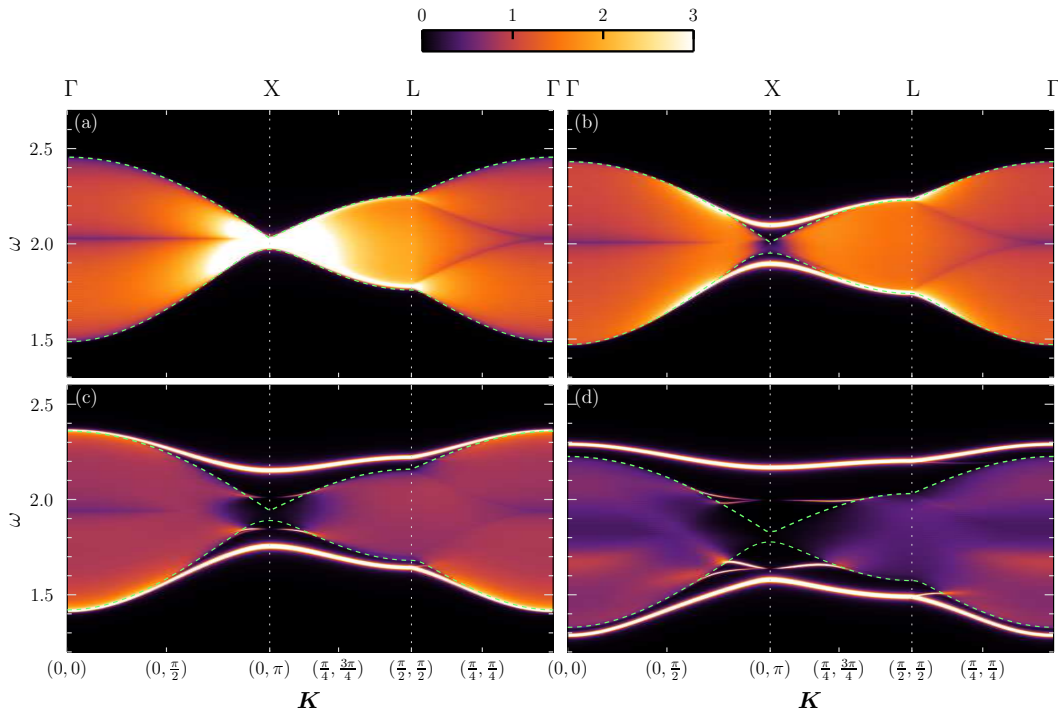


FIGURE 7.20: Spectral density of the toric code in the magnetic field $h_x = h_z = 0.06$ and (a) $h_y = 0$, (b) $h_y = 0.1$, (c) $h_y = 0.2$, (d) $h_y = 0.3$. See Figure 7.5 for a comparison with the corresponding energy spectrum. The amplitude of $\mathcal{S}(\mathbf{K}, \omega)$ corresponds to the color scale at the top. The continuum boundaries are highlighted by green dashed lines.

for the density of states in Figure 7.10. While at $h_y = 0$ the maximum of $\mathcal{S}(\mathbf{K}, \omega)$ is concentrated around the point $\mathbf{K} = (0, \pi)$ [or equivalently $\mathbf{K} = (\pi, 0)$], bound states induced by a finite transverse field accommodate most of the spectral weight so that effectively a pseudo-gap at $\mathbf{K} = (0, \pi)$ is formed. It should not be overlooked that for the given parameters the lowest-energy gap of the system is the one-particle gap at $\Delta < 1$. However, as already remarked earlier, the one-particle physics is not relevant for the observable at hand.

Finally, we consider the system in the h_z - h_y -plane. For $h_y = 0$, the model is isospectral to the transverse-field Ising model (see Section 4.3) so that naturally our results should apply to the Ising model as well. To the best of our knowledge, this is the first study of a two-particle dynamical correlation function for the Ising model. As shown in Figure 7.21, the most notable difference to the case with a finite h_x -field in Figure 7.20 is the loss of spectral weight at energies close to $\omega = 2$; which becomes more pronounced with increasing h_y . At large transverse fields, one effectively obtains two distinct energy bands with most weight accumulated in the lower band. Even though there seems to be a bound state close to the continuum edge around the Γ point, using our results from Figure 7.6 we argue that this is an effect of a finite ϵ so that the spectral density is actually very high at the band edge, but there is no bound state at the point Γ .

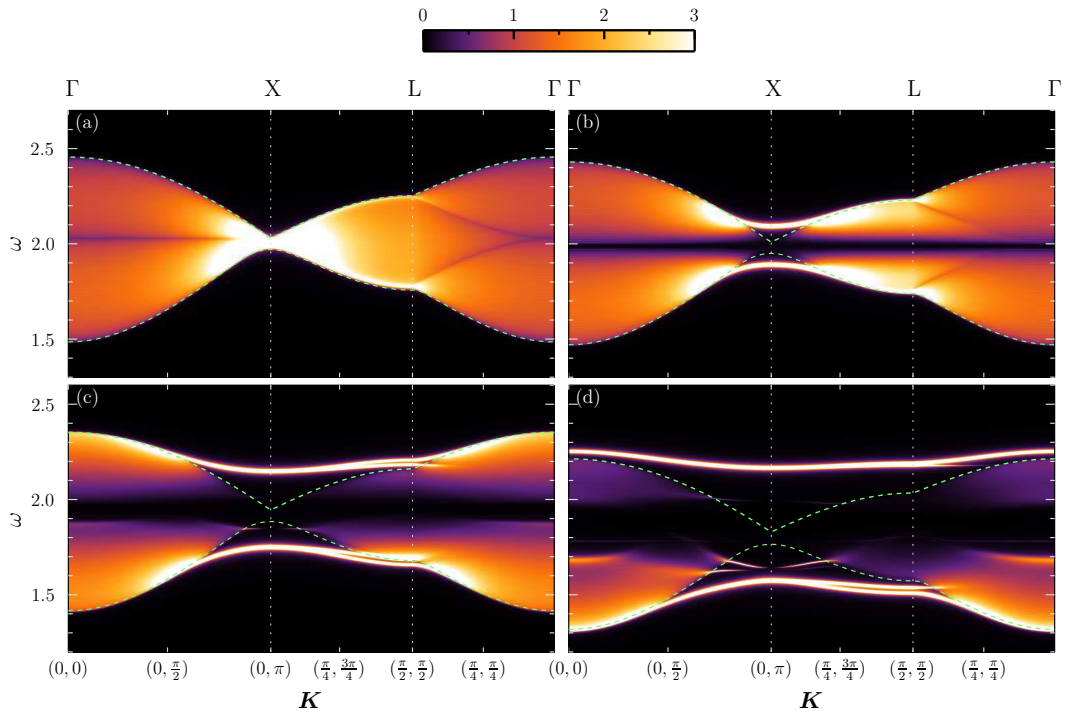


FIGURE 7.21: Spectral density of the toric code in the magnetic field $h_x = 0$, $h_z = 0.06$ and (a) $h_y = 0$, (b) $h_y = 0.1$, (c) $h_y = 0.2$, (d) $h_y = 0.3$. See Figure 7.6 for a comparison with the corresponding energy spectrum. The amplitude of $\mathcal{S}(\mathbf{K}, \omega)$ corresponds to the color scale at the top. The boundaries of the continuum are highlighted by green dashed lines.

Certainly it would be interesting to observe how the spectral densities change, as one approaches the boundary of the topological phase. In principle this problem could be tackled with optimized perturbation theory [87, 169] or, for $h_y = 0$, with quantum Monte Carlo, and shall be put forward for future projects.

7.4 Chapter summary

In this final chapter on the toric code in a uniform field, the spectral properties of the two-particle subspace in the topological phase have been studied. We have gained insight into the dependence of the spectrum on the magnetic field and, in particular, the behavior of collective bound states as well as dynamical correlation functions of the perturbed toric code in its topologically-ordered phase.

The bound states have been classified by their adiabatic connection to the exact eigenstates of the toric code in a transverse field. We have found elementary differences between the two distinct two-particle sectors of the toric code: \mathcal{H}^b and \mathcal{H}^f . In \mathcal{H}^b , the particle pair is always of the same flavor, thus the boundaries of the continuum hardly depend on the ratio h_x/h_z . By contrast, in the subspace \mathcal{H}^f , where one always has a

charge-flux pair, the continuum depends strongly on this ratio. While in the sector \mathcal{H}^b the energetic minimum of the lowest-lying bound state is always found at $\mathbf{K} = (0, 0)$, it does depend on \mathbf{K} in \mathcal{H}^f . It seems that bound states (in \mathcal{H}^b as well as in \mathcal{H}^f) are not likely to condense (and thus drive the phase transition) before the one-particle gap vanishes. However, an analysis of the two-particle subspace at larger magnetic fields is necessary to verify this statement.

For the first time, the density of states as well as two-particle dynamical correlation functions have been computed in the topological phase of the toric code in a magnetic field. In the special case of a single parallel field, our results are also relevant for the transverse-field Ising model. A plethora of structures inside the continuum has been revealed and interpreted as a superposition of local minima and maxima at 'saddle'-modes energies, as well as decaying bound states. We have shown that an increasing transverse magnetic field drives spectral weight out of the two-particle continuum into the bound (as well as antibound) states. Depending on the symmetry of the observable (symmetric or antisymmetric), certain bound states acquire the most spectral weight, while others are suppressed, corresponding to the symmetry of the adiabatically connected exact eigenstates of the toric code in a single transverse field. For certain directions of the magnetic field the bound states dominate the spectral density at low energies.

Kitaev's honeycomb model

One of the biggest obstacles in an experimental realization of the toric code is certainly the appearance of exotic multi-spin interactions which consist of four-body terms and require an absence of two- and three-body interactions. In experimentally accessible materials, the nearest-neighbor interaction is most often the dominant one. The topic of the present chapter is the Kitaev model on a honeycomb lattice. This model is based solely on two-spin interactions and therefore seems to be less difficult to implement than the toric code. Indeed, many experimental proposals have been already made for this model [51–53, 170, 171]. Moreover, Kitaev's honeycomb model is a prominent example of a topologically-ordered system and features, despite its simplicity, Abelian, non-Abelian and fermionic elementary excitations [36]. In the isolated dimer limit (see below), it is directly related to the toric code which emerges as an effective model at fourth order in perturbation theory [36, 50]. Furthermore, there is an extensive number of conserved quantities so that it is possible to solve the model exactly, as well as construct the exact ground state.

Within this chapter, we introduce the Kitaev model as well as its generalizations. We propose a new extension of the model which leads to an infinite set of exactly solvable models with Abelian vortices as elementary excitations in the low-energy regime [81]. At the isotropic point (also referred to as 'graphene point' in the following), all of these models are equivalent to the original one and have a vanishing gap. A time-reversal symmetry breaking term, e.g., a magnetic field, may open this gap, leading to a topological phase with non-Abelian (Ising-type) elementary excitations. Interestingly, the system can also be tuned into a topological phase where elementary excitations are Abelian \mathbb{Z}_2 anyons, by opening the gap without breaking the time-reversal symmetry. We are able to explain this gap-opening mechanism by considering the problem as a

special case of graphene in a *strongly-modulated* magnetic field, thereby establishing a new type of metal-insulator transition in this highly topical material [172].

8.1 Definitions and basic properties

The Kitaev model describes quantum spins-1/2 located at the vertices of a hexagonal lattice and interact via the Hamiltonian

$$H = - \sum_{\alpha=x,y,z} \sum_{(i,j)_\alpha} J_\alpha \sigma_i^\alpha \sigma_j^\alpha, \quad (8.1)$$

where σ_i^α are the usual Pauli matrices at sites i , and $(i,j)_\alpha$ denotes a link of type α , connecting sites i and j . In what follows, we consider only $J_\alpha > 0$; however, as we shall see below, the ground-state energy of this model does not depend on the sign of J_α . In the original model [36], Kitaev considered the case where the type of the link ($\alpha = x, y$, or z) depends only on its orientation, as depicted in Figure 8.1. The three-spin term breaks time-reversal symmetry and is essential to open a gap in the non-Abelian phase of the model¹. Before we discuss the physical properties of this model in detail, let us briefly

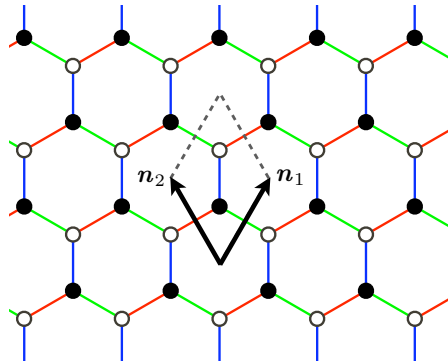


FIGURE 8.1: The Kitaev model with two sites per unit cell spanned by vectors \mathbf{n}_1 and \mathbf{n}_2 . Red, green, and blue links represent x , y , and z links respectively.

review its most important variations. The Kitaev model can also be defined on different lattices [173–177] or with a different underlying algebra [12, 178]. For spin-1/2, the exact solvability of this model is generally preserved, if the following two constraints are satisfied: (i) each site of the system must be trivalent, and (ii) the three links connected to a given site are of different types (x , y , and z). Thus, the Hamiltonian (8.1) can be defined and solved on any trivalent graph. In Ref. [81], we suggested to consider the Kitaev model on a honeycomb lattice but for different configurations of links, as for example the ones shown in Figure 8.2. The number of possible link distributions permitted by the condition (i) and (ii) is equivalent to the number of dimer covering on

¹To be more precise, this gap is required in order for the non-Abelian statistics to be well defined.

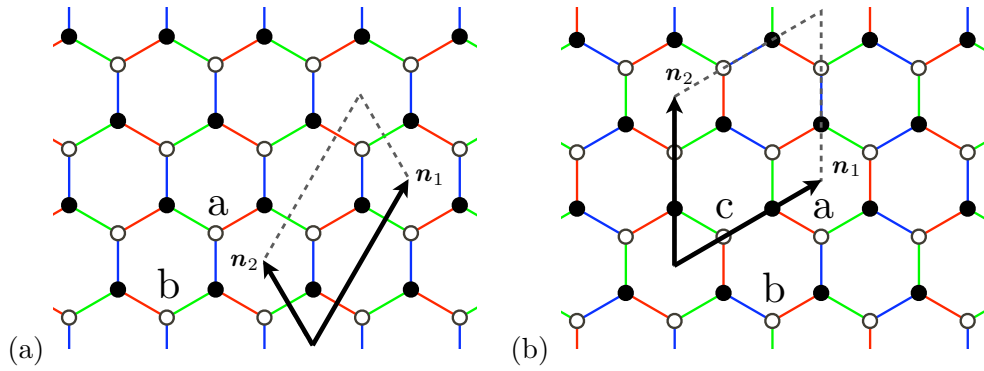


FIGURE 8.2: Variations of the Kitaev model with (a) four sites per unit cell and (b) six sites per unit cell. Conventions are the same as in Fig. 8.1 and labels 'a', 'b', and 'c' refer to the different kinds of plaquettes.

the honeycomb lattice. A simple way to see this, is to consider, without loss of generality, the limit $J_z \gg J_x, J_y$. A valid link configuration yields a set of strongly linked pairs of sites (dimers) weakly coupled by J_x and J_y , as shown in Figure 8.3.

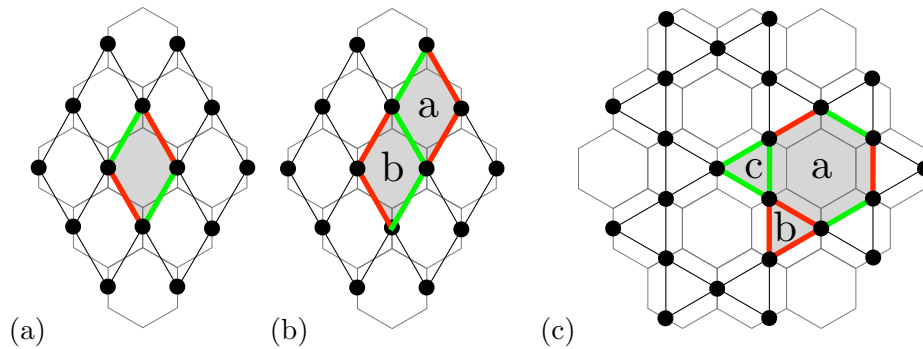


FIGURE 8.3: Effective lattices obtained in the isolated-dimer limit $J_z \gg J_x, J_y$ through a replacement of z -dimers by effective sites (filled black circles). The effective lattice of the original Kitaev model is shown in (a). The analogue effective lattices of the models from Figure 8.2 are presented in (b) and (c). Gray-shaded areas show the different types of effective plaquettes identified by the same labels as in Figure 8.2. Red (green) bonds denote x (y) links.

The honeycomb lattice has two sites per unit cell so that any periodic dimer covering will have $2n$ sites per unit cell. The distribution of link types in the original model, as shown in Figure 8.1, corresponds to $n = 1$ and shall be called 'covering I' in the following. For the bigger unit cells of link distributions shown in Figure 8.2 one finds $n = 2$ and $n = 3$ so that these models will be referred to as 'covering II' and 'covering III'. On the honeycomb lattice, the infinite number of dimer configurations (and thus the infinite number of models) will generally yield effective triangle-, square-, pentagon- and hexagon-plaquettes. As we shall see below, the shape of the effective plaquettes is directly related to the fundamental properties of the model.

The exact solvability of the Kitaev model and its generalizations roots on the fact that there is an extensive number of conserved quantities. The Hamiltonian (8.1) indeed commutes with every plaquette operator W_p , defined as

$$W_p = \prod_{i \in p} \sigma_i^{\text{out}(i)}, \quad (8.2)$$

where p is a hexagonal plaquette of the honeycomb lattice and $\text{out}(i)$ denotes the type of the link, connected to site i and facing outward with respect to p [36, 50]. Furthermore, all W_p operators commute with each other, as can be straightforwardly derived from the algebraic properties of Pauli operators (on the honeycomb lattice plaquettes share either zero, or an even number of sites), and have eigenvalues $w_p = \pm 1$ due to $W_p^2 = \mathbf{1}$. Following Kitaev [36], it is common to characterize the conserved \mathbb{Z}_2 degrees of freedom by saying that there is a vortex on plaquette p , if $w_p = -1$ and no vortex if $w_p = +1$. Since $[H, W_p] = 0$, one can diagonalize H in each vortex sector given by a configuration of the w_p 's. This is realized by an exact mapping to non-interacting fermions, to be discussed in the next section. However, let us anticipate the important result that in the transformed model one can use Lieb's argument [179] to argue that the ground state lies in the vortex-free sector. Similar to our discussion of the toric code in Chapter 4, not only the plaquette operators but rather all closed-loop operators W_l with $W_l = \prod_{i \in l} \sigma_i^{\text{out}(i)}$ are conserved. Especially for a lattice on a closed manifold with genus g , one can pick up our argumentation from Chapter 4 to assert that the ground-state degeneracy depends on the number of non-contractible loops, and consequently on the genus, which is a clear indication of topological order. To be more precise the number of degenerate ground states is 2^{2g} in the Abelian phase of the model. It should be mentioned that if one breaks the time-reversal symmetry, e.g., by exposing the model to a magnetic field, the model can be tuned into a distinct topological phase with non-Abelian Ising anyons as elementary excitations [36], where the degeneracy of the ground state in the presence of $2n$ well-separated anyons on a torus is 2^{2n} [180, 181]. However, we will not include time-reversal symmetry breaking terms in the following considerations.

As has been already mentioned earlier, the honeycomb model and the toric code are deeply related. Kitaev has shown [36] that perturbation theory for weakly-coupled dimers in the limit $J_z \gg J_x, J_y$ yields only a constant energy shift up to order three. At order four, the first non-trivial term has the same algebraic structure as the plaquette and star interactions we know from the toric code [see (4.1)]. Indeed, the effective model at order four is exactly connected to the toric code by a unitary transformation [36]. Thus the ground states in both models are in the same topological phase. A perturbation theory of higher order has been presented in Refs. [50, 79, 80]. Beyond order four, one obtains an extended toric code with multi-plaquette interactions. The same approach

has been used to investigate low-energy properties of the models shown in Figure 8.2. While covering I and covering II are rather similar, in the case of covering III an effective toric-code-like Hamiltonian on the kagome lattice emerges. The phase diagrams as well as the effective vortex-vortex interactions of these new dimer covering models have been studied in Refs. [81, 182].

8.2 Mapping to fermions

After the rather general discussion in the last paragraph, let us turn to the explicit solution of the model(s) and discuss the structure of the resulting phase diagram. Kitaev's idea was to use an enlarged Hilbert space where a single fermionic mode a_m is represented by *two* so-called Majorana modes c_{2m-1} and c_{2m}

$$c_{2m-1} = a_m + a_m^\dagger, \quad (8.3)$$

$$c_{2m} = \frac{1}{i} \left(a_m - a_m^\dagger \right). \quad (8.4)$$

Although one would expect that it is more complicated to work in a Hilbert space with a larger dimension, as we shall see below, this transformation brings the initial Hamiltonian to a simpler form. Obviously the properties of the Majorana operators are very different from fermions since the majoranas are identical to their own antiparticles and obey the commutator relation

$$c_m c_n + c_n c_m = 2\delta_{nm}. \quad (8.5)$$

A single spin-1/2 at site j is represented by two fermionic modes (say $a_{j,1}$ and $a_{j,2}$) and in the Majorana language, by four operators

$$c_{j,1} = a_{j,1} + a_{j,1}^\dagger, \quad c_{j,2} = \frac{1}{i} \left(a_{j,1} - a_{j,1}^\dagger \right), \quad (8.6)$$

$$c_{j,3} = a_{j,2} + a_{j,2}^\dagger, \quad c_{j,4} = \frac{1}{i} \left(a_{j,2} - a_{j,2}^\dagger \right). \quad (8.7)$$

In the following, we will use the helpful notation introduced by Kitaev [36]

$$c_{j,1} = b_j^x, \quad c_{j,2} = b_j^y, \quad c_{j,3} = b_j^z, \quad c_{j,4} = c_j. \quad (8.8)$$

The initial two-dimensional subspace (also called physical subspace) of the extended four-dimensional Hilbert space at site j can be identified by using the local projector $D_j = b_j^x b_j^y b_j^z c_j$ which acts as the identity in the original Hilbert space of the Kitaev

model. The Pauli operators σ_j^α become $\tilde{\sigma}_j^\alpha$ in the extended Hilbert space.

$$\tilde{\sigma}_j^x = ib_j^x c_j, \quad \tilde{\sigma}_j^y = ib_j^y c_j, \quad \tilde{\sigma}_j^z = ib_j^z c_j. \quad (8.9)$$

These operators fulfill the usual Pauli algebra and preserve the physical subspace since they commute with D_j . Finally the Hamiltonian (8.1) is transformed to

$$\tilde{H} = \frac{i}{2} \sum_{j,k} J_{jk} \hat{u}_{jk}^\alpha c_j c_k, \quad (8.10)$$

with $\hat{u}_{jk}^\alpha = ib_j^\alpha b_k^\alpha$. The operators \hat{u}_{jk}^α commute with the Hamiltonian and with each other. Due to (8.5), their eigenvalues are $u_{jk}^\alpha = \pm 1$. Thus, \tilde{H} obviously describes free fermions in a static \mathbb{Z}_2 gauge field. The transformed plaquette operator \tilde{W}_p is represented by a product of \hat{u}_{jk}^α along the boundary of a plaquette:

$$\tilde{W}_p = \prod_{j,k \in \text{boundary}(p)} \hat{u}_{jk}^\alpha. \quad (8.11)$$

It can easily be checked that the eigenvalues of \tilde{W}_p are indeed ± 1 . Every vortex configuration corresponds to a certain gauge. However, this correspondence is not unique, e.g., the vortex-free sector can be fixed by setting every u_{jk}^α to +1 (or to -1), as well as setting exclusively u_{jk}^z to +1 (or to -1) and so on. Generally, any vortex subspace can be realized by fixing the gauge fields. Then the problem is reduced to the one of free fermions, and numerical diagonalization can be applied efficiently. One should keep in mind that due to the enlarged Hilbert space a projection onto the physical subspace is necessary. This can in principle be avoided by using an alternative mapping based on Jordan-Wigner transformation [183], but we shall stick to the approach used by Kitaev.

The spectrum of the original Kitaev model (covering I) in the vortex-free subspace ($w_p = +1, \forall p$) consists of two fermionic bands $\varepsilon(\mathbf{k})$. Using Fourier transformation, one obtains the analytical result:

$$\varepsilon(\mathbf{k}) = \pm |f(\mathbf{k})|, \quad (8.12)$$

$$f(\mathbf{k}) = 2 \left(J_x e^{i\mathbf{k} \cdot \mathbf{n}_1} + J_y e^{i\mathbf{k} \cdot \mathbf{n}_2} + J_z \right), \quad (8.13)$$

with momentum \mathbf{k} and unit vectors in real space \mathbf{n}_i , defined in Figure 8.1. The fermionic gap for the case of covering I is then a linear function of the two-spin couplings J_i :

$$\Delta_I = \text{Max} \{2(J_z - J_x - J_y), 0\}, \quad (8.14)$$

where without loss of generality we consider the parameter region $J_z \geq J_x, J_y$. While for covering II we find the same expression for the gap, the covering III yields a totally

different result (see Ref. [81] for more details)

$$\Delta_{\text{III}} = 2\sqrt{J_x^2 + J_y^2 + J_z^2 - J_x J_y - J_y J_z - J_z J_x}. \quad (8.15)$$

A symmetric view on the resulting phase diagrams is given in the Figure 8.4.

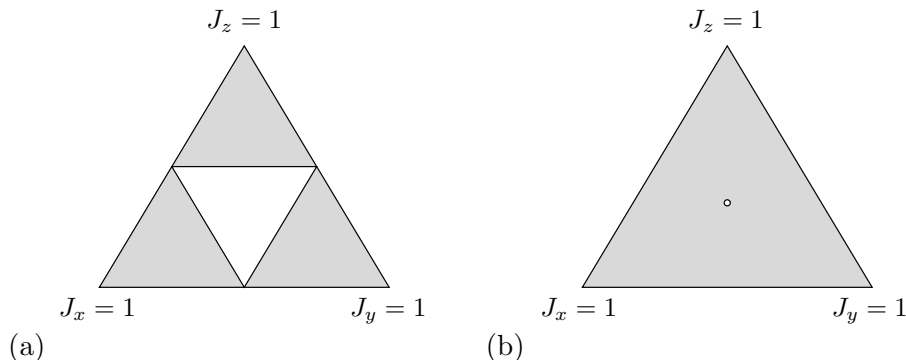


FIGURE 8.4: Phase diagrams of the Kitaev model for various dimer coverings. We choose a common parametrization of the two-spin couplings J_α , where $J_\alpha \geq 0$, and the depicted triangle lies on the plane intersecting each of the three J_α -axes at the points $J_\alpha = 1$. (a) Covering I and covering II have an equivalent phase diagram where the shaded areas are gapped and the white triangle in the center highlights the gapless domain. (b) The model described by covering III has a dramatically different phase diagram where the system is gapped everywhere except at the isotropic point. For any covering, one finds Abelian anyons as elementary excitations in the gapped regions as long as any time-reversal symmetry breaking operators are absent, otherwise also elementary excitations with non-Abelian statistics can arise [36, 81].

Kitaev has shown that in the gapped phases (shaded areas in Figure 8.4), vortices behave as Abelian anyons. Their statistics can be demonstrated explicitly with the same method we used in Section 4.2. More elegantly, one can simply argue that in the gapped phase the model is adiabatically connected to the dimer limit where we know that an extended toric code emerges as the effective low-energy theory. Therefore, the properties of elementary excitations must be the same. A finite magnetic field (or generally any time-reversal symmetry breaking operator) opens the fermionic gap inside the otherwise gapless regions of the phase diagram and gives rise non-Abelian excitations which are Ising anyons. This has been shown in Ref. [36] by computing the so-called Chern number [184] which is a topological invariant often used to characterize topological phases. We refer to Refs. [36, 185] for the precise definition of the Chern invariant. For our purposes it is sufficient to know that, as rigorously shown by Kitaev [36], this integer is directly related to the statistics of elementary excitations. An even (odd) Chern number unambiguously signals that the elementary excitations are Abelian (non-Abelian) anyons.

Certainly, the appearance of topological phases with Abelian as well as non-Abelian elementary excitations in a simple lattice model is quite fascinating and can be understood

in a formal as well as in a physical way, as shall be briefly explained in the following. A surprising variety of topological phases is generated when the Kitaev model is considered on a square-octagon lattice [174, 186], and a finite three-spin coupling² is included. This coupling breaks the time-reversal symmetry and is controlled by the amplitude K . Here, the Chern invariant is used to *distinguish* topological phases. As explained by Kells et al. in Ref. [186], due to the doubled number of energy bands (the unit cell of the square-octagon lattice contains four sites) the so-called transfer of Chern integers between distinct energy modes leads to a larger number of possible values for Chern numbers. Phases with different (odd as well as even) Chern numbers are realized by varying the parameters J_α and K . Lahtinen et al. [187] have found a variety of Abelian phases in the original Kitaev model on the honeycomb lattice by considering periodic vortex patterns (instead of the vortex-free sector). On the one hand, a multi-band spectrum and a Chern integer exchange mechanism similar to Ref. [186] is obtained. On the other hand, the emergence of different topological phases can be traced back to vortex-vortex interactions³.

Both works discussed in the previous paragraph (Refs. [186, 187]) rely on the (time-reversal symmetry breaking) three-spin coupling in order to open a fermionic gap at the isotropic point. Surprisingly, we find that even without a time-reversal symmetry breaking term this gap can be opened at the isotropic point and thus give rise to new Abelian phases. We shall explain the gap-opening mechanism in a more general setup in the following section.

8.3 Fate of Dirac points in a vortex superlattice

Motivated by the Kitaev model and its mapping onto Majorana fermions in a gauge field [see (8.10)], we consider the general problem of non-interacting fermions on the honeycomb lattice in the presence of magnetic vortices. Here, similarly to Ref. [188], the flux per plaquette can be tuned continuously, in contrast to the Kitaev model where this flux is restricted to two distinct values. Our main goal in this section is to show that, depending on a superlattice of vortices, a gap may open at zero energy. These results directly apply to Kitaev's honeycomb model in a vortex superlattice. At the same time we illustrate an original example of a metal-insulator transition induced by a strongly-modulated magnetic field in graphene (see below).

The electronic properties of graphene are commonly obtained from a tight-binding approximation on the honeycomb lattice. Its band structure has been known since several

²We remark that even when this coupling is included, the model is still exactly solvable [36].

³To be precise, Lahtinen et al. derive an effective model for Majorana fermions, where the effective interaction is renormalized by a fixed vortex configuration [187].

decades [189] and its modifications in the presence of a uniform magnetic field have been first investigated more than twenty years ago by Rammal [190]. The surprising experimental discovery of graphene by Geim and Novoselov [191] in 2004 has led to a Nobel prize and renewed the interest in this topic (see Ref. [192] for a review). One of graphene's most salient features in zero field is the existence of a point-like Fermi surface at zero energy, the celebrated Dirac points, giving rise to a relativistic dispersion in their neighborhood (the so-called Dirac cones). Interestingly, these discrete zero-energy states are still present when a uniform magnetic field is added [190, 193]. The stability of these states has led several groups to analyze the influence of a nonuniform magnetic field and it is now commonly accepted that a *smoothly*-modulated magnetic field is not sufficient to open a gap at zero energy [194–196]. In what follows, we will show that it is actually possible to open this gap by considering the opposite limit of a *strongly*-modulated magnetic field. In this case, unlike previous studies [194–196], one cannot neglect the coupling between Dirac cones which is directly responsible for this dramatic effect. As a consequence, the opening of the gap does not require the simultaneous presence of a scalar and a vector potentials.

To analyze this problem, we consider a vortex superlattice with fluxes $\pm\phi$ as depicted in Fig. 8.5. Our choice is motivated by the commensurability of the triangular and hexagonal structures and by the fact that this alternated pattern leads to the smallest possible unit cell of the superlattice. In the small- ϕ limit, we show that, although the system remains gapless at first order, a gap proportional to ϕ^2 may open, providing a nice example of a metal-insulator transition induced by a magnetic field in the honeycomb lattice. We derive the necessary and sufficient condition to open this gap in terms of the superlattice periodicity and we give an expression of the gap at order two in the small- ϕ limit. When the size of the superlattice unit cell increases, i.e., in the limit of vanishing vortex density ν , we find that the gap vanishes as $\nu \ln \nu^{-1}$. Although obtained in a perturbative framework, our conclusions remain qualitatively valid for arbitrary fluxes as checked by exact diagonalizations. Furthermore, at $\phi = \phi_0/2$ (ϕ_0 being the elementary flux quantum), the same gap-opening mechanism applies to the celebrated Kitaev model [36] introduced in the previous sections. However, in the case of graphene we consider free fermions, in contrast to the Kitaev model which is mapped to 'free' Majorana particles in an extended Hilbert space.

The starting point of our study is the following tight-binding Hamiltonian

$$H_{\text{tb}} = - \sum_{\langle i,j \rangle} t_{i,j} |i\rangle\langle j|, \quad (8.16)$$

where $|i\rangle$ denotes a spinless-electron state localized on site i . The sum is performed over all nearest-neighbor sites of the honeycomb lattice and the hopping term in the

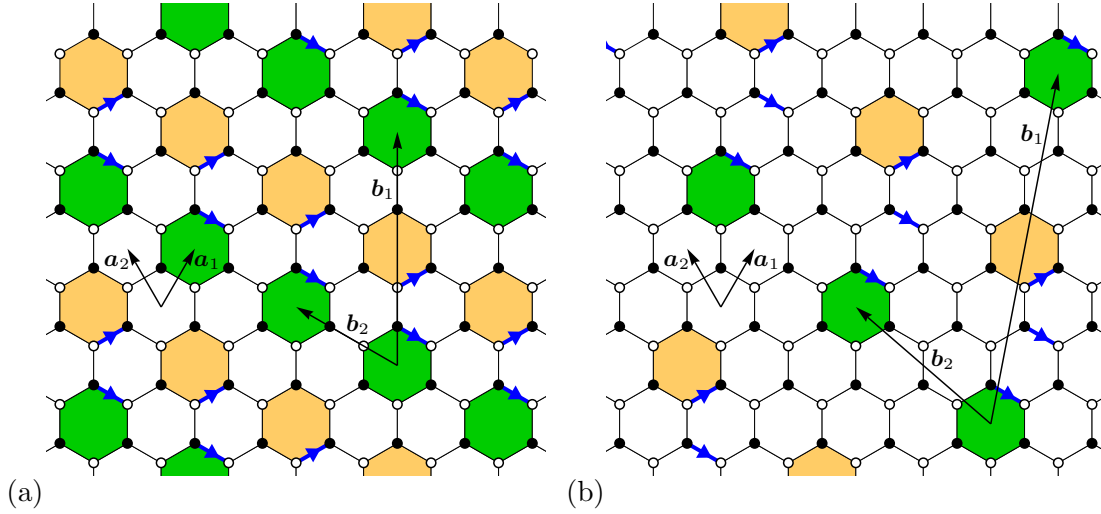


FIGURE 8.5: A piece of the magnetic vortex superlattice $\mathcal{L}(p, q)$ spanned by primitive vectors \mathbf{b}_1 and \mathbf{b}_2 for the specific cases (a) $p = 1, q = 1$, and (b) $p = 2, q = 1$. Vectors \mathbf{a}_1 and \mathbf{a}_2 are primitive vectors of the honeycomb lattice. Green (orange) plaquettes contain a flux $+\phi$ ($-\phi$), whereas white plaquettes are flux-free. Blue links with arrows indicate oriented hopping terms “carrying” the flux.

presence of a vector potential \mathbf{A} is given by the so-called Peierls substitution [197]: $t_{i,j} = t e^{\frac{2i\pi}{\phi_0} \int_i^j \mathbf{A} \cdot d\mathbf{l}}$. Thus, setting the flux and energy scales to unity ($\phi_0 = t = 1$), the (oriented) product of the hopping terms over a closed loop is simply $e^{2i\pi\phi}$, where ϕ is the dimensionless magnetic flux inside the corresponding loop.

The vortex superlattice considered here is defined as follows. Let us assume that there is a flux $+\phi$ in the elementary plaquette centered in \mathbf{r} . Then, the superlattice $\mathcal{L}(p, q)$ is generated by requiring that the plaquette located at $\mathbf{r} + \mathbf{b}_1/2$ contains a flux $-\phi$ and the one located at $\mathbf{r} + \mathbf{b}_2$ contains a flux $+\phi$, where

$$\mathbf{b}_1 = 2(p \mathbf{a}_1 + q \mathbf{a}_2), \quad (8.17)$$

$$\mathbf{b}_2 = -q \mathbf{a}_1 + (p + q) \mathbf{a}_2. \quad (8.18)$$

Vectors \mathbf{a}_1 and \mathbf{a}_2 are primitive vectors of the honeycomb lattice, and p, q are positive integers. In the following, without loss of generality, we only consider the case $p \geq q$. It is straightforward to check that the total flux per unit cell of $\mathcal{L}(p, q)$ spanned by \mathbf{b}_1 and \mathbf{b}_2 is zero. In addition, the vortex density, defined as the number of vortices per number of plaquettes in a unit cell, is simply given by

$$\nu = \frac{1}{p^2 + pq + q^2}. \quad (8.19)$$

A convenient gauge choice realizing such a flux pattern can be obtained starting from an initial $+\phi$ plaquette center and by choosing $t_{i,j} = e^{2i\pi\phi}$ for all links crossed by going p times in direction \mathbf{a}_1 and then q times in the direction \mathbf{a}_2 (see Figure 8.5 for concrete

examples). The orientation of the first link fixes all others since we wish to have a flux $-\phi$ in the final plaquette and zero in all intermediate ones. In other words, one creates a string of links carrying the flux. This string connects a vortex to an antivortex. As a side remark, let us note that with this gauge choice one can study any value of the flux without changing the size of the unit cell, in deep contrast with the uniform field problem discussed in Ref. [190].

As for any bipartite lattice, the spectrum of H_{tb} is symmetric with respect to the energy $\varepsilon = 0$ for all ϕ . For $\phi = 0$, it consists of two symmetric bands [189]

$$\varepsilon_{\pm}(\mathbf{k}) = \pm \left\{ 3 + 2 \cos(\mathbf{k} \cdot \mathbf{a}_1) + 2 \cos(\mathbf{k} \cdot \mathbf{a}_2) + 2 \cos[\mathbf{k} \cdot (\mathbf{a}_1 - \mathbf{a}_2)] \right\}^{1/2}. \quad (8.20)$$

We point out that this spectrum is exactly equivalent to the one of the Kitaev honeycomb model in the vortex-free sector, as introduced in (8.12), in the isotropic point $J_x = J_y = J_z = 1/2$. The symmetric bands touch at $\varepsilon = 0$ when the momentum \mathbf{k} coincides with the so-called Dirac points $\mathbf{D} = \frac{1}{3}\mathbf{a}_1^* + \frac{2}{3}\mathbf{a}_2^*$ and $\mathbf{D}' = \frac{2}{3}\mathbf{a}_1^* + \frac{1}{3}\mathbf{a}_2^*$, where \mathbf{a}_1^* and \mathbf{a}_2^* are primitive vectors of the reciprocal lattice associated to \mathbf{a}_1 and \mathbf{a}_2 ($\mathbf{a}_i^* \cdot \mathbf{a}_j = 2\pi\delta_{i,j}$). Consequently, the energy $\varepsilon = 0$ is four-fold degenerate for $\phi = 0$. We aim to determine the fate of these zero-energy states for $\phi \neq 0$. Note that in the limiting case $\phi = 1/2$, this problem is equivalent to Kitaev's honeycomb model with a fixed vortex sector, the vortices being placed on the superlattice $\mathcal{L}(p, q)$.

To address this problem, we shall analyze perturbatively the small- ϕ limit. However, one can already predict that if the perturbation does not couple any of the two eigenstates corresponding to \mathbf{D} with the two eigenstates corresponding to \mathbf{D}' , the system will remain gapless. Indeed, in this case, the single-cone approximation proposed in Refs. [194–196] can be made safely, leading to a finite gap only when a scalar as well as a vector potential are present. Thus, to open the gap one must have a perturbing potential which couples these two two-fold degenerate subspaces. Since this potential has, by construction, the same periodicity as $\mathcal{L}(p, q)$, this condition requires the existence of a reciprocal lattice vector associated to \mathbf{b}_1 and \mathbf{b}_2 which equals $\mathbf{D}' - \mathbf{D}$. In the following we will prove that this condition is equivalent to

$$\frac{1}{\nu} = 0 \pmod{3}, \quad (8.21)$$

where ν is the vortex density defined in (8.19). Dirac states then have a momentum $\mathbf{k} = (0, 0) \pmod{(\mathbf{b}_1^*, \mathbf{b}_2^*)}$ where \mathbf{b}_1^* and \mathbf{b}_2^* are primitive vectors of the reciprocal lattice associated to \mathbf{b}_1 and \mathbf{b}_2 ($\mathbf{b}_i^* \cdot \mathbf{b}_j = 2\pi\delta_{i,j}$). Let us underline that this is a necessary condition which might not be sufficient to open a gap but, as we shall see, it is. The explicit

expression of the reciprocal lattice vectors is found to be

$$\mathbf{b}_1^* = \frac{\nu}{2} \left[(p+q) \mathbf{a}_1^* + q \mathbf{a}_2^* \right], \quad (8.22)$$

$$\mathbf{b}_2^* = \nu (-q \mathbf{a}_1^* + p \mathbf{a}_2^*). \quad (8.23)$$

The necessary condition to couple the Dirac points yields

$$n \mathbf{b}_1^* + m \mathbf{b}_2^* = \pm \frac{1}{3} (\mathbf{a}_1^* - \mathbf{a}_2^*), \quad (8.24)$$

with $(n, m) \in \mathbb{Z}^2$. These equations are satisfied for

$$p = \pm (m - n), \quad (8.25)$$

$$q = \mp \frac{m + 2n}{2}. \quad (8.26)$$

Thus we obtain

$$\frac{1}{\nu} = p^2 + pq + q^2 = \frac{3}{4} (m^2 - 2mn + 4n^2). \quad (8.27)$$

Using the fact that p and q have been defined as integers, one follows that $1/\nu$ must be a multiple of three, hence (8.21) is indeed a required property of the vortex-superlattice potential to open a gap in graphene.

A naive first-order degenerate perturbation theory consists in considering the subspace spanned by the four Dirac states, denoted $|\psi\rangle_i$. At $\mathbf{k} = (0, 0)$ and zero flux, these states can be constructed exactly, as shall be explained in the following. We recall that the honeycomb lattice, as pictured in Figure 8.5, is built from two sublattices, say, Λ_b and Λ_w , each consisting of black and white sites respectively. Without loss of

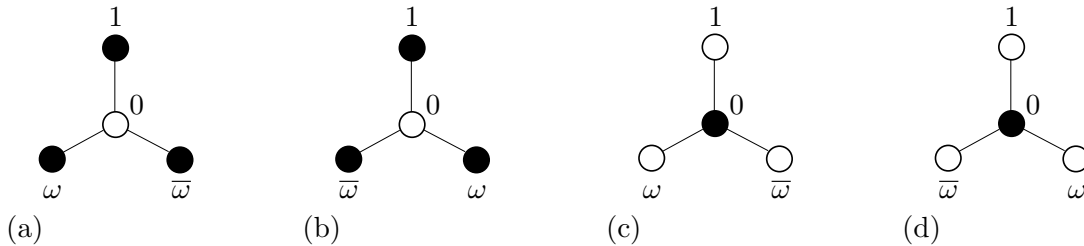


FIGURE 8.6: Exact construction of zero-energy eigenstates of H_{tb} at zero momentum (in the base \mathbf{b}_i^*) and flux $\phi = 0$. The figure shows elementary constituents of the honeycomb lattice as well as the corresponding amplitudes for the four Dirac states (a) $|\psi\rangle_1$, (b) $|\psi\rangle_2$, (c) $|\psi\rangle_3$, and (d) $|\psi\rangle_4$. Note that the cyclic order of the weights in each state is the same on every site.

generality we focus on the construction of the state $|\psi\rangle_1$. Here, all sites of sublattice Λ_w have zero-amplitudes, and the ones from sublattice Λ_b have weights 1, $\omega = e^{2i\pi/3}$ and

$\bar{\omega} = e^{-2i\pi/3}$ (which are the third roots of unity), as depicted in Figure 8.6 (a). Due to the trivalence of the lattice, every site from Λ_w is connected to exactly three sites from Λ_b (and vice versa). Therefore the action of the Hamiltonian H_{tb} on $|\psi\rangle_1$ leads to either a sum of three zeroes, or $1 + \omega + \bar{\omega} = 0$. Thus the state $|\psi\rangle_1$ is indeed a zero-energy eigenstate of the problem. The remaining three states can now be constructed in a similar way, by conjugating the amplitudes [Figure 8.6 (b)] and interchanging Λ_b and Λ_w [Figure 8.6 (c)-(d)]. It is important to note that the presented construction recipe works only if the amplitudes can be placed in a periodic way. This implies the condition

$$(p \bmod 3) = (q \bmod 3). \quad (8.28)$$

As can easily be checked, this is exactly equivalent to the condition (8.21) which selects the subclass of vortex superlattices $\mathcal{L}(p, q)$, we were interested in from the outset.

For small ϕ , the Hamiltonian (8.16) can be rewritten as

$$H_{\text{tb}} = H_0 + V, \quad (8.29)$$

$$= - \sum_{\langle i, j \rangle} |i\rangle\langle j| - \sum_{\langle i, j \rangle} \left(e^{2i\pi\phi(i, j)} - 1 \right) |i\rangle\langle j|, \quad (8.30)$$

$$= - \sum_{\langle i, j \rangle} |i\rangle\langle j| - \sum_{\langle i, j \rangle} (2i\pi\phi - 2\pi^2\phi^2 + \dots) |i\rangle\langle j|, \quad (8.31)$$

where H_0 is the unperturbed part with $\phi = 0$, and V is the flux-dependent perturbation with $\phi(i, j) = \phi$ on links $\langle i, j \rangle$ which we choose to fix the gauge (see for example Figure 8.5) and $\phi(i, j) = 0$ on all other links. Following standard perturbation theory [114], the perturbative expansion of (8.29) in the small ϕ limit yields

$$H_{\text{tb}} = h_0 + h_1 + h_2 + \dots, \quad (8.32)$$

$$h_0 = E_0 P_0, \quad (8.33)$$

$$h_1 = P_0 V P_0, \quad (8.34)$$

$$h_2 = P_0 V S V P_0, \quad (8.35)$$

where the eigenvalues of h_i are proportional to ϕ^i , E_0 is the ground-state energy and P_0 the projector onto the ground-state subspace U_0 . S is a resolvent operator, defined as follows

$$S = - \frac{1 - P_0}{H_0 - E_0}. \quad (8.36)$$

As we already know, the zero-energy level of H_{tb} is four-fold degenerate ($E_0 = 0$). The corresponding subspace U_0 is spanned by the Dirac states which we can construct exactly for any vortex superlattice $\mathcal{L}(p, q)$. Using our gauge choice, introduced in the paragraph

following (8.19), as well as the basis $|\psi\rangle_i$, introduced above, we find for general p and q at order one

$$P_0 V P_0 = \begin{pmatrix} 0 & 0 & M_1 & M_2 \\ 0 & 0 & M_2 & M_1 \\ M_1^* & M_2^* & 0 & 0 \\ M_2^* & M_1^* & 0 & 0 \end{pmatrix}. \quad (8.37)$$

The exact construction of the basis states allows us to derive general results for the matrix elements M_i . For arbitrary vortex superlattices $\mathcal{L}(p, q)$ we find

$$M_1 = i\pi\phi(p - q\omega), \quad (8.38)$$

$$M_2 = 0. \quad (8.39)$$

The zeroes of the corresponding characteristic polynomial

$$P(\lambda) = (\lambda^2 + \pi^2\phi^2\nu)^2, \quad (8.40)$$

are then clearly $\pm\pi\phi\sqrt{\nu}$. This way, we find, at order one and any vortex superlattice $\mathcal{L}(p, q)$, the finite gap $\Delta[\mathbf{k} = (0, 0)] = 2\pi\phi\sqrt{\nu}$.

One should bear in mind that the perturbation can shift the Dirac cones [198] (without renormalizing the Fermi velocity at $\varepsilon = 0$). In this case $\Delta[\mathbf{k} = (0, 0)]$ would not be the minimal gap. The reason is that the condition (8.21) together with the similar conic dispersions near \mathbf{D} and \mathbf{D}' implies that states in the vicinity of the Dirac cones are also coupled by the perturbation and one generally must look for $\mathbf{k} \neq (0, 0)$ states which have a lower gap. Of course, the corresponding subspace depends directly on the vector potential. For vortex configurations fulfilling (8.21), we indeed find that, at first order in ϕ , the Dirac cones are shifted along the boundary of the Brillouin zone. For $\nu \leq 1/12$ we obtain the *exact* result that the state which has the lowest-positive energy is found for

$$\mathbf{k}_0 = -\frac{\phi}{2}\mathbf{b}_2^*. \quad (8.41)$$

We have checked by exact diagonalizations that (8.41) is valid even for large values of the flux ϕ (outside the perturbative regime). While this remarkable result remains to be understood, we conjecture that the state with the lowest positive energy is always found at \mathbf{k}_0 . Of course, the corresponding energy may be degenerate and found also for other momenta as is, for example, the case for $\phi = 1/2$.

As a next step, we perform degenerate perturbation theory in the $\mathbf{k} = \mathbf{k}_0$ subspace. Consistently with exact diagonalization results, we find that all matrix elements of h_1 are exactly zero. At second order, the computation becomes more involved, even though the condition (8.41) greatly simplifies the problem. Thus, we first concentrate on vortex superlattices with highest vortex densities satisfying condition (8.21). The second-order term of the gap can be computed analytically for certain cases, as it is presented in Table 8.1.

$1/\nu$	p	q	$\Delta/(\pi\phi)^2$
3	1	1	1/3
9	3	0	5/21
12	2	2	1/6
21	4	1	0.077586
27	3	3	0.061324
36	6	0	11/130

TABLE 8.1: Gap $\Delta(\mathbf{k}_0) = 0$ at order ϕ^2 for the first values of $1/\nu$ satisfying Eq. (8.21). For $1/\nu = 21$ and 27 , the gap cannot be expressed as a simple fraction and we only give the first digits obtained numerically.

Although, in general, it is difficult to get a simple expression of Δ for arbitrary vortex superlattices $\mathcal{L}(p, q)$, one can derive exact formulas for the special case $q = 0$ (p being a multiple of 3) that allow one to (numerically) investigate large unit cell systems that would be out of reach with exact diagonalizations. From now on, we will mainly focus on this subset of configurations for which the gap at order 2 reads

$$\frac{\Delta(p, q = 0)}{(\pi\phi)^2} = \mathcal{C}_p - \sqrt{\mathcal{B}_p^2 + \left(\mathcal{A}_p - \frac{1}{p}\right)^2}, \quad (8.42)$$

with

$$\begin{aligned} \mathcal{A}_p = \frac{1}{2p^4} \sum_{n=0}^{p-1} \sum_{m=1}^{2p-1} \frac{\xi(p, m)}{\varepsilon^2(m, n)} \left\{ 3 + 4 \cos \left[\pi \left(\frac{m}{p} + \frac{2}{3} \right) \right] + 2 \cos \left[2\pi \left(\frac{m}{p} - \frac{1}{3} \right) \right] \right\} \\ \times \left\{ 1 + \cos \left(\frac{2\pi n}{p} \right) + \cos \left[\frac{\pi}{p} (2n - m) \right] \right\}, \end{aligned} \quad (8.43)$$

$$\begin{aligned} \mathcal{B}_p = \frac{1}{2p^4} \sum_{n=0}^{p-1} \sum_{m=1}^{2p-1} \frac{\xi(p, m)}{\varepsilon^2(m, n)} \left\{ 3 + 4 \cos \left[\pi \left(\frac{m}{p} + \frac{2}{3} \right) \right] + 2 \cos \left[2\pi \left(\frac{m}{p} - \frac{1}{3} \right) \right] \right\} \\ \times \left\{ \sin \left(\frac{2\pi n}{p} \right) + \sin \left[\frac{\pi}{p} (2n - m) \right] \right\}, \end{aligned} \quad (8.44)$$

$$\begin{aligned} \mathcal{C}_p = \frac{4}{p^4} \sum_{n=0}^{p-1} \sum_{m=1}^{2p-1} \frac{\xi(p, m)}{\varepsilon^2(m, n)} \left[\cos \left(\frac{2\pi m}{p} \right) - \cos \left(\frac{\pi m}{p} \right) \right] \\ \times \left\{ 1 + \cos \left(\frac{2\pi n}{p} \right) + \cos \left[\frac{\pi}{p} (2n - m) \right] \right\}, \end{aligned} \quad (8.45)$$

where the sum over m is performed over odd integers only. For convenience, we have introduced $\varepsilon^2(m, n) = \varepsilon_{\pm}^2(\mathbf{k} = \frac{m}{2p}\mathbf{a}_1^* + \frac{n}{p}\mathbf{a}_2^*)$ [see (8.20)], and

$$\xi(p, m) = \begin{cases} \sin^{-2}\left(\frac{3\pi m}{2p}\right) & \text{if } m \neq 0 \pmod{\frac{p}{3}}, \\ \frac{1-(-1)^{p/3}}{2} & \text{otherwise.} \end{cases} \quad (8.46)$$

In the large- p limit, it is clear that Δ vanishes because one has to recover the spectral properties of the zero-flux problem. To analyze this infinitely-diluted vortex limit, we computed the gap using Eq. (8.42) up to $p = 20000$. A close inspection of \mathcal{A}_p , \mathcal{B}_p , and \mathcal{C}_p led us to conjecture that the gap vanishes as $\Delta/\phi^2 \sim \nu \ln \nu^{-1}$ in the large- $(p = 1/\sqrt{\nu})$ limit. A convincing check of this result is displayed in Fig. 8.7.

A natural question that arises at this stage concerns the behavior of the gap away from the perturbative regime analyzed up to now. To investigate arbitrary fluxes, one must diagonalize H numerically but the main advantage is that one only has to consider the subspace corresponding to $\mathbf{k} = \mathbf{k}_0$ where the lowest-positive energy state lies. However, for arbitrary fluxes, one is restricted to small values of p since the number of sites per unit cell is $4p^2$ and we need the full spectrum of the $\mathbf{k} = \mathbf{k}_0$ subspace. In Fig. 8.8, we

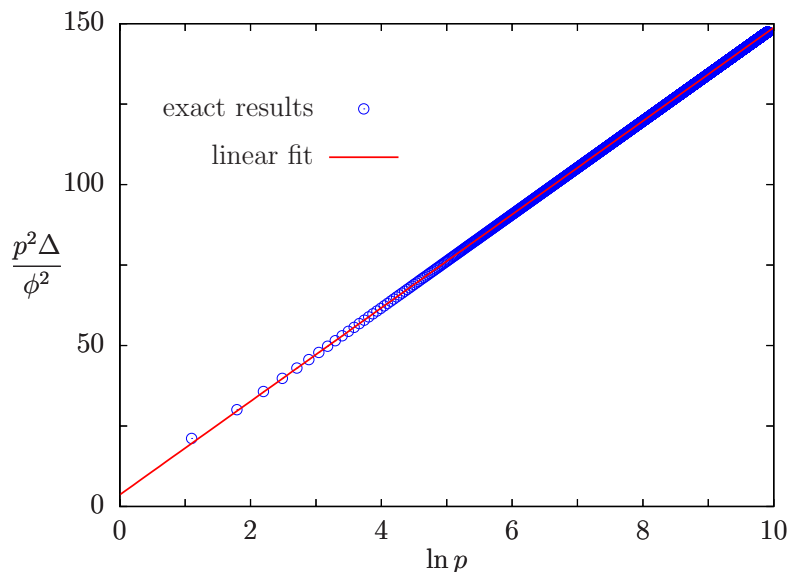


FIGURE 8.7: Behavior of $p^2\Delta/\phi^2$ as a function of $\ln p$ (for $q = 0$) in the small- ϕ limit. Exact results are obtained from Eq. (8.42) and the full line is a linear fit in good agreement with the conjecture discussed in the text.

display the behavior of the gap as a function of ϕ and for $q = 0$ and $p = 3, 6, \dots, 51$. As can be seen, Δ is a monotonously decreasing (increasing) function of p (of ϕ in the interval $[0, 1/2]$). We have also observed that the way Δ vanishes when p increases depends on ϕ . However, the lack of large- p data prevents to perform a sound analysis of these behaviors.

As already observed in the small- ϕ limit (see Table 8.1), the maximum value of the gap is obtained for the largest vortex density satisfying Eq. (8.21), i.e., $\nu = 1/3$, but it is also obtained for the largest possible flux, i.e., $\phi = 1/2$. In this case we can derive the exact expression of the gap. Since the unit cell of the vortex superlattice which realizes the vortex filling $\nu = 1/3$ consists of six sites, one has to diagonalize a 6×6 matrix. Denoting x^* , the smallest-positive root of the following polynomial

$$P(x) = x^6 - 18x^5 + 117x^4 - 340x^3 + 428x^2 - 176x + 16, \quad (8.47)$$

one gets

$$\Delta(p = 1, q = 1, \phi = 1/2) = 2\sqrt{x^*} \simeq 0.70884. \quad (8.48)$$

Let us remind that for $\phi = 1/2$ the problem considered here is directly connected to

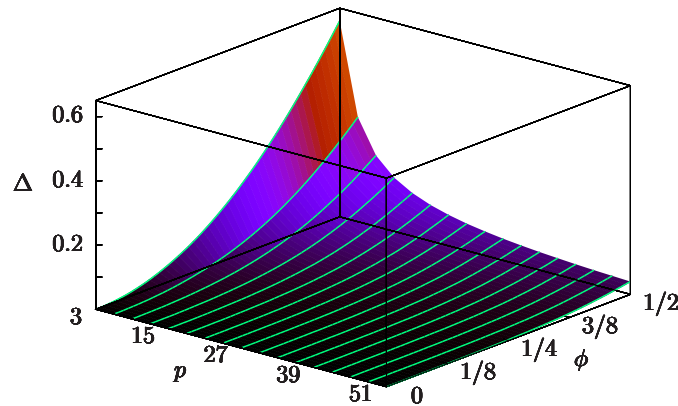


FIGURE 8.8: Δ as a function of ϕ and p (for $q = 0$). The maximum is reached for $p = 3$ and $\phi = 1/2$ where $\Delta \simeq 0.611132$.

Kitaev's honeycomb model, where the value of the (effective) flux in each elementary plaquette is restricted to $\phi = 0$ or $1/2$. This correspondence allowed Kitaev to identify the vortex configuration where the ground state of his system (Fermi sea at half-filling in the present electron language) lies. Indeed, as early suggested in the flux-phase framework [199–201], the lowest energy at half-filling is obtained for $\phi = 0$. In this problem, the more general question was: for a given electron density, what is the flux density (and the flux pattern) which minimizes the energy? Although the answer has been provided by Lieb [179] for the special case of half-filling, exact results are still missing for arbitrary electron density.

An interesting question is how to observe this metal-insulator transition induced by a vortex superlattice in the honeycomb lattice. Obviously, the main difficulty is the realization of the superlattice with the *ad hoc* parameters. The most realistic choice would be a flux $\phi = 1/2$ for which vortices and antivortices are equivalent and one

can use the exact correspondence to the Kitaev model for which many experimental proposals exist [51–53, 170, 171]. Otherwise, in the context of graphene, a type-II superconductor might be used in the mixed state where the Abrikosov vortex lattice is found. Then, given $\phi = 1/2$, one could think about gluing a graphene sheet on top of the superconductor. However, one faces the problem that the vortex core is much larger than a single elementary plaquette. One therefore has to investigate the gap-opening problem in the presence of extended though localized flux spots. Another appealing approach would be to consider optical flux lattices recently suggested in Refs. [202, 203] that seem especially adapted to our problem.

Finally, given the occurrence of Dirac points in many experimental devices (see Refs. [198, 204] for a recent discussion), we hope that the present work will motivate further investigations concerning the fate of these singularities in the presence of a vortex superlattice.

8.4 Chapter summary

In this study, we have introduced an infinite family of exactly solvable models based on Kitaev’s exactly solvable honeycomb model on trivalent lattices. The original model by Kitaev is one of the simplest examples of a system with a topologically-ordered ground state. The gapped elementary excitations are fermions as well as Abelian \mathbb{Z}_2 anyons. When a time-reversal symmetry breaking terms is added, new topological phases arise with non-Abelian Ising anyons as elementary excitations. In literature, a variety of extensions of the Kitaev model has been proposed, most of which suggest to change the lattice (maintaining its trivalent structure). In contrast, our idea is to keep the honeycomb lattice and change the link configurations or, for a fixed link distribution, to vary the flux configurations. As we have shown, changing the distribution of coupling types in the Kitaev model can lead to major changes in the phase diagram, e.g., in our covering III the gapless phase is reduced to a single point. We have investigated the effect of vortex superlattices in Kitaev’s original model (at its isotropic point) by considering it as a special case of graphene in a strongly-modulated magnetic field. Surprisingly, certain vortex configurations may open a gap. We explain the gap opening mechanism by showing that a magnetic superlattice leads to a direct coupling of the Dirac cones. In addition, we perform a second-order perturbation theory and obtain the gap as a function of the superlattice.

The present study raises a complementary question: given a flux density, what is the flux pattern which maximizes the gap? Undoubtedly, this question is even more difficult and the answer likely depends on the electron density. For the Kitaev model (half-filling and $\phi = 0, 1/2$), we investigated several periodic configurations corresponding to

fixed flux density ν satisfying (8.21) and we are led to conjecture that the flux pattern maximizing the gap is always $\mathcal{L}(3, 0)$. One way to understand this result is to argue that the vortex-vortex interaction for $\phi = 1/2$ leads to a formation of a triangular (Abrikosov-like) superlattice as an optimal pattern. However, it would be valuable to prove this result rigorously. Alternatively, one could also try to find gapped flux configurations for arbitrary ν . It would also be worth adding further hopping processes, as discussed in Ref. [205], that may give rise to a nontrivial insulator. Such considerations are clearly beyond the scope of the present work, but we hope to have underlined that interesting phenomena may occur for nontrivial vortex configurations in the honeycomb lattice (see also Refs. [187, 188] for related studies of the Kitaev model). An obvious consequence of our results for the Kitaev model is that there must be a finite gapped region around the isotropic point where a gap is induced by the vortex superlattice. The reason is that an insulator, as the one considered here, is robust to small deformations like for example anisotropies in the hopping elements.

Summary and Discussion

In this chapter we outline the results obtained in this thesis and give a perspective for further studies.

Computational aspects

We have considered the toric code in a uniform magnetic field. In contrast to previous studies, limited to a single transverse or parallel fields, we allow the field to point in an arbitrary direction. As we have explained in Section 4.3, this brings about a substantial increase in complexity concerning the quantum fluctuations. Therefore, we have optimized the pCUT method to give results valid in the thermodynamic limit from calculations on finite rectangular checkerboard graphs with open boundary conditions.

With this optimization, we were able to perform perturbation theory up to high orders. We have computed the series expansion of the ground-state energy in the low-field limit up to order 10, the single-quasi-particle dispersion up to order 8 (order 9, in a parallel field), and matrix elements of the effective two-quasi-particle sub-block up to order 6. In the high-field limit, we have computed the series expansion of the ground-state energy, as well as the single quasi-particle dispersion up to order 5. For the specific case of zero transverse field and a symmetric parallel field ($h_x = h_z$) the series have been obtained up to order 7.

A possible optimization of this procedure could be a full graph expansion. Also one could use floats instead of rational numbers for the coefficients of the series. Obviously, a magnetic field in a specific direction is much easier to handle. Thus it could be useful to perform a series expansion for particular interesting points that we have identified in

the phase diagram.

Phase diagram of the toric code

Using various extrapolation schemes and our perturbative series of the single-anyon dispersion, as well as iPEPS data provided by Dr. Román Orús, we have determined the boundary of the topological phase of the toric code in a magnetic field. For specific points of the phase diagram we were able to compare to known results and estimate the precision of our calculations. In a three-dimensional view, the topological phase of the toric code is bounded by two second-order and one first-order phase transition planes. In regions where the phase transition is of second order, we have computed critical exponents which agree with the universality class of the 3d Ising model. The phase transition on the symmetry plane $h_x = h_z$ clearly belongs to a different universality class. In the high-field limit, results are less conclusive. However, it seems that the first-order transition line in the plane $h_y = 0$ evolves into an additional first-order plane for $h_y > 0$.

Several open questions concerning the phase diagram still remain. It is not fully clear whether the continuously varying gap exponent on the symmetry plane $h_x = h_z$ is a physical feature or rather a crossover between parameter regions with different universality classes. A natural task would be to use iPEPS in order to investigate the shape of the first-order transition plane which we roughly outlined with high-field expansions. Additionally, one could try to push these expansions to higher orders and analyze the behavior of bound states in the high-field limit. It would be interesting to find out whether the intersection point $\mathcal{P}_{\text{crit}}$ of all three phase transition planes is a conformal quantum critical point or not. We have observed a remarkable agreement in our series extrapolations at $\mathcal{P}_{\text{crit}}$. Thus, we were able to determine its precise location and found gap exponents very close to $z = 2$ and $\nu = 0.5$. Furthermore, it would be interesting to see what kind of physics is found in models similar to the toric code, i.e., lattice models with topologically-ordered ground states. Possible candidates are the toric code with asymmetric or negative amplitudes of charges and fluxes, the toric code on different lattices, the \mathbb{Z}_N toric code or string-net models.

Bound states and dynamical correlation functions

We have computed matrix elements of the effective low-energy Hamiltonian in the two-quasi-particle subspace. In a next step, we have used exact diagonalizations to determine the spectrum in the bosonic as well as in the fermionic channels of the model. We have

found and analyzed bound states and their dependence on the magnetic field. In addition, we have computed the density of states as well as dynamical correlation functions and have studied how they are affected by a magnetic field. We have understood certain features of the two-particle continuum from single-particle dispersions and found a symmetry argument, explaining why the spectral density of certain bound states is very high or suppressed.

Of course, the most exciting continuation of this study would be a comparison with experimental data. However, to this day, the toric code has not been realized, although many experimental proposals exist. The fate of bound states in the parameter region close to the phase transition could be determined with optimized perturbation theory which allows to extrapolate the matrix elements of the effective Hamiltonian. The analysis of spectral densities close to the phase transition point should also involve a study of the four-particle channel which cannot be neglected for relatively high magnetic fields. However, it is a highly non-trivial task to obtain and especially diagonalize the four-particle block of the effective Hamiltonian.

Kitaev's honeycomb model

We have found that, in its gapless phase, Kitaev's honeycomb model may acquire a gap in the presence of a vortex superlattice. This is particularly interesting because this vortex lattice does not break the time-reversal symmetry. We have generalized the problem to the one of graphene in a strongly-modulated magnetic field and have explained how the symmetry of the vortex superlattice is the relevant factor in the gap-opening mechanism. Using perturbation theory, we have shown that this gap vanishes as $\nu \ln \nu^{-1}$ in the limit of low vortex density ν .

Since we have only studied a certain subclass of vortex superlattices (the ones with the triangular symmetry of the honeycomb), it is natural to ask whether other vortex configurations (regular or random) would open this gap or minimize the energy for a fixed vortex filling.

Concluding remarks

In this thesis, we aimed to learn more about topological phases under a perturbation. We have analyzed two standard models in this area of research: Kitaev's toric code and honeycomb models. These models are among the simplest ones with topologically ordered ground states, and therefore often serve as trial candidates to study the properties of topologically-ordered matter as well as properties of elementary excitations with fractionalized quantum numbers. They are good candidates to realize a topological quantum

memory so that it is important to know how stable the topological phase is under external perturbations. We have answered this question for the toric code in a uniform magnetic field through a quantitative analysis of the boundaries of its topological phase. Despite a tremendous interest in the toric code, this model has not yet been realized in an experiment. The spectral properties of the toric code in a magnetic field, especially the dynamical correlation functions computed in this thesis, predict distinct features one should observe in an experiment. In Kitaev's honeycomb model, we have found an interesting gap-opening mechanism and we have illuminated the connection between this model in a vortex superlattice and graphene in a strongly modulated magnetic field.

Our study of topological quantum phase transitions in the toric code has been performed by means of series expansions in combination with a variational method. This approach opens a promising route to study a wide range of distinct models with topologically ordered ground states.

Effective operators

A.1 Toric code in the low-field limit

When the toric code is perturbed by a uniform magnetic field, the action of Pauli matrices can be represented in terms of charge and flux creation and annihilation operators. The perturbing operators act on individual spins of the lattice and thus modify the local eigenvalues of the neighboring stars and plaquettes. In the same spirit as in Section 5.3.1, we introduce a notation where a local state on an elementary piece of the toric code lattice is represented by set of bits. For example, the state shown in Figure A.1 will be denoted as $|00000\rangle$ since it contains zero

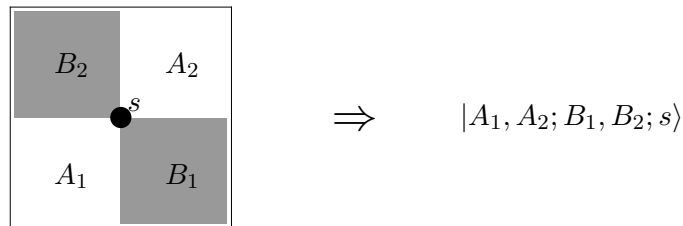


FIGURE A.1: Representing a local toric code state by a set of bits. The eigenvalues of A_s (white tiles) and B_p (gray tiles) are either +1 or -1, depending on whether a particle is present or not. Our convention is that an absent particle is represented by a bit 0, otherwise the bit is set to 1. The bit s represents the spin-1/2 degree of freedom and will be set to 0 (1) if the corresponding spin is up (down). We follow the convention that the degrees of freedom denoted on the left are represented by the ket-vector on the right, where operators are replaced by bits representing the corresponding eigenvalues.

particles and the spin is down. With this notation at hand the action of Pauli operators has been summarized in Tables A.1, A.2, and A.3.

T_0		T_{+2}		T_{-2}		
$ 10; B_1 B_2; 0\rangle$	\rightarrow	$ 01; B_1 B_2; 0\rangle$	$ 00; B_1 B_2; 0\rangle \rightarrow 11; B_1 B_2; 0\rangle$ $ 00; B_1 B_2; 1\rangle \rightarrow - 11; B_1 B_2; 1\rangle$	$ 11; B_1 B_2; 0\rangle$	\rightarrow	$ 00; B_1 B_2; 0\rangle$
$ 01; B_1 B_2; 0\rangle$	\rightarrow	$ 10; B_1 B_2; 0\rangle$		$ 11; B_1 B_2; 1\rangle$	\rightarrow	$- 00; B_1 B_2; 1\rangle$
$ 10; B_1 B_2; 1\rangle$	\rightarrow	$- 01; B_1 B_2; 1\rangle$				
$ 01; B_1 B_2; 1\rangle$	\rightarrow	$- 10; B_1 B_2; 1\rangle$				

TABLE A.1: Action of σ^z . B_1 and B_2 can independently be replaced by bits 0 or 1.

T_0		T_{+2}		T_{-2}	
$ A_1 A_2; 10; 0\rangle$	$\rightarrow A_1 A_2; 01; 1\rangle$	$ A_1 A_2; 00; 0\rangle$	$\rightarrow A_1 A_2; 11; 1\rangle$	$ A_1 A_2; 11; 0\rangle$	$\rightarrow A_1 A_2; 00; 1\rangle$
$ A_1 A_2; 01; 0\rangle$	$\rightarrow A_1 A_2; 10; 1\rangle$	$ A_1 A_2; 00; 1\rangle$	$\rightarrow A_1 A_2; 11; 0\rangle$	$ A_1 A_2; 11; 1\rangle$	$\rightarrow A_1 A_2; 00; 0\rangle$
$ A_1 A_2; 10; 1\rangle$	$\rightarrow A_1 A_2; 01; 0\rangle$				
$ A_1 A_2; 01; 1\rangle$	$\rightarrow A_1 A_2; 10; 0\rangle$				

TABLE A.2: Action of σ^x . A_1 and A_2 can independently be replaced by bits 0 or 1.

T_0		T_{+2}		T_{-2}	
$ 11; 00; 0\rangle$	$\rightarrow i 00; 11; 1\rangle$	$ 10; 00; 0\rangle$	$\rightarrow i 01; 11; 1\rangle$	$ 01; 11; 0\rangle$	$\rightarrow i 10; 00; 1\rangle$
$ 11; 00; 1\rangle$	$\rightarrow -i 00; 11; 0\rangle$	$ 01; 00; 0\rangle$	$\rightarrow i 10; 11; 1\rangle$	$ 10; 11; 0\rangle$	$\rightarrow i 01; 00; 1\rangle$
$ 00; 11; 0\rangle$	$\rightarrow i 11; 00; 1\rangle$	$ 00; 10; 0\rangle$	$\rightarrow i 11; 01; 1\rangle$	$ 11; 01; 0\rangle$	$\rightarrow i 00; 10; 1\rangle$
$ 00; 11; 1\rangle$	$\rightarrow -i 11; 00; 0\rangle$	$ 00; 01; 0\rangle$	$\rightarrow i 11; 10; 1\rangle$	$ 11; 10; 0\rangle$	$\rightarrow i 00; 01; 1\rangle$
$ 10; 10; 0\rangle$	$\rightarrow i 01; 01; 1\rangle$	$ 10; 00; 1\rangle$	$\rightarrow -i 01; 11; 0\rangle$	$ 01; 11; 1\rangle$	$\rightarrow -i 10; 00; 0\rangle$
$ 10; 01; 0\rangle$	$\rightarrow i 01; 10; 1\rangle$	$ 01; 00; 1\rangle$	$\rightarrow -i 10; 11; 0\rangle$	$ 10; 11; 1\rangle$	$\rightarrow -i 01; 00; 0\rangle$
$ 01; 10; 0\rangle$	$\rightarrow i 10; 01; 1\rangle$	$ 00; 10; 1\rangle$	$\rightarrow -i 11; 01; 0\rangle$	$ 11; 01; 1\rangle$	$\rightarrow -i 00; 10; 0\rangle$
$ 01; 01; 0\rangle$	$\rightarrow i 10; 10; 1\rangle$	$ 00; 01; 1\rangle$	$\rightarrow -i 11; 10; 0\rangle$	$ 11; 10; 1\rangle$	$\rightarrow -i 00; 01; 0\rangle$
$ 10; 10; 1\rangle$	$\rightarrow -i 01; 01; 0\rangle$				
$ 10; 01; 1\rangle$	$\rightarrow -i 01; 10; 0\rangle$				
$ 01; 10; 1\rangle$	$\rightarrow -i 10; 01; 0\rangle$				
$ 01; 01; 1\rangle$	$\rightarrow -i 10; 10; 0\rangle$				
			T_{+4}		T_{-4}
		$ 00; 00; 0\rangle$	$\rightarrow i 11; 11; 1\rangle$	$ 11; 11; 0\rangle$	$\rightarrow i 00; 00; 1\rangle$
		$ 00; 00; 1\rangle$	$\rightarrow -i 11; 11; 0\rangle$	$ 11; 11; 1\rangle$	$\rightarrow -i 00; 00; 0\rangle$

TABLE A.3: Action of σ^y .

A.2 Toric code in the high-field limit

In the following, we list the effective action of the toric code operators in the limit of high magnetic fields. The 2^4 possible four-spin states of the elementary cell will be denoted, similarly to the previous paragraph, by a set of four bits where 0 represents a spin up and 1 represents a spin down. The action of \tilde{A}_s [as defined in (5.94)] is gathered into tables where each header shows the corresponding effective particle creation and annihilation operator T_n .

T_{+4}	
$ 0000\rangle$	$\rightarrow -\sin^4 \phi 1111\rangle$

T_{-4}	
$ 1111\rangle$	$\rightarrow -\sin^4 \phi 0000\rangle$

T_{+3}	
$ 1000\rangle$	$\rightarrow -\cos \phi \sin^3 \phi 1111\rangle$
$ 0100\rangle$	$\rightarrow -\cos \phi \sin^3 \phi 1111\rangle$
$ 0010\rangle$	$\rightarrow -\cos \phi \sin^3 \phi 1111\rangle$
$ 0001\rangle$	$\rightarrow -\cos \phi \sin^3 \phi 1111\rangle$
$ 0000\rangle$	$\rightarrow \cos \phi \sin^3 \phi (1110\rangle + 1101\rangle + 1011\rangle + 0111\rangle)$

T_{-3}	
$ 1111\rangle$	$\rightarrow -\cos \phi \sin^3 \phi (1000\rangle + 0100\rangle + 0010\rangle + 0001\rangle)$
$ 1110\rangle$	$\rightarrow \cos \phi \sin^3 \phi 0000\rangle$
$ 1101\rangle$	$\rightarrow \cos \phi \sin^3 \phi 0000\rangle$
$ 1011\rangle$	$\rightarrow \cos \phi \sin^3 \phi 0000\rangle$
$ 0111\rangle$	$\rightarrow \cos \phi \sin^3 \phi 0000\rangle$

T_0	
$ 1111\rangle$	$\rightarrow -\cos^4\phi 1111\rangle$
$ 1110\rangle$	$\rightarrow -\cos^2\phi \sin^2\phi \left(1101\rangle + 1011\rangle + 0111\rangle \right) + \cos^4\phi 1110\rangle$
$ 1101\rangle$	$\rightarrow -\cos^2\phi \sin^2\phi \left(1110\rangle + 1011\rangle + 0111\rangle \right) + \cos^4\phi 1101\rangle$
$ 1011\rangle$	$\rightarrow -\cos^2\phi \sin^2\phi \left(1110\rangle + 1101\rangle + 0111\rangle \right) + \cos^4\phi 1011\rangle$
$ 0111\rangle$	$\rightarrow -\cos^2\phi \sin^2\phi \left(1110\rangle + 1101\rangle + 1011\rangle \right) + \cos^4\phi 0111\rangle$
$ 1100\rangle$	$\rightarrow \cos^2\phi \sin^2\phi \left(1010\rangle + 1001\rangle + 0110\rangle + 0101\rangle \right) - \cos^4\phi 1100\rangle - \sin^4\phi 0011\rangle$
$ 1010\rangle$	$\rightarrow \cos^2\phi \sin^2\phi \left(1100\rangle + 1001\rangle + 0110\rangle + 0011\rangle \right) - \cos^4\phi 1010\rangle - \sin^4\phi 0101\rangle$
$ 1001\rangle$	$\rightarrow \cos^2\phi \sin^2\phi \left(1100\rangle + 1010\rangle + 0101\rangle + 0011\rangle \right) - \cos^4\phi 1001\rangle - \sin^4\phi 0110\rangle$
$ 0110\rangle$	$\rightarrow \cos^2\phi \sin^2\phi \left(1100\rangle + 1010\rangle + 0101\rangle + 0011\rangle \right) - \sin^4\phi 1001\rangle - \cos^4\phi 0110\rangle$
$ 0101\rangle$	$\rightarrow \cos^2\phi \sin^2\phi \left(1100\rangle + 1001\rangle + 0110\rangle + 0011\rangle \right) - \sin^4\phi 1010\rangle - \cos^4\phi 0101\rangle$
$ 0011\rangle$	$\rightarrow \cos^2\phi \sin^2\phi \left(1010\rangle + 1001\rangle + 0110\rangle + 0101\rangle \right) - \sin^4\phi 1100\rangle - \cos^4\phi 0011\rangle$
$ 1000\rangle$	$\rightarrow -\cos^2\phi \sin^2\phi \left(0100\rangle + 0010\rangle + 0001\rangle \right) + \cos^4\phi 1000\rangle$
$ 0100\rangle$	$\rightarrow -\cos^2\phi \sin^2\phi \left(1000\rangle + 0010\rangle + 0001\rangle \right) + \cos^4\phi 0100\rangle$
$ 0010\rangle$	$\rightarrow -\cos^2\phi \sin^2\phi \left(1000\rangle + 0100\rangle + 0001\rangle \right) + \cos^4\phi 0010\rangle$
$ 0001\rangle$	$\rightarrow -\cos^2\phi \sin^2\phi \left(1000\rangle + 0100\rangle + 0010\rangle \right) + \cos^4\phi 0001\rangle$
$ 0000\rangle$	$\rightarrow -\cos^4\phi 0000\rangle$

Action of the operator \tilde{B}_p as defined in (5.95).

T_{+4}	
$ 0000\rangle$	$\rightarrow -(\cos\phi \cos\theta - i \sin\theta)^4 1111\rangle$

T_{-4}	
$ 1111\rangle$	$\rightarrow -(\cos\phi \cos\theta + i \sin\theta)^4 0000\rangle$

T_{+3}	
$ 1000\rangle$	$\rightarrow \sin\phi \cos\theta (\cos\phi \cos\theta - i \sin\theta)^3 1111\rangle$
$ 0100\rangle$	$\rightarrow \sin\phi \cos\theta (\cos\phi \cos\theta - i \sin\theta)^3 1111\rangle$
$ 0010\rangle$	$\rightarrow \sin\phi \cos\theta (\cos\phi \cos\theta - i \sin\theta)^3 1111\rangle$
$ 0001\rangle$	$\rightarrow \sin\phi \cos\theta (\cos\phi \cos\theta - i \sin\theta)^3 1111\rangle$
$ 0000\rangle$	$\rightarrow -\sin\phi \cos\theta (\cos\phi \cos\theta - i \sin\theta)^3 \left(1110\rangle + 1101\rangle + 1011\rangle + 0111\rangle \right)$

T_{-3}	
$ 1111\rangle$	$\rightarrow \sin\phi \cos\theta (\cos\phi \cos\theta + i \sin\theta)^3 \left(1000\rangle + 0100\rangle + 0010\rangle + 0001\rangle \right)$
$ 1110\rangle$	$\rightarrow -\sin\phi \cos\theta (\cos\phi \cos\theta + i \sin\theta)^3 0000\rangle$
$ 1101\rangle$	$\rightarrow -\sin\phi \cos\theta (\cos\phi \cos\theta + i \sin\theta)^3 0000\rangle$
$ 1011\rangle$	$\rightarrow -\sin\phi \cos\theta (\cos\phi \cos\theta + i \sin\theta)^3 0000\rangle$
$ 0111\rangle$	$\rightarrow -\sin\phi \cos\theta (\cos\phi \cos\theta + i \sin\theta)^3 0000\rangle$

T_{+2}	
$ 1100\rangle$	$\rightarrow -\sin^2\phi \cos^2\theta (\cos\phi \cos\theta - i \sin\theta)^2 1111\rangle$
$ 1010\rangle$	$\rightarrow -\sin^2\phi \cos^2\theta (\cos\phi \cos\theta - i \sin\theta)^2 1111\rangle$
$ 1001\rangle$	$\rightarrow -\sin^2\phi \cos^2\theta (\cos\phi \cos\theta - i \sin\theta)^2 1111\rangle$
$ 0110\rangle$	$\rightarrow -\sin^2\phi \cos^2\theta (\cos\phi \cos\theta - i \sin\theta)^2 1111\rangle$
$ 0101\rangle$	$\rightarrow -\sin^2\phi \cos^2\theta (\cos\phi \cos\theta - i \sin\theta)^2 1111\rangle$
$ 0011\rangle$	$\rightarrow -\sin^2\phi \cos^2\theta (\cos\phi \cos\theta - i \sin\theta)^2 1111\rangle$
$ 1000\rangle$	$\rightarrow \sin^2\phi \cos^2\theta (\cos\phi \cos\theta - i \sin\theta)^2 \left(1110\rangle + 1101\rangle + 1011\rangle \right) - (\cos\phi \cos\theta - i \sin\theta)^3 (\cos\phi \cos\theta + i \sin\theta) 0111\rangle$
$ 0100\rangle$	$\rightarrow \sin^2\phi \cos^2\theta (\cos\phi \cos\theta - i \sin\theta)^2 \left(1110\rangle + 1101\rangle + 0111\rangle \right)$

Appendix B

Series results

B.1 Hopping amplitudes of a dressed charge

In the following, we list the hopping amplitudes of a single dressed charge in the low-field regime of the toric code (4.23). The series are valid for $h_z \geq h_x$ and $J = 1/2$. The same quantities for a single flux can be obtained by interchanging h_x and h_z . The amplitude $t_{p,q}$ denotes the hopping distance $p\mathbf{n}_1 + q\mathbf{n}_2$, where \mathbf{n}_1 and \mathbf{n}_2 are unit vectors as defined in Figure 5.2. Due to the symmetries of the lattice, hopping amplitudes are related through:

$$t_{p,q} = t_{p,-q} = t_{-p,q} = t_{-p,-q} = t_{q,p} = t_{q,-p} = t_{-q,p} = t_{-q,-p}. \quad (\text{B.1})$$

$$\begin{aligned} t_{0,0} = & 5h_x^4 + 92h_x^6 + \frac{35649}{16}h_x^8 - h_y^2 - \frac{33}{8}h_x^2h_y^2 - \frac{919}{16}h_x^4h_y^2 - \frac{25082609}{27648}h_x^6h_y^2 - \frac{15}{16}h_y^4 - \frac{13877}{1152}h_x^2h_y^4 \\ & - \frac{72913739}{497664}h_x^4h_y^4 - \frac{575}{384}h_y^6 - \frac{671160793}{19906560}h_x^2h_y^6 - \frac{26492351}{7962624}h_y^8 + 2h_z^2 - 3h_x^2h_z^2 - \frac{305}{8}h_x^4h_z^2 - \frac{14157}{16}h_x^6h_z^2 \\ & - \frac{33}{8}h_y^2h_z^2 - \frac{1151}{16}h_x^2h_y^2h_z^2 - \frac{14899273}{13824}h_x^4h_y^2h_z^2 - \frac{76861}{6912}h_x^4h_y^2h_z^2 - \frac{22739089}{124416}h_x^2h_y^4h_z^2 - \frac{181798829}{6635520}h_y^6h_z^2 \\ & + \frac{35}{2}h_z^4 - \frac{313}{8}h_x^2h_z^4 - \frac{9441}{16}h_x^4h_z^4 - \frac{391}{32}h_y^2h_z^4 - \frac{2101903}{1728}h_x^2h_y^2h_z^4 - \frac{11536717}{82944}h_y^4h_z^4 + 247h_z^6 \\ & - \frac{24103}{32}h_x^2h_z^6 + \frac{609899}{3072}h_y^2h_z^6 + \frac{161105}{32}h_z^8 \end{aligned} \quad (\text{B.2})$$

$$\begin{aligned} t_{1,0} = & -h_z + \frac{1}{2}h_x^2h_z + \frac{27}{8}h_x^4h_z + \frac{495}{8}h_x^6h_z + \frac{11}{16}h_y^2h_z - \frac{813}{128}h_x^2h_y^2h_z - \frac{445163}{9216}h_x^4h_y^2h_z + \frac{17}{16}h_y^4h_z \\ & + \frac{102397}{27648}h_x^2h_y^4h_z + \frac{799973}{442368}h_y^6h_z + \frac{1}{2}h_z^3 - \frac{1}{16}h_x^2h_z^3 - \frac{3281}{128}h_x^4h_z^3 + \frac{9}{2}h_y^2h_z^3 - \frac{135671}{1536}h_x^2h_y^2h_z^3 \\ & + \frac{9548657}{331776}h_y^4h_z^3 + 12h_z^5 - \frac{51}{2}h_x^2h_z^5 + \frac{136239}{2048}h_y^2h_z^5 + \frac{12805}{64}h_z^7. \end{aligned} \quad (\text{B.3})$$

$$\begin{aligned} t_{1,1} = & \frac{29}{8}h_x^2h_y^2 + \frac{827}{24}h_x^4h_y^2 + \frac{20736661}{36864}h_x^6h_y^2 + \frac{613}{144}h_x^2h_y^4 + \frac{3102203}{27648}h_x^4h_y^4 + \frac{120571481}{9953280}h_x^2h_y^6 - h_z^2 + h_x^2h_z^2 \\ & + \frac{133}{8}h_x^4h_z^2 + \frac{11467}{48}h_x^6h_z^2 - \frac{13}{16}h_y^2h_z^2 + \frac{629}{64}h_x^2h_y^2h_z^2 + \frac{825287}{55296}h_x^4h_y^2h_z^2 - \frac{85889}{13824}h_y^4h_z^2 - \frac{890875}{18432}h_x^2h_y^4h_z^2 \\ & - \frac{427538329}{39813120}h_y^6h_z^2 - h_z^4 + \frac{19}{16}h_x^2h_z^4 + \frac{1053}{32}h_x^4h_z^4 - \frac{2437}{384}h_y^2h_z^4 - \frac{152113}{27648}h_x^2h_y^2h_z^4 - \frac{187632779}{1990656}h_y^4h_z^4 + \frac{63}{8}h_z^6 \\ & - \frac{11509}{384}h_x^2h_z^6 - \frac{54431}{2304}h_y^2h_z^6 + \frac{17895}{64}h_z^8 \end{aligned} \quad (\text{B.4})$$

$$\begin{aligned}
t_{2,0} = & \frac{53}{32}h_x^2h_y^2 + \frac{2183}{128}h_x^4h_y^2 + \frac{32311505}{110592}h_x^6h_y^2 + \frac{3941}{2304}h_x^2h_y^4 + \frac{6761239}{165888}h_x^4h_y^4 + \frac{9895379}{3981312}h_x^2h_y^6 - \frac{1}{2}h_z^2 + \frac{1}{2}h_x^2h_z^2 \\
& + \frac{341}{32}h_x^4h_z^2 + \frac{24735}{128}h_x^6h_z^2 - \frac{13}{32}h_y^2h_z^2 + \frac{2157}{128}h_x^2h_y^2h_z^2 + \frac{4378379}{36864}h_x^4h_y^2h_z^2 - \frac{837}{1024}h_y^4h_z^2 + \frac{86341045}{1990656}h_x^2h_y^4h_z^2 \\
& - \frac{7903961}{6635520}h_y^6h_z^2 - 3h_z^4 + \frac{179}{32}h_x^2h_z^4 + \frac{11985}{128}h_x^4h_z^4 - \frac{3059}{384}h_y^2h_z^4 + \frac{542923}{8192}h_x^2h_y^2h_z^4 - \frac{165213637}{3981312}h_y^4h_z^4 - 10h_z^6 \\
& + \frac{8461}{384}h_x^2h_z^6 - \frac{17653717}{221184}h_y^2h_z^6 + \frac{12621}{128}h_z^8. \tag{B.5}
\end{aligned}$$

$$\begin{aligned}
t_{2,1} = & \frac{399}{128}h_x^2h_y^2h_z + \frac{463265}{9216}h_x^4h_y^2h_z + \frac{29353}{55296}h_x^2h_y^4h_z - \frac{3}{2}h_z^3 + \frac{9}{4}h_x^2h_z^3 + \frac{4539}{128}h_x^4h_z^3 - \frac{291}{256}h_y^2h_z^3 + \frac{8587}{768}h_x^2h_y^2h_z^3 \\
& - \frac{1104643}{331776}h_y^4h_z^3 - \frac{37}{4}h_z^5 + \frac{5629}{256}h_x^2h_z^5 - \frac{99085}{4608}h_y^2h_z^5 - \frac{4153}{64}h_z^7. \tag{B.6}
\end{aligned}$$

$$\begin{aligned}
t_{2,2} = & -\frac{10245295}{221184}h_x^4h_y^4 + \frac{105}{8}h_x^2h_y^2h_z^2 + \frac{2893055}{27648}h_x^4h_y^2h_z^2 + \frac{1914511}{55296}h_x^2h_y^4h_z^2 - \frac{15}{4}h_z^4 + \frac{15}{2}h_x^2h_z^4 + \frac{2025}{16}h_x^4h_z^4 \\
& - \frac{705}{128}h_y^2h_z^4 + \frac{699847}{4608}h_x^2h_y^2h_z^4 - \frac{29850151}{1327104}h_y^4h_z^4 - \frac{75}{2}h_z^6 + \frac{13695}{128}h_x^2h_z^6 - \frac{6331517}{55296}h_y^2h_z^6 - \frac{55503}{128}h_z^8 \tag{B.7}
\end{aligned}$$

$$\begin{aligned}
t_{3,0} = & \frac{87}{128}h_x^2h_y^2h_z + \frac{19935}{2048}h_x^4h_y^2h_z - \frac{266531}{55296}h_x^2h_y^4h_z - \frac{1}{2}h_z^3 + \frac{3}{4}h_x^2h_z^3 + \frac{1603}{128}h_x^4h_z^3 - \frac{97}{256}h_y^2h_z^3 + \frac{34231}{1024}h_x^2h_y^2h_z^3 \\
& - \frac{207655}{331776}h_y^4h_z^3 - \frac{83}{8}h_z^5 + \frac{6543}{256}h_x^2h_z^5 - \frac{787477}{36864}h_y^2h_z^5 - \frac{8039}{64}h_z^7. \tag{B.8}
\end{aligned}$$

$$\begin{aligned}
t_{3,1} = & -\frac{2537401}{110592}h_x^4h_y^4 + \frac{1089}{128}h_x^2h_y^2h_z^2 + \frac{7474717}{110592}h_x^4h_y^2h_z^2 + \frac{48015}{2048}h_x^2h_y^4h_z^2 - \frac{5}{2}h_z^4 + 5h_x^2h_z^4 + \frac{11037}{128}h_x^4h_z^4 \\
& - \frac{235}{64}h_y^2h_z^4 + \frac{3092063}{18432}h_x^2h_y^2h_z^4 - \frac{26099579}{1990656}h_y^4h_z^4 - \frac{305}{8}h_z^6 + \frac{7085}{64}h_x^2h_z^6 - \frac{12238883}{110592}h_y^2h_z^6 - \frac{64661}{128}h_z^8. \tag{B.9}
\end{aligned}$$

$$t_{3,2} = \frac{8803}{256}h_x^2h_y^2h_z^3 - \frac{35}{4}h_z^5 + \frac{175}{8}h_x^2h_z^5 - \frac{35635}{2048}h_y^2h_z^5 - \frac{2345}{16}h_z^7. \tag{B.10}$$

$$t_{3,3} = \frac{62973}{512}h_x^2h_y^2h_z^4 - \frac{105}{4}h_z^6 + \frac{315}{4}h_x^2h_z^6 - \frac{137535}{2048}h_y^2h_z^6 - \frac{4515}{8}h_z^8. \tag{B.11}$$

$$\begin{aligned}
t_{4,0} = & \frac{1007}{4096}h_x^4h_y^4 + \frac{249}{128}h_x^2h_y^2h_z^2 + \frac{62541}{4096}h_x^4h_y^2h_z^2 + \frac{678299}{110592}h_x^2h_y^4h_z^2 - \frac{5}{8}h_z^4 + \frac{5}{4}h_x^2h_z^4 + \frac{2937}{128}h_x^4h_z^4 - \frac{235}{256}h_y^2h_z^4 \\
& + \frac{259249}{2048}h_x^2h_y^2h_z^4 - \frac{14847863}{7962624}h_y^4h_z^4 - \frac{109}{4}h_z^6 + \frac{20693}{256}h_x^2h_z^6 - \frac{903937}{12288}h_y^2h_z^6 - \frac{141187}{256}h_z^8. \tag{B.12}
\end{aligned}$$

$$t_{4,1} = \frac{16759}{1024}h_x^2h_y^2h_z^3 - \frac{35}{8}h_z^5 + \frac{175}{16}h_x^2h_z^5 - \frac{35635}{4096}h_y^2h_z^5 - \frac{1981}{16}h_z^7. \tag{B.13}$$

$$t_{4,2} = \frac{744777}{8192}h_x^2h_y^2h_z^4 - \frac{315}{16}h_z^6 + \frac{945}{16}h_x^2h_z^6 - \frac{412605}{8192}h_y^2h_z^6 - \frac{4137}{8}h_z^8. \tag{B.14}$$

$$t_{4,3} = -\frac{1155}{16}h_z^7. \tag{B.15}$$

$$t_{4,4} = -\frac{15015}{64}h_z^8. \tag{B.16}$$

$$t_{5,0} = \frac{3013}{1024}h_x^2h_y^2h_z^3 - \frac{7}{8}h_z^5 + \frac{35}{16}h_x^2h_z^5 - \frac{7127}{4096}h_y^2h_z^5 - \frac{1043}{16}h_z^7. \tag{B.17}$$

$$t_{5,1} = \frac{8901}{256}h_x^2h_y^2h_z^4 - \frac{63}{8}h_z^6 + \frac{189}{8}h_x^2h_z^6 - \frac{82521}{4096}h_y^2h_z^6 - 357h_z^8. \tag{B.18}$$

$$t_{5,2} = -\frac{693}{16}h_z^7. \tag{B.19}$$

$$t_{5,3} = -\frac{3003}{16}h_z^8. \tag{B.20}$$

$$t_{6,0} = \frac{43839}{8192}h_x^2h_y^2h_z^4 - \frac{21}{16}h_z^6 + \frac{63}{16}h_x^2h_z^6 - \frac{27507}{8192}h_y^2h_z^6 - \frac{1191}{8}h_z^8. \tag{B.21}$$

$$t_{6,1} = -\frac{231}{16}h_z^7. \tag{B.22}$$

$$t_{6,2} = -\frac{3003}{32}h_z^8. \tag{B.23}$$

$$t_{7,0} = -\frac{33}{16}h_z^7. \quad (\text{B.24})$$

$$t_{7,1} = -\frac{429}{16}h_z^8. \quad (\text{B.25})$$

$$t_{8,0} = -\frac{429}{128}h_z^8. \quad (\text{B.26})$$

B.2 Two-particle hopping amplitudes

As introduced in Section 5.1.3, the two-quasi-particle sector of the particle-conserving effective Hamiltonian H_{eff} is described by a semi-infinite hermitian matrix

$$H|_{2qp} = H_0 + H_1 + H_2, \quad (\text{B.27})$$

where H_0 yields a constant energy shift of 2 since we set $J = 1/2$. Therefore, in what follows, we only consider the non-trivial part of the Hamiltonian: $H_1 + H_2$. The semi-infinite tail of this matrix can be constructed using one-particle hopping amplitudes given in Appendix B.1. Hopping amplitudes relevant for the finite 'head' (the size of which depends on the maximal perturbation order) are listed in the following tables. We computed these amplitudes up to order 6. However, they are too numerous to be listed in a written form so that we only give the first three orders. The remaining amplitudes are available upon request.

Hopping amplitudes in the subspace \mathcal{H}^f are denoted by $t_{\mathbf{d}',\tau';\mathbf{t}_{\text{cm}}}^{\mathbf{d},\tau}$ where τ and τ' are the initial and final pair types, \mathbf{d} and \mathbf{d}' are the corresponding mutual particle distances, and \mathbf{t}_{cm} the hopping distance of the center of mass. To keep a clear overview, we list the indices and the corresponding hopping amplitudes in a tabular form. The following table contains only hopping amplitudes which cannot be recovered from the symmetry relation

$$t_{\mathbf{d}',\tau';\mathbf{t}_{\text{cm}}}^{\mathbf{d},\tau} = t_{\mathbf{d}',\tau';-\mathbf{t}_{\text{cm}}}^{\mathbf{d},\tau} = t_{\mathbf{d},\tau;\mathbf{t}_{\text{cm}}}^{\mathbf{d}',\tau'} \quad , \quad (\text{B.28})$$

where the complex conjugate is denoted by an asterisk.

τ	\mathbf{d}	τ'	\mathbf{d}'	\mathbf{t}_{cm}	$t_{\mathbf{d}',\tau';\mathbf{t}_{\text{cm}}}^{\mathbf{d},\tau}$
c	{0, 2}	c	{1, -1}	{1/2, -3/2}	$\frac{1}{2}h_z^3$
c	{0, 2}	c	{1, -1}	{3/2, -1/2}	$\frac{1}{2}h_z^3$
c	{0, 2}	c	{1, -1}	{1/2, 1/2}	$\frac{1}{2}h_x^2h_z + \frac{3}{2}h_z^3 + \frac{29}{32}h_y^2h_z$
c	{0, 2}	c	{1, 1}	{1/2, 3/2}	$\frac{1}{2}h_z^3$
c	{0, 2}	c	{1, 1}	{3/2, 1/2}	$\frac{1}{2}h_z^3$
c	{0, 2}	c	{1, 1}	{1/2, -1/2}	$\frac{1}{2}h_x^2h_z + \frac{3}{2}h_z^3 + \frac{29}{32}h_y^2h_z$
c	{0, 2}	f	{0, 2}	{0, 1}	$-i h_x h_y h_z$
c	{0, 2}	f	{0, 2}	{1, 0}	$h_y^2 + i 2h_x h_y h_z$
c	{0, 2}	f	{1, -3}	{1/2, 1/2}	$\frac{1}{2}h_x h_y^2$
c	{0, 2}	f	{1, -3}	{3/2, -1/2}	$\frac{1}{2}h_x h_y^2$
c	{0, 2}	f	{1, -1}	{3/2, 1/2}	$\frac{1}{2}h_x h_y^2$
c	{0, 2}	f	{1, -1}	{1/2, -1/2}	$-\frac{3}{4}h_x h_y^2 + \frac{3}{4}h_x h_z^2 - i \frac{1}{2}h_y h_z$
c	{0, 2}	f	{1, 1}	{3/2, -1/2}	$\frac{1}{2}h_x h_y^2$
c	{0, 2}	f	{1, 1}	{1/2, 1/2}	$-\frac{3}{4}h_x h_y^2 + \frac{3}{4}h_x h_z^2 - i \frac{1}{2}h_y h_z$
c	{0, 2}	f	{1, 3}	{1/2, -1/2}	$\frac{1}{2}h_x h_y^2$
c	{0, 2}	f	{1, 3}	{3/2, 1/2}	$\frac{1}{2}h_x h_y^2$

c	{0, 2}	f	{2, -2}	{1, -1}	$-i \frac{1}{2} h_x h_y h_z$
c	{0, 2}	f	{2, -2}	{0, 0}	$-i h_x h_y h_z$
c	{0, 2}	f	{2, 0}	{0, 1}	$-i h_x h_y h_z$
c	{0, 2}	f	{2, 0}	{1, 0}	$-i h_x h_y h_z$
c	{0, 2}	f	{2, 2}	{1, 1}	$-i \frac{1}{2} h_x h_y h_z$
c	{0, 2}	f	{2, 2}	{0, 0}	$-i h_x h_y h_z$
c	{1, -3}	f	{0, 2}	{1/2, 1/2}	$\frac{1}{2} h_y^2 h_z$
c	{1, -3}	f	{0, 2}	{3/2, -1/2}	$\frac{1}{2} h_y^2 h_z$
c	{1, -3}	f	{1, -1}	{1, -1}	$-i \frac{1}{2} h_y h_z^2$
c	{1, -3}	f	{1, 1}	{0, 1}	$-i h_y h_z^2$
c	{1, -3}	f	{1, 3}	{0, 0}	$i h_y^3$
c	{1, -1}	c	{1, -1}	{1, -1}	$\frac{1}{2} h_z^2$
c	{1, -1}	c	{1, -1}	{0, 0}	$-\frac{5}{4} h_y^2 + 4 h_z^2$
c	{1, -1}	c	{2, -2}	{3/2, -3/2}	$\frac{1}{2} h_z^3$
c	{1, -1}	c	{2, -2}	{1/2, -1/2}	$\frac{1}{2} h_x^2 h_z + \frac{1}{2} h_z^3 + \frac{29}{32} h_y^2 h_z$
c	{1, -1}	c	{2, 0}	{1/2, -3/2}	$\frac{1}{2} h_z^3$
c	{1, -1}	c	{2, 0}	{3/2, -1/2}	$\frac{1}{2} h_z^3$
c	{1, -1}	c	{2, 0}	{1/2, 1/2}	$\frac{1}{2} h_x^2 h_z + \frac{3}{2} h_z^3 + \frac{29}{32} h_y^2 h_z$
c	{1, -1}	c	{2, 2}	{1/2, -1/2}	$\frac{1}{2} h_z^3$
c	{1, -1}	c	{2, 2}	{1/2, 3/2}	$-\frac{1}{2} h_z^3$
c	{1, -1}	c	{2, 2}	{3/2, 1/2}	$-\frac{1}{2} h_z^3$
c	{1, -1}	f	{0, 2}	{3/2, 1/2}	$\frac{1}{2} h_y^2 h_z$
c	{1, -1}	f	{0, 2}	{1/2, -1/2}	$\frac{3}{4} h_x^2 h_z - \frac{3}{4} h_y^2 h_z - i \frac{1}{2} h_x h_y$
c	{1, -1}	f	{1, -3}	{1, -1}	$-i \frac{1}{2} h_x^2 h_y$
c	{1, -1}	f	{1, 1}	{1, 1}	$i \frac{1}{2} h_x^2 h_y$
c	{1, -1}	f	{1, 1}	{1, -1}	$i \frac{1}{2} h_y h_z^2$
c	{1, -1}	f	{1, 1}	{0, 0}	$h_x h_z + i \left(\frac{1}{8} h_y^3 + \frac{3}{2} h_x^2 h_y + \frac{3}{2} h_y h_z^2 - h_y \right)$
c	{1, -1}	f	{1, 3}	{0, 1}	$-i h_x^2 h_y$
c	{1, -1}	f	{2, -2}	{1/2, 1/2}	$\frac{3}{2} h_y^2 h_z$
c	{1, -1}	f	{2, 0}	{1/2, 3/2}	$\frac{1}{2} h_y^2 h_z$
c	{1, -1}	f	{2, 0}	{1/2, -1/2}	$\frac{3}{4} h_x^2 h_z - \frac{3}{4} h_y^2 h_z - i \frac{1}{2} h_x h_y$
c	{1, -1}	f	{2, 2}	{1/2, 1/2}	$\frac{3}{4} h_x^2 h_z + \frac{1}{4} h_y^2 h_z - i \frac{1}{2} h_x h_y$
c	{1, -1}	f	{3, -1}	{1, -1}	$-i \frac{1}{2} h_x^2 h_y$
c	{1, -1}	f	{3, 1}	{1, 0}	$-i h_x^2 h_y$
c	{1, -1}	f	{3, 3}	{1, 1}	$-i \frac{1}{2} h_x^2 h_y$
c	{1, 1}	c	{1, 1}	{1, 1}	$\frac{1}{2} h_z^2$
c	{1, 1}	c	{1, 1}	{0, 0}	$-\frac{5}{4} h_y^2 + 4 h_z^2$
c	{1, 1}	c	{2, -2}	{1/2, -3/2}	$-\frac{1}{2} h_z^3$
c	{1, 1}	c	{2, -2}	{1/2, 1/2}	$\frac{1}{2} h_z^3$
c	{1, 1}	c	{2, -2}	{3/2, -1/2}	$-\frac{1}{2} h_z^3$
c	{1, 1}	c	{2, 0}	{1/2, 3/2}	$\frac{1}{2} h_z^3$
c	{1, 1}	c	{2, 0}	{3/2, 1/2}	$\frac{1}{2} h_z^3$
c	{1, 1}	c	{2, 0}	{1/2, -1/2}	$\frac{1}{2} h_x^2 h_z + \frac{3}{2} h_z^3 + \frac{29}{32} h_y^2 h_z$
c	{1, 1}	c	{2, 2}	{3/2, 3/2}	$\frac{1}{2} h_z^3$
c	{1, 1}	c	{2, 2}	{1/2, 1/2}	$\frac{1}{2} h_x^2 h_z + \frac{1}{2} h_z^3 + \frac{29}{32} h_y^2 h_z$
c	{1, 1}	f	{0, 2}	{3/2, -1/2}	$\frac{1}{2} h_y^2 h_z$
c	{1, 1}	f	{0, 2}	{1/2, 1/2}	$\frac{3}{4} h_x^2 h_z - \frac{3}{4} h_y^2 h_z - i \frac{1}{2} h_x h_y$
c	{1, 1}	f	{1, -3}	{0, 1}	$-i h_x^2 h_y$
c	{1, 1}	f	{1, -1}	{1, -1}	$i \frac{1}{2} h_x^2 h_y$
c	{1, 1}	f	{1, -1}	{1, 1}	$i \frac{1}{2} h_y h_z^2$
c	{1, 1}	f	{1, -1}	{0, 0}	$h_x h_z + i \left(\frac{1}{8} h_y^3 + \frac{3}{2} h_x^2 h_y + \frac{3}{2} h_y h_z^2 - h_y \right)$
c	{1, 1}	f	{1, 3}	{1, 1}	$-i \frac{1}{2} h_x^2 h_y$
c	{1, 1}	f	{2, -2}	{1/2, -1/2}	$\frac{3}{4} h_x^2 h_z + \frac{1}{4} h_y^2 h_z - i \frac{1}{2} h_x h_y$
c	{1, 1}	f	{2, 0}	{1/2, -3/2}	$\frac{1}{2} h_y^2 h_z$

c	{1, 1}	f	{2, 0}	{1/2, 1/2}	$\frac{3}{4}h_x^2h_z - \frac{3}{4}h_y^2h_z - i\frac{1}{2}h_xh_y$
c	{1, 1}	f	{2, 2}	{1/2, -1/2}	$\frac{3}{2}h_y^2h_z$
c	{1, 1}	f	{3, -3}	{1, -1}	$-i\frac{1}{2}h_x^2h_y$
c	{1, 1}	f	{3, -1}	{1, 0}	$-ih_x^2h_y$
c	{1, 1}	f	{3, 1}	{1, 1}	$-i\frac{1}{2}h_x^2h_y$
c	{1, 3}	f	{0, 2}	{1/2, -1/2}	$\frac{1}{2}h_y^2h_z$
c	{1, 3}	f	{0, 2}	{3/2, 1/2}	$\frac{1}{2}h_y^2h_z$
c	{1, 3}	f	{1, -3}	{0, 0}	ih_y^3
c	{1, 3}	f	{1, -1}	{0, 1}	$-ih_yh_z^2$
c	{1, 3}	f	{1, 1}	{1, 1}	$-i\frac{1}{2}h_yh_z^2$
c	{2, -2}	f	{0, 2}	{1, -1}	$-i\frac{1}{2}h_xh_yh_z$
c	{2, -2}	f	{0, 2}	{0, 0}	$-ih_xh_yh_z$
c	{2, -2}	f	{1, -1}	{1/2, 1/2}	$\frac{3}{2}h_xh_y^2$
c	{2, -2}	f	{1, 1}	{1/2, -1/2}	$\frac{1}{4}h_xh_y^2 + \frac{3}{4}h_xh_z^2 - i\frac{1}{2}h_yh_z$
c	{2, -2}	f	{2, 0}	{1, -1}	$-i\frac{1}{2}h_xh_yh_z$
c	{2, -2}	f	{2, 0}	{0, 0}	$-ih_xh_yh_z$
c	{2, -2}	f	{2, 2}	{0, 1}	$-i\frac{1}{2}h_xh_yh_z$
c	{2, -2}	f	{2, 2}	{1, 0}	$-i\frac{1}{2}h_xh_yh_z$
c	{2, 0}	f	{0, 2}	{0, 1}	$-ih_xh_yh_z$
c	{2, 0}	f	{0, 2}	{1, 0}	$-ih_xh_yh_z$
c	{2, 0}	f	{1, -1}	{1/2, 3/2}	$\frac{1}{2}h_xh_y^2$
c	{2, 0}	f	{1, -1}	{1/2, -1/2}	$-\frac{3}{4}h_xh_y^2 + \frac{3}{4}h_xh_z^2 - i\frac{1}{2}h_yh_z$
c	{2, 0}	f	{1, 1}	{1/2, -3/2}	$\frac{1}{2}h_xh_y^2$
c	{2, 0}	f	{1, 1}	{1/2, 1/2}	$-\frac{3}{4}h_xh_y^2 + \frac{3}{4}h_xh_z^2 - i\frac{1}{2}h_yh_z$
c	{2, 0}	f	{2, -2}	{1, -1}	$-i\frac{1}{2}h_xh_yh_z$
c	{2, 0}	f	{2, -2}	{0, 0}	$-ih_xh_yh_z$
c	{2, 0}	f	{2, 0}	{1, 0}	$-ih_xh_yh_z$
c	{2, 0}	f	{2, 0}	{0, 1}	$h_y^2 + i2h_xh_yh_z$
c	{2, 0}	f	{2, 2}	{1, 1}	$-i\frac{1}{2}h_xh_yh_z$
c	{2, 0}	f	{2, 2}	{0, 0}	$-ih_xh_yh_z$
c	{2, 0}	f	{3, -1}	{1/2, -3/2}	$\frac{1}{2}h_xh_y^2$
c	{2, 0}	f	{3, -1}	{1/2, 1/2}	$\frac{1}{2}h_xh_y^2$
c	{2, 0}	f	{3, 1}	{1/2, -1/2}	$\frac{1}{2}h_xh_y^2$
c	{2, 0}	f	{3, 1}	{1/2, 3/2}	$\frac{1}{2}h_xh_y^2$
c	{2, 2}	f	{0, 2}	{1, 1}	$-i\frac{1}{2}h_xh_yh_z$
c	{2, 2}	f	{0, 2}	{0, 0}	$-ih_xh_yh_z$
c	{2, 2}	f	{1, -1}	{1/2, 1/2}	$\frac{1}{4}h_xh_y^2 + \frac{3}{4}h_xh_z^2 - i\frac{1}{2}h_yh_z$
c	{2, 2}	f	{1, 1}	{1/2, -1/2}	$\frac{3}{2}h_xh_y^2$
c	{2, 2}	f	{2, -2}	{0, 1}	$-i\frac{1}{2}h_xh_yh_z$
c	{2, 2}	f	{2, -2}	{1, 0}	$-i\frac{1}{2}h_xh_yh_z$
c	{2, 2}	f	{2, 0}	{1, 1}	$-i\frac{1}{2}h_xh_yh_z$
c	{2, 2}	f	{2, 0}	{0, 0}	$-ih_xh_yh_z$
c	{3, -3}	f	{1, 1}	{1, -1}	$-i\frac{1}{2}h_yh_z^2$
c	{3, -1}	f	{1, -1}	{1, -1}	$-i\frac{1}{2}h_yh_z^2$
c	{3, -1}	f	{1, 1}	{1, 0}	$-ih_yh_z^2$
c	{3, -1}	f	{2, 0}	{1/2, -3/2}	$\frac{1}{2}h_y^2h_z$
c	{3, -1}	f	{2, 0}	{1/2, 1/2}	$\frac{1}{2}h_y^2h_z$
c	{3, -1}	f	{3, 1}	{0, 0}	ih_y^3
c	{3, 1}	f	{1, -1}	{1, 0}	$-ih_yh_z^2$
c	{3, 1}	f	{1, 1}	{1, 1}	$-i\frac{1}{2}h_yh_z^2$
c	{3, 1}	f	{2, 0}	{1/2, -1/2}	$\frac{1}{2}h_y^2h_z$
c	{3, 1}	f	{2, 0}	{1/2, 3/2}	$\frac{1}{2}h_y^2h_z$
c	{3, 1}	f	{3, -1}	{0, 0}	ih_y^3
c	{3, 3}	f	{1, -1}	{1, 1}	$-i\frac{1}{2}h_yh_z^2$

f	{0, 2}	f	{1, -1}	{1/2, -3/2}	$\frac{1}{2}h_x^3$
f	{0, 2}	f	{1, -1}	{3/2, -1/2}	$\frac{1}{2}h_x^3$
f	{0, 2}	f	{1, -1}	{1/2, 1/2}	$\frac{3}{2}h_x^3 + \frac{29}{32}h_x h_y^2 + \frac{1}{2}h_x h_z^2$
f	{0, 2}	f	{1, 1}	{1/2, 3/2}	$\frac{1}{2}h_x^3$
f	{0, 2}	f	{1, 1}	{3/2, 1/2}	$\frac{1}{2}h_x^3$
f	{0, 2}	f	{1, 1}	{1/2, -1/2}	$\frac{3}{2}h_x^3 + \frac{29}{32}h_x h_y^2 + \frac{1}{2}h_x h_z^2$
f	{1, -1}	f	{1, -1}	{1, -1}	$\frac{1}{2}h_x^2$
f	{1, -1}	f	{1, -1}	{0, 0}	$4h_x^2 - \frac{5}{4}h_y^2$
f	{1, -1}	f	{2, -2}	{3/2, -3/2}	$\frac{1}{2}h_x^3$
f	{1, -1}	f	{2, -2}	{1/2, -1/2}	$\frac{1}{2}h_x^3 + \frac{29}{32}h_x h_y^2 + \frac{1}{2}h_x h_z^2$
f	{1, -1}	f	{2, 0}	{1/2, -3/2}	$\frac{1}{2}h_x^3$
f	{1, -1}	f	{2, 0}	{3/2, -1/2}	$\frac{1}{2}h_x^3$
f	{1, -1}	f	{2, 0}	{1/2, 1/2}	$\frac{3}{2}h_x^3 + \frac{29}{32}h_x h_y^2 + \frac{1}{2}h_x h_z^2$
f	{1, -1}	f	{2, 2}	{1/2, -1/2}	$\frac{1}{2}h_x^3$
f	{1, -1}	f	{2, 2}	{1/2, 3/2}	$-\frac{1}{2}h_x^3$
f	{1, -1}	f	{2, 2}	{3/2, 1/2}	$-\frac{1}{2}h_x^3$
f	{1, 1}	f	{1, 1}	{1, 1}	$\frac{1}{2}h_x^2$
f	{1, 1}	f	{1, 1}	{0, 0}	$4h_x^2 - \frac{5}{4}h_y^2$
f	{1, 1}	f	{2, -2}	{1/2, -3/2}	$-\frac{1}{2}h_x^3$
f	{1, 1}	f	{2, -2}	{1/2, 1/2}	$\frac{1}{2}h_x^3$
f	{1, 1}	f	{2, -2}	{3/2, -1/2}	$-\frac{1}{2}h_x^3$
f	{1, 1}	f	{2, 0}	{1/2, 3/2}	$\frac{1}{2}h_x^3$
f	{1, 1}	f	{2, 0}	{3/2, 1/2}	$\frac{1}{2}h_x^3$
f	{1, 1}	f	{2, 0}	{1/2, -1/2}	$\frac{3}{2}h_x^3 + \frac{29}{32}h_x h_y^2 + \frac{1}{2}h_x h_z^2$
f	{1, 1}	f	{2, 2}	{3/2, 3/2}	$\frac{1}{2}h_x^3$
f	{1, 1}	f	{2, 2}	{1/2, 1/2}	$\frac{1}{2}h_x^3 + \frac{29}{32}h_x h_y^2 + \frac{1}{2}h_x h_z^2$

TABLE B.1: Hopping amplitudes of particle pairs in the low-field limit of the toric code, as defined in Section 5.1.3. Here, we consider the subspace \mathcal{H}^f .

Hopping amplitudes in the subspace \mathcal{H}^b are denoted by $t_{\mathbf{d}', \mathbf{d}, \mathbf{t}_{\text{cm}}}$, where \mathbf{d} and \mathbf{d}' are the initial and final mutual distances of the particle pair and \mathbf{t}_{cm} the hopping distance of the center of mass. We follow the convention that the distances are always given in a coordinate system where the *charge* is at the origin. To keep a clear overview, we list the indices and the corresponding hopping amplitudes in a tabular form. The following table contains only hopping amplitudes which cannot be recovered from the symmetry relation

$$t_{\mathbf{d}', \mathbf{d}, \mathbf{t}_{\text{cm}}} = t_{\mathbf{d}, \mathbf{d}', \mathbf{t}_{\text{cm}}}^* = \tilde{t}_{\mathbf{d}', \mathbf{d}, -\mathbf{t}_{\text{cm}}}, \quad (\text{B.29})$$

where the complex conjugate is denoted by an asterisk and in \tilde{t} the field variables are subject to the transformation $h_x \rightarrow h_z$, $h_y \rightarrow -h_y$, and $h_z \rightarrow h_x$.

\mathbf{d}	\mathbf{d}'	\mathbf{t}_{cm}	$t_{\mathbf{d}', \mathbf{d}, \mathbf{t}_{\text{cm}}}$	\mathbf{d}	\mathbf{d}'	\mathbf{t}_{cm}	$t_{\mathbf{d}', \mathbf{d}, \mathbf{t}_{\text{cm}}}$
{-3, -2}	{0, -1}	{3/2, 1/2}	$-\frac{3}{2}h_x^3$	{-1, 0}	{1, 0}	{0, 1}	$i \left(\frac{1}{4}h_y^3 + \frac{3}{2}h_x^2 h_y + \frac{3}{2}h_y h_z^2 - h_y \right)$
{-3, -2}	{0, 1}	{3/2, 3/2}	$-\frac{1}{2}h_x^3$	{-1, 0}	{1, 2}	{2, 0}	$-i \frac{1}{2}h_x^2 h_y$
{-3, -2}	{1, 0}	{1, 0}	$i \frac{1}{2}h_x^2 h_y$	{-1, 0}	{1, 2}	{0, 2}	$i h_x^2 h_y$
{-3, -2}	{1, 0}	{1, 2}	$-i \frac{1}{2}h_x^2 h_y$	{-1, 0}	{1, 2}	{1, -1}	$-i \frac{1}{2}h_x h_y h_z$
{-3, -2}	{2, -1}	{1/2, 1/2}	$\frac{1}{2}h_x h_y^2$	{-1, 0}	{1, 2}	{1, 1}	$-\frac{1}{2}h_x^2 - i \frac{1}{2}h_x h_y h_z$
{-3, 0}	{0, -1}	{3/2, -1/2}	$-\frac{3}{2}h_x^3$	{-1, 0}	{1, 2}	{0, 0}	$-i \left(-\frac{1}{2}h_x^2 h_y + \frac{1}{2}h_y h_z^2 \right)$
{-3, 0}	{0, 1}	{3/2, 1/2}	$-\frac{3}{2}h_x^3$	{-1, 0}	{2, -3}	{3/2, -3/2}	$-\frac{1}{2}h_x^3$
{-3, 0}	{1, 0}	{1, -1}	$i h_x^2 h_y$	{-1, 0}	{2, -1}	{3/2, -1/2}	$-\frac{1}{2}h_x^3$
{-3, 0}	{1, 0}	{1, 1}	$-i h_x^2 h_y$	{-1, 0}	{2, -1}	{1/2, 1/2}	$-\frac{1}{4}h_x^2 h_z - \frac{3}{4}h_y^2 h_z - i \frac{1}{2}h_x h_y$

{-3, 0}	{2, -1}	{1/2, -1/2}	$\frac{1}{2}h_x h_y^2$	{-1, 0}	{2, -1}	{1/2, -3/2}	$\frac{1}{4}h_x^2 h_z - \frac{1}{4}h_y^2 h_z + i\frac{1}{2}h_x h_y$
{-3, 0}	{2, 1}	{1/2, 1/2}	$-\frac{1}{2}h_x h_y^2$	{-1, 0}	{2, 1}	{3/2, 1/2}	$\frac{1}{2}h_x^3$
{-3, 0}	{3, 0}	{0, 1}	$i h_y^3$	{-1, 0}	{2, 1}	{1/2, 3/2}	$-\frac{1}{4}h_x^2 h_z + \frac{1}{4}h_y^2 h_z - i\frac{1}{2}h_x h_y$
{-3, 2}	{0, -1}	{3/2, -3/2}	$-\frac{1}{2}h_x^3$	{-1, 0}	{2, 1}	{1/2, -1/2}	$\frac{1}{4}h_x^2 h_z + \frac{3}{4}h_y^2 h_z + i\frac{1}{2}h_x h_y$
{-3, 2}	{0, 1}	{3/2, -1/2}	$-\frac{3}{2}h_x^3$	{-1, 0}	{2, 3}	{3/2, 3/2}	$-\frac{1}{2}h_x^3$
{-3, 2}	{1, 0}	{1, -2}	$i\frac{1}{2}h_x^2 h_y$	{-1, 0}	{3, -2}	{1, -2}	$i\frac{1}{2}h_x^2 h_y$
{-3, 2}	{1, 0}	{1, 0}	$-i\frac{1}{2}h_x^2 h_y$	{-1, 0}	{3, -2}	{1, 0}	$-i\frac{1}{2}h_x^2 h_y$
{-3, 2}	{2, 1}	{1/2, -1/2}	$-\frac{1}{2}h_x h_y^2$	{-1, 0}	{3, 0}	{1, -1}	$i h_x^2 h_y$
{-2, -3}	{-1, 0}	{1/2, 3/2}	$-\frac{3}{2}h_x^3$	{-1, 0}	{3, 0}	{1, 1}	$-i h_x^2 h_y$
{-2, -3}	{-1, 2}	{1/2, 1/2}	$\frac{1}{2}h_x h_y^2$	{-1, 0}	{3, 2}	{1, 0}	$i\frac{1}{2}h_x^2 h_y$
{-2, -3}	{0, 1}	{0, 1}	$i\frac{1}{2}h_x^2 h_y$	{-1, 0}	{3, 2}	{1, 2}	$-i\frac{1}{2}h_x^2 h_y$
{-2, -3}	{0, 1}	{2, 1}	$-i\frac{1}{2}h_x^2 h_y$	{-1, 2}	{0, -3}	{1/2, -1/2}	$\frac{1}{2}h_x h_y^2$
{-2, -3}	{1, 0}	{3/2, 3/2}	$-\frac{1}{2}h_x^3$	{-1, 2}	{0, -1}	{1/2, -3/2}	$-\frac{1}{2}h_x^3$
{-2, -1}	{-1, -2}	{1/2, -1/2}	$\frac{1}{2}h_x^3 + \frac{11}{16}h_x h_y^2 + \frac{1}{2}h_x h_z^2$	{-1, 2}	{0, -1}	{3/2, -1/2}	$\frac{1}{4}h_x^2 h_z - \frac{1}{4}h_y^2 h_z - i\frac{1}{2}h_x h_y$
{-2, -1}	{-1, 0}	{1/2, -3/2}	$\frac{9}{32}h_x h_y^2$	{-1, 2}	{0, -1}	{1/2, 1/2}	$-\frac{3}{4}h_x h_y^2 - \frac{1}{4}h_x h_z^2 - i\frac{1}{2}h_y h_z$
{-2, -1}	{-1, 0}	{1/2, 5/2}	$\frac{9}{32}h_x h_y^2$	{-1, 2}	{0, 1}	{5/2, -1/2}	$\frac{9}{32}h_x h_y^2$
{-2, -1}	{-1, 0}	{1/2, 1/2}	$\frac{1}{2}h_x^3 + \frac{9}{8}h_x h_y^2 + \frac{1}{2}h_x h_z^2$	{-1, 2}	{0, 1}	{3/2, 1/2}	$\frac{9}{32}h_y^2 h_z$
{-2, -1}	{-1, 2}	{1/2, 3/2}	$-\frac{3}{2}h_x^3$	{-1, 2}	{0, 1}	{1/2, -1/2}	$\frac{1}{2}h_x^3 + \frac{9}{8}h_x h_y^2 + \frac{1}{2}h_x h_z^2$
{-2, -1}	{-1, 2}	{1/2, -1/2}	$\frac{1}{2}h_x h_y^2$	{-1, 2}	{1, -2}	{2, -1}	$-i\frac{1}{2}h_x^2 h_y$
{-2, -1}	{0, -1}	{2, 1}	$-i\frac{1}{2}h_x^2 h_y$	{-1, 2}	{1, -2}	{1, 0}	$-i h_x h_y h_z$
{-2, -1}	{0, -1}	{1, 2}	$-i\frac{1}{2}h_x h_y h_z$	{-1, 2}	{1, -2}	{0, 1}	$-i\frac{1}{2}h_y h_z^2$
{-2, -1}	{0, -1}	{0, 1}	$-i\frac{1}{2}h_y h_z^2$	{-1, 2}	{1, 0}	{2, 0}	$-i\frac{1}{2}h_x^2 h_y$
{-2, -1}	{0, -1}	{1, 0}	$-h_x^2 + i\frac{1}{2}h_x h_y h_z$	{-1, 2}	{1, 0}	{1, 1}	$-i\frac{1}{2}h_x h_y h_z$
{-2, -1}	{0, 1}	{0, 2}	$i\frac{1}{2}h_x^2 h_y$	{-1, 2}	{1, 0}	{0, 2}	$-i h_y h_z^2$
{-2, -1}	{0, 1}	{2, 0}	$-i h_x^2 h_y$	{-1, 2}	{1, 0}	{1, -1}	$\frac{1}{2}h_x^2 - i\frac{1}{2}h_x h_y h_z$
{-2, -1}	{0, 1}	{1, -1}	$-i\frac{1}{2}h_x h_y h_z$	{-1, 2}	{1, 0}	{0, 0}	$-i\left(-\frac{1}{2}h_x^2 h_y + \frac{1}{2}h_y h_z^2\right)$
{-2, -1}	{0, 1}	{1, 1}	$-\frac{1}{2}h_x^2 + i\frac{1}{2}h_x h_y h_z$	{-1, 2}	{2, -1}	{3/2, -3/2}	$\frac{1}{2}h_x^3$
{-2, -1}	{0, 1}	{0, 0}	$i\left(\frac{1}{2}h_x^2 h_y - \frac{1}{2}h_y h_z^2\right)$	{-1, 2}	{2, -1}	{1/2, -1/2}	$-\frac{3}{2}h_y^2 h_z$
{-2, -1}	{1, -2}	{3/2, -1/2}	$-\frac{3}{2}h_x^3$	{-1, 2}	{2, 1}	{3/2, -1/2}	$\frac{3}{2}h_x^3$
{-2, -1}	{1, -2}	{1/2, 1/2}	$\frac{1}{2}h_y^2 h_z$	{-1, 2}	{2, 1}	{1/2, 1/2}	$-\frac{1}{2}h_y^2 h_z$
{-2, -1}	{1, 0}	{3/2, 1/2}	$-\frac{1}{2}h_x^3$	{0, -3}	{0, 1}	{1, 1}	$-i h_x^2 h_y$
{-2, -1}	{1, 0}	{1/2, -1/2}	$-\frac{1}{4}h_x^2 h_z - \frac{3}{4}h_y^2 h_z + i\frac{1}{2}h_x h_y$	{0, -3}	{0, 1}	{1, -1}	$-i h_y h_z^2$
{-2, -1}	{1, 0}	{1/2, 3/2}	$\frac{1}{4}h_x^2 h_z - \frac{1}{4}h_y^2 h_z - i\frac{1}{2}h_x h_y$	{0, -3}	{0, 3}	{1, 0}	$i h_y^3$
{-2, -1}	{1, 2}	{3/2, 3/2}	$-\frac{1}{2}h_x^3$	{0, -3}	{1, 0}	{1/2, 3/2}	$-\frac{3}{2}h_x^3$
{-2, -1}	{1, 2}	{1/2, 1/2}	$\frac{3}{2}h_y^2 h_z$	{0, -3}	{1, 2}	{1/2, 1/2}	$-\frac{1}{2}h_x h_y^2$
{-2, -1}	{2, -1}	{0, 0}	h_y^2	{0, -1}	{0, -1}	{2, 0}	$\frac{1}{4}h_y^2$
{-2, -1}	{2, -1}	{1, -1}	$i\frac{1}{2}h_x^2 h_y$	{0, -1}	{0, -1}	{0, 2}	$-i h_x h_y h_z$
{-2, -1}	{2, -1}	{1, 1}	$-i\frac{1}{2}h_x^2 h_y$	{0, -1}	{0, -1}	{0, 0}	$2h_x^2 - \frac{1}{2}h_y^2 + 2h_z^2$
{-2, -1}	{2, -1}	{0, 2}	$-i\frac{1}{2}h_x h_y h_z$	{0, -1}	{0, -1}	{1, 1}	$-i\left(-\frac{1}{2}h_x^2 h_y - \frac{1}{2}h_y h_z^2\right)$
{-2, -1}	{2, 1}	{1, 0}	$i\frac{1}{2}h_x^2 h_y$	{0, -1}	{0, -1}	{1, -1}	$i\left(\frac{1}{2}h_x^2 h_y + \frac{1}{2}h_y h_z^2\right)$
{-2, -1}	{2, 1}	{1, 2}	$-i\frac{1}{2}h_x^2 h_y$	{0, -1}	{0, 1}	{3, 0}	$i\frac{1}{8}h_x^3$
{-2, -1}	{2, 1}	{0, 1}	$-i h_x h_y h_z$	{0, -1}	{0, 1}	{1, 2}	$-i\frac{1}{2}h_x^2 h_y$
{-2, -1}	{3, -2}	{1/2, -1/2}	$\frac{1}{2}h_x h_y^2$	{0, -1}	{0, 1}	{1, -2}	$-i\frac{1}{2}h_y h_z^2$
{-2, -1}	{3, 0}	{1/2, 1/2}	$\frac{1}{2}h_x h_y^2$	{0, -1}	{0, 1}	{1, 0}	$i\left(\frac{1}{4}h_x^3 + \frac{3}{2}h_x^2 h_y + \frac{3}{2}h_y h_z^2 - h_y\right)$
{-2, 1}	{-1, -2}	{1/2, -3/2}	$-\frac{3}{2}h_x^3$	{0, -1}	{0, 3}	{1, 1}	$-i h_x^2 h_y$
{-2, 1}	{-1, -2}	{1/2, 1/2}	$\frac{1}{2}h_x h_y^2$	{0, -1}	{0, 3}	{1, -1}	$-i h_y h_z^2$
{-2, 1}	{-1, 0}	{1/2, -5/2}	$\frac{9}{32}h_x h_y^2$	{0, -1}	{1, -2}	{5/2, -1/2}	$\frac{9}{32}h_x h_y^2$
{-2, 1}	{-1, 0}	{1/2, 3/2}	$\frac{9}{32}h_x h_y^2$	{0, -1}	{1, -2}	{3/2, 1/2}	$\frac{9}{32}h_y^2 h_z$
{-2, 1}	{-1, 0}	{1/2, -1/2}	$\frac{1}{2}h_x^3 + \frac{9}{8}h_x h_y^2 + \frac{1}{2}h_x h_z^2$	{0, -1}	{1, -2}	{1/2, -1/2}	$\frac{1}{2}h_x^3 + \frac{9}{8}h_x h_y^2 + \frac{1}{2}h_x h_z^2$
{-2, 1}	{-1, 2}	{1/2, 1/2}	$\frac{1}{2}h_x^3 + \frac{11}{16}h_x h_y^2 + \frac{1}{2}h_x h_z^2$	{0, -1}	{1, 0}	{1/2, 5/2}	$\frac{9}{32}h_x h_y^2$
{-2, 1}	{0, -1}	{2, 0}	$-i h_x^2 h_y$	{0, -1}	{1, 0}	{5/2, 1/2}	$\frac{9}{32}h_x h_y^2$
{-2, 1}	{0, -1}	{1, 1}	$-i\frac{1}{2}h_x h_y h_z$	{0, -1}	{1, 0}	{1/2, 1/2}	$\frac{3}{2}h_x^3 + \frac{5}{8}h_x h_y^2 - h_x$
{-2, 1}	{0, -1}	{0, 2}	$-i\frac{1}{2}h_y h_z^2$	{0, -1}	{1, 0}	{3/2, 3/2}	$\frac{1}{16}h_y^2 h_z$
{-2, 1}	{0, -1}	{1, -1}	$-\frac{1}{2}h_x^2 + i\frac{1}{2}h_x h_y h_z$	{0, -1}	{1, 0}	{3/2, -1/2}	$\frac{1}{4}h_x^2 h_z - \frac{1}{32}h_y^2 h_z + i\frac{1}{2}h_x h_y$

{-2, 1}	{0, -1}	{0, 0}	$i \left(\frac{1}{2} h_x^2 h_y - \frac{1}{2} h_y h_z^2 \right)$	{0, -1}	{1, 0}	{1/2, -3/2}	$-\frac{1}{32} h_x h_y^2 + \frac{1}{4} h_x h_z^2 + i \frac{1}{2} h_y h_z$
{-2, 1}	{0, 1}	{0, 1}	$i \frac{1}{2} h_x^2 h_y$	{0, -1}	{1, 2}	{1/2, 3/2}	$\frac{1}{2} h_x^3$
{-2, 1}	{0, 1}	{2, -1}	$-i \frac{1}{2} h_x^2 h_y$	{0, -1}	{1, 2}	{3/2, 1/2}	$-\frac{1}{4} h_x^2 h_z + \frac{1}{4} h_y^2 h_z - i \frac{1}{2} h_x h_y$
{-2, 1}	{0, 1}	{1, -2}	$-i \frac{1}{2} h_x h_y h_z$	{0, -1}	{1, 2}	{1/2, -1/2}	$\frac{3}{4} h_x h_y^2 + \frac{1}{4} h_x h_z^2 - i \frac{1}{2} h_y h_z$
{-2, 1}	{0, 1}	{1, 0}	$-h_x^2 + i \frac{1}{2} h_x h_y h_z$	{0, -1}	{2, -1}	{0, 1}	$-i \frac{1}{2} h_x^2 h_y$
{-2, 1}	{1, -2}	{3/2, -3/2}	$-\frac{1}{2} h_x^3$	{0, -1}	{2, -1}	{2, -1}	$i \frac{1}{2} h_x^2 h_y$
{-2, 1}	{1, -2}	{1/2, -1/2}	$\frac{3}{2} h_y^2 h_z$	{0, -1}	{2, -1}	{1, -2}	$i \frac{1}{2} h_x h_y h_z$
{-2, 1}	{1, 0}	{3/2, -1/2}	$\frac{1}{2} h_x^3$	{0, -1}	{2, -1}	{1, 0}	$-h_x^2 - i \frac{1}{2} h_x h_y h_z$
{-2, 1}	{1, 0}	{1/2, -3/2}	$-\frac{1}{4} h_x^2 h_z + \frac{1}{4} h_y^2 h_z + i \frac{1}{2} h_x h_y$	{0, -1}	{2, 1}	{0, 2}	$-i \frac{1}{2} h_x^2 h_y$
{-2, 1}	{1, 0}	{1/2, 1/2}	$\frac{1}{4} h_x^2 h_z + \frac{3}{4} h_y^2 h_z - i \frac{1}{2} h_x h_y$	{0, -1}	{2, 1}	{2, 0}	$i h_x^2 h_y$
{-2, 1}	{1, 2}	{3/2, 1/2}	$-\frac{3}{2} h_x^3$	{0, -1}	{2, 1}	{1, -1}	$i \frac{1}{2} h_x h_y h_z$
{-2, 1}	{1, 2}	{1/2, -1/2}	$\frac{1}{2} h_y^2 h_z$	{0, -1}	{2, 1}	{1, 1}	$-\frac{1}{2} h_x^2 - i \frac{1}{2} h_x h_y h_z$
{-2, 1}	{2, -1}	{1, -2}	$i \frac{1}{2} h_x^2 h_y$	{0, -1}	{2, 1}	{0, 0}	$-i \left(-\frac{1}{2} h_x^2 h_y + \frac{1}{2} h_y h_z^2 \right)$
{-2, 1}	{2, -1}	{1, 0}	$-i \frac{1}{2} h_x^2 h_y$	{0, -1}	{2, 3}	{0, 1}	$i \frac{1}{2} h_x^2 h_y$
{-2, 1}	{2, -1}	{0, 1}	$-i h_x h_y h_z$	{0, -1}	{2, 3}	{2, 1}	$-i \frac{1}{2} h_x^2 h_y$
{-2, 1}	{2, 1}	{0, 0}	$-h_y^2$	{0, -1}	{3, -2}	{3/2, -1/2}	$-\frac{3}{2} h_x^3$
{-2, 1}	{2, 1}	{1, -1}	$i \frac{1}{2} h_x^2 h_y$	{0, -1}	{3, 0}	{3/2, 1/2}	$-\frac{3}{2} h_x^3$
{-2, 1}	{2, 1}	{1, 1}	$-i \frac{1}{2} h_x^2 h_y$	{0, -1}	{3, 2}	{3/2, 3/2}	$-\frac{1}{2} h_x^3$
{-2, 1}	{2, 1}	{0, 2}	$-i \frac{1}{2} h_x h_y h_z$	{0, 1}	{0, 1}	{2, 0}	$\frac{1}{4} h_y^2$
{-2, 1}	{3, 0}	{1/2, -1/2}	$-\frac{1}{2} h_x h_y^2$	{0, 1}	{0, 1}	{0, 2}	$i h_x h_y h_z$
{-2, 1}	{3, 2}	{1/2, 1/2}	$-\frac{1}{2} h_x h_y^2$	{0, 1}	{0, 1}	{0, 0}	$2h_x^2 - \frac{1}{2} h_y^2 + 2h_z^2$
{-2, 3}	{-1, -2}	{1/2, -1/2}	$\frac{1}{2} h_x h_y^2$	{0, 1}	{0, 1}	{1, -1}	$-i \left(-\frac{1}{2} h_x^2 h_y - \frac{1}{2} h_y h_z^2 \right)$
{-2, 3}	{-1, 0}	{1/2, -3/2}	$-\frac{3}{2} h_x^3$	{0, 1}	{0, 1}	{1, 1}	$i \left(\frac{1}{2} h_x^2 h_y + \frac{1}{2} h_y h_z^2 \right)$
{-2, 3}	{0, -1}	{2, -1}	$-i \frac{1}{2} h_x^2 h_y$	{0, 1}	{1, -2}	{1/2, -3/2}	$\frac{1}{2} h_x^3$
{-2, 3}	{0, -1}	{0, 1}	$-i \frac{1}{2} h_y h_z^2$	{0, 1}	{1, -2}	{3/2, -1/2}	$-\frac{1}{4} h_x^2 h_z + \frac{1}{4} h_y^2 h_z - i \frac{1}{2} h_x h_y$
{-2, 3}	{1, 0}	{3/2, -3/2}	$\frac{1}{2} h_x^3$	{0, 1}	{1, -2}	{1/2, 1/2}	$\frac{3}{4} h_x h_y^2 + \frac{1}{4} h_x h_z^2 - i \frac{1}{2} h_y h_z$
{-1, -2}	{-1, 0}	{1, 2}	$-i \frac{1}{2} h_x^2 h_y$	{0, 1}	{1, 0}	{1/2, -5/2}	$-\frac{9}{32} h_x h_y^2$
{-1, -2}	{-1, 0}	{2, 1}	$-i \frac{1}{2} h_x h_y h_z$	{0, 1}	{1, 0}	{5/2, -1/2}	$-\frac{9}{32} h_x h_y^2$
{-1, -2}	{-1, 0}	{1, 0}	$-i \frac{1}{2} h_y h_z^2$	{0, 1}	{1, 0}	{1/2, -1/2}	$-\frac{3}{2} h_x^3 - \frac{5}{8} h_x h_y^2 + h_x$
{-1, -2}	{-1, 0}	{0, 1}	$-h_x^2 + i \frac{1}{2} h_x h_y h_z$	{0, 1}	{1, 0}	{3/2, -3/2}	$-\frac{1}{16} h_y^2 h_z$
{-1, -2}	{-1, 2}	{0, 0}	h_y^2	{0, 1}	{1, 0}	{3/2, 1/2}	$-\frac{1}{4} h_x^2 h_z + \frac{1}{32} h_y^2 h_z - i \frac{1}{2} h_x h_y$
{-1, -2}	{-1, 2}	{1, 1}	$-i \frac{1}{2} h_x^2 h_y$	{0, 1}	{1, 0}	{1/2, 3/2}	$\frac{1}{32} h_x h_y^2 - \frac{1}{4} h_x h_z^2 - i \frac{1}{2} h_y h_z$
{-1, -2}	{-1, 2}	{2, 0}	$-i \frac{1}{2} h_x h_y h_z$	{0, 1}	{1, 2}	{5/2, 1/2}	$\frac{9}{32} h_x h_y^2$
{-1, -2}	{-1, 2}	{1, -1}	$-i \frac{1}{2} h_y h_z^2$	{0, 1}	{1, 2}	{3/2, -1/2}	$\frac{9}{32} h_y^2 h_z$
{-1, -2}	{0, -1}	{5/2, 1/2}	$\frac{9}{32} h_x h_y^2$	{0, 1}	{1, 2}	{1/2, 1/2}	$\frac{1}{2} h_x^3 + \frac{9}{8} h_x h_y^2 + \frac{1}{2} h_x h_z^2$
{-1, -2}	{0, -1}	{3/2, -1/2}	$\frac{9}{32} h_y^2 h_z$	{0, 1}	{2, -3}	{2, -1}	$-i \frac{1}{2} h_x^2 h_y$
{-1, -2}	{0, -1}	{1/2, 1/2}	$\frac{1}{2} h_x^3 + \frac{9}{8} h_x h_y^2 + \frac{1}{2} h_x h_z^2$	{0, 1}	{2, -3}	{0, 1}	$-i \frac{1}{2} h_y h_z^2$
{-1, -2}	{0, 1}	{1/2, 3/2}	$-\frac{1}{2} h_x^3$	{0, 1}	{2, -1}	{2, 0}	$-i h_x^2 h_y$
{-1, -2}	{0, 1}	{3/2, 1/2}	$\frac{1}{4} h_x^2 h_z - \frac{1}{4} h_y^2 h_z - i \frac{1}{2} h_x h_y$	{0, 1}	{2, -1}	{1, 1}	$-i \frac{1}{2} h_x h_y h_z$
{-1, -2}	{0, 1}	{1/2, -1/2}	$-\frac{3}{4} h_x h_y^2 - \frac{1}{4} h_x h_z^2 - i \frac{1}{2} h_y h_z$	{0, 1}	{2, -1}	{0, 2}	$-i \frac{1}{2} h_y h_z^2$
{-1, -2}	{0, 3}	{1/2, 1/2}	$\frac{1}{2} h_x h_y^2$	{0, 1}	{2, -1}	{1, -1}	$\frac{1}{2} h_x^2 + i \frac{1}{2} h_x h_y h_z$
{-1, -2}	{1, 0}	{2, 0}	$i \frac{1}{2} h_x^2 h_y$	{0, 1}	{2, -1}	{0, 0}	$i \left(\frac{1}{2} h_x^2 h_y - \frac{1}{2} h_y h_z^2 \right)$
{-1, -2}	{1, 0}	{0, 2}	$-i h_x^2 h_y$	{0, 1}	{2, 1}	{2, 1}	$-i \frac{1}{2} h_x^2 h_y$
{-1, -2}	{1, 0}	{1, -1}	$i \frac{1}{2} h_x h_y h_z$	{0, 1}	{2, 1}	{1, 2}	$-i \frac{1}{2} h_x h_y h_z$
{-1, -2}	{1, 0}	{1, 1}	$-\frac{1}{2} h_x^2 + i \frac{1}{2} h_x h_y h_z$	{0, 1}	{2, 1}	{0, 1}	$-i \frac{1}{2} h_y h_z^2$
{-1, -2}	{1, 0}	{0, 0}	$i \left(\frac{1}{2} h_x^2 h_y - \frac{1}{2} h_y h_z^2 \right)$	{0, 1}	{2, 1}	{1, 0}	$h_x^2 + i \frac{1}{2} h_x h_y h_z$
{-1, -2}	{1, 2}	{0, 1}	$i \frac{1}{2} h_x^2 h_y$	{0, 1}	{3, -2}	{3/2, -3/2}	$\frac{1}{2} h_x^3$
{-1, -2}	{1, 2}	{2, 1}	$-i \frac{1}{2} h_x^2 h_y$	{0, 1}	{3, 0}	{3/2, -1/2}	$\frac{3}{2} h_x^3$
{-1, -2}	{1, 2}	{1, 0}	$-i h_x h_y h_z$	{0, 1}	{3, 2}	{3/2, 1/2}	$\frac{3}{2} h_x^3$
{-1, -2}	{2, -1}	{3/2, 1/2}	$-\frac{3}{2} h_x^3$	{0, 3}	{1, -2}	{1/2, -1/2}	$-\frac{1}{2} h_x h_y^2$
{-1, -2}	{2, -1}	{1/2, -1/2}	$\frac{1}{2} h_y^2 h_z$	{0, 3}	{1, 0}	{1/2, -3/2}	$\frac{3}{2} h_x^3$
{-1, -2}	{2, 1}	{3/2, 3/2}	$-\frac{1}{2} h_x^3$	{1, -2}	{1, 0}	{1, 0}	$i \frac{1}{2} h_x^2 h_y$
{-1, -2}	{2, 1}	{1/2, 1/2}	$\frac{3}{2} h_y^2 h_z$	{1, -2}	{1, 0}	{2, -1}	$i \frac{1}{2} h_x h_y h_z$
{-1, 0}	{-1, 0}	{0, 2}	$\frac{1}{4} h_y^2$	{1, -2}	{1, 0}	{1, -2}	$i \frac{1}{2} h_y h_z^2$

{-1, 0}	{-1, 0}	{2, 0}	$-i h_x h_y h_z$	{1, -2}	{1, 0}	{0, 1}	$-h_x^2 + i \frac{1}{2} h_x h_y h_z$
{-1, 0}	{-1, 0}	{0, 0}	$2h_x^2 - \frac{1}{2} h_y^2 + 2h_z^2$	{1, -2}	{1, 2}	{0, 0}	$-h_y^2$
{-1, 0}	{-1, 0}	{1, -1}	$-i \left(-\frac{1}{2} h_x^2 h_y - \frac{1}{2} h_y h_z^2 \right)$	{1, -2}	{1, 2}	{1, 1}	$-i \frac{1}{2} h_x^2 h_y$
{-1, 0}	{-1, 0}	{1, 1}	$-i \left(-\frac{1}{2} h_x^2 h_y - \frac{1}{2} h_y h_z^2 \right)$	{1, -2}	{1, 2}	{2, 0}	$-i \frac{1}{2} h_x h_y h_z$
{-1, 0}	{-1, 2}	{1, 0}	$-i \frac{1}{2} h_x^2 h_y$	{1, -2}	{1, 2}	{1, -1}	$-i \frac{1}{2} h_y h_z^2$
{-1, 0}	{-1, 2}	{2, -1}	$-i \frac{1}{2} h_x h_y h_z$	{1, -2}	{2, -1}	{1/2, 1/2}	$\frac{1}{2} h_x^3 + \frac{11}{16} h_x h_y^2 + \frac{1}{2} h_x h_z^2$
{-1, 0}	{-1, 2}	{1, -2}	$-i \frac{1}{2} h_y h_z^2$	{1, -2}	{2, 1}	{1/2, 3/2}	$-\frac{3}{2} h_x^3$
{-1, 0}	{-1, 2}	{0, 1}	$-h_x^2 - i \frac{1}{2} h_x h_y h_z$	{1, -2}	{2, 1}	{1/2, -1/2}	$\frac{1}{2} h_x h_y^2$
{-1, 0}	{0, -3}	{1/2, -3/2}	$-\frac{3}{2} h_x^3$	{1, -2}	{2, 3}	{1/2, 1/2}	$-\frac{1}{2} h_x h_y^2$
{-1, 0}	{0, -1}	{1/2, -5/2}	$\frac{9}{32} h_x h_y^2$	{1, 0}	{1, 0}	{0, 2}	$\frac{1}{4} h_y^2$
{-1, 0}	{0, -1}	{5/2, -1/2}	$\frac{9}{32} h_x h_y^2$	{1, 0}	{1, 0}	{2, 0}	$i h_x h_y h_z$
{-1, 0}	{0, -1}	{1/2, -1/2}	$\frac{3}{2} h_x^3 + \frac{5}{8} h_x h_y^2 - h_x$	{1, 0}	{1, 0}	{0, 0}	$2h_x^2 - \frac{1}{2} h_y^2 + 2h_z^2$
{-1, 0}	{0, -1}	{3/2, -3/2}	$\frac{1}{16} h_y^2 h_z$	{1, 0}	{1, 0}	{1, -1}	$i \left(\frac{1}{2} h_x^2 h_y + \frac{1}{2} h_y h_z^2 \right)$
{-1, 0}	{0, -1}	{3/2, 1/2}	$\frac{1}{4} h_x^2 h_z - \frac{1}{32} h_y^2 h_z - i \frac{1}{2} h_x h_y$	{1, 0}	{1, 0}	{1, 1}	$i \left(\frac{1}{2} h_x^2 h_y + \frac{1}{2} h_y h_z^2 \right)$
{-1, 0}	{0, -1}	{1/2, 3/2}	$-\frac{1}{32} h_x h_y^2 + \frac{1}{4} h_x h_z^2 - i \frac{1}{2} h_y h_z$	{1, 0}	{1, 2}	{1, 2}	$-i \frac{1}{2} h_x^2 h_y$
{-1, 0}	{0, 1}	{1/2, 5/2}	$\frac{9}{32} h_x h_y^2$	{1, 0}	{1, 2}	{2, 1}	$-i \frac{1}{2} h_x h_y h_z$
{-1, 0}	{0, 1}	{5/2, 1/2}	$\frac{9}{32} h_x h_y^2$	{1, 0}	{1, 2}	{1, 0}	$-i \frac{1}{2} h_y h_z^2$
{-1, 0}	{0, 1}	{1/2, 1/2}	$\frac{3}{2} h_x^3 + \frac{5}{8} h_x h_y^2 - h_x$	{1, 0}	{1, 2}	{0, 1}	$h_x^2 + i \frac{1}{2} h_x h_y h_z$
{-1, 0}	{0, 1}	{3/2, 3/2}	$\frac{1}{16} h_y^2 h_z$	{1, 0}	{2, -3}	{1/2, -3/2}	$-\frac{3}{2} h_x^3$
{-1, 0}	{0, 1}	{3/2, -1/2}	$\frac{1}{4} h_x^2 h_z - \frac{1}{32} h_y^2 h_z - i \frac{1}{2} h_x h_y$	{1, 0}	{2, -1}	{1/2, -5/2}	$\frac{9}{32} h_x h_y^2$
{-1, 0}	{0, 1}	{1/2, -3/2}	$-\frac{1}{32} h_x h_y^2 + \frac{1}{4} h_x h_z^2 - i \frac{1}{2} h_y h_z$	{1, 0}	{2, -1}	{1/2, 3/2}	$\frac{9}{32} h_x h_y^2$
{-1, 0}	{0, 3}	{1/2, 3/2}	$-\frac{3}{2} h_x^3$	{1, 0}	{2, -1}	{1/2, -1/2}	$\frac{1}{2} h_x^3 + \frac{9}{8} h_x h_y^2 + \frac{1}{2} h_x h_z^2$
{-1, 0}	{1, -2}	{2, 0}	$-i \frac{1}{2} h_x^2 h_y$	{1, 0}	{2, 1}	{1/2, -3/2}	$\frac{9}{32} h_x h_y^2$
{-1, 0}	{1, -2}	{1, 1}	$-i \frac{1}{2} h_x h_y h_z$	{1, 0}	{2, 1}	{1/2, 5/2}	$\frac{9}{32} h_x h_y^2$
{-1, 0}	{1, -2}	{0, 2}	$-i h_y h_z^2$	{1, 0}	{2, 1}	{1/2, 1/2}	$\frac{1}{2} h_x^3 + \frac{9}{8} h_x h_y^2 + \frac{1}{2} h_x h_z^2$
{-1, 0}	{1, -2}	{1, -1}	$-\frac{1}{2} h_x^2 - i \frac{1}{2} h_x h_y h_z$	{1, 0}	{2, 3}	{1/2, 3/2}	$\frac{3}{2} h_x^3$
{-1, 0}	{1, -2}	{0, 0}	$-i \left(-\frac{1}{2} h_x^2 h_y + \frac{1}{2} h_y h_z^2 \right)$	{1, 2}	{2, -3}	{1/2, -1/2}	$-\frac{1}{2} h_x h_y^2$
{-1, 0}	{1, 0}	{0, 3}	$i \frac{1}{8} h_y^3$	{1, 2}	{2, -1}	{1/2, -3/2}	$\frac{3}{2} h_x^3$
{-1, 0}	{1, 0}	{2, -1}	$i \frac{1}{2} h_x^2 h_y$	{1, 2}	{2, -1}	{1/2, 1/2}	$-\frac{1}{2} h_x h_y^2$
{-1, 0}	{1, 0}	{2, 1}	$-i \frac{1}{2} h_x^2 h_y$	{1, 2}	{2, 1}	{1/2, -1/2}	$-\frac{1}{2} h_x^3 - \frac{11}{16} h_x h_y^2 - \frac{1}{2} h_x h_z^2$

TABLE B.2: Hopping amplitudes of particle pairs in the low-field limit of the toric code, as defined in Section 5.1.3. Here, we consider the subspace \mathcal{H}^b .

B.3 High-field series expansions

In the following, we list series expansions of the ground-state energy per site as well as the one-particle gap. Both expressions are polynomials in the variable J/\tilde{h}_z (see Section 5.2 for details). The lengthy coefficients of these polynomials are themselves polynomials in sines as well as cosines of ϕ and θ , which are angles determining the direction of the magnetic field in a spherical coordinate system. To keep a clear overview we summarize the monomials

$$C \cos^p \theta \cos^q \phi \sin^r \theta \sin^s \phi \quad (\text{B.30})$$

in tabular form where each monomial is denoted by its characteristic numbers p , q , r , s , and C . To give an example, using Table B.3, the order-one coefficient of the ground-state energy expansion reads

$$-\frac{1}{2} \cos^4 \theta \sin^4 \phi - \frac{1}{2} \cos^4 \phi, \quad (\text{B.31})$$

which is in agreement with (5.101) calculated in Section 5.2. Let us remind that at order zero the ground-state energy per site is $\tilde{h}_z = \sqrt{h_x^2 + h_x^2 + h_x^2}$ and the one particle gap is $2\tilde{h}_z$. In the following, we list the results for the first three orders of the expansion. The orders four and five are available upon request.

(i) Ground-state energy

p	q	r	s	C
4	0	0	4	-1/2
0	4	0	0	-1/2

TABLE B.3: Order 1 contribution to the ground-state energy per site.

p	q	r	s	C	p	q	r	s	C	p	q	r	s	C
8	8	0	0	-1/8	6	0	2	6	-4	2	0	6	2	-2/3
8	6	0	2	-2/3	4	4	4	0	-3/4	0	6	0	2	-4
8	4	0	4	-3/2	4	4	0	4	6	0	4	0	4	-3/2
8	2	0	6	-4	4	2	4	2	-2	0	2	0	6	-2/3
6	6	2	0	-1/2	4	0	4	4	-3/2	0	0	8	0	-1/8
6	4	2	2	-2	2	2	6	0	-1/2	0	0	0	8	-1/8
6	2	2	4	-3	2	2	2	4	2					

TABLE B.4: Order 2 contribution to the ground-state energy per site.

p	q	r	s	C	p	q	r	s	C	p	q	r	s	C
12	8	0	4	-7/12	8	0	4	8	-21	4	0	8	4	-7/12
12	6	0	6	-29/9	6	8	2	2	8/3	4	0	4	8	-1
12	4	0	8	-21	6	6	2	4	34/3	2	6	2	4	-26
12	2	0	10	16	6	4	2	6	70	2	4	6	2	8/9
10	6	2	4	-7/3	6	2	6	4	-7/3	2	4	2	6	13
10	4	2	6	-29/3	6	2	2	8	-26	2	2	6	4	2/9
10	2	2	8	-42	6	0	6	6	-29/9	2	2	2	8	2/9
10	0	2	10	16	4	8	0	4	-143/3	0	10	0	2	16
8	10	0	2	8/9	4	6	4	2	8/3	0	8	0	4	-21
8	8	0	4	50/9	4	6	0	6	57	0	6	0	6	-29/9
8	6	0	6	57	4	4	4	4	6	0	4	4	4	-1
8	4	4	4	-7/2	4	4	0	8	50/9	0	4	0	8	-7/12
8	4	0	8	-143/3	4	2	4	6	13					
8	2	4	6	-29/3	4	2	0	10	8/9					

TABLE B.5: Order 3 contribution to the ground-state energy per site.

(ii) One-particle gap

p	q	r	s	C	p	q	r	s	C
4	2	0	2	-6	0	4	0	0	4
4	0	0	4	4	0	2	0	2	-6
2	0	2	2	-6					

TABLE B.6: Order 1 contribution to the one-particle gap.

p	q	r	s	C	p	q	r	s	C	p	q	r	s	C
8	8	0	0	-1/2	4	4	4	0	-3	2	0	2	6	4
8	6	0	2	-6	4	4	0	4	-308/3	0	6	0	2	56
8	4	0	4	-12	4	2	4	2	-18	0	4	0	4	-12
8	2	0	6	56	4	2	0	6	12	0	2	4	2	4
6	6	2	0	-2	4	0	4	4	-12	0	2	0	6	-6
6	4	2	2	-18	2	4	2	2	16	0	0	8	0	-1/2
6	2	2	4	-24	2	2	6	0	-2	0	0	0	8	-1/2
6	0	2	6	56	2	2	2	4	-20					
4	6	0	2	12	2	0	6	2	-6					

TABLE B.7: Order 2 contribution to the one-particle gap.

p	q	r	s	C	p	q	r	s	C	p	q	r	s	C
12	10	0	2	-17/8	6	8	2	2	6	2	8	2	2	-96
12	8	0	4	105/2	6	6	2	4	404	2	6	2	4	2200/3
12	6	0	6	-1598/9	6	4	6	2	-85/4	2	4	6	2	10/3
12	4	0	8	756	6	4	2	6	-20440/9	2	4	2	6	-5324/9
12	2	0	10	-224	6	2	6	4	210	2	2	6	4	956/9
10	8	2	2	-85/8	6	2	2	8	2200/3	2	2	2	8	956/9
10	6	2	4	210	6	0	6	6	-1598/9	2	0	10	2	-17/8
10	4	2	6	-1598/3	6	0	2	10	-32	2	0	6	6	-160/9
10	2	2	8	1512	4	10	0	2	-64	2	0	2	10	1/2
10	0	2	10	-224	4	8	0	4	10772/9	0	10	0	2	-224
8	10	0	2	11/6	4	6	4	2	7	0	8	0	4	756
8	8	0	4	1340/9	4	6	0	6	-15116/9	0	6	4	2	-32
8	6	4	2	-85/4	4	4	4	4	1084/3	0	6	0	6	-1598/9
8	6	0	6	-15116/9	4	4	0	8	1340/9	0	4	4	4	172/3
8	4	4	4	315	4	2	8	2	-85/8	0	4	0	8	105/2
8	4	0	8	10772/9	4	2	4	6	-1828/3	0	2	8	2	1/2
8	2	4	6	-1598/3	4	2	0	10	11/6	0	2	4	6	-160/9
8	2	0	10	-64	4	0	8	4	105/2	0	2	0	10	-17/8
8	0	4	8	756	4	0	4	8	172/3					

TABLE B.8: Order 3 contribution to the one-particle gap.

B.4 Spectral densities coefficients

The series expansions of coefficients $A_{\mathbf{K}\mathbf{d}\tau}$ for the observable σ^z , as defined in (7.57), have been computed up to order four. Given the sheer number of coefficients we present only the first few orders of this expansion (up to order two). The full list is available electronically upon request. In the upcoming tables, we will follow the notation $\mathbf{K} = \{K_x, K_y\}$ and $\mathbf{d} = \{d_x, d_y\}$. The flavor of the particle pair will be denoted by 'c' for charges and 'f' for fluxes.

τ	d	$A_{\mathbf{K}d\tau}$
c	{0, 2}	$(h_z - \frac{1}{2}h_x h_y) \cos\left(\frac{K_x - K_y}{2}\right)$
c	{1, 1}	$1 - \frac{1}{2}h_x^2 - \frac{7}{32}h_y^2 - \frac{5}{4}h_z^2 + \frac{1}{4}h_z^2(3 \cos K_x \cos K_y + \sin K_x \sin K_y)$
c	{1, -1}	$\frac{3}{2}h_z^2(\cos K_x + \cos K_y)$
c	{1, -3}	$\frac{1}{4}h_z^2[1 + 5 \cos(K_x - K_y)]$
c	{1, 3}	$\frac{1}{2}h_z^2(\cos K_x + 5 \cos K_y)$
c	{2, 0}	$(h_z - \frac{1}{2}h_x h_y) \cos\left(\frac{K_x - K_y}{2}\right)$
c	{2, 2}	$(h_z - \frac{1}{2}h_x h_y) \cos\left(\frac{K_x + K_y}{2}\right)$
c	{3, -1}	$\frac{1}{4}h_z^2[1 + 5 \cos(K_x - K_y)]$
c	{3, 1}	$\frac{1}{2}h_z^2(5 \cos K_x + \cos K_y)$
c	{3, 3}	$\frac{1}{4}h_z^2[1 + 5 \cos(K_x + K_y)]$
f	{0, 2}	$-\frac{i}{8}h_x h_y \cos\left(\frac{K_x + K_y}{2}\right)$
f	{1, -1}	$-\frac{i}{4}h_y$
f	{2, 0}	$-\frac{i}{8}h_x h_y \cos\left(\frac{K_x + K_y}{2}\right)$
f	{2, -2}	$-\frac{i}{8}h_x h_y \cos\left(\frac{K_x - K_y}{2}\right)$

TABLE B.9: Coefficients of the non-symmetric observable $\mathcal{O}^{2,0}(\mathbf{r}_b)$.

τ	d	$A_{\mathbf{K}d\tau}$
c	{0, 2}	$(h_z - \frac{1}{2}h_x h_y) \cos\left(\frac{K_x + K_y}{2}\right)$
c	{1, -1}	$1 - \frac{1}{2}h_x^2 - \frac{7}{32}h_y^2 - \frac{5}{4}h_z^2 + \frac{1}{4}h_z^2(3 \cos K_x \cos K_y - \sin K_x \sin K_y)$
c	{1, 1}	$\frac{3}{2}h_z^2(\cos K_x + \cos K_y)$
c	{1, 3}	$\frac{1}{4}h_z^2[1 + 5 \cos(K_x + K_y)]$
c	{1, -3}	$\frac{1}{2}h_z^2(\cos K_x + 5 \cos K_y)$
c	{2, 0}	$(h_z - \frac{1}{2}h_x h_y) \cos\left(\frac{K_x + K_y}{2}\right)$
c	{2, -2}	$(h_z - \frac{1}{2}h_x h_y) \cos\left(\frac{K_x - K_y}{2}\right)$
c	{3, 1}	$\frac{1}{4}h_z^2[1 + 5 \cos(K_x + K_y)]$
c	{3, -1}	$\frac{1}{2}h_z^2(5 \cos K_x + \cos K_y)$
c	{3, -3}	$\frac{1}{4}h_z^2[1 + 5 \cos(K_x - K_y)]$
f	{0, 2}	$-\frac{i}{8}h_x h_y \cos\left(\frac{K_x - K_y}{2}\right)$
f	{1, 1}	$-\frac{i}{4}h_y$
f	{2, 0}	$-\frac{i}{8}h_x h_y \cos\left(\frac{K_x - K_y}{2}\right)$
f	{2, 2}	$-\frac{i}{8}h_x h_y \cos\left(\frac{K_x + K_y}{2}\right)$

TABLE B.10: Coefficients of the non-symmetric observable $\mathcal{O}^{2,0}(\mathbf{r}_r)$.

τ	d	$A_{\mathbf{K}d\tau}$
c	{0, 2}	$(2h_z - ih_x h_y) \cos\frac{K_x}{2} \cos\frac{K_y}{2}$
c	{1, -1}	$1 - \frac{1}{2}h_x^2 - \frac{7}{32}h_y^2 - \frac{5}{4}h_z^2 + \frac{1}{4}h_z^2(6 \cos K_y + 6 \cos K_y + 3 \cos K_x \cos K_y - \sin K_x \sin K_y)$
c	{1, 1}	$1 - \frac{1}{2}h_x^2 - \frac{7}{32}h_y^2 - \frac{5}{4}h_z^2 + \frac{1}{4}h_z^2(6 \cos K_y + 6 \cos K_y + 3 \cos K_x \cos K_y + \sin K_x \sin K_y)$
c	{1, 3}	$\frac{1}{4}h_z^2[1 + 2 \cos K_x + 10 \cos K_y + 5 \cos(K_x + K_y)]$
c	{1, -3}	$\frac{1}{4}h_z^2[1 + 2 \cos K_x + 10 \cos K_y + 5 \cos(K_x - K_y)]$
c	{2, 0}	$(2h_z - ih_x h_y) \cos\frac{K_x}{2} \cos\frac{K_y}{2}$
c	{2, -2}	$(h_z - \frac{1}{2}h_x h_y) \cos\left(\frac{K_x - K_y}{2}\right)$
c	{2, 2}	$(h_z - \frac{1}{2}h_x h_y) \cos\left(\frac{K_x + K_y}{2}\right)$
c	{3, 1}	$\frac{1}{4}h_z^2[1 + 10 \cos K_x + 2 \cos K_y + 5 \cos(K_x + K_y)]$
c	{3, -1}	$\frac{1}{4}h_z^2[1 + 10 \cos K_x + 2 \cos K_y + 5 \cos(K_x - K_y)]$
c	{3, -3}	$\frac{1}{4}h_z^2[1 + 5 \cos(K_x - K_y)]$
c	{3, 3}	$\frac{1}{4}h_z^2[1 + 5 \cos(K_x + K_y)]$
f	{0, 2}	$-\frac{i}{4}h_x h_y \cos\frac{K_x}{2} \cos\frac{K_y}{2}$
f	{1, -1}	$-\frac{i}{4}h_y$

f	{1, 1}	$-\frac{i}{4}h_y$
f	{2, 0}	$-\frac{i}{4}h_x h_y \cos \frac{K_x}{2} \cos \frac{K_y}{2}$
f	{2, -2}	$-\frac{i}{8}h_x h_y \cos \left(\frac{K_x - K_y}{2} \right)$
f	{2, 2}	$-\frac{i}{8}h_x h_y \cos \left(\frac{K_x + K_y}{2} \right)$

TABLE B.11: Coefficients of the symmetric observable $[\mathcal{O}^{2,0}(\mathbf{r}_b) + \mathcal{O}^{2,0}(\mathbf{r}_r)]/\sqrt{2}$.

τ	d	$A_{\mathbf{K}d\tau}$
c	{0, 2}	$(2h_z - ih_x h_y) \sin \frac{K_x}{2} \sin \frac{K_y}{2}$
c	{1, -1}	$-1 + \frac{1}{2}h_x^2 + \frac{7}{32}h_y^2 + \frac{5}{4}h_z^2 + \frac{1}{4}h_z^2 [6 \cos K_x + 6 \cos K_y - 3 \cos K_x \cos K_y + \sin K_x \sin K_y]$
c	{1, 1}	$1 - \frac{1}{2}h_x^2 - \frac{7}{32}h_y^2 - \frac{5}{4}h_z^2 - \frac{1}{4}h_z^2 [6 \cos K_x + 6 \cos K_y - 3 \cos K_x \cos K_y - \sin K_x \sin K_y]$
c	{1, 3}	$\frac{1}{4}h_z^2 [-1 + 2 \cos K_x + 10 \cos K_y - 5 \cos(K_x + K_y)]$
c	{1, -3}	$\frac{1}{4}h_z^2 [1 - 2 \cos K_x - 10 \cos K_y + 5 \cos(K_x - K_y)]$
c	{2, 0}	$(2h_z - ih_x h_y) \sin \frac{K_x}{2} \sin \frac{K_y}{2}$
c	{2, -2}	$(-h_z + \frac{i}{2}h_x h_y) \cos \left(\frac{K_x - K_y}{2} \right)$
c	{2, 2}	$(h_z - \frac{i}{2}h_x h_y) \cos \left(\frac{K_x + K_y}{2} \right)$
c	{3, 1}	$-\frac{1}{4}h_z^2 [1 - 10 \cos K_x - 2 \cos K_y + 5 \cos(K_x + K_y)]$
c	{3, -1}	$\frac{1}{4}h_z^2 [1 - 10 \cos K_x - 2 \cos K_y + 5 \cos(K_x - K_y)]$
c	{3, -3}	$-\frac{1}{4}h_z^2 [1 + 5 \cos(K_x - K_y)]$
c	{3, 3}	$\frac{1}{4}h_z^2 [1 + 5 \cos(K_x + K_y)]$
f	{0, 2}	$\frac{i}{4}h_x h_y \sin \frac{K_x}{2} \sin \frac{K_y}{2}$
f	{1, -1}	$-\frac{i}{4}h_y$
f	{1, 1}	$\frac{i}{4}h_y$
f	{2, 0}	$\frac{i}{4}h_x h_y \sin \frac{K_x}{2} \sin \frac{K_y}{2}$
f	{2, -2}	$-\frac{i}{8}h_x h_y \cos \left(\frac{K_x - K_y}{2} \right)$
f	{2, 2}	$\frac{i}{8}h_x h_y \cos \left(\frac{K_x + K_y}{2} \right)$

TABLE B.12: Coefficients of the antisymmetric observable $[\mathcal{O}^{2,0}(\mathbf{r}_b) - \mathcal{O}^{2,0}(\mathbf{r}_r)]/\sqrt{2}$.

Appendix C

Spectral densities

In this paragraph, we present spectral densities computed for the toric code in a magnetic field $\mathbf{h} = (h_x, h_y, h_z)$ for the observable σ^z . In the symmetric case $(\mathcal{O}_r + \mathcal{O}_b)/\sqrt{2}$ (see Section 7.3 for notation), we have investigated the subspace $h_z \geq h_x$. However, it might also be interesting to consider a direction of the magnetic field with $h_x > h_z$ because, in contrast to the exact spectrum of the two-quasi-particle subspace, the spectral density is obviously not symmetric in h_x and h_z . In the following three plots we vary the ratio h_x/h_z and show how the spectral density depends on the transverse field h_y for each ratio.

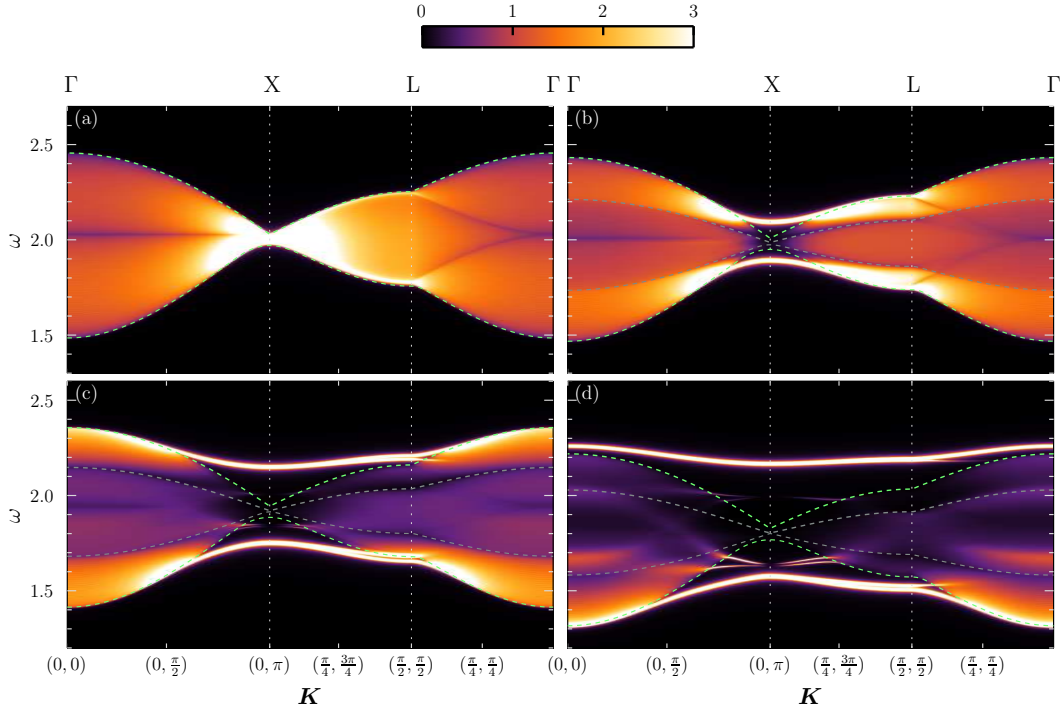


FIGURE C.1: Spectral density of the toric code in the magnetic field $h_x = 0.03$, $h_z = 0.06$ and (a) $h_y = 0$, (b) $h_y = 0.1$, (c) $h_y = 0.2$, (d) $h_y = 0.3$. The continuum boundaries of charge-pairs (flux-pairs) are highlighted by green (gray) dashed lines.

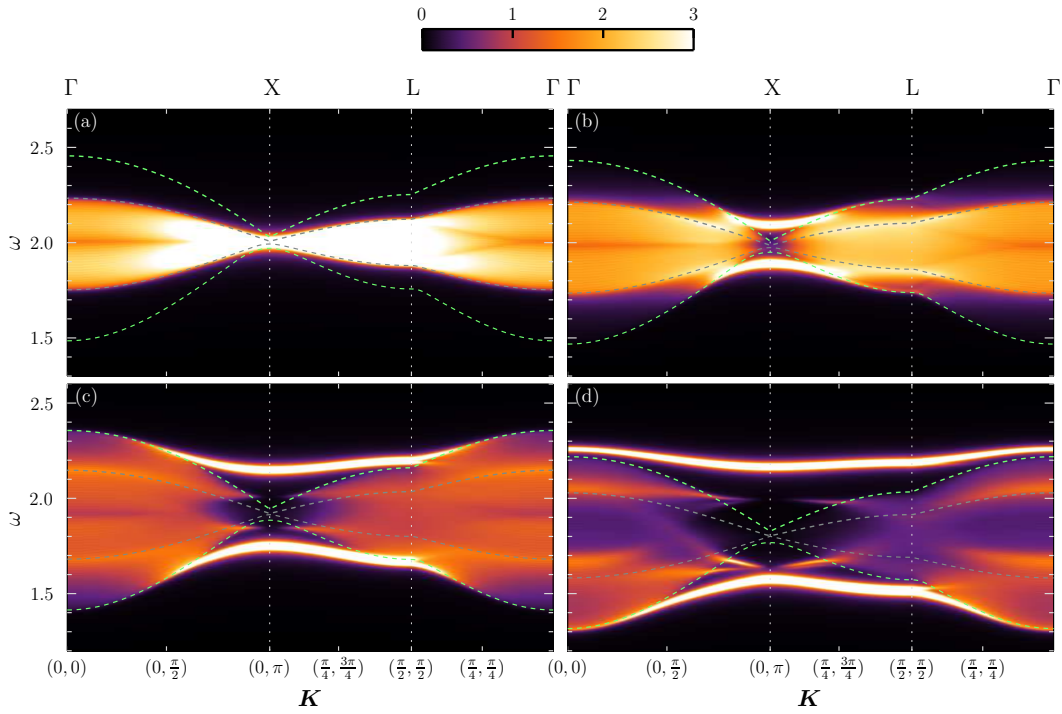


FIGURE C.2: Spectral density of the toric code in the magnetic field $h_x = 0.06$, $h_z = 0.03$ and (a) $h_y = 0$, (b) $h_y = 0.1$, (c) $h_y = 0.2$, (d) $h_y = 0.3$. The continuum boundaries of charge-pairs (flux-pairs) are highlighted by green (gray) dashed lines. Here, we have used a broadening $\epsilon = 0.008$.

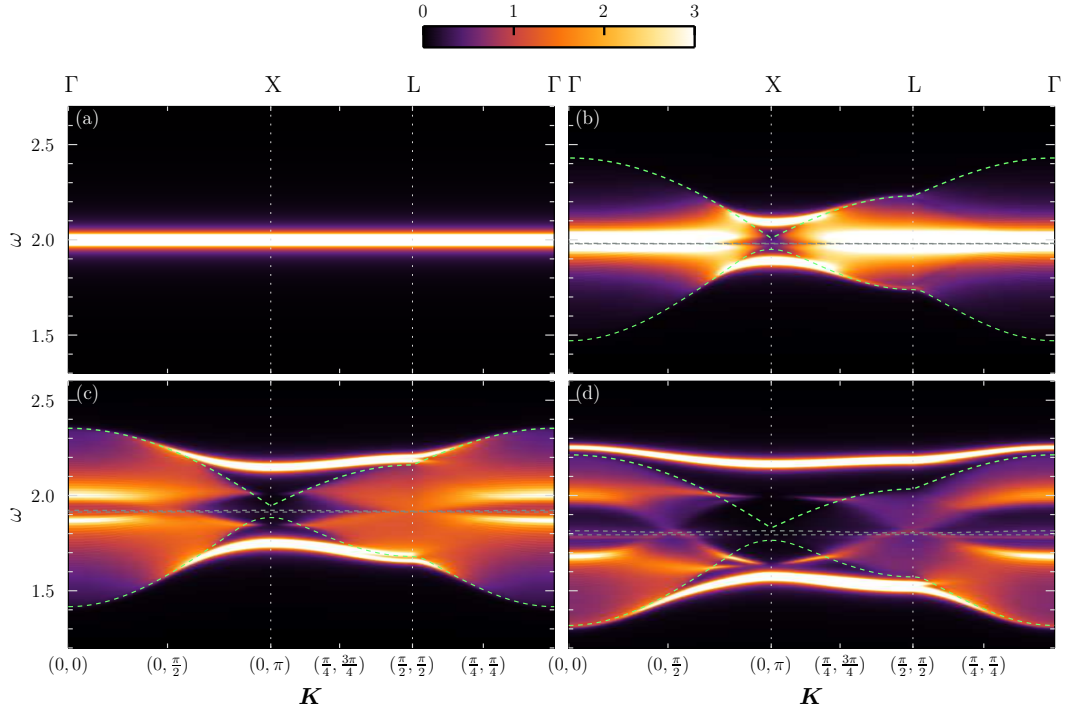


FIGURE C.3: Spectral density of the toric code in the magnetic field $h_x = 0.06$, $h_z = 0$ and (a) $h_y = 0$, (b) $h_y = 0.1$, (c) $h_y = 0.2$, (d) $h_y = 0.3$. The continuum boundaries of charge-pairs (flux-pairs) are highlighted by green (gray) dashed lines. Here, we have used a broadening $\epsilon = 0.008$.

Let us shortly discuss the presented figures. While for $h_z > h_x$ the boundaries of the continuum are determined by charge pairs (we remind that in the currently considered sector of the two-particle subspace, charges and fluxes only appear in pairs), energies of flux pairs are limited by a distinct region, e.g., the one clearly visible in Figure C.1 (b). These boundaries have been computed from single-particle dispersions of charges and fluxes, and seem to match perfectly with according features in the spectral density. In the parameter range $h_z < h_x$, the roles of charges and fluxes concerning the continuum boundaries are interchanged.

The spectral density of the observable σ^z shows interesting features for $h_x > h_z$. For example, at zero transverse field the weight of charges is fully suppressed [see Figure C.2 (a) and Figure C.3 (a)]

While in Section 7.3.3 we have discussed the symmetrized observable, in the following plots we show the non-symmetric as well as the antisymmetric cases. In the non-symmetric cases the observable acts on a specific sublattice (see Fig. 7.13), while in the antisymmetric case there is an alternating sign in the action of the observable on each sublattice. As we have discussed in Section 7.3, in the presented plots one clearly observes differences in the distribution of the spectral density into the symmetric as well as antisymmetric bound states.

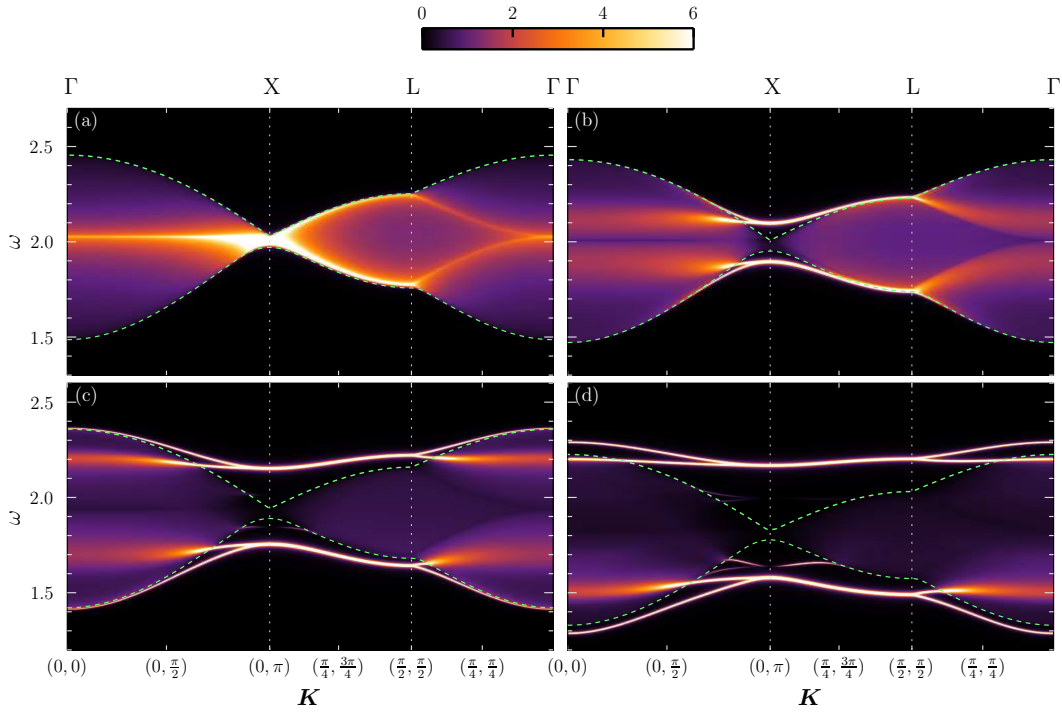


FIGURE C.4: Spectral density $\mathcal{S}(\mathbf{K}, \omega)$ of the observable \mathcal{O}_b of the toric code in the magnetic field $h_x = h_z = 0.06$ and (a) $h_y = 0$, (b) $h_y = 0.1$, (c) $h_y = 0.2$, (d) $h_y = 0.3$. See Figure 7.5 for a comparison with the corresponding energy spectrum. The amplitude of $\mathcal{S}(\mathbf{K}, \omega)$ corresponds to the color scale at the top. The continuum boundaries are highlighted by green dashed lines.

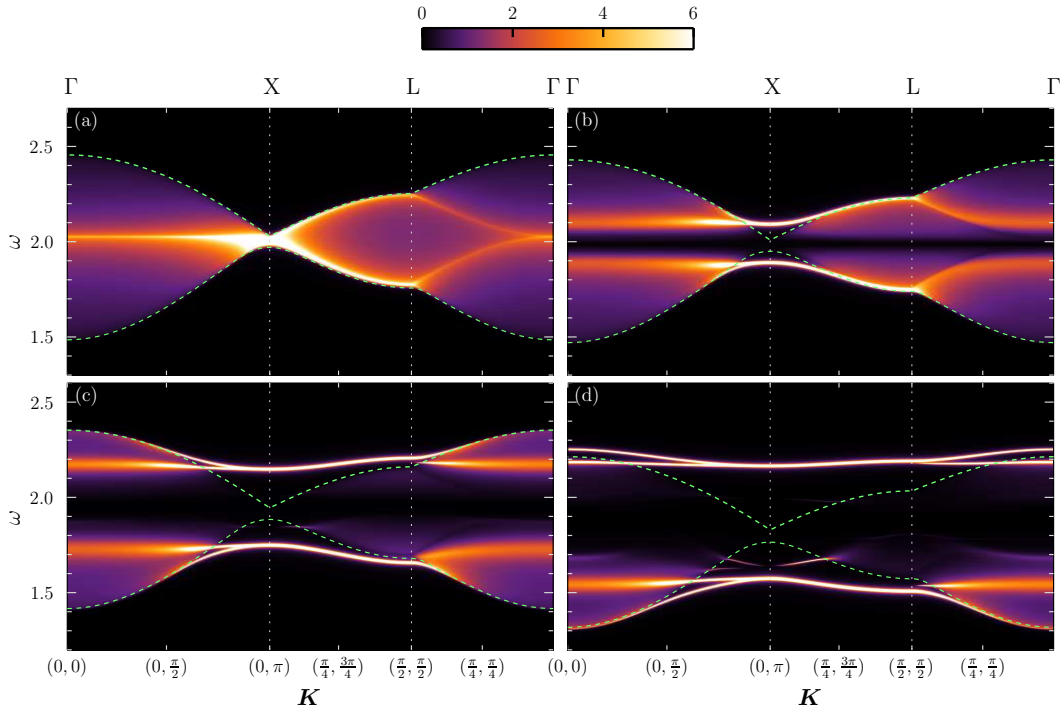


FIGURE C.5: Spectral density $\mathcal{S}(\mathbf{K}, \omega)$ of the observable \mathcal{O}_b of the toric code in the magnetic field $h_x = 0$, $h_z = 0.06$ and (a) $h_y = 0$, (b) $h_y = 0.1$, (c) $h_y = 0.2$, (d) $h_y = 0.3$. See Figure 7.6 for a comparison with the corresponding energy spectrum. The amplitude of $\mathcal{S}(\mathbf{K}, \omega)$ corresponds to the color scale at the top. The continuum boundaries are highlighted by green dashed lines.

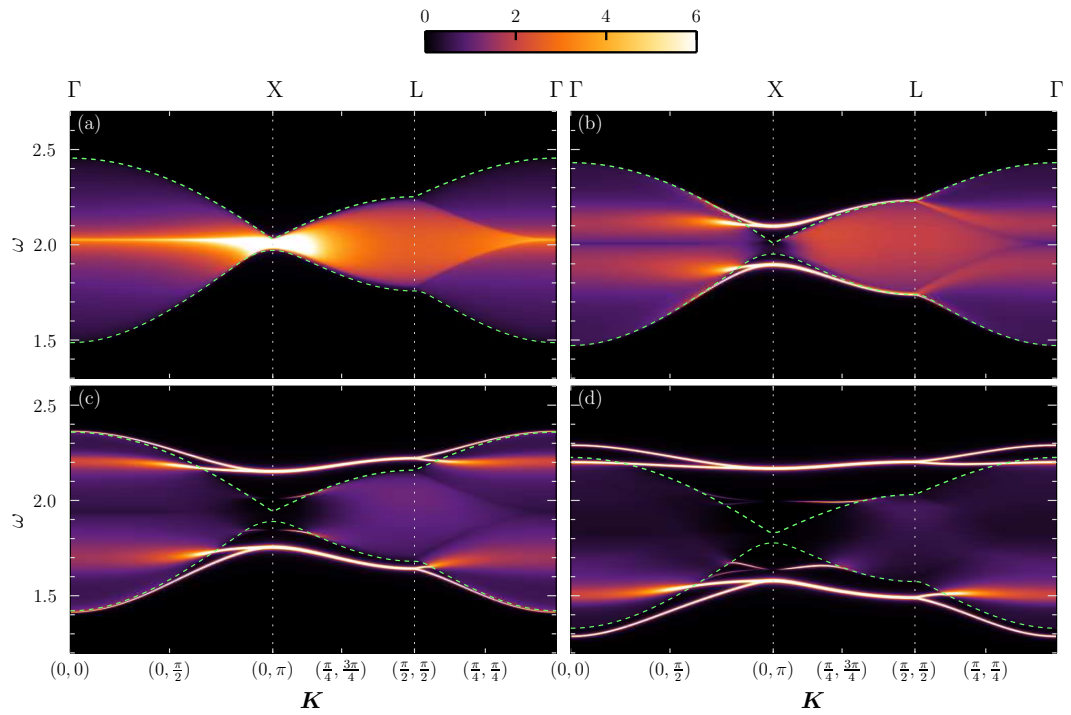


FIGURE C.6: Spectral density $\mathcal{S}(\mathbf{K}, \omega)$ of the observable \mathcal{O}_r of the toric code in the magnetic field $h_x = h_z = 0.06$ and (a) $h_y = 0$, (b) $h_y = 0.1$, (c) $h_y = 0.2$, (d) $h_y = 0.3$. See Figure 7.5 for a comparison with the corresponding energy spectrum. The amplitude of $\mathcal{S}(\mathbf{K}, \omega)$ corresponds to the color scale at the top. The continuum boundaries are highlighted by green dashed lines.

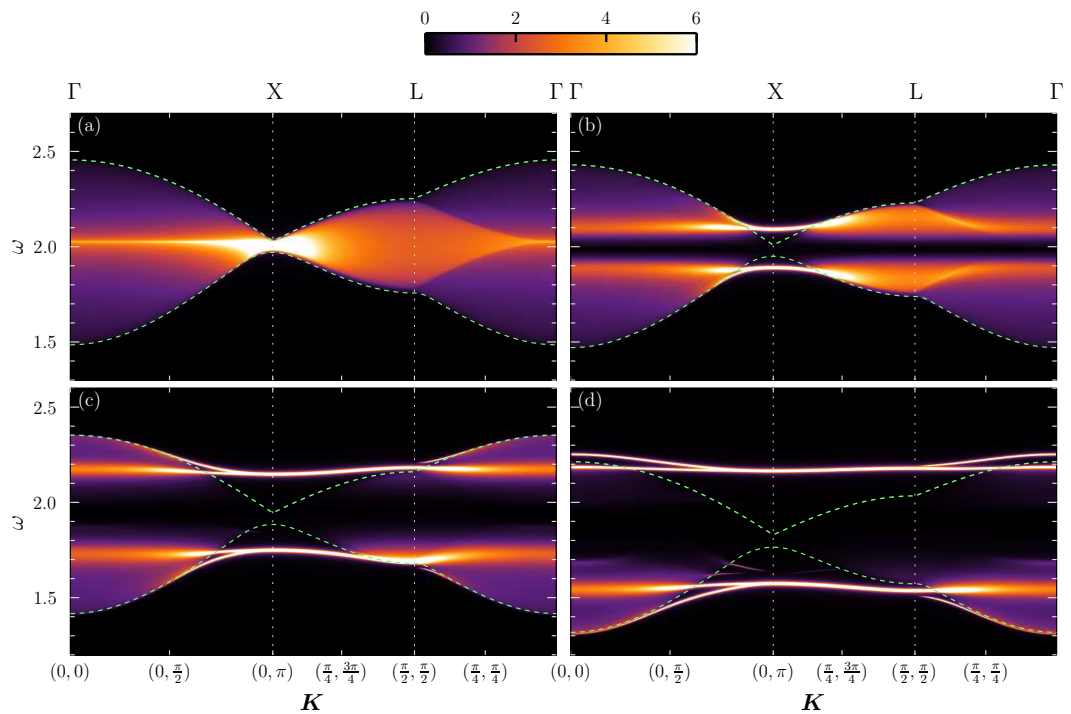


FIGURE C.7: Spectral density $\mathcal{S}(\mathbf{K}, \omega)$ of the observable \mathcal{O}_r of the toric code in the magnetic field $h_x = 0$, $h_z = 0.06$ and (a) $h_y = 0$, (b) $h_y = 0.1$, (c) $h_y = 0.2$, (d) $h_y = 0.3$. See Figure 7.6 for a comparison with the corresponding energy spectrum. The amplitude of $\mathcal{S}(\mathbf{K}, \omega)$ corresponds to the color scale at the top. The continuum boundaries are highlighted by green dashed lines.

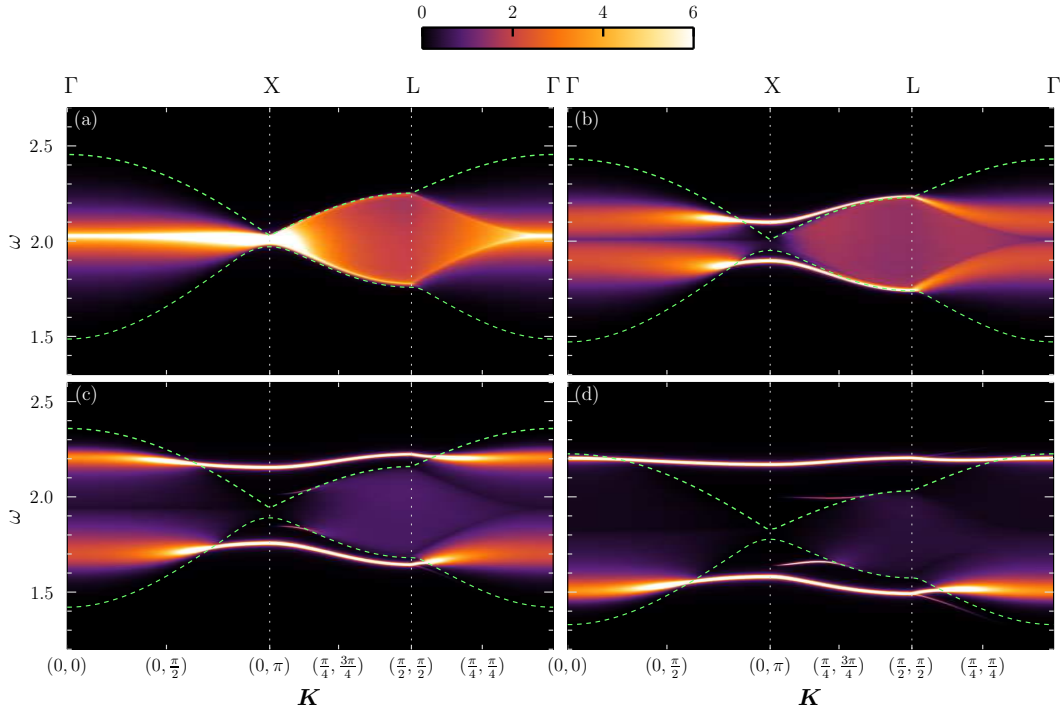


FIGURE C.8: Spectral density $\mathcal{S}(\mathbf{K}, \omega)$ of the observable $(\mathcal{O}_b - \mathcal{O}_r)/\sqrt{2}$ of the toric code in the magnetic field $h_x = h_z = 0.06$ and (a) $h_y = 0$, (b) $h_y = 0.1$, (c) $h_y = 0.2$, (d) $h_y = 0.3$. See Figure 7.5 for a comparison with the corresponding energy spectrum. The amplitude of $\mathcal{S}(\mathbf{K}, \omega)$ corresponds to the color scale at the top. The continuum boundaries are highlighted by green dashed lines.

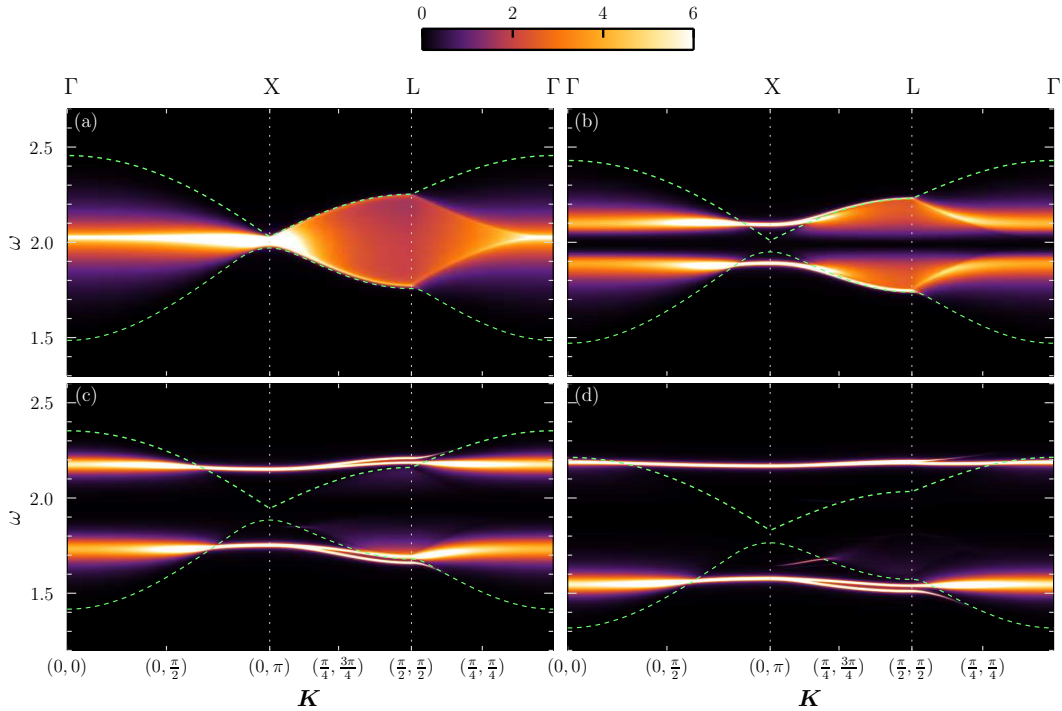


FIGURE C.9: Spectral density $\mathcal{S}(\mathbf{K}, \omega)$ of the observable $(\mathcal{O}_b - \mathcal{O}_r)/\sqrt{2}$ of the toric code in the magnetic field $h_x = 0$, $h_z = 0.06$ and (a) $h_y = 0$, (b) $h_y = 0.1$, (c) $h_y = 0.2$, (d) $h_y = 0.3$. See Figure 7.6 for a comparison with the corresponding energy spectrum. The amplitude of $\mathcal{S}(\mathbf{K}, \omega)$ corresponds to the color scale at the top. The continuum boundaries are highlighted by by green dashed lines.

Bibliography

- [1] L. D. LANDAU. *Theory of phase transformations. I.* *Phys. Z. Sowjetunion* **11**, 26 (1937).
- [2] L. D. LANDAU. *Theory of phase transformations. II.* *Phys. Z. Sowjetunion* **11**, 545 (1937).
- [3] L. D. LANDAU, E. M. LIFSCHITZ. *Statistische Physik.* In *Lehrbuch der Theoretischen Physik*, edited by G. HEBER, volume 5. Akademie Verlag Berlin (1970).
- [4] X. G. WEN. *Vacuum degeneracy of chiral spin states in compactified space.* *Phys. Rev. B* **40**, 7387 (1989).
- [5] X. G. WEN, Q. NIU. *Ground-state degeneracy of the fractional quantum Hall states in the presence of a random potential and on high-genus Riemann surfaces.* *Phys. Rev. B* **41**, 9377 (1990).
- [6] X. G. WEN, F. WILCZEK, A. ZEE. *Chiral spin states and superconductivity.* *Phys. Rev. B* **39**, 11413 (1989).
- [7] R. B. LAUGHLIN. *The relationship between high-temperature superconductivity and the fractional quantum Hall effect.* *Science* **242**, 525 (1988).
- [8] D. C. TSUI, H. L. STORMER, A. C. GOSSARD. *Two-dimensional magnetotransport in the extreme quantum limit.* *Phys. Rev. Lett.* **48**, 1559 (1982).
- [9] R. B. LAUGHLIN. *Anomalous quantum Hall effect: An incompressible quantum fluid with fractionally charged excitations.* *Phys. Rev. Lett.* **50**, 1395 (1983).
- [10] E. WITTEN. *Topological quantum field theory.* *Commun. Math. Phys.* **117**, 353 (1988).
- [11] X. G. WEN. *Quantum Field Theory of Many-Body Systems.* Oxford University Press (2004).
- [12] Z. NUSSINOV, G. ORTIZ. *Sufficient symmetry conditions for topological quantum order.* *Proc. Natl. Acad. Sci. U.S.A.* **106**, 16944 (2009).
- [13] Z. NUSSINOV, G. ORTIZ. *A symmetry principle for topological quantum order.* *Ann. Phys.* **324**, 977 (2009).
- [14] M. OSHIKAWA, T. SENTHIL. *Fractionalization, topological order, and quasiparticle statistics.* *Phys. Rev. Lett.* **96**, 060601 (2006).
- [15] J. M. LEINAAS, J. MYRHEIM. *On the theory of identical particles.* *Nuovo Cimento Soc. Ital. Fis. B* **37**, 1 (1977).
- [16] F. WILCZEK. *Quantum mechanics of fractional-spin particles.* *Phys. Rev. Lett.* **49**, 957 (1982).
- [17] Y. AHARONOV, D. BOHM. *Significance of electromagnetic potentials in the quantum theory.* *Phys. Rev.* **115**, 485 (1959).
- [18] D. AROVAS, J. R. SCHRIEFFER, F. WILCZEK. *Fractional statistics and the quantum Hall effect.* *Phys. Rev. Lett.* **53**, 722 (1984).

- [19] F. E. CAMINO, W. ZHOU, V. J. GOLDMAN. *Realization of a Laughlin quasiparticle interferometer: Observation of fractional statistics.* *Phys. Rev. B* **72**, 075342 (2005).
- [20] P. BONDERSON, A. KITAEV, K. SHTENDEL. *Detecting non-Abelian statistics in the $\nu=5/2$ fractional quantum Hall state.* *Phys. Rev. Lett.* **96**, 016803 (2006).
- [21] A. STERN. *Anyons and the quantum Hall effect. a pedagogical review.* *Ann. Phys.* **323**, 204 (2008).
- [22] C. NAYAK, S. H. SIMON, A. STERN, M. FREEDMAN, S. DAS SARMA. *Non-Abelian anyons and topological quantum computation.* *Rev. Mod. Phys.* **80**, 1083 (2008).
- [23] R. WILLETT, J. P. EISENSTEIN, H. L. STÖRMER, D. C. TSUI, A. C. GOSSARD, J. H. ENGLISH. *Observation of an even-denominator quantum number in the fractional quantum Hall effect.* *Phys. Rev. Lett.* **59**, 1776 (1987).
- [24] G. MOORE, N. READ. *Nonabelions in the fractional quantum Hall effect.* *Nucl. Phys. B* **360**, 362 (1991).
- [25] M. DOLEV, M. HEIBLUM, V. UMANSKY, A. STERN, D. MAHALU. *Observation of a quarter of an electron charge at the $\nu = 5/2$ quantum Hall state.* *Nature (London)* **452**, 829 (2008).
- [26] R. L. WILLETT, L. N. PFEIFFER, K. W. WEST. *Alternation and interchange of $e/4$ and $e/2$ period interference oscillations consistent with filling factor $5/2$ non-Abelian quasiparticles.* *Phys. Rev. B* **82**, 205301 (2010).
- [27] R. L. WILLETT, C. NAYAK, K. SHTENDEL, L. N. PFEIFFER, K. W. WEST. *Magnetic field-tuned Aharonov-Bohm oscillations and evidence for non-Abelian anyons at $\nu=5/2$.* *arXiv:1301.2639* (2013).
- [28] A. KITAEV. *Fault-tolerant quantum computation by anyons.* *Ann. Phys.* **303**, 2 (2003).
- [29] P. W. ANDERSON. *Resonating valence bonds: A new kind of insulator?* *Mater. Res. Bull.* **8**, 153 (1973).
- [30] D. S. ROKHSAR, S. A. KIVELSON. *Superconductivity and the quantum hard-core dimer gas.* *Phys. Rev. Lett.* **61**, 2376 (1988).
- [31] R. MOESSNER, S. L. SONDHI. *Resonating valence bond phase in the triangular lattice quantum dimer model.* *Phys. Rev. Lett.* **86**, 1881 (2001).
- [32] L. BALENTS. *Spin liquids in frustrated magnets.* *Nature (London)* **464**, 199 (2010).
- [33] P. W. ANDERSON. *The resonating valence bond state in La_2CuO_4 and superconductivity.* *Science* **235**, 1196 (1987).
- [34] O. I. MOTRUNICH, T. SENTHIL. *Exotic order in simple models of bosonic systems.* *Phys. Rev. Lett.* **89**, 277004 (2002).
- [35] M. A. LEVIN, X.-G. WEN. *String-net condensation: a physical mechanism for topological phases.* *Phys. Rev. B* **71**, 045110 (2005).
- [36] A. KITAEV. *Anyons in an exactly solved model and beyond.* *Ann. Phys.* **321**, 2 (2006).
- [37] D. GOTTESMAN. *Class of quantum error-correcting codes saturating the quantum hamming bound.* *Phys. Rev. A* **54**, 1862 (1996).
- [38] A. Y. KITAEV. *Quantum computations: algorithms and error correction.* *Russ. Math. Surv.* **52**, 1191 (1997).
- [39] X.-G. WEN. *Quantum orders in an exact soluble model.* *Phys. Rev. Lett.* **90**, 016803 (2003).
- [40] E. DENNIS, A. KITAEV, A. LANDAHL, J. PRESKILL. *Topological quantum memory.* *J. Math. Phys.* **43**, 4452 (2002).
- [41] S. S. BULLOCK, G. K. BRENNEN. *Qudit surface codes and gauge theory with finite cyclic groups.* *J. Phys. A* **40**, 3481 (2007).

- [42] M. D. SCHULZ, S. DUSUEL, R. ORÚS, J. VIDAL, K. P. SCHMIDT. *Breakdown of a perturbed Z_N topological phase*. *New J. Phys.* **14**, 025005 (2012).
- [43] Y. J. HAN, R. RAUSSENDORF, L. M. DUAN. *Scheme for demonstration of fractional statistics of anyons in an exactly solvable model*. *Phys. Rev. Lett.* **98**, 150404 (2007).
- [44] H. WEIMER, M. MULLER, I. LESANOVSKY, P. ZOLLER, H. P. BUCHLER. *A Rydberg quantum simulator*. *Nat. Phys.* **6**, 382 (2010).
- [45] L. B. IOFFE, M. V. FEIGEL'MAN, A. IOSELEVICH, D. IVANOV, M. TROYER, G. BLATTER. *Topologically protected quantum bits using Josephson junction arrays*. *Nature (London)* **415**, 503 (2002).
- [46] B. DOUÇOT, L. B. IOFFE, J. VIDAL. *Discrete non-Abelian gauge theories in Josephson-junction arrays and quantum computation*. *Phys. Rev. B* **69**, 214501 (2004).
- [47] J. T. BARREIRO, M. MULLER, P. SCHINDLER, D. NIGG, T. MONZ, M. CHWALLA, M. HENNRICH, C. F. ROOS, P. ZOLLER, R. BLATT. *An open-system quantum simulator with trapped ions*. *Nature (London)* **470**, 486 (2011).
- [48] N. LANG, H. P. BÜCHLER. *Minimal instances for toric code ground states*. *Phys. Rev. A* **86**, 022336 (2012).
- [49] J. K. PACHOS, W. WIECZOREK, C. SCHMID, N. KIESEL, R. POHLNER, H. WEINFURTER. *Revealing anyonic features in a toric code quantum simulation*. *New J. Phys.* **11**, 083010 (2009).
- [50] J. VIDAL, K. P. SCHMIDT, S. DUSUEL. *Perturbative approach to an exactly solved problem: Kitaev honeycomb model*. *Phys. Rev. B* **78**, 245121 (2008).
- [51] L.-M. DUAN, E. DEMLER, M. D. LUKIN. *Controlling spin exchange interactions of ultracold atoms in optical lattices*. *Phys. Rev. Lett.* **91**, 090402 (2003).
- [52] A. MICHELI, G. K. BRENNEN, P. ZOLLER. *A toolbox for lattice-spin models with polar molecules*. *Nat. Phys.* **2**, 341 (2006).
- [53] J. Q. YOU, X.-F. SHI, X. HU, F. NORI. *Quantum emulation of a spin system with topologically protected ground states using superconducting quantum circuits*. *Phys. Rev. B* **81**, 014505 (2010).
- [54] J. CHALOUPKA, G. JACKELI, G. KHALIULLIN. *Kitaev-Heisenberg model on a honeycomb lattice: Possible exotic phases in iridium oxides A_2IrO_3* . *Phys. Rev. Lett.* **105**, 027204 (2010).
- [55] Y. SINGH, S. MANNI, J. REUTHER, T. BERLIJN, R. THOMALE, W. KU, S. TREBST, P. GEGENWART. *Relevance of the Heisenberg-Kitaev model for the honeycomb lattice iridates A_2IrO_3* . *Phys. Rev. Lett.* **108**, 127203 (2012).
- [56] B. A. BERNEVIG, T. L. HUGHES, S.-C. ZHANG. *Quantum spin Hall effect and topological phase transition in $HgTe$ quantum wells*. *Science* **314**, 1757 (2006).
- [57] M. KÖNIG, S. WIEDMANN, C. BRÜNE, A. ROTH, H. BUHMANN, L. W. MOLENKAMP, X. L. QI, S. C. ZHANG. *Quantum spin Hall insulator state in $HgTe$ quantum wells*. *Science* **318**, 766 (2007).
- [58] M. Z. HASAN, C. L. KANE. *Topological insulators*. *Rev. Mod. Phys.* **82**, 3045 (2010).
- [59] J. E. MOORE. *The birth of topological insulators*. *Nature (London)* **464**, 194 (2010).
- [60] J. D. SAU, R. M. LUTCHYN, S. TEWARI, S. DAS SARMA. *Generic new platform for topological quantum computation using semiconductor heterostructures*. *Phys. Rev. Lett.* **104**, 040502 (2010).
- [61] A. R. AKHMEROV, J. NILSSON, C. W. J. BEENAKKER. *Electrically detected interferometry of Majorana fermions in a topological insulator*. *Phys. Rev. Lett.* **102**, 216404 (2009).
- [62] L. FU, C. L. KANE, E. J. MELE. *Topological insulators in three dimensions*. *Phys. Rev. Lett.* **98**, 106803 (2007).
- [63] H. ZHANG, C. X. LIU, X. L. QI, X. DAI, Z. FANG, S. C. ZHANG. *Topological insulators in Bi_2Se_3 , Bi_2Te_3 and Sb_2Te_3 with a single Dirac cone on the surface*. *Nat. Phys.* **5**, 438 (2009).
- [64] S. BRAVYI, M. B. HASTINGS, S. MICHALAKIS. *Topological quantum order: stability under local perturbations*. *J. Math. Phys.* **51**, 093512 (2010).

- [65] S. TREBST, P. WERNER, M. TROYER, K. SHTENDEL, C. NAYAK. *Breakdown of a topological phase: quantum phase transition in a loop gas model with tension.* *Phys. Rev. Lett.* **98**, 070602 (2007).
- [66] I. S. TUPITSYN, A. KITAEV, N. V. PROKOF'EV, P. C. E. STAMP. *Topological multicritical point in the phase diagram of the toric code model and three-dimensional lattice gauge Higgs model.* *Phys. Rev. B* **82**, 085114 (2010).
- [67] F. WU, Y. DENG, N. PROKOF'EV. *Phase diagram of the toric code model in a parallel magnetic field.* *Phys. Rev. B* **85**, 195104 (2012).
- [68] J. VIDAL, S. DUSUEL, K. P. SCHMIDT. *Low-energy effective theory of the toric code model in a parallel magnetic field.* *Phys. Rev. B* **79**, 033109 (2009).
- [69] J. VIDAL, R. THOMALE, K. P. SCHMIDT, S. DUSUEL. *Self-duality and bound states of the toric code model in a transverse field.* *Phys. Rev. B* **80**, 081104 (2009).
- [70] C. CASTELNOVO, C. CHAMON. *Entanglement and topological entropy of the toric code at finite temperature.* *Phys. Rev. B* **76**, 184442 (2007).
- [71] Z. NUSSINOV, G. ORTIZ. *Autocorrelations and thermal fragility of anyonic loops in topologically quantum ordered systems.* *Phys. Rev. B* **77**, 064302 (2008).
- [72] S. IBLISDIR, D. PÉREZ-GARCÍA, M. AGUADO, J. PACHOS. *Scaling law for topologically ordered systems at finite temperature.* *Phys. Rev. B* **79**, 134303 (2009).
- [73] A. KAY. *Nonequilibrium reliability of quantum memories.* *Phys. Rev. Lett.* **102**, 070503 (2009).
- [74] J. R. WOOTTON, J. K. PACHOS. *Bringing order through disorder: localization of errors in topological quantum memories.* *Phys. Rev. Lett.* **107**, 030503 (2011).
- [75] V. MURG, F. VERSTRAETE, J. I. CIRAC. *Variational study of hard-core bosons in a two-dimensional optical lattice using projected entangled pair states.* *Phys. Rev. A* **75**, 033605 (2007).
- [76] J. JORDAN, R. ORÚS, G. VIDAL, F. VERSTRAETE, J. I. CIRAC. *Classical simulation of infinite-size quantum lattice systems in two spatial dimensions.* *Phys. Rev. Lett.* **101**, 250602 (2008).
- [77] R. ORÚS, G. VIDAL. *Simulation of two-dimensional quantum systems on an infinite lattice revisited: corner transfer matrix for tensor contraction.* *Phys. Rev. B* **80**, 094403 (2009).
- [78] F. VERSTRAETE, M. M. WOLF, D. PEREZ-GARCIA, J. I. CIRAC. *Criticality, the area law, and the computational power of projected entangled pair states.* *Phys. Rev. Lett.* **96**, 220601 (2006).
- [79] S. DUSUEL, K. P. SCHMIDT, J. VIDAL. *Creation and manipulation of anyons in the Kitaev model.* *Phys. Rev. Lett.* **100**, 177204 (2008).
- [80] K. P. SCHMIDT, S. DUSUEL, J. VIDAL. *Emergent fermions and anyons in the Kitaev model.* *Phys. Rev. Lett.* **100**, 057208 (2008).
- [81] M. KAMFOR, S. DUSUEL, J. VIDAL, K. P. SCHMIDT. *Kitaev model and dimer coverings on the honeycomb lattice.* *J. Stat. Mech.: Theory Exp.* (2010) P08010.
- [82] F. WEGNER. *Flow-equations for Hamiltonians.* *Ann. Phys. (Leipzig)* **506**, 77 (1994).
- [83] C. KNETTER, G. S. UHRIG. *Perturbation theory by flow equations: dimerized and frustrated $S = 1/2$ chain.* *Eur. Phys. J. B* **13**, 209 (2000).
- [84] S. D. GLAZEK, K. G. WILSON. *Renormalization of Hamiltonians.* *Phys. Rev. D* **48**, 5863 (1993).
- [85] J. STEIN. *Flow equations and the strong-coupling expansion for the Hubbard model.* *J. Stat. Phys.* **88**, 487 (1997).
- [86] C. KNETTER, K. P. SCHMIDT, G. S. UHRIG. *The structure of operators in effective particle-conserving models.* *J. Phys. A* **36**, 7889 (2003).
- [87] C. KNETTER, K. P. SCHMIDT, G. S. UHRIG. *High order perturbation theory for spectral densities of multi-particle excitations: $S = 1/2$ two-leg Heisenberg ladder.* *Eur. Phys. J. B* **36**, 525 (2003).
- [88] A. MIELKE. *Flow equations for band-matrices.* *Eur. Phys. J. B* **5**, 605 (1998).

- [89] S. KEHREIN, A. MIELKE, P. NEU. *Flow equations for the spin-boson problem*. *Z. Phys. B* **99**, 269 (1995).
- [90] C. P. HEIDBRINK, G. S. UHRIG. *Landau's quasiparticle mapping: Fermi liquid approach and Luttinger liquid behavior*. *Phys. Rev. Lett.* **88**, 146401 (2002).
- [91] T. FISCHER, S. DUFFE, G. S. UHRIG. *Adapted continuous unitary transformation to treat systems with quasi-particles of finite lifetime*. *New J. Phys.* **12**, 033048 (2010).
- [92] N. A. DRESCHER, T. FISCHER, G. S. UHRIG. *Truncation errors in self-similar continuous unitary transformations*. *Eur. Phys. J. B* **79**, 225 (2011).
- [93] H. KRULL, N. A. DRESCHER, G. S. UHRIG. *Enhanced perturbative continuous unitary transformations*. *Phys. Rev. B* **86**, 125113 (2012).
- [94] C. KNETTER, A. BÜHLER, E. MÜLLER-HARTMANN, G. S. UHRIG. *Dispersion and symmetry of bound states in the Shastry-Sutherland model*. *Phys. Rev. Lett.* **85**, 3958 (2000).
- [95] C. KNETTER, K. P. SCHMIDT, M. GRÜNINGER, G. S. UHRIG. *Fractional and integer excitations in quantum antiferromagnetic spin 1/2 ladders*. *Phys. Rev. Lett.* **87**, 167204 (2001).
- [96] S. DUSUEL, J. VIDAL. *Continuous unitary transformations and finite-size scaling exponents in the Lipkin-Meshkov-Glick model*. *Phys. Rev. B* **71**, 224420 (2005).
- [97] K. P. SCHMIDT, J. DORIER, A. M. LÄUCHLI, F. MILA. *Supersolid phase induced by correlated hopping in spin-1/2 frustrated quantum magnets*. *Phys. Rev. Lett.* **100**, 090401 (2008).
- [98] M. KARGARIAN, H. BOMBIN, M. A. MARTIN-DELGADO. *Topological color codes and two-body quantum lattice Hamiltonians*. *New J. Phys.* **12**, 025018 (2010).
- [99] S. DUSUEL, M. KAMFOR, R. ORÚS, K. P. SCHMIDT, J. VIDAL. *Robustness of a perturbed topological phase*. *Phys. Rev. Lett.* **106**, 107203 (2011).
- [100] C. KNETTER. *Perturbative continuous unitary transformations: spectral properties of low dimensional spin systems*. Ph.D. thesis, Universität zu Köln (2003).
- [101] K. P. SCHMIDT. *Spectral properties of quasi one-dimensional quantum antiferromagnets. Perturbative continuous unitary transformations*. Ph.D. thesis, Universität zu Köln (2004).
- [102] S. DUSUEL, M. KAMFOR, K. P. SCHMIDT, R. THOMALE, J. VIDAL. *Bound states in two-dimensional spin systems near the Ising limit: a quantum finite-lattice study*. *Phys. Rev. B* **81**, 064412 (2010).
- [103] C. J. MORNINGSTAR, M. WEINSTEIN. *Contractor renormalization group technology and exact Hamiltonian real-space renormalization group transformations*. *Phys. Rev. D* **54**, 4131 (1996).
- [104] H. Y. YANG, K. P. SCHMIDT. *Effective models for gapped phases of strongly correlated quantum lattice models*. *Europhys. Lett.* **94**, 17004 (2011).
- [105] M. GELFAND, R. SINGH, D. HUSE. *Perturbation expansions for quantum many-body systems*. *J. Stat. Phys.* **59**, 1093 (1990).
- [106] M. P. GELFAND, R. R. P. SINGH. *High-order convergent expansions for quantum many particle systems*. *Adv. Phys.* **49**, 93 (2000).
- [107] J. OITMAA, C. HAMER, W. ZHENG. *Series expansion methods for strongly interacting lattice models*. Cambridge University Press, Cambridge (2006).
- [108] A. A. ABRIKOSOV, L. P. GORKOV, I. E. DZYALOSHINSKI. *Methods of quantum field theory in statistical physics*. Dover, New York (1975).
- [109] H. PRIMAS. *Generalized perturbation theory in operator form*. *Rev. Mod. Phys.* **35**, 710 (1963).
- [110] L. G. MARLAND. *Series expansions for the zero-temperature transverse Ising model*. *J. Phys. A* **14**, 2047 (1981).
- [111] L. P. KADANOFF, M. KOHMOTO. *Quantum mechanical ground states, nonlinear Schrödinger equations and linked cluster expansions*. *J. Phys. A* **14**, 1291 (1981).

- [112] E. SCHRÖDINGER. *Quantisierung als Eigenwertproblem*. *Ann. Phys. (Leipzig)* **385**, 437 (1926).
- [113] T. KATO. *On the convergence of the perturbation method. I*. *Prog. Theor. Phys.* **4**, 514 (1949).
- [114] M. TAKAHASHI. *Half-filled Hubbard model at low temperature*. *J. Phys. C* **10**, 1289 (1977).
- [115] T. DE NEEF, I. G. ENTING. *Series expansions from the finite lattice method*. *J. Phys. A* **10**, 801 (1977).
- [116] I. G. ENTING. *Finite lattice series expansions for the triangular lattice*. *J. Phys. A* **13**, L279 (1980).
- [117] H. ARISUE, T. FUJIWARA, K. TABATA. *Higher orders of the high-temperature expansion for the Ising model in three dimensions*. *Nucl. Phys. B (Proc. Suppl.)* **129-130**, 774 (2004).
- [118] B. DOUÇOT, M. V. FEIGEL'MAN, L. B. IOFFE, A. S. IOSELEVICH. *Protected qubits and Chern-Simons theories in Josephson junction arrays*. *Phys. Rev. B* **71**, 024505 (2005).
- [119] A. HAMMA, D. A. LIDAR. *Adiabatic preparation of topological order*. *Phys. Rev. Lett.* **100**, 030502 (2008).
- [120] H. W. J. BLÖTE, Y. DENG. *Cluster Monte Carlo simulation of the transverse Ising model*. *Phys. Rev. E* **66**, 066110 (2002).
- [121] H. X. HE, C. J. HAMER, J. OITMAA. *High-temperature series expansions for the (2+1)-dimensional Ising model*. *J. Phys. A* **23**, 1775 (1990).
- [122] J. OITMAA, C. J. HAMER, Z. WEIHONG. *Low-temperature series expansions for the (2+1)-dimensional Ising model*. *J. Phys. A* **24**, 2863 (1991).
- [123] E. FRADKIN, S. H. SHENKER. *Phase diagrams of lattice gauge theories with Higgs fields*. *Phys. Rev. D* **19**, 3682 (1979).
- [124] C. XU, J. E. MOORE. *Strong-weak coupling self-duality in the two-dimensional quantum phase transition of $p + ip$ superconducting arrays*. *Phys. Rev. Lett.* **93**, 047003 (2004).
- [125] C. XU, J. E. MOORE. *Reduction of effective dimensionality in lattice models of superconducting arrays and frustrated magnets*. *Nucl. Phys. B* **716**, 487 (2005).
- [126] Z. NUSSINOV, E. FRADKIN. *Discrete sliding symmetries, dualities, and self-dualities of quantum orbital compass models and $p + ip$ superconducting arrays*. *Phys. Rev. B* **71**, 195120 (2005).
- [127] R. RAUSSENDORF, H. J. BRIEGEL. *A one way quantum computer*. *Phys. Rev. Lett.* **86**, 5188 (2001).
- [128] A. C. DOHERTY, S. D. BARTLETT. *Identifying phases of quantum many-body systems that are universal for quantum computation*. *Phys. Rev. Lett.* **103**, 020506 (2009).
- [129] H. KALIS, D. KLAGGES, R. ORÚS, K. P. SCHMIDT. *Fate of the cluster state on the square lattice in a magnetic field*. *Phys. Rev. A* **86**, 022317 (2012).
- [130] K. I. KUGEL', D. I. KHOMSKII. *The Jahn-Teller effect and magnetism: transition metal compounds*. *Sov. Phys. Usp.* **25**, 231 (1982).
- [131] J. DORIER, F. BECCA, F. MILA. *Quantum compass model on the square lattice*. *Phys. Rev. B* **72**, 024448 (2005).
- [132] H. D. CHEN, C. FANG, J. HU, H. YAO. *Quantum phase transition in the quantum compass model*. *Phys. Rev. B* **75**, 144401 (2007).
- [133] S. WENZEL, W. JANKE. *Monte Carlo simulations of the directional-ordering transition in the two-dimensional classical and quantum compass model*. *Phys. Rev. B* **78**, 064402 (2008).
- [134] R. ORÚS, A. C. DOHERTY, G. VIDAL. *First order phase transition in the anisotropic quantum orbital compass model*. *Phys. Rev. Lett.* **102**, 077203 (2009).
- [135] C. DOMB, M. F. SYKES. *On metastable approximations in co-operative assemblies*. *Proc. Roy. Soc. A* **235**, pp. 247 (1956).

- [136] C. DOMB, M. F. SYKES. *On the susceptibility of a ferromagnetic above the Curie point.* *Proc. Roy. Soc. A* **240**, pp. 214 (1957).
- [137] A. J. GUTTMANN. *Asymptotic analysis of power-series expansions.* In *Phase transitions and critical phenomena*, edited by C. DOMB, J. L. LEBOWITZ, volume 13. New York: Academic Press (1989).
- [138] A. J. GUTTMANN. *On the critical behaviour of self-avoiding walks. II.* *J. Phys. A* **22**, 2807 (1989).
- [139] H. PADÉ. *Sur la représentation approchée d'une fonction par des fractions rationnelles.* *Ann. Ecole Norm.* **9**, 3 (1892).
- [140] G. A. BAKER, P. R. GRAVES-MORRIS. *Padé approximants.* Encyclopaedia of mathematics and its applications. Addison-Wesley, Reading, MA (1981).
- [141] A. J. GUTTMANN, G. S. JOYCE. *On a new method of series analysis in lattice statistics.* *J. Phys. A* **5**, L81 (1972).
- [142] D. L. HUNTER, G. A. BAKER. *Methods of series analysis. III. Integral approximant methods.* *Phys. Rev. B* **19**, 3808 (1979).
- [143] M. E. FISHER, H. AU-YANG. *Inhomogeneous differential approximants for power series.* *J. Phys. A* **12**, 1677 (1979).
- [144] J. J. REHR, G. S. JOYCE, A. J. GUTTMANN. *A recurrence technique for confluent singularity analysis of power series.* *J. Phys. A* **13**, 1587 (1980).
- [145] V. I. YUKALOV, E. P. YUKALOVA. *Self-similar perturbation theory.* *Ann. Phys.* **277**, 219 (1999).
- [146] E. P. YUKALOVA, V. I. YUKALOV, S. GLUZMAN. *Self-similar factor approximants for evolution equations and boundary-value problems.* *Ann. Phys.* **323**, 3074 (2008).
- [147] S. GLUZMAN, V. YUKALOV. *Self-similar extrapolation from weak to strong coupling.* *J. Math. Chem.* **48**, 883 (2010).
- [148] S. GLUZMAN, V. I. YUKALOV, D. SORNETTE. *Self-similar factor approximants.* *Phys. Rev. E* **67**, 026109 (2003).
- [149] J. S. R. CHISHOLM. *Rational approximants defined from double power series.* *Math. Comp.* **27**, 841 (1973).
- [150] M. E. FISHER, R. M. KERR. *Partial differential approximants for multicritical singularities.* *Phys. Rev. Lett.* **39**, 667 (1977).
- [151] G. VIDAL. *Efficient classical simulation of slightly entangled quantum computations.* *Phys. Rev. Lett.* **91**, 147902 (2003).
- [152] P. CORBOZ, R. ORÚS, B. BAUER, G. VIDAL. *Simulation of strongly correlated fermions in two spatial dimensions with fermionic projected entangled-pair states.* *Phys. Rev. B* **81**, 165104 (2010).
- [153] F. VERSTRAETE, J. I. CIRAC. *Matrix product states represent ground states faithfully.* *Phys. Rev. B* **73**, 094423 (2006).
- [154] M. B. HASTINGS. *Solving gapped Hamiltonians locally.* *Phys. Rev. B* **73**, 085115 (2006).
- [155] S. MONDAL, D. SEN, K. SENGUPTA. *Non-equilibrium Dynamics of Quantum Systems: Order Parameter Evolution, Defect Generation, and Qubit Transfer*, volume 802 of *Lecture Notes in Physics*. Springer Berlin / Heidelberg (2010).
- [156] M. HASENBUSCH. *Finite size scaling study of lattice models in the three-dimensional Ising universality class.* *Phys. Rev. B* **82**, 174433 (2010).
- [157] S. V. ISAKOV, P. FENDLEY, A. W. W. LUDWIG, S. TREBST, M. TROYER. *Dynamics at and near conformal quantum critical points.* *Phys. Rev. B* **83**, 125114 (2011).
- [158] F. ALET, J. L. JACOBSEN, G. MISGUICH, V. PASQUIER, F. MILA, M. TROYER. *Interacting classical dimers on the square lattice.* *Phys. Rev. Lett.* **94**, 235702 (2005).

- [159] F. ALET, Y. IKHLEF, J. L. JACOBSEN, G. MISGUICH, V. PASQUIER. *Classical dimers with aligning interactions on the square lattice*. *Phys. Rev. E* **74**, 041124 (2006).
- [160] R. J. BAXTER. *Eight-vertex model in lattice statistics*. *Phys. Rev. Lett.* **26**, 832 (1971).
- [161] R. J. BAXTER. *Exactly Solved Models in Statistical Mechanics*. Academic Press, London (1982).
- [162] F. C. ALCARAZ, M. J. MARTINS. *Critical spin models with continuously varying exponents*. *Phys. Rev. Lett.* **61**, 1529 (1988).
- [163] E. ARDONNE, P. FENDLEY, E. FRADKIN. *Topological order and conformal quantum critical points*. *Ann. Phys.* **310**, 493 (2004).
- [164] C. KNETTER, K. P. SCHMIDT, G. S. UHRIG. *Multi-particle excitations and spectral densities in quantum spin-systems*. *Physica B* **312**, 527 (2002).
- [165] K. P. SCHMIDT, G. S. UHRIG. *Spectral properties of magnetic excitations in cuprate two-leg ladder systems*. *Mod. Phys. Lett. B* **19**, 1179 (2005).
- [166] X. G. WEN. *Mean-field theory of spin-liquid states with finite energy gap and topological orders*. *Phys. Rev. B* **44**, 2664 (1991).
- [167] D. G. PETTIFOR, D. L. WEAIRE. *The recursion method and its applications*. In *Solid-State Sciences*, volume 58, p. 22. Springer-Verlag (1984).
- [168] E. R. GAGLIANO, C. A. BALSEIRO. *Dynamical properties of quantum many-body systems at zero temperature*. *Phys. Rev. Lett.* **59**, 2999 (1987).
- [169] P. M. STEVENSON. *Optimized perturbation theory*. *Phys. Rev. D* **23**, 2916 (1981).
- [170] L. JIANG, G. K. BRENNEN, A. V. GORSHKOV, K. HAMMERER, M. HAFEZI, E. DEMLER, M. D. LUKIN, P. ZOLLER. *Anyonic interferometry and protected memories in atomic spin lattices*. *Nat. Phys.* **4**, 482 (2008).
- [171] G. JACKELI, G. KHALIULLIN. *Mott insulators in the strong spin-orbit coupling limit: From Heisenberg to a quantum compass and Kitaev models*. *Phys. Rev. Lett.* **102**, 017205 (2009).
- [172] M. KAMFOR, S. DUSUEL, K. P. SCHMIDT, J. VIDAL. *Fate of Dirac points in a vortex superlattice*. *Phys. Rev. B* **84**, 153404 (2011).
- [173] H. YAO, S. A. KIVELSON. *Exact chiral spin liquid with non-Abelian anyons*. *Phys. Rev. Lett.* **99**, 247203 (2007).
- [174] S. YANG, D. L. ZHOU, C. P. SUN. *Mosaic spin models with topological order*. *Phys. Rev. B* **76**, 180404 (2007).
- [175] S. DUSUEL, K. P. SCHMIDT, J. VIDAL, R. L. ZAFFINO. *Perturbative study of the Kitaev model with spontaneous time-reversal symmetry breaking*. *Phys. Rev. B* **78**, 125102 (2008).
- [176] S. MANDAL, N. SURENDRAN. *Exactly solvable Kitaev model in three dimensions*. *Phys. Rev. B* **79**, 024426 (2009).
- [177] G. BASKARAN, G. SANTHOSH, R. SHANKAR. *Exact quantum spin liquids with Fermi surfaces in spin-half models*. *arXiv:0908.1614v3* (2009).
- [178] H. YAO, S. C. ZHANG, S. A. KIVELSON. *Algebraic spin liquid in an exactly solvable spin model*. *Phys. Rev. Lett.* **102**, 217202 (2009).
- [179] E. H. LIEB. *Flux phase of the half-filled band*. *Phys. Rev. Lett.* **73**, 2158 (1994).
- [180] M. STONE, S.-B. CHUNG. *Fusion rules and vortices in $p_x + ip_y$ superconductors*. *Phys. Rev. B* **73**, 014505 (2006).
- [181] V. LAHTINEN, G. KELLS, A. CAROLLO, T. STITT, J. VALA, J. K. PACHOS. *Spectrum of the non-Abelian phase in Kitaev's honeycomb lattice model*. *Ann. Phys.* **323**, 2286 (2008).
- [182] M. KAMFOR. *Effective low-energy theory for the kagomerized Kitaev model*. Master's thesis, TU Dortmund (2009).

- [183] X. Y. FENG, G. M. ZHANG, T. XIANG. *Topological characterization of quantum phase transitions in a spin-1/2 model*. *Phys. Rev. Lett.* **98**, 087204 (2007).
- [184] J. E. AVRON, R. SEILER, B. SIMON. *Homotopy and quantization in condensed matter physics*. *Phys. Rev. Lett.* **51**, 51 (1983).
- [185] S. S. CHERN. *Characteristic classes of Hermitian manifolds*. *Ann. Math.* **47**, 85 (1946).
- [186] G. KELLS, J. KAILASVUORI, J. K. SLINGERLAND, V. J. *Kaleidoscope of topological phases with multiple Majorana species*. *New J. Phys.* **13**, 095014 (2011).
- [187] V. LAHTINEN, A. W. W. LUDWIG, J. K. PACHOS, S. TREBST. *Topological liquid nucleation induced by vortex-vortex interactions in Kitaev's honeycomb model*. *Phys. Rev. B* **86**, 075115 (2012).
- [188] A. BERMUDEZ, N. GOLDMAN, A. KUBASIAK, M. LEWENSTEIN, M. A. MARTIN-DELGADO. *Topological phase transitions in the non-Abelian honeycomb lattice*. *New J. Phys.* **12**, 033041 (2010).
- [189] P. R. WALLACE. *The band theory of graphite*. *Phys. Rev.* **71**, 622 (1947).
- [190] R. RAMMAL. *Landau level spectrum of Bloch electrons in a honeycomb lattice*. *J. Phys. France* **46**, 1345 (1985).
- [191] K. S. NOVOSELOV, A. K. GEIM, S. V. MOROZOV, D. JIANG, Y. ZHANG, S. V. DUBONOS, I. V. GRIG ORIEVA, A. A. FIRSOV. *Electric field effect in atomically thin carbon films*. *Science* **306**, 666 (2004).
- [192] A. H. CASTRO NETO, F. GUINEA, N. M. R. PERES, K. S. NOVOSELOV, A. K. GEIM. *The electronic properties of graphene*. *Rev. Mod. Phys.* **81**, 109 (2009).
- [193] K. ESAKI, M. SATO, M. KOHMOTO, B. I. HALPERIN. *Zero modes, energy gap, and edge states of anisotropic honeycomb lattice in a magnetic field*. *Phys. Rev. B* **80**, 125405 (2009).
- [194] I. SNYMAN. *Gapped state of a carbon monolayer in periodic magnetic and electric fields*. *Phys. Rev. B* **80**, 054303 (2009).
- [195] F. GUINEA, T. LOW. *Band structure and gaps of triangular graphene superlattices*. *Phil. Trans. R. Soc. A* **368**, 5391 (2010).
- [196] X. LIN, H. WANG, H. PAN, H. XU. *Gap opening in single-layer graphene in the presence of periodic scalar and vector potentials within the continuum model*. *Phys. Lett. A* **376**, 584 (2012).
- [197] R. PEIERLS. *Zur Theorie des Diamagnetismus von Leitungselektronen*. *Z. Phys.* **80**, 763 (1933).
- [198] K. ASANO, C. HOTTA. *Designing Dirac points in two-dimensional lattices*. *Phys. Rev. B* **83**, 245125 (2011).
- [199] Y. HASEGAWA, P. LEDERER, T. M. RICE, P. B. WIEGMANN. *Theory of electronic diamagnetism in two-dimensional lattices*. *Phys. Rev. Lett.* **63**, 907 (1989).
- [200] G. MONTAMBAUX. *Comment on "Theory of electronic diamagnetism in two-dimensional lattices"*. *Phys. Rev. Lett.* **63**, 1657 (1989).
- [201] Y. HASEGAWA, Y. HATSUGAI, M. KOHMOTO, G. MONTAMBAUX. *Stabilization of flux states on two-dimensional lattices*. *Phys. Rev. B* **41**, 9174 (1990).
- [202] N. R. COOPER. *Optical flux lattices for ultracold atomic gases*. *Phys. Rev. Lett.* **106**, 175301 (2011).
- [203] N. R. COOPER, J. DALIBARD. *Optical flux lattices for two-photon dressed states*. *Europhys. Lett.* **95**, 66004 (2011).
- [204] D. JARIWALA, A. SRIVASTAVA, P. M. AJAYAN. *Graphene synthesis and band gap opening*. *J. Nanosci. Nanotechnol.* **11**, 6621 (2011).
- [205] F. D. M. HALDANE. *Model for a quantum Hall effect without Landau levels: Condensed-matter realization of the "parity anomaly"*. *Phys. Rev. Lett.* **61**, 2015 (1988).

Declaration of Authorship

I, Michael Kamfor, declare that this thesis titled, “Robustness and spectroscopy of the toric code in a magnetic field” and the work presented in it are my own. I confirm that:

- This work was done wholly or mainly while in candidature for a research degree at the TU Dortmund and the UPMC Paris.
- Where any part of this thesis has previously been submitted for a degree or any other qualification at this University or any other institution, this has been clearly stated.
- Where I have consulted the published work of others, this is always clearly attributed.
- Where I have quoted from the work of others, the source is always given. With the exception of such quotations, this thesis is entirely my own work.
- I have acknowledged all main sources of help.
- Where the thesis is based on work done by myself jointly with others, I have made clear exactly what was done by others and what I have contributed myself.

Signed: _____

Date: _____

Acknowledgements

I would first like to thank both of my thesis advisers, Dr. Kai P. Schmidt and Dr. Julien Vidal. I appreciate their excellent assistance and guidance throughout my studies and during the preparation of this thesis. I think that the close collaboration we have established during the last few years has been very rewarding.

I substantially profited from valuable advices and important ideas of Dr. Sébastien Dusuel.

I thank Prof. Philippe Lecheminant, Prof. Roderich Moessner, and Prof. Götz S. Uhrig for being the referees of this work.

Dr. Román Orús has provided the iPEPS data for the toric code in a field, for which I am very thankful.

I have enjoyed being able to work in Dortmund as well as Paris and having met many different people and great physicists. I thank my colleagues at the Lehrstuhl für Theoretische Physik I/II in Dortmund and the LPTMC in Paris for a friendly atmosphere, in particular Marc D. Schulz (who also proof-read the manuscript), Nils A. Drescher, HongYu Yang, Kris Cöster, Dominik Ixert, Michael Powalski, Björn Zelinski, Daniel Klagges, Karim Essafi and Emmanuel Jolibois. Furthermore, I thank Dr. Carsten Raas for technical assistance.

I thank my friends and family, especially Ulla Gleich, for their support and patience.